This is to certify that the
dissertation entitled

SECONDARY STRUCTURE AND MEMBRANE INSERTION OF THE MEMBRANE-ASSOCIATED INFLUENZA FUSION PEPTIDE PROBED BY SOLID-STATE NUCLEAR MAGNETIC RESONANCE

presented by

Yan Sun

has been accepted towards fulfillment
of the requirements for the

Ph.D. degree in Department of Chemistry

David P. Weliky
Major Professor's Signature

June 11, 2009
Date

SECONDARY STRUCTURE AND MEMBRANE INSERTION OF THE MEMBRANE-ASSOCIATED INFLUENZA FUSION PEPTIDE PROBED BY SOLID-STATE NUCLEAR MAGNETIC RESONANCE

By

Yan Sun

A DISSERTATION

Submitted to
Michigan State University
in partial fulfillment of the requirements
for the degree of

DOCTOR OF PHILOSOPHY

Chemistry

2009

ABSTRACT

SECONDARY STRUCTURE AND MEMBRANE INSERTION OF THE MEMBRANE-ASSOCIATED INFLUENZA FUSION PEPTIDE PROBED BY SOLID-STATE NUCLEAR MAGNETIC RESONANCE

By

Yan Sun

An initial step in infection by the influenza virus is joining or "fusion" of the membrane of the virus with the membrane of the endosome of the host cell and consequent release of the viral nucleocapsid into the host cell cytoplasm. Fusion is mediated by the influenza viral hemagglutinin protein (HA) which is activated by the low pH of the endosome. The ~20 N-terminal amino acids of the HA_2 domain of HA are known as the 'fusion peptide' (IFP) which binds to the endosomal membrane and plays a critical role in fusion catalysis. The chemically synthesized IFP induces vesicle fusion in a pH-dependent manner and is a model system for understanding some aspects of viral fusion.

In this work, solid-state NMR was used to probe the structure of membrane-associated IFP and its correlation with fusogenic function. It was observed that IFP has predominant helical conformation in membranes lacking cholesterol and β strand conformation in membranes that contained cholesterol. For either membrane composition, the overall IFP conformation has little dependence on pH. Low pH triggered IFP- induced fusion between vesicles that did not contain cholesterol or between vesicles that contained cholesterol. The combination of structural and functional data suggested that both the helical and the β strand conformations of IFP could induce vesicle fusion.

In membranes which lacked cholesterol, IFP was determined to have the helix-turn-helix motif with the turn formed around Glu-11 and/or Asn-12. The N-terminal helix extends from Leu-2 to Ile-10 or from Leu-2 to Glu-11. The first conformation was observed at both pHs and the latter one was only observed at pH 5.0. The ^{13}CO–^{31}P and ^{13}CO–^{19}F distance measurements by the REDOR technique indicated that both the IFP N- and C-termini have close contact to the lipid phosphate headgroups and the middle region of IFP is inserted into a single leaflet of the membrane. Based on these data, we proposed an inverted boomerang IFP structural model in membranes without cholesterol. More contacts between IFP labeled ^{13}COs and the membrane bilayer center were detected for membrane-associated IFP at pH 5.0 which may be correlated to the more deeply inserted or more population of inserted IFP at fusogenic pH 5.0 relative to the non-fusogenic pH 7.4.

In addition, static ^{15}N chemical shifts and ^{15}N-^{1}H dipolar couplings were used to probe the tilt angle of the IFP N-terminal helix relative to the bicelle normal. The data were well fitted with a model of the fast rotation of the IFP N-terminal helix about its own axis with a tilt angle of ~45° from the bicelle normal. The motion and orientation of the IFP N-terminal helix are intrinsic properties of the IFP sequence and are independent of the sample pH and the mutation of Gly-1 to Ser or Val.

Dedicated to Wei Qiang

ACKNOWLEDGEMENTS

It is a great pleasure to express my gratitude to all the people who have helped me to complete the dissertation.

First and foremost, I would like to sincerely thank Prof. David Weliky for his guidance, understanding, encouragement and incredible patience. He has been a very supportive advisor and provided me lots of good ideas throughout my graduate career, yet he has always given me great freedom to do research which allowed me to grow into an independent scientist. He always has faith in my ability and he's willing to share his own tough or happy experience with me to encourage me to overcome difficulties and believe in myself. When he reviewed my first paper, he asked me to sit at his side and discussed with me how to revise each paragraph. That was the time when I tremendously improved my scientific writing ability and start to think and write as a reviewer.

I'd also like to thank all my committee members, Prof. John McCracken, Prof. Gavin Reid and Prof. James Geiger, for their input, valuable discussions and guidance over the years. My gratitude also goes to Prof. Michael Feig, who is generous with his time and insights, both on my research and on my career. He has been a good source in discussions about my research project and his ideas greatly inspired me.

I am grateful for the help from the Max T. Rogers NMR facility, MSU Mass Spectrometer Facility and the CTA Biomolecular NMR Facility. I especially appreciate the expertise and patience of Mr. Kermit Johnson and Dr. Daniel Holmes. I would like to acknowledge and thank Dr. Jiadi Xu and Dr. Jochem

Struppe for the help they gave me on the 900 MHz Bruker spectrometer. Dr. Jiadi Xu kindly assisted me in the static 2D NMR experiments and generously passed me his own experience with NMR hardware and software. I also extend my gratitude to Afra Panahi for her warm heart and the useful discussions on research.

I would like to take the opportunity to thank the former and current members in Prof. David Weliky's group: Dr. Charles Gabrys, Dr. Kelly Sackett, Dr. Jaime Curtis-Fisk, Matthew Nethercott, Erica Schwander, Scott Schmick, Jacob Billcheck, Dr. Zhaoxiong Zheng, Dr. Michele Bodner and Angela Karst. They are a wonderful group of people to work with. I am particularly thankful to Dr. Zhaoxiong Zheng, not only being a great senior to learn NMR from, but also being a good friend who always provides me good advices in so many ways.

Finally, and most importantly, I would like to thank my husband Wei Qiang, as the dearest friend and an amazingly supporting colleague. It is his support, encouragement and unwavering love which have kept me walking all the way up to where I am today. I thank my parents for their love and indulgence, allowing me to pursuit anything I want. Also, I thank Qiang's parents, who have provided me unending support and encouragement and showed me the true value of hard working.

TABLE OF CONTENTS

LIST OF TABLES

LIST OF FIGURES

LIST OF SYMBOLS AND ABBREVIATIONS

HIV	Human immunodeficiency virus
AIDS	Acquired immunodeficiency syndrome
HA	Hemagglutinin
IFP	Influenza fusion peptide
HFP	HIV fusion peptide
CD	Circular dichroism
ESR	Electron spin resonance
FTIR	Fourier transform infrared
NMR	Nuclear magnetic resonance
MAS	Magic angle spinning
RF	Radiofrequency
CP	Cross polarization
REDOR	Rotational-echo double resonance
r	Distance
d	Dipolar coupling
fpCTDQBU	Constant-time double-quantum buildup with finite pulses
PDSD	Proton-driven spin diffusion
PISEMA	Polarization-inversion spin exchange at the magic angle
FMOC	9-fluorenylmethoxycarbonyl
DTPC	1,2-di-O-tetradecyl-*sn*-glycero-3-phosphocholine
DTPG	1,2-di-O-tetradecyl-*sn*-glycero-3-[phospho-*rac*-(1-glycerol)]
POPC	1-palmitoyl-2-oleoyl-*sn*-glycero-3-phosphocholine

DHPC	1,2-Di-O-Hexyl-*sn*-Glycero-3-Phosphocholine
16-^{19}F-DPPC	1-palmitoyl-2-(16-fluoropalmitoyl)-*sn*-glycero-3-Phosphocholine
POPG	1-palmitoyl-2-oleoyl-*sn*-glycero-3-[phospho-*rac*-(1-glycerol)]
$DMPC_{d54}$	1,2-Dimyristoyl-D54-*sn*-Glycero-3-Phosphocholine
5-^{19}F-DPPC	1-palmitoyl-2-(5-fluoropalmitoyl)-*sn*-glycero-3-Phosphocholine
HEPES	*N*-(2-hydroxyethyl)-piperazine-*N'*-2-ethanesulfonic acid
MES	2-(*N*-morpholino)-ethanesulfonic acid
HFPmn	HFP monomer
HFPdm	HFP dimer
CHOL	Cholesterol
NAV	N-acetylvaline
TPPM	two- pulse phase modulation
CW	Continuous wave
PI-WIM-z	polarization inversion – windowless isotropic mixing – polarization exchange between z-component of magnetization
τ	Dephasing time
CSA	Chemical shift anisotropy
γ_N, γ_H	Gyromagnetic ratios of ^{15}N and ^{1}H
σ	Chemical shift tensor
ϑ	Angle between N-H vector and the magnetic field
φ, ψ	Peptide dihedral angles
σ_{11}, σ_{22}, σ_{33}	Principal values of the chemical shift tensors

$\nu_{\|\|}$	Rigid limit ^{15}N-^{1}H dipolar splitting
ρ	Rotational angle about the helix axis
τ	Tilt angle of the helical axis with respect to the magnetic field
α, β	Euler angles between the helix rotational axis and the principal axes of the rigid lattice chemical shift tensors
θ	Angle between the helix rotational axis and the external magnetic field
η	Angle between the N-H vector and the helix rotational axis
ζ	Angle between the N-H vector and the principal axis σ_{33}
λ	Angle between the bicelle normal and the external magnetic field
θ'	Angle between the helix axis and the bicelle normal

Chapter 1 Introduction

1.1 BACKGROUND

Enveloped viruses such as influenza, chicken pox, measles (Rubeola), and AIDS (HIV) are encapsulated by a membrane which is acquired upon budding from an infected cell. Penetration of viruses into the target cells requires the joining or "fusion" of viral and host cell membranes.[1-3] After the fusion process, a fusion pore is formed across the two membranes which allows the viral gene to enter its host, as evidenced by the electron micrography of HIV viral infection (cf. Figure 1).[4] Although the membrane free energies are approximately equal before and after fusion has occurred, membrane fusion rates are typically very slow in the absence of a catalyst. For this reason, enveloped viruses contain "fusion proteins" which catalyze the fusion process. For a subgroup of enveloped viruses termed type I such as HIV and influenza, their fusion proteins share similar structural and folding motifs, suggesting a comparable fusion mechanism.[5] Therefore the clarification of the structural features of fusion proteins and the consequent understanding of the fusion mechanism have been increasingly viewed as bases of rational antiviral drug designs for type I viruses in general. In addition, the mechanism of viral/host cell fusion induced by fusion proteins resembles that of intracellular vesicle fusion mediated by the SNARE proteins,[6] so investigating the function of viral fusion proteins may provide additional insight into the understanding of cellular transport processes.

For all the fusion proteins, the N-terminal region, termed the fusion peptide (FP), is relatively apolar and plays a critical role in initiating fusion. Synthetic FP

analogs have been reported to induce vesicle fusion and the red blood cell fusion in the absence of the rest of fusion proteins.[7-9] The site directed mutation/fusion activity relationship are similar for viral/cell fusion and FP-induced vesicle fusion.[10-14] Therefore, understanding the structure of fusion peptides should be important for understanding the fusion mechanism.

The overall goal of our research is to understand some aspects of the fusion peptide-induced membrane fusion. I choose influenza fusion peptide (IFP) to carry out most of my research on the studies of FP structure and the FP/membrane interaction. Because influenza viral fusion is induced by a simple change of pH (cf. Figure 2) rather than binding to the host cell membrane proteins (as in the case of HIV),[15] influenza served as the most studied system for fusion research. My approach has been to study most of the critical aspects of the membrane-associated IFP, including the secondary structure, IFP membrane location and the insertion angle of helical form of IFPs.

1. Structural Biology of Viral Fusion Proteins

Membrane fusion is characterized by the mixing of lipid molecules of viral and host cell membranes and the lipid bilayers eventually merge into one united whole membrane. There are four proposed steps in viral/host cell membrane fusion:[16] (1) Viral/host cell bindings; (cf. Figure 1a) (2) formation of small fusion pores through which electrolytes can pass; (3) mixing of viral and host cell lipids; (cf. Figure 1b) (4) formation of a large fusion pore through which large molecules can pass and creation of a single virus/host cell moiety. (cf. Figure 1c and d)

Steps (1), (3) and (4) were experimentally observed as shown by the electron micrograph in Figure 1. There is no experimental proof for the step (2). The fusion process is controlled on a temporal and molecular basis such that the host cell remains intact and can protect the viral genetic material until

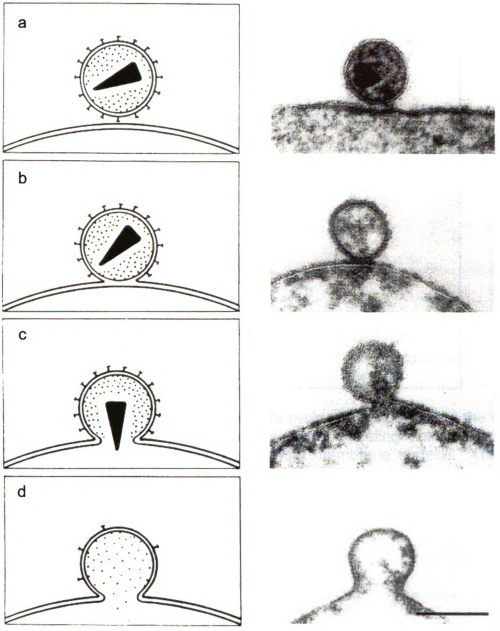

Figure 1. HIV Infection: (Left) Model of infection process. (Right) Freeze fracture electron micrography of a virion.

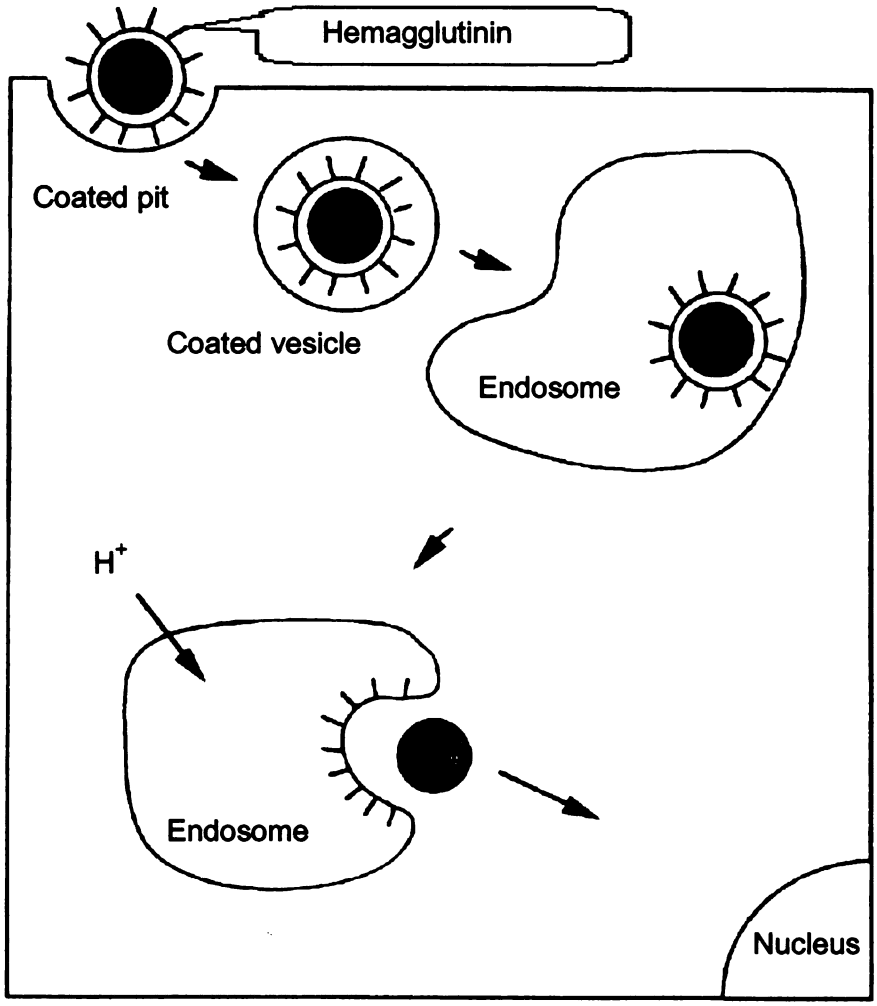

Figure 2. The first half of the influenza viral life cycle. The virus enters the cell by endocytosis. The pH drops in the endosome, initiating conformational changes of the hemagglutinin protein on the viral membrane surface. These conformational changes ultimately lead to fusion of the viral and endosomal membranes and release of the viral contents into the cell.

infection. The activation energy barrier between the initial two separate bilayers and the merged state is hypothesized to be provided by the conformational change of fusion proteins.

For the influenza virus, the fusion protein is hemagglutinin (HA) and is abundant on the surface of the virus. HA consists of a HA1 domain that lies outside the virus and a HA2 domain which is composed of a ~185-residue ectodomain that is outside the virus, a ~25-residue transmembrane domain, and a ~10-residue endodomain that is inside the virus.[17] Prior to infection of a respiratory epithelial host cell, the pH of the virus exterior is 7.4 (cf. Figure 2) and the HA1 domain and the HA2 ectodomain are joined by a single disulfide bond. There is a crystal structure of HA1 and the HA2 ectodomain at pH 7.5 which showed that a HA trimer is formed by association of three HA2 ectodomains and that the three HA1 partners are located on the outside of the HA2 core (cf. Figure 3a).[17] The structure undergoes a drastic change in the process of fusion which is shown in Figure 3[18] and 4[19]. The fusion starts from binding of the HA1 domains to the terminal sialic acids of glycoproteins and glycolipids on the surface of a host cell which leads to endocytosis of the virus into the cell. The cell physiology results in pumping of protons into the endosome and lowering of the pH of the endosome to ~5.2 (cf. Figure 2). At this pH, HA has a different equilibrium structural state which is characterized by cleavage of the disulfide bond between HA1 and HA2, release of HA1 from the HA2 trimer, and a major conformational change of the HA2 molecules within the trimer (cf. Figure 4). Some of these pH-dependent structural differences have been understood from comparison of the

previously discussed pH 7.5 HA1/HA2 structure and a pH 5 structure of a HA2 trimer for which residues 38-175 of HA2 were resolved as shown in figure 3b.[18] Fusion between the viral membrane and the endosomal membrane occurs only after these structural changes have occurred and leads to release of the viral nucleocapsid into the host cell cytoplasm and subsequent insertion of the viral genetic material into the host genome.[15, 20]

The ~20 N-terminal residues of HA2 domain are relatively apolar and are known as the fusion peptide or IFP. The IFP plays a critical role in fusion, as evidenced by disruption of fusion activity for HA with point mutations in the IFP. In the pH 7.5 HA1/HA2 structure, the IFP was buried within the HA1/HA2 trimer. The pH 5.0 HA2 structure did not include the IFP or the transmembrane domain but did suggest that these regions are near the same end of the molecule. Other experiments have shown that after fusion has occurred, the IFP and transmembrane domain of HA2 are the only HA2 regions which are deeply membrane-inserted.[21-25] The overall literature data support a model in which the lowered pH leads to exposure of the IFP followed by IFP insertion into the endosomal membrane and then membrane fusion. The role of the IFP in membrane fusion catalysis is probably related to its perturbation of the endosomal membrane.

Peptides with the IFP sequence have been studied as models to understand the role of the IFP in influenza viral fusion and there is experimental evidence which supports the utility of the peptide model system. For example, introduction of the IFP into a vesicle solution results in mixing of lipids between

vesicles. Such mixing is one characteristic of vesicle fusion. There has also been investigation of IFPs with the same point mutations as were studied in the IFP domains of whole HA proteins. There are good correlations in the mutation-activity relationships of IFP-induced vesicle fusion and HA-catalyzed fusion of cell membranes.[10] Another interesting aspect of IFP is that much greater vesicle fusion is induced at pH 5 than at pH 7.4. A direct comparison cannot be made to HA-induced fusion because the IFP is buried in HA at pH 7.4 whereas the IFP peptide is initially free in solution at both pHs. However, the pH-dependence of IFP-induced vesicle fusion has still been studied in part because comparison of IFPs at different pHs is more straightforward than comparison of wild-type and mutant IFPs.[15, 26-28] It is interesting that pH-dependent vesicle fusion has also been observed for HA2 constructs which contain the IFP including a full ectodomain "FHA2"construct .[29] At pH 5 and lower HA2:lipid ratios, FHA2 induces ~10-fold greater vesicle fusion than does IFP.

In the pH 7.5 HA1/HA2 crystal structure, the buried IFP has an extended conformation.[17, 30] There have been NMR structures of the IFP peptide in detergent micelles at pH 5 which showed a N-terminal helix from residues 2-10 followed by a turn followed by a C-terminal 3_{10}-helix from residues 13-18. The angle between the axes of the two helices was ~105° (cf. Figure 5a). The IFP structure in detergent at pH 7.4 showed a N-terminal helix from residues 2-9 followed by a turn and a C-terminal region with mostly extended secondary structure (cf. Figure 5b).[31, 32] For pH 5 samples containing IFP associated with membranes which lack cholesterol, IFP structure has been studied by circular

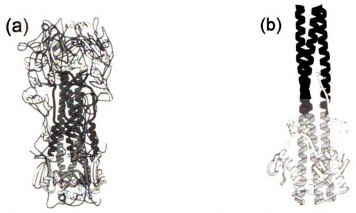

Figure 3. Ribbon diagram of Influenza hemagglutinin glycoprotein at (a) pH 7.4[17] and (b) pH 5.0[18]. The structure at pH 7.4 included residues 4-328 of HA1 and residues 1-175 of HA2. The structure at pH 5.0 shows residues 12-16 of HA1 and residues 40-153 of HA2 for one monomer; residues 11-16 of HA1 and residues 40-162 of HA2 for another monomer; and residues 10-17 of HA1 and residues 40-162 of HA2 for the third monomer.

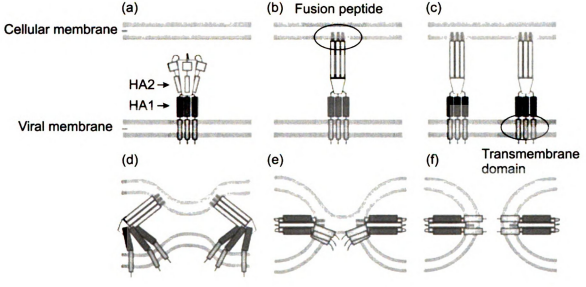

Figure 4. Proposed mechanism for Influenza membrane fusion.[19] (a) HA protein conformation at pH 7.4. (b) Upon exposure to the low pH found in endosomes, HA forms an extended conformation and the N-terminal fusion peptide inserts into the target membrane. (c) Several HA proteins are thought to be involved. (d) Protein refolding begins and the released free energy cause the membranes to bend to each other. (e) Formation of the hemifusion intermediate in which the outer leaflets of membranes mix. (f) Protein refolding completes and the fusion pore is formed. The fusion peptide and the transmembrane domain are in the same membrane and interact with each other. Only the HA structures in (a) and (f) have been observed by crystallography but many biological data support other proposed steps.

dichroism (CD), infrared, electron spin resonance (ESR), and solid-state nuclear magnetic resonance (NMR) spectroscopies.[33-35] There is general agreement that IFP adopts helical form at pH 5.

As noted above, the IFP induces much greater vesicle fusion at pH 5.0 than at pH 7.4 and there have been some studies of membrane-associated structure at the two pHs to detect structural differences which may correlate with the different functional activities. In membranes without cholesterol, there appear to be similar fractions of helical conformation at the two pHs as determined by analysis of CD and infrared spectra.[33] The pH dependence of the membrane location of the N-terminal IFP helix has also been investigated and was motivated by the idea that the IFP membrane location is related to membrane perturbation and fusion activity. For example, infrared spectra have provided information about the angle between an IFP helix axis and the membrane normal and the derived angles have been 45° or 65°, both independent of pH.[33, 36] The membrane insertion depths of particular IFP residues have been investigated with analysis of effects of relaxation agents on the ESR linewidths of spin-labeled IFPs, which can provide information on the IFP helix orientation relative to the membrane bilayer normal. In one study, a 15° degree change was observed for the helix formed by the N-terminal first ten residues (cf. Figure 5).[19] In some contrast, only a 3° helix orientational change was detected in similar ESR study using the IFP region of a HA2 ectodomain construct.

There have also been molecular dynamics investigations of IFP in detergent and in membranes[37-42] . Several of these studies showed structures

similar to those observed by NMR in detergent [37, 40, 41]. In some contrast, another study found that the IFP is a single continuous helix located near the phosphate headgroups with an angle of 78° between the helix axis and the membrane normal [42]. In this study, the pH dependence was also examined by using different protonation states of glutamic acids or aspartic acids and it is shown that there was little pH dependence of the equilibrium structure or membrane location. This study also considered an IFP trimer because of the trimeric oligomerization of HA2 and found a variety of stable membrane locations and tilt angles for the three IFP helices. For example, one configuration had the three helices located close to the phosphate headgroups with tilt angles of 80°, 70°, and 60° and another configuration had two of the IFP helices located near the phosphate headgroups with tilt angles of 60° and 50° while the third IFP helix had its deepest insertion 12 Å from the phosphate headgroups and a tilt angle of 35°. Another simulation also predicted that the monomeric IFP lies at the water-bilayer interface and is parallel to the membrane surface.[38]

Those discrepancies indicate that the IFP structure and membrane location merit further investigation, especially in a more biologically relevant environment with a higher resolution method. In our research, a detailed study of the IFP structure was carried out, which considers the effect of membrane cholesterol and pH. The pH-dependent membrane location and orientation of IFP helix were also explored in a systematic way at an atomic resolution level.

2. Membrane bilayers as model biomembrane systems

A biomembrane consists of a fluid phospholipid bilayer intercalated with proteins, carbohydrates, and their complexes. Phospholipids are molecules that are composed of a polar head group and a hydrophobic acyl tail. The major lipid component of biomembranes includes phosphatidylcholine, phosphatidylserine, phosphatidylinositol, phosphatidylethanolamine, phosphatidylglycerol and sphingomyelin. Upon suspension in water, phospholipids themselves can form liposomes which are closed bilayer vesicles. They're generally several hundred Å in diameter and ~50 Å in thickness, depending on the preparation protocol and the lipids in use. The self-sealed bilayer system is an excellent model to study membrane-bound proteins and peptides.

In my research, phosphatidylcholine and phosphatidylglycerol are mainly used due to the significant amount of phosphatidylcholine and the presence of negatively charged components in the real biomembranes of both influenza virus and infected respiratory epithelial cells.[43-46]

Addition of a certain amount of detergent or short chain lipids to the phospholipids can drive the formation of uniform sized bilayers which are rimmed by the short chain lipids.[47-49] These disk-like bilayers, termed bicelles, automatically align in the presence of the external magnetic field with their bicelle normal perpendicular to the magnetic field (cf. Figure 6a).[48, 50-52] The uniform alignment is due to the interaction of the anisotropy of the bicelle magnetic susceptibility and the magnetic field. This alignment can be flipped 90°, where the bicelle normal is parallel to the magnetic field (cf. Figure 6b), by adding lanthanide ions into the bicelle solution which changes the anisotropy of bicelle

magnetic susceptibility.[53] The bicelle system is ideal for the study of the relative orientation of peptide residing in bicelles. It is important that bicelles are intact in the presence of the fusion peptides to maintain their alignment in the magnetic field. My studies with both influenza and HIV fusion peptides showed that the alignment of bicelles is not affected by the fusion peptides and the IFP has good alignment when bound with bicelles.

(a)

(b)

Figure 5. Solution NMR showed that IFP in DPC micelles has helix-turn-(3_{10}-helix) structure at (a) pH 5.0 (PDB ID: 1ibn) and has helix-turn-extended structure at (b) pH 7.4 (PDB ID: 1ibo). The N-terminal helix has an insertion angle of ~38° and ~23° with respect to the membrane surface at pH 5.0 and pH 7.4, respectively.

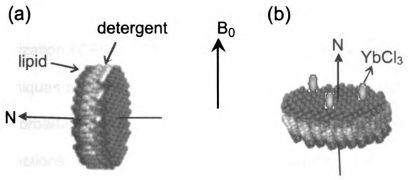

Figure 6: Representation of aligned bicelles with their normals (a) perpendicular to the external magnetic field (B_0) or (b) parallel to B_0 due to the addition of $YbCl_3$.

3. Solid-State NMR measurements of membrane-bound FPs

Solid-state nuclear magnetic resonance (NMR) spectroscopy is a unique method to determine the atomic-level structure of large biological systems. Since the problems with broad lines and low sensitivity have been mitigated by the introduction of magic angle spinning (MAS) and multiple radiofrequency (RF) pulse sequences, solid-state NMR has been especially useful for systems which are difficult to crystallize for X-ray analysis or too big to have fast tumbling motion for solution NMR. Useful parameters such as chemical shifts and magnetic dipolar coupling measured by solid-state NMR provide valuable information for the structure determination of solid systems. There are two principle advantages of solid-state NMR over the more established X-ray crystallography and solution NMR spectroscopy: (1) crystals are not required and (2) large (>30,000 molecular weight) systems can be studied.[54, 55] Recently, systems including the β-amyloid fibrils implicated in Alzheimer's disease[56, 57], the E. coli serine receptor[58], and a HIV-1 peptide/neutralizing antibody complex[59] have been studied by solid state NMR.

Several techniques have been applied in my research. (1) Cross polarization (*CP*) and MAS were generally used in most of the solid-state NMR techniques to increase the signals.[60] For most static solid samples, NMR peaks are broadened by anisotropic effects, such as dipolar and quadrupolar interactions, due to the slow molecular tumbling rates. These effects can be greatly reduced and peaks can be subsequently narrowed by MAS, whereby the NMR sample is rotated at kHz frequencies about an axis tilted at the "magic angle" $\tan^{-1}\sqrt{2}$, or 54.7° relative to the static external magnetic field direction. Cross-polarization increases the signal of nuclei with low gyromagnetic ratio such as ^{13}C, ^{15}N by transferring the spin polarization from species with high gyromagnetic ratio, e.g. ^{1}H. (2) Rotational-echo double resonance (REDOR) under MAS condition permits the detection of heteronuclear magnetic dipole-dipole couplings.[61] The distances (r) between two heteronuclei such as ^{13}CO–^{15}N, ^{13}CO–^{31}P and ^{13}C–^{19}F can be determined from the measured magnetic dipole-dipole couplings (d) based on $r = (C/d)^{1/3}$, where the value of constant C is calculated from the nuclear isotopes. (3) Likewise, the constant-time double-quantum buildup with finite pulses (fpCTDQBU) technique permits the detection of homonuclear magnetic dipole-dipole coupling and the distance between two homonuclei such as ^{13}C–^{13}C can be determined based on a similar formula between r and d.[62-67] Those distance measurements provide a lot of valuable information on membrane-associated IFP conformation and the membrane location of IFP. The distance measurements between ^{13}CO–^{15}N and ^{13}C–^{13}C nuclei allow us to discriminate different IFP conformations in a more quantitative

way. The ^{13}CO and ^{15}N labels are carefully chosen so that the distances between ^{13}CO–^{15}N and ^{13}C–^{13}C are shorter in a helical conformation compared to the distances between the same labeled pair in an extended conformation. In addition the dipolar-coupling measurements between ^{13}CO of IFP and ^{31}P or ^{19}F of phospholipids allow the measurement of the distances between the IFP backbone and the membrane surface (^{31}P) or interior (^{19}F) which can be used to study membrane location of IFP. (4) The proton-driven spin diffusion (PDSD) technique detects the ^{13}C–^{13}C correlation of the membrane-associated IFPs.[63] A short mixing time is used so that only intra-residue crosspeaks are observed which provides chemical shift information of ^{13}C labeled residues as the basis for the secondary structure determination of IFP. (5) The PISEMA-type (polarization-inversion spin exchange at the magic angle) technique detects the chemical shifts and heteronuclear magnetic dipole-dipole coupling for static (non-MAS) samples, eg. ^{15}N chemical shifts and ^{15}N–^{1}H dipolar coupling of selectively ^{15}N labeled bicelle-associated IFP.[68, 69] These values are anisotropic, i.e. the values depend on the orientation of the N-H vector, which can be correlated to the orientation of the peptide in the bicelle system.

The utilization of these innovative techniques enables a detailed investigation of the structure of the membrane-associated IFP. The chemical shift measurements combined with ^{13}CO–^{15}N and ^{13}CO–^{13}CO dipole-dipole measurements revealed that IFP adopts a major helical conformation in the membranes lacking cholesterol and β strand conformation in cholesterol-containing membranes. For IFP in membranes lacking cholesterol, the helical

conformation does not change as a function of pH, i.e. both the N-terminal and C-terminal residues are helical at pH 5.0 and pH 7.4. This result is different from the measurements of micelle-associated IFP using solution NMR as shown in Figure 5.[31] The break in the middle of the IFP helix in this model of micelle-associated IFP was also observed for the membrane-associated IFP by the ^{13}C–^{13}C chemical shifts. But the observed break region turned out to have two conformations instead of the simple turn suggested by the solution NMR measurement.

This work also focused on the investigation of the membrane location and tilt angle of IFP helix relative to the membrane bilayer normal. The ^{15}N chemical shift and N-H dipolar coupling measurements suggested that the N-terminal helix of IFP has a fast rotational motion relative to the helix axis and the angle between the helix axis and the membrane bilayer normal is ~45°. Both the motion and the helix tilt angle is independent of mutations to Gly-1 and to pH change. The distance measurement between IFP backbone ^{13}CO and ^{31}P on the membrane bilayer surface or ^{19}F in the membrane interior showed that IFP is inserted into the membrane hydrophobic interior. An inverted boomerang structure was proposed with the N- and C-terminal regions of IFP in close contact with the membrane phosphorus headgroups and the middle region inserted into the outer leaflets of membranes. The inserted IFP has no gross positional change for samples at different pHs.

1.2 REFERENCES

1. Blumenthal, R.; Dimitrov, D. S.; Hoffman, J. F.; Jamieson, J. C., *Membrane fusion In Handbook of Physiology, Section 14: Cell Physiology.* Oxford: New York, **1997**, 563-603.

2. Dimitrov, D. S., Cell biology of virus entry. *Cell* **2000**, 101, (7), 697-702.

3. Eckert, D. M.; Kim, P. S., Mechanisms of viral membrane fusion and its inhibition. *Annu. Rev. Biochem.* **2001,** 70, 777-810.

4. Hernandez, L. D.; Hoffman, L. R.; Wolfsberg, T. G.; White, J. M., Virus-cell and cell-cell fusion. *Annu. Rev. Cell. Dev. Biol.* **1996,** 12, 627-661.

5. Kielian, M.; Rey, F. A., Virus membrane-fusion proteins: more than one way to make a hairpin. *Nature Reviews Microbiology* **2006,** 4, 67-76.

6. Weber, T.; Zemelman., B. V.; McNew, J. A.; Westermann, B. Gmachl, M.; Parlati, F.; Söllner, T. H.; Rothman, J. E., SNAREpins: Minimal Machinery for Membrane Fusion. *Cell* **1998,** 92, 759-772.

7. Durell, S. R.; Martin, I.; Ruysschaert, J. M.; Shai, Y.; Blumenthal, R., What studies of fusion peptides tell us about viral envelope glycoprotein-mediated membrane fusion. *Mol. Membr. Biol.* **1997,** 14, (3), 97-112.

8. Rafalski, M.; Lear, J. D.; DeGrado, W. F., Phospholipid interactions of synthetic peptides representing the N-terminus of HIV gp41. *Biochemistry* **1990,** 29, (34), 7917-7922.

9. Slepushkin, V. A.; Melikyan, G. B.; Sidorova, M. S.; Chumakov, V. M.; Andreev, S. M.; Manulyan, R. A.; Karamov, E. V., Interaction of human immunodeficiency virus (HIV-1) fusion peptides with artificial lipid membranes. *Biochem. Biophys. Res. Commun.* **1990,** 172, (2), 952-957.

10. Steinhauer, D. A.; Wharton, S. A.; Skehel, J. J.; Wiley, D. C., Studies of the membrane-fusion activities of fusion peptide mutants of influenza-virus hemagglutinin. *J. Virol.* **1995,** 69, (11), 6643-6651.

11. Freed, E. O.; Myers, D. J.; Risser, R., Characterization of the fusion domain of the human immunodeficiency virus type 1 envelope glycoprotein gp41. *Proc. Natl. Acad. Sci. U.S.A.* **1990,** 87, (12), 4650-4654.

12. Freed, E. O.; Delwart, E. L.; Buchschacher, G. L., Jr.; Panganiban, A. T., A mutation in the human immunodeficiency virus type 1 transmembrane glycoprotein gp41 dominantly interferes with fusion and infectivity. *Proc. Natl. Acad. Sci. U.S.A.* **1992,** 89, (1), 70-74.

13. Schaal, H.; Klein, M.; Gehrmann, P.; Adams, O.; Scheid, A., Requirement of N-terminal amino acid residues of gp41 for human immunodeficiency virus type 1-mediated cell fusion. *J. Virol.* **1995,** 69, (6), 3308-3314.

14. Delahunty, M. D.; Rhee, I.; Freed, E. O.; Bonifacino, J. S., Mutational analysis of the fusion peptide of the human immunodeficiency virus type 1: identification of critical glycine residues. *Virology* **1996,** 218, (1), 94-102.

15. Murata, M.; Sugahara, Y.; Takahashi, S.; Ohnishi, S., PH-Dependent Membrane-Fusion Activity of a Synthetic 20 Amino-Acid Peptide With the Same Sequence As That of the Hydrophobic Segment of Influenza-Virus Hemagglutinin. *J. Biochem.* **1987,** 102, (4), 957-962.

16. Bentz, J., Membrane fusion mediated by coiled coils: a hypothesis. *Biophys. J.* **2000,** 78, (2), 886-900.

17. Wilson, I. A.; Skehel, J. J.; Wiley, D. C., Structure of the haemagglutinin membrane glycoprotein of influenza virus at 3 A resolution. *Nature* **1981,** 289, (5796), 366-373.

18. Bullough, P. A.; Hughson, F. M.; Skehel, J. J.; Wiley, D. C., Structure of influenza haemagglutinin at the pH of membrane fusion. *Nature* **1994,** 371, (6492), 37-43.

19. Jardetzky, T. S.; Lamb, R. A., Virology: A class act. *Nature* **2004,** 427, 307-308.

20. Hughson, F. M., Structural characterization of viral fusion proteins. *Current Biology* **1995,** 5, (3), 265-274.

21. Gething, M. J.; Doms, R. W.; York, D.; White, J., Studies On the Mechanism of Membrane-Fusion - Site-Specific Mutagenesis of the Hemagglutinin of Influenza-Virus. *J. Cell Biol.* **1986,** 102, (1), 11-23.

22. Daniels, R. S.; Downie, J. C.; Hay, A. J.; Knossow, M.; Skehel, J. J.; Wang, M. L.; Wiley, D. C., Fusion Mutants of the influenza-virus hemagglutinin glycoprotein. *Cell* **1985,** 40, (2), 431-439.

23. Orlich, M.; Rott, R., Thermolysin activation mutants with changes in the fusogenic region of an influenza-virus hemagglutinin. *J. Viro.* **1994,** 68, (11), 7537-7539.

24. Durrer, P.; Galli. C.; Hoenke, S.; Corti, C.; Gluck, R.; Vorherr, T.; Brunner, J.; Walker, J. A.; Kawaoka, Y.; importance of conserved amino-acids at the cleavage site of the hemagglutinin of a virulent avian influenza-a virus. *J. gene. Virol.* **1993,** 74, 311-314.

25. Durrer, P.; Galli, C.; Hoenke, S.; Corti, C.; Gluck, R.; Vorherr, T.; Brunner, J., H^+-induced membrane insertion of influenza virus hemagglutinin involves the HA2 amino-terminal fusion peptide but not the coiled coil region. *J. Biol. Chem.* **1996,** 271, (23), 13417-13421.

26. Qiao, H.; Armstrong, R. T.; Melikyan, G. B.; Cohen, F. S.; White, J. M., A specific point mutant at position 1 of the influenza hemagglutinin fusion peptide displays a hemifusion phenotype. *Mol. Biol. Cell* **1999,** 10, (8), 2759-2769.

27. Wharton, S. A.; Martin, S. R.; Ruigrok, R. W. H.; Skehel, J. J.; Wiley, D. C., Membrane-Fusion By Peptide Analogs of Influenza-Virus Hemagglutinin. *J. Gene. Virol.* **1988,** 69, 1847-1857.

28. Lear, J. D.; Degrado, W. F., Membrane-binding and conformational properties of peptides representing the NH_2 terminus of influenza HA2. *J. Biol. Chem.* **1987,** 262, (14), 6500-6505.

29. Curtis-Fisk, J.; Preston, C.; Zheng, Z. X.; Worden, R. M.; Weliky, D. P., Solid-state NMR structural measurements on the membrane-associated influenza fusion protein ectodomain. *J. Am. Chem. Soc.* **2007,** 129, (37), 11320.

30. Chen, J.; Skehel, J. J.; Wiley, D. C., N- and C-terminal residues combine in the fusion-pH influenza hemagglutinin HA(2) subunit to form an N cap that terminates the triple-stranded coiled coil. *Proc. Natl. Acad. Sci. U S A* **1999,** 96, (16), 8967-8972.

31. Han, X.; Bushweller, J. H.; Cafiso, D. S.; Tamm, L. K., Membrane structure and fusion-triggering conformational change of the fusion domain from influenza hemagglutinin. *Nat. Struct. Biol.* **2001,** 8, (8), 715-720.

32. Lai, A. L.; Park, H.; White, J. M.; Tamm, L. K., Fusion Peptide of Influenza Hemagglutinin Requires a Fixed Angle Boomerang Structure for Activity. *J. Biol. Chem.* **2006,** 281, (9), 5760-5770.

33. Luneberg, J.; Martin, I.; Nussler, F.; Ruysschaert, J. M.; Herrmann, A., Structure and Topology of the Influenza-Virus Fusion Peptide in Lipid Bilayers. *J. Biol. Chem.* **1995,** 270, (46), 27606-27614.

34. Macosko, J. C.; Kim, C. H.; Shin, Y. K., The membrane topology of the fusion peptide region of influenza hemagglutinin determined by spin-labeling EPR. *J. Mol. Biol.* **1997,** 267, (5), 1139-1148.

35. Wasniewski, C. M.; Parkanzky, P. D.; Bodner, M. L.; Weliky, D. P., Solid-state nuclear magnetic resonance studies of HIV and influenza fusion peptide orientations in membrane bilayers using stacked glass plate samples. *Chem. Phys. Lipids* **2004,** 132, (1), 89-100.

36. Ishiguro, R.; Kimura, N.; Takahashi, S., Orientation of fusion-active synthetic peptides in phospholipid bilayers: Determination by Fourier transform infrared spectroscopy. *Biochemistry* **1993,** 32, (37), 9792-9797.

37. Vaccaro, L.; Cross, K. J.; Kleinjung, J.; Straus, S. K.; Thomas, D. J.; Wharton, S. A.; Skehel, J. J.; Fraternali, F., Plasticity of Influenza Haemagglutinin Fusion Peptides and Their Interaction with Lipid Bilayers. *Biophys. J.* **2005,** 88, 25-36.

38. Bechor, D.; Ben-Tal, N., Implicit solvent model studies of the interactions of the influenza hemagglutinin fusion peptide with lipid bilayers. *Biophys. J.* **2001,** 80, (2), 643-655.

39. Spassov, V. Z.; Yan, L.; Szalma, S., Introducing an implicit membrane in generalized Born/solvent accessibility continuum solvent models. *J. Phys. Chem. B* **2002,** 106, (34), 8726-8738.

40. Huang, Q.; Chen, C. L.; Herrmann, A., Bilayer Conformation of Fusion Peptide of Influenza Virus Hemagglutinin:A Molecular Dynamics Simulation Study. *Biophys. J.* **2004,** 87, (1), 14-22.

41. Lague, P.; Roux, B.; Pastor, R. W., Molecular dynamics simulations of the influenza hemagglutinin fusion peptide in micelles and bilayers: Conformational analysis of peptide and lipids. *J. Mol. Biol.* **2005,** 354, (5), 1129-1141.

42. Sammalkorpi, M.; Lazaridis, T., Configuration of influenza hemagglutinin fusion peptide monomers and oligomers in membranes. *BBA-Biomembranes* **2007,** 1768, (1), 30-38.

43. Worman, H. J.; Brasitus, T. A.; Dudeja, P. K.; Fozzard, H. A.; Field, M., Relationship Between Lipid Fluidity and Water Permeability of Bovine Tracheal Epithelial-Cell Apical Membranes. *Biochemistry* **1986,** 25, (7), 1549-1555.

44. Scheiffele, P.; Rietveld, A.; Wilk, T.; Simons, K., Influenza Viruses Select Ordered Lipid Domains during Budding from the Plasma Membrane. *J. Biol. Chem.* **1999,** 274, (4), 2038-2044.

45. Lenard, J.; Compans, R. W., The membrane structure of lipid-containing viruses. *BBA-Biomembranes* **1974,** 344, (1), 51-94.

46. Blom, T. S.; Koivusalo, M.; Kuismanen, E.; Kostiainen, R.; Somerharju, P.; Ikonen, E., Mass Spectrometric Analysis Reveals an Increase in Plasma Membrane Polyunsaturated Phospholipid Species upon Cellular Cholesterol Loading. *Biochemistry* **2001,** 40, (48), 14635–14644.

47. Sanders, C. R.; Landis, G. C., Reconstitution of membrane proteins into lipid-rich bilayered mixed micelles for NMR studies. *Biochemistry* **1995,** 34, (12), 4030-4040.

48. Sanders, C. R.; Prosser, R. S., Bicelles: a model membrane system for all seasons? *Structure* **1998,** 6, (10), 1227-1234.

49. Sanders, C. R.; Hareb, B. J.; Howardc, K. P.; Prestegardc, J. H., Magnetically-oriented phospholipid micelles as a tool for the study of membrane-associated molecules. *Prog. Nucl. Magn. Reson. Spec.* **1994,** 26, 421-444.

50. Forrest, B. J.; Reeves, L. W., New lyotropic liquid crystals composed of finite nonspherical micelles. *Chem. Rev.* **1981,** 81, (1), 1–14.

51. Davis, J. H., Deuterium nuclear magnetic resonances of exchange-labeled gramicidin in an oriented lyotropic nematic phase. *Biochemistry* **1988,** 27, (1), 428–436.

52. Sanders, C. R., Solid state 13C NMR of unlabeled phosphatidylcholine bilayers: spectral assignments and measurement of carbon-phosphorus dipolar couplings and 13C chemical shift anisotropies. *Biophys. J.* **1993,** 64, (1), 171-181.

53. Howard, K. P.; Opella, S. J., High-Resolution Solid-State NMR Spectra of Integral Membrane Proteins Reconstituted into Magnetically Oriented Phospholipid Bilayers. *J. Magn.. Reson. B* **1996,** 112, 91-94.

54. Griffin, R. G., Dipolar recoupling in MAS spectra of biological solids. *Nat Struct. Biol.* **1998,** 5 Suppl, 508-512.

55. Marassi, F. M.; Opella, S. J., NMR structural studies of membrane proteins. *Curr. Opin. Struct. Biol.* **1998,** 8, (5), 640-648.

56. Benzinger, T. L.; Gregory, D. M.; Burkoth, T. S.; Miller-Auer, H.; Lynn, D. G.; Botto, R. E.; Meredith, S. C., Propagating structure of Alzheimer's b-amyloid(10-35) is parallel b-sheet with residues in exact register. *Proc. Natl. Acad. Sci. U.S.A.* **1998,** 95, (23), 13407-13412.

57. Lansbury, P. T.; Costa, P.R.; Griffiths, J. M.; Simon, E. J.; Auger, M.; Halverson, K. J.; Kocisko, D. A.; Hendsch, Z. S.; Ashburn, T. T.; Spencer, R. G.; Tidor, B.; Griffin, R.G., Structural Model for the Beta-amyloid Fibril Based on Interstrand Alignment of an anti-parallel-sheet Comprising a C-terminal Peptide. *Nature Struc. Biol.* **1995,** 2, (11), 990-998.

58. Wang, J.; Balazs, Y. S.; Thompson, L. K., Solid-state REDOR NMR distance measurements at the ligand site of a bacterial chemotaxis membrane receptor. *Biochemistry* **1997,** 36, (7), 1699-1703.

59. Weliky, D. P.; Bennett, A. E.; Zvi, A.; Anglister, J.; Steinbach, P. J.; Tycko, R., Solid-state NMR evidence for an antibody-dependent conformation of the V3 loop of HIV-1 gp120. *Nat. Struct. Biol.* **1999,** 6, (2), 141-5.

60. Pines, A.; Gibby, M. G.; Waugh, J. S., Proton enhanced nuclear magnetic resonance of dilute spins in solids. *J. Chem. Phys.* **1973,** 59, 569-590.

61. Gullion, T., Introduction to rotational-echo, double-resonance NMR. *Concepts Magn. Reson.* **1998,** 10, (5), 277-289.

62. Balbach, J. J.; Petkova, A. T.; Oyler, N. A.; Antzutkin, O. N.; Gordon, D. J.; Meredith, S. C.; Tycko, R., Supramolecular structure in full-length Alzheimer's b-amyloid fibrils: Evidence for a parallel b-sheet organization from solid-state nuclear magnetic resonance. *Biophys. J.* **2002,** 83, (2), 1205-1216.

63. Bennett, A. E.; Ok, J. H.; Griffin, R. G.; Vega, S., Chemical-shift correlation spectroscopy in rotating solids - radio frequency-driven dipolar recoupling and longitudinal exchange. *J. Chem. Phys.* **1992,** 96, (11), 8624-8627.

64. Gullion, T.; Vega, S., A simple magic angle spinning NMR experiment for the dephasing of rotational echoes of dipolar coupled homonuclear spin pairs. *Chem. Phys. Lett.* **1992,** 194, (4-6), 423-428.

65. Bennett, A. E.; Rienstra, C. M.; Griffiths, J. M.; Zhen, W. G.; Lansbury, P. T.; Griffin, R. G., Homonuclear radio frequency-driven recoupling in rotating solids. *J. Chem. Phys.* **1998,** 108, (22), 9463-9479.

66. Bennett, A. E.; Weliky, D. P.; Tycko, R., Quantitative conformational measurements in solid state NMR by constant-time homonuclear dipolar recoupling. *J. Am. Chem. Soc.* **1998,** 120, (19), 4897-4898.

67. Ishii, Y., ^{13}C-^{13}C dipolar recoupling under very fast magic angle spinning in solid-state nuclear magnetic resonance: Applications to distance measurements, spectral assignments, and high-throughput secondary-structure determination. *J. Chem. Phys.* **2001,** 114, (19), 8473-8483.

68. Dvinskikh, S. V.; Durr, U.; Yamamoto, K.; Ramamoorthy, A., A high-resolution solid-state NMR approach for the structural studies of bicelles. *J. AM. Chem. Soc.* **2006,** 128, 6326-6327.

69. Dvinskikh, S. V.; Yamamoto, K.; Ramamoorthy, A., Separated local field NMR spectroscopy by windowless isotropic mixing. *Chem. Phys. Lett.* **2006,** 419, 168-173.

Chapter 2 Materials and Methods

2.1 MATERIALS

Wang resins and 9-fluorenylmethoxycarbonyl (FMOC) amino acids were obtained from Peptides International (Louisville, KY), Calbiochem-Novabiochem (La Jolla, CA), and Advanced Chemtech (Louisville, KY). Isotopically labeled amino acids were obtained from Cambridge Isotope Laboratories (Andover, MA) and were Fmoc-protected using literature procedures.[1, 2] The lipids 1,2-di-O-tetradecyl-*sn*-glycero-3-phosphocholine (DTPC), 1,2-di-O-tetradecyl-*sn*-glycero-3-[phospho-*rac*-(1-glycerol)] (DTPG), 1-palmitoyl-2-oleoyl-*sn*-glycero-3-phosphocholine (POPC), 1,2-Di-O-Hexyl-*sn*-Glycero-3-Phosphocholine (DHPC), 1-palmitoyl-2-(16-fluoropalmitoyl)-*sn*-glycero-3-phosphocholine (16-^{19}F-DPPC), 1-palmitoyl-2-oleoyl-*sn*-glycero-3-[phospho-*rac*-(1-glycerol)] (POPG) and 1,2-Dimyristoyl-D54-*sn*-Glycero-3-Phosphocholine ($DMPC_{d54}$) were obtained from Avanti Polar Lipids (Alabaster, AL). 1-palmitoyl-2-(5-fluoropalmitoyl)-*sn*-glycero-3-phosphocholine (5-^{19}F-DPPC) was custom synthesized by Avanti Polar Lipids (Alabaster, AL). *N*-(2-hydroxyethyl)-piperazine-*N'*-2-ethanesulfonic acid (HEPES) and 2-(*N*-morpholino)-ethanesulfonic acid (MES) were purchased from Sigma-Aldrich (St. Louis, MO). The buffer solution used in the study contained 10 mM HEPES/5 mM MES at pH 5.0 or 7.4 with 0.01% (w/v) NaN_3 preservative.

2.2 SAMPLE PREPARATION

1. IFP and HFP Synthesis

All IFP contained the sequence GLFGAIAGFIENGWEGMIDGGGKKKKG-NH_2 in which the underlined part is the 20 N-terminal residues of the influenza A X31 strain hemagglutinin fusion protein. All HFPmn had the sequence AVGIGALFLGFLGAAGS-TMGARSWKKKKKG-NH_2 and the underlined part is the 23 N-terminal residues of the HIV gp41 fusion protein. The HFPdm, the abbreviation of a HFP dimer, had additional cysteines in the above sequence which are used to cross-link HFP monomers into a dimer. The construction of a HFP dimer is shown in Figure 7. A set of peptides were synthesized in order to probe the conformation of the fusion peptide region. The labeling schemes of synthesized IFPs are listed in Table 1. The non-native lysines increased aqueous solubility and resulted in monomeric peptide in the buffer solution prior to membrane binding.[3] Peptides were either synthesized using an ABI 431A peptide synthesizer (Foster City, CA) or synthesized manually in 5 mL polypropylene columns from Pierce (Rockford, IL) and FMOC chemistry. Peptides were cleaved from the resin for 2-3 hours using a mixture of TFA:thioanisole:1,2-ethanedithiol:anisole in a 90:4:4:2 volume ratio. TFA was removed from the cleavage filtrate with nitrogen gas and peptides were precipitated with cold t-butyl methyl ether. The HFPdm was formed by cross-linking two HFP monomers with a disulfide bond between the cysteines of two peptide strands. All peptides were purified by reversed-phased high performance liquid chromatography using a semi-preparative C_{18} column and a water-

Table 1. Labeling scheme of IFPs and HFPs

Peptide	Labeled residues
IFP-G1$_C$	Gly-1 ^{13}CO
IFP-L2$_C$	Leu-2 ^{13}CO
IFP-F3$_C$	Phe-3 ^{13}CO
IFP-A7$_C$G8$_C$	Ala-7 and Gly-8 ^{13}CO
IFP-G16$_C$	Gly-16 ^{13}CO
IFP-G20$_C$	Gly-20 ^{13}CO
IFP-A5$_C$F9$_N$	Ala-5 ^{13}CO and Phe-9 ^{15}N
IFP-F9$_C$G13$_N$	Phe-9 ^{13}CO and Gly-13 ^{15}N
IFP-G13$_C$M17$_N$	Gly-13 ^{13}CO and Met-17 ^{15}N
IFP-G1$_N$	Gly-1 ^{15}N
IFP-L2$_N$	Leu-2 ^{15}N
IFP-F3$_N$	Phe-3 ^{15}N
IFP-G4$_N$	Gly-4 ^{15}N
IFP-A5$_N$	Ala-5 ^{15}N
IFP-I6$_N$	Ile-6 ^{15}N
IFP-A7$_N$	Ala- ^{15}N
IFP-G8$_N$	Gly-8 ^{15}N
IFP-F9$_N$	Phe-9 ^{15}N
IFP-I10$_N$	Ile-10 ^{15}N
IFP-U$_N$	^{15}N for residues 1 – 10
IFP-F3$_N$A7$_N$	Phe-3 and Ala-7 ^{15}N
IFP-(G1S)-F3$_N$A7$_N$	IFP G1S mutant with Phe-3 and Ala-7 ^{15}N labels
IFP-(G1V)-F3$_N$A7$_N$	IFP G1V mutant with Phe-3 and Ala-7 ^{15}N labels
IFP-I10E11$_U$	Ile-10 and Glu-11 uniform ^{13}C, ^{15}N label
IFP-N12G13$_U$	Asn-12 and Gly-13 uniform ^{13}C, ^{15}N label
IFP-E11V$_C$N12A$_C$	IFP E11VN12A mutant with Val-11 and Ala-12 ^{13}CO labels
IFP-N12A$_C$G13$_C$	IFP N12A mutant with Ala-12 and Gly-13 ^{13}CO labels
IFP-(E11VN12A)-A5$_C$F9$_N$	IFP E11VN12A mutant with Ala-5 ^{13}CO and Phe-9 ^{15}N labels
IFP-(N12A)-A5$_C$F9$_N$	IFP N12A mutant with Ala-5 ^{13}CO and Phe-9 ^{15}N labels
HFPmn-U$_N$	HFP monomer with ^{15}N labels for residue 1 – 14
HFPmn-G5A6L7$_N$	HFP monomer with , Gly-5, Ala-6, Leu-7 ^{15}N labels
HFPmn-A14A15G16$_N$	HFP monomer with , Ala-14, Ala-15, Gly-16 ^{15}N labels
HFPdm-A6$_N$	HFP dimer with Ala-6 ^{15}N labels

acetonitrile gradient containing 0.1% TFA. Mass spectroscopy was used for peptide identification.

AVGIGALFLGFLGAAGSTMGARSWKKKKKCG
AVGIGALFLGFLGAAGSTMGARSWKKKKKCG

Figure 7. Construct of HFP dimer. Two HFP monomers cross linked at Cys to form dimer.

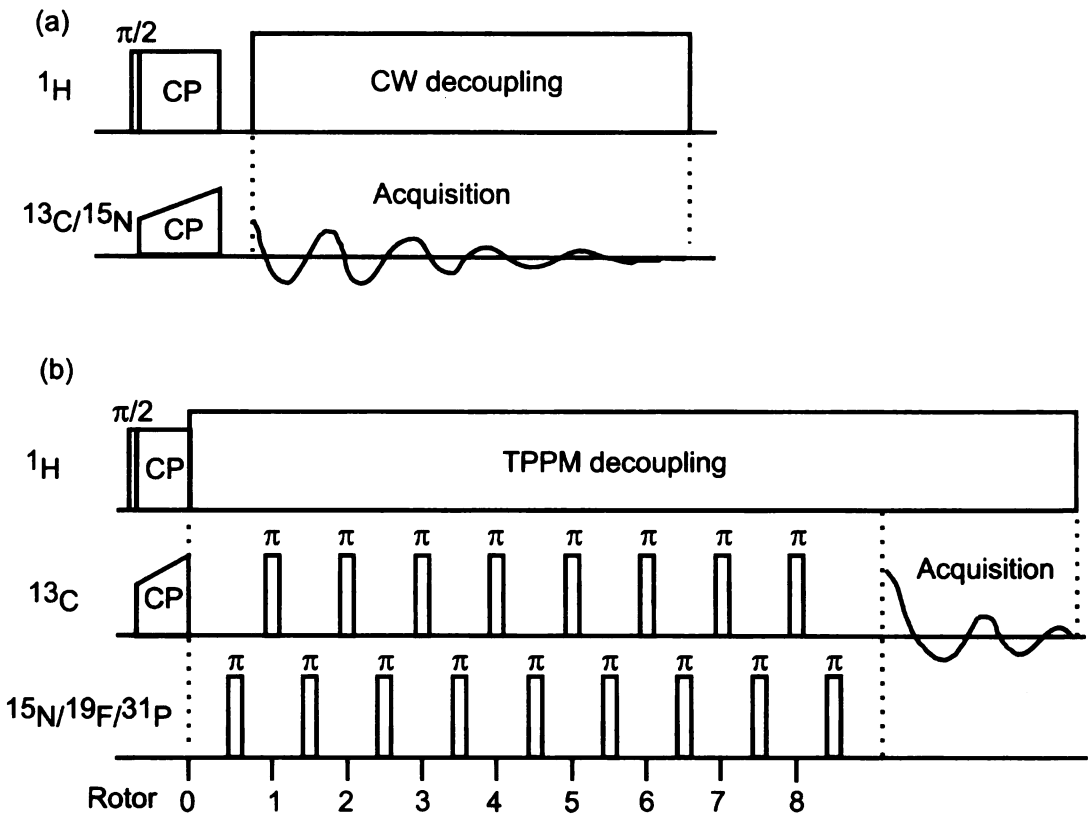

Figure 8. Pulse sequences (a) Cross-polarization. Magnetization is transferred from ^{1}H to ^{13}C or ^{15}N during *CP*. ^{1}H continuous wave (CW) decoupling was applied during acquisition. (b) ^{13}C REDOR. *CP* transfers the ^{1}H transverse magnetization to ^{13}C. ^{13}C magnetization is dephased (i.e., reduced) by the dipolar coupling between ^{13}C and ^{15}N, ^{31}P or ^{19}F nuclei mediated by the π pulses per rotor period. ^{13}C chemical shift is refocused by multiple π pulses.

2. Membrane sample preparation for MAS solid state NMR

Most vesicle samples were made with DTPC/DTPG lipids in a 4:1 mol ratio. The reason for the major DTPC fraction was the significant quantity of phosphatidylcholine lipids in membranes of host cells of the influenza virus.[4] Incorporation of the minor DTPG fraction was based on the small quantity of negatively charged lipids in these membranes.[4] In addition, PC/PG mixtures of this approximate composition have been previously used in structural and functional studies of the influenza fusion peptide and protein.[5-11] Use of ether-linked rather than ester-linked lipids simplified the data analysis which was based on the ^{13}CO signal from the labeled IFP. Ether-linked lipids don't have carbonyl groups and the natural abundance ^{13}CO signal was therefore minimized.[12] Some samples were prepared with a "DTPC/DTPG/CHOL" (8:2:5 mol ratio) membrane composition which reflected the significant fraction of cholesterol in the membranes of the influenza virus and its host cells.[4, 13] A few samples were prepared with a "POPC/POPG" (4:1). Samples for the ^{13}C–^{1} ^{9}F REDOR experiments were prepared with "DTPC/DTPG/16-^{19}F-DPPC (or 5-^{19}F-DPPC)" (8:2:1 mol ratio) membrane composition. The incorporation of fluorinated lipids provided spin labels for the detection of the location of IFPs relative to the membrane interior. The samples with 100% ^{19}F-DPPC lipid were not used because a 100% 16-^{19}F-DPPC lipid sample forms a non-bilayer structure.[14] Studies with HFP and various mol fraction of 5-^{19}F-DPPC showed that ^{13}CO–^{19}F dephasing reaches a constant and maximum value over 0.07-0.14 mol fraction

range. Static ^{31}P spectra were consistent with overall bilayer structure in samples containing 9 mol% 5-^{19}F-DPPC and HFPs.[15]

The sample preparation protocol began with dissolution in chloroform of lipids (20 μmol total) or lipids (20 μmol total) and cholesterol. The chloroform was removed under a stream of nitrogen followed by overnight vacuum pumping. The lipid film was suspended in 2 mL aqueous buffer solution and was homogenized with ten freeze-thaw cycles. Large unilamellar vesicles were formed by extrusion through a 100 nm diameter polycarbonate filter (Avestin, Ottawa, ON). Quantitation of IFP was done using A_{280} and ε_{280} = 5700 cm^{-1} M^{-1} and 0.8 μmol IFP was dissolved in 2 mL aqueous buffer solution which was then added to the vesicle solution. The pH of the IFP/vesicle solution was adjusted to either 7.4 or 5.0 and the mixture was gently vortexed for a couple of hours and then ultracentrifuged at ~150000g for five hours. The membrane pellet with associated bound IFP was transferred to a 4 mm diameter magic angle spinning (MAS) NMR rotor. The pH of the hydrated pellet was also checked before and after the NMR experiments using pH paper.

3. Membrane sample preparation for static solid state NMR

Oriented bicelle samples were also prepared using predominant ether- rather than ester-linked lipids because of the greater chemical stability of the ether-linked lipids.[16] DTPC (52.9 μmol), $DMPC_{d54}$ (1.1 μmol), and DHPC (16.9 μmol) lipids were dissolved in chloroform in a round bottom flask. Bicelle alignment was monitored using ^2H NMR of the $DMPC_{d54}$ lipids. IFP (1.1 μmol) or

HFP (0.6 μmol) was dissolved in a mixture of trifluoroethanol/chloroform (4:1) in another round bottom flask and vortexed to ensure full solubilization before being added to the lipid solution. Solvents were removed by a gentle nitrogen gas stream followed by vacuum over night. Deuterium depleted water or aqueous buffer solution (150 μL) was added to the dry IFP/lipid mixture. The pH was adjusted to pH 7.4 or pH 5.0 with small aliquots of 1 M HCl or NaOH solutions. The pH was checked before and after NMR measurement using pH paper and did not change with time. Several cycles of vortex/freeze/thaw were carried out until the solution turned clear and flowed freely after being chilled in an ice-bath for 5 minutes. Samples prepared by this protocol were transferred into glass tubes with 5 mm diameter, 1 cm length, and ~120 μL volume. The tubes were sealed with custom-machined Kel-F inserts covered with parafilm or rubber plungers from 1 mL disposable syringes which can be pierced by a syringe to remove air bubbles from the sample and ensure a tight seal. Samples placed in the NMR spectrometer had their bicelle normals aligned perpendicular to the magnetic field direction at the temperature of 40 °C. Samples with bicelle normals aligned parallel to the magnetic field direction were obtained with Yb^{3+} at 7 mM concentration which was attained by adding ~5 μL 200 mM $YbCl_3$ solution to the bicelle solution.

Unaligned "powder" samples were prepared in a manner similar to that used for the bicelle samples. The final sample composition was ~1 μmol IFP or HFP, ~54 μmol DTPC, and ~150 μL water, and the pH was adjusted to 5.0 or 7.4.

4. N-acetylvaline Sample Preparation

Synthesis of ^{15}N or ^{13}CO-labeled N-acetylvaline (^{15}N-NAV or ^{13}CO-NAV) began by dissolving 1 mmol selectively labeled valine and 2 mmol acetic anhydride in a mixture of 0.5 mL acetic acid and 0.5 mL water. The solution was sonicated for 2 minutes. Additional cycles were done of addition of 2 mmol acetic anhydride and 2 minutes of sonication. After each cycle, the presence of valine was qualitatively monitored with addition of ninhydrin to a small aliquot of the solution. The reaction was considered complete when the solution remained clear after ninhydrin addition. Excess acetic anhydride and solvents were removed with nitrogen gas and cyclohexane was added during this process to facilitate the removal of water. The remaining solid ^{15}N-NAV or ^{13}CO-NAV was dissolved in acetone. The container was wrapped in aluminum foil and after slow evaporation of the acetone, single crystals of ^{15}N-NAV or ^{13}CO-NAV were formed with ~$2 \times 2 \times 2$ mm dimensions.

2.3 MAS SOLID-STATE NMR

1. General MAS NMR spectroscopy

Most experiments were done on a 9.4 T solid-state NMR spectrometer (Varian Infinity Plus, Palo Alto, CA) using a triple-resonance MAS probe in double resonance $^{1}H/^{13}C$ configuration for fpCTDQBU and PDSD experiments, in triple resonance $^{1}H/^{13}C/^{15}N$ configuration for ^{13}C–^{15}N REDOR experiments and in triple resonance $^{1}H/^{31}P/^{13}C$ configuration for ^{13}C–^{31}P REDOR experiments. For the ^{13}C–^{19}F REDOR experiment, a quadruple-resonance MAS probe was used in

triple resonance $^{1}H/^{19}F/^{13}C$ configuration. Both probes were equipped for 4 mm diameter rotors. The ^{1}H, ^{19}F, ^{13}C, ^{31}P and ^{15}N frequencies were 398.7, 375.1, 161.5, 100.3, and 40.5 MHz respectively. The ^{13}C and ^{15}N shifts were externally referenced to the methylene resonance of adamantane at 40.5 ppm and to $(^{15}NH_4)_2SO_4$ resonance at 26.5 ppm respectively. The ^{13}C referencing allowed direct comparison with ^{13}C shift databases derived from liquid-state NMR assignments of proteins.[17, 18] These databases are appropriate for solid-state NMR data as evidenced by similar ^{13}C shifts observed for the same protein in either aqueous solution or the microcrystalline state.[19-21] Samples were typically cooled with nitrogen gas at -50 °C because ^{13}C signals were larger at lower temperature and motional averaging of dipolar couplings was reduced. Some experiments were done at 0°C or ambient temperature to investigate the temperature dependence of chemical shifts or internuclear dipolar coupling.

2. CP MAS spectroscopy

The *CP* MAS experiment provided chemical shift information in samples that contain selectively ^{13}CO or ^{15}N labeled IFP. The *CP* pulse sequence is displayed in Figure 8a. Simultaneous rf radiation of both the *S* (^{1}H) and *I* (^{13}C or ^{15}N) nuclei such that both isotopes effectively precess at the same frequency allows the transverse polarization transfer of *S* spin to *I* spin through heteronuclear dipolar coupling.

For membrane bilayer samples that contained ^{13}CO labeled IFPs, the ^{1}H and ^{13}C pulse lengths were approximately obtained by direct pulsing on

adamantane. The *CP* matching condition was obtained by running ramped *CP* on the lyophilized "I4" peptide which had sequence AcAEAAAKEAAAKEAAAKA-NH_2 and which was ^{13}CO labeled at Ala-9 and ^{15}N labeled at Ala-13.[22] Calibration of the ^1H $\pi/2$ pulse and ^{13}C $\pi/2$ and π pulses was done with the *CP* "Z-filter" sequence (*CP* – $\pi/2$ – τ_z – π – acquisition). The parameters generally used were ~45 kHz $\pi/2$ pulse, ~54 kHz *CP* and ~60 kHz CW decoupling for ^1H and a 58-69 kHz ramped *CP* field for ^{13}C. The contact time and recycle delay were 1 ms and 1 s respectively and phase cycling included ^1H $\pi/2$, *x*, –*x*, *x*, –*x*; ^1H *CP*, *y*, *y*, *y*, *y*; ^{13}C *CP*, –*y*, –*y*, –*x*, –*x*; receiver, –*x*, *x*, *y*, –*y*.

For samples that contained ^{15}N labeled IFPs, the ^1H and ^{15}N pulse lengths were approximately obtained by direct pulsing on $^{15}(NH_4)_2SO_4$ and the *CP* matching condition was obtained by running ramped *CP* on ^{15}N-NAV. The ^1H $\pi/2$, ^{15}N $\pi/2$ and π pulses were calibrated with *CP* "Z-filter" sequence using the ^{15}N-NAV sample. The general parameters included ~51 kHz ^1H $\pi/2$ pulse, 1.0 ms ramped cross-polarization with 23–26 kHz ^{15}N and ~20 kHz ^1H Rabi frequencies, ~50 kHz ^1H decoupling. The recycle delay was 4 s and phase cycling was the same as listed above for the *CP* MAS experiments of ^{13}CO labeled samples.

3. REDOR spectroscopy

The REDOR experiment provided structural information in samples that contained a ^{13}CO and a heteronuclear spin (e.g. ^{15}N, ^{19}F or ^{31}P) labels. The REDOR sequence is shown in Figure 8b, which includes: (1) a ^1H $\pi/2$ pulse; (2) a cross-polarization period on-resonance ^1H and ^{13}C fields; (3) a dephasing

period of duration τ during which there is one ^{13}C π pulse at the beginning of each rotor cycle except for the first cycle and for some acquisitions, a heteronuclear spin (e.g. ^{15}N, ^{19}F or ^{31}P) π pulse in the middle of each cycle; and (4) ^{13}C detection. For each sample and each τ, two spectra were acquired. The heteronuclear pulses were absent during the dephasing period of the "S_0" acquisition and during each rotor cycle, MAS averaged to zero the ^{13}C evolution due to heteronuclear dipolar coupling (e.g. ^{13}C–^{15}N, ^{13}C–^{19}F or ^{13}C–^{31}P). During the "S_1" acquisition, incorporation of one heteronuclear π pulse per rotor cycle disrupted the MAS averaging and resulted in reduction of signals of ^{13}C nuclei close to heteronuclei. Spectra were acquired for different τ and XY-8 phase cycling (*x*, *y*, *x*, *y*, *y*, *x*, *y*, *x*) was used for the heteronuclear π pulses and for all of the ^{13}C π pulses except the final pulse. Individual S_0 or S_1 transients were added with phase cycling: ^{1}H $\pi/2$, *x*, –*x*, *x*, –*x*; ^{1}H *CP*, *y*, *y*, *y*, *y*; ^{13}C *CP*, –*y*, –*y*, –*x*, –*x*; final ^{13}C π pulse, –*y*, –*y*, –*x*, –*x*; receiver, –*x*, *x*, *y*, –*y*. The differences in the ^{13}C signal intensities of the S_0 and S_1 spectra as a function of τ were used to determine the dipolar coupling (*d*) and the distance (*r*) between the labeled nuclei.

For the ^{13}C–^{15}N REDOR experiments, the ^{1}H, ^{13}C and ^{15}N pulse lengths and the ^{1}H-^{13}C cross-polarization matching condition were calibrated with the lyophilized "I4" peptide mentioned before. The typical experimental parameters included 8000 Hz MAS frequency, 44 kHz ^{1}H $\pi/2$ pulse, 54 kHz ^{1}H field and 58-69 kHz ramped ^{13}C field during the *CP* period, 62 kHz ^{13}C π pulse, 28 kHz ^{15}N π pulse and 93 kHz two- pulse phase modulation (TPPM) ^{1}H decoupling during the

dephasing and detection periods. The durations for the cross-polarization period and recycle delay were 1 ms and 1 s, respectively.

The ^{13}C–^{31}P REDOR experiments provided information on the proximity of the IFP backbone relative to the membrane surface which has ^{31}P nuclei. The *CP* matching condition and the ^{1}H $\pi/2$, ^{13}C $\pi/2$ and π pulses were calibrated with the lyophilized "I4" peptide. The ^{31}P π pulse length was set with the *CP* "Z-filter" using the ^{31}P signals from the phosphate headgroups of the membrane samples. The typical parameters included 8000 Hz MAS frequency, ~50 kHz ^{1}H $\pi/2$ pulse, 52 kHz ^{1}H field and 58-69 kHz ramped ^{13}C field during the 1 ms *CP* period, ~50 kHz ^{13}C π pulse, ~60 kHz ^{31}P π pulse, ~100 kHz TPPM ^{1}H decoupling during the dephasing and detection periods and 1 s recycle delay.

The ^{13}C–^{19}F REDOR experiments provided information on the proximity of IFP backbone relative to either the membrane center (16-^{19}F) or the midpoint between the membrane surface and membrane center (5-^{19}F). In these experiments, the membrane bilayers were incorporated with some DPPC lipid which has ^{19}F substituted for a ^{1}H at either the terminal C16 or the C5 position of the *sn*2 acyl chain. The 16-^{19}F is located at the membrane center while the 5-^{19}F is located at the midpoint of the bilayer longitude between the membrane surface and bilayer center. The experimental parameters were validated using a lyophilized sample containing helical peptide which had the sequence EQLLKALEFLLKELLEKL with ^{13}CO label at Leu-10 and Phe-9 was substituted with *p*-fluorophenylalanine.[23] The typical parameters included 8000 Hz MAS frequency, ~50 kHz ^{1}H $\pi/2$ pulse, ~50 kHz ^{1}H field and 55-66 kHz ramped ^{13}C

field during the 1 ms *CP* period, ~50 kHz ^{13}C π pulse and ~33 kHz ^{19}F π pulse during the dephasing period, ~95 kHz TPPM ^{1}H decoupling during the dephasing and detection periods and 1 s recycle delay.

4. fpCTDQBU spectroscopy

The fpCTDQBU experiment was used to determine the ^{13}CO–^{13}CO dipolar coupling and distance in samples in which the IFP was ^{13}CO labeled at two adjacent residues. The fpCTDQBU sequence can be represented as $CP_{90\pm\zeta}$ – $(fpRFDR)_L$ – $\pi/2_\zeta$ – $\pi/2_0$ – $(fpRFDR)_M$ – $\pi/2_{180}$ – $\pi/2_{90}$ – $(fpRFDR)_N$ – *acquisition* where *L*, *M* and *N* refer to the number of rotor periods in each *fpRFDR* period and other subscripts refer to the rf phases (Figure 9). The sequence was implemented in a manner similar to the REDOR sequence with S_0 and S_1 spectra and a dephasing period $\tau = 2L\tau_R$ where τ_R was the duration of a single rotor cycle. Increasing values of τ were obtained by incrementing *L* and decrementing *N* by the same number while keeping *M* constant. For each value of τ and each ζ = 0, 90, 180, or 270, a distinct spectrum was obtained and the S_0 and S_1 spectra were $S_0 = S_{\zeta=90} + S_{\zeta=270}$ and $S_1 = S_{\zeta=0} + S_{\zeta=180}$.[22]

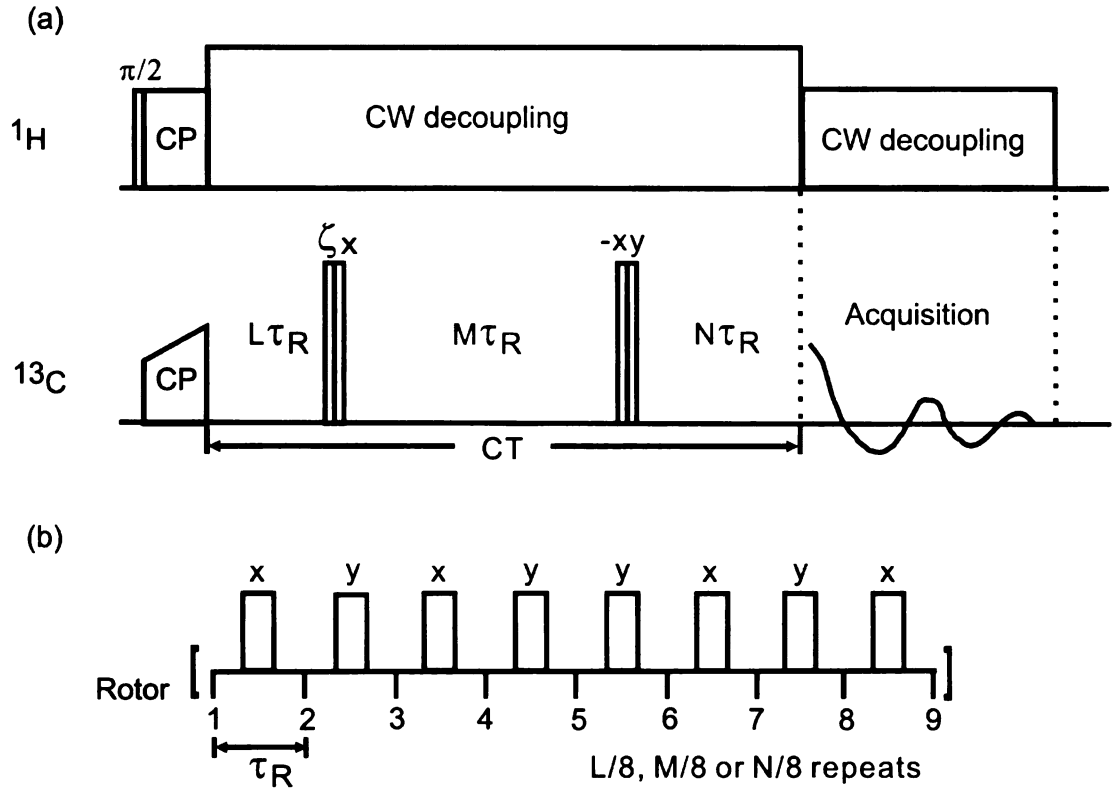

Figure 9. fpCTDQBU pulse sequence. (a) The displayed fpCTDQBU pulse sequence included: (1) *CP* from ^{1}H to ^{13}C; (2) a constant-time (*CT*) period of $(L + M + N)\tau_R$ duration where *L*, *M* and *N* were integral multiples of 8, and τ_R was the duration of a single rotor period; and (3) acquisition period. Continuous wave ^{1}H decoupling was applied during the *CT* and acquisition periods. A pair of back-to-back ^{13}C $\pi/2$ pulses separated the $L\tau_R$ and $M\tau_R$ periods and another pair separated the $M\tau_R$ and $N\tau_R$ periods. (b) Pulses during $L\tau_R$, $M\tau_R$ and $N\tau_R$ periods. There was one π pulse per rotor cycle. The ^{13}C *CP* rf phase was $\zeta + \pi/2$ and the phase of each ^{13}C $\pi/2$ and π pulses is noted above the pulse. For $\zeta = y$ or $-y$, the evolution of the transverse ^{13}C magnetization due to ^{13}C-^{13}C dipolar coupling was averaged to zero and S_0 data were obtained and for $\zeta = x$ or $-x$, the evolution was not averaged to zero and S_1 data were obtained. The duration of ^{13}C recoupling or dephasing period $\tau = 2L\tau_R$, and data with increasing τ were obtained by incrementing *L* and decrementing *N* while keep constant *M* and constant $(L + M + N)$.

For the experimental parameter calibrations of fpCTDQBU, a polycrystalline N-acetyl leucine (NAL) sample was used which was ^{13}C labeled at the acetyl and carboxyl positions. Typical experimental parameters included 8000 Hz MAS frequency, 46 kHz ^{1}H $\pi/2$ pulse, 1.0 ms cross-polarization period with 54 kHz ^{1}H field and 58-69 kHz ramped ^{13}C field, 22 KHz ^{13}C π pulses with XY-8 phase cycling, continuous wave ^{1}H decoupling during the evolution and acquisition periods with Rabi frequencies of ~70 and ~60 kHz, respectively, and 1.5 s recycle delay. The experiment was done with "constant time" so that for all values of τ, $M = L + N$.

5. PDSD spectroscopy

The proton-driven spin diffusion (PDSD) experiment provided $^{13}C/^{13}C$ correlation spectra for membrane-associated IFPs. The ^{13}C chemical shifts from the cross peak assignments can be used to determine the secondary structure of IFP. The pulse sequence is shown in Figure 10 which contains an initial ^{1}H $\pi/2$ pulse followed by a ^{1}H–^{13}C *CP*, an evolution period t_1, a ^{13}C $\pi/2$ pulse that rotated the ^{13}C transverse magnetization to the longitudinal axis, a spin diffusion period τ during which ^{13}C magnetization was mixed among nearby nuclei, a second ^{13}C $\pi/2$ pulse that rotated the ^{13}C magnetization back to the transverse plane, and a detection period t_2. A ~70 KHz ^{1}H decoupling field with TPPM was applied during t_1 and t_2, but not during τ.[24] The ^{1}H and ^{13}C pulses were calibrated with a NAL sample which was uniformly ^{13}C labeled. The following parameters were typical for PDSD experiments: 10000 kHz MAS frequency, 36-42 kHz ramp

on the ^{13}C *CP* rf field, 56 kHz ^{1}H *CP* rf field, 25 μs t_1 dwell time, 200 t_1 values, 20 μs t_2 dwell time, 256 t_1 points, 10 ms exchange time, and 1 s recycle delay. Hypercomplex data were obtained by acquiring two individual FIDs for each t_1 point with either a ^{13}C $(\pi/2)_x$ or $(\pi/2)_y$ pulse at the end of the t_1 evolution period. For the first of these t_1 FIDs, individual transients had the following phase cycling scheme: first ^{13}C $\pi/2$ pulse, I*x*, –*x*, *x*, –*x*, *x*, –*x*, *x*, –*x*; second ^{13}C $\pi/2$ pulse, *x*, *x*, *y*, *y*, –*x*, –*x*, –*y*, –*y*; receiver, *y*, –*y*, –*x*, *x*, –*y*, *y*, *x*, –*x*. For the other t_1 FIDs, the first ^{13}C $\pi/2$ pulse followed *y*, –*y*, *y*, –*y*, *y*, –*y*, *y*, –*y* cycling.

6. Experimental data analysis

For the REDOR and fpCTDQBU experiments, the differences in the ^{13}C signal intensities of the S_0 and S_1 spectra at different *r* can be used to calculate the internuclear dipolar coupling and distance which are quantitatively related to each other. For a single spin labeled pair, the dipolar coupling *d* in Hz and distance *r* in Å are related by the following equations:

$$r_{CN} = (3100/d_{CN})^{1/3} \ (^{13}C–^{15}N \text{ pair}) \qquad (2.1)$$

$$r_{CP} = (12250/d_{CP})^{1/3} \ (^{13}C–^{31}P \text{ pair}) \qquad (2.2)$$

$$r_{CF} = (28540/d_{CF})^{1/3} \ (^{13}C–^{19}F \text{ pair}) \qquad (2.3)$$

$$r_{CC} = (7700/d_{CC})^{1/3} \ (^{13}C–^{13}C \text{ pair}) \qquad (2.4)$$

These determinations relied on integrations of the ^{13}CO regions of the S_0 and S_1 spectra and the resulting integrated intensities were denoted "S_0" and "S_1" respectively. An experimental fractional dephasing

$$(\Delta S/S_0)^{exp} = \left(S_0^{exp} - S_1^{exp}\right)/S_0^{exp} \quad (2.5)$$

was calculated for each τ. Determination of d also relied on calculation of theoretical dephasing $(\Delta S/S_0)^{sim}$ for different values of d and τ. For the REDOR data, the theoretical dephasing was calculated:

$$(\Delta S/S_0)^{sim} = 1 - \left[J_0\left(\sqrt{2}\lambda\right)\right]^2 + 2\sum_{k=1}^{5} \frac{\left[J_k\left(\sqrt{2}\lambda\right)\right]^2}{16k^2 - 1} \quad (2.6)$$

where $\lambda = d\tau$ and J_k is the k^{th} order Bessel function of the first kind.[25] Eq. 2.6 is based on a model of a single spin pair separated by a single distance. This was a reasonable model for the labeled spin pair which made the dominant contribution to $(\Delta S/S_0)^{exp}$.

For the fpCTDQBU data, $(\Delta S/S_0)^{sim}$ values were calculated using the SIMPSON program, which is a computer program for a fast and accurate numerical simulations of multiple-pulse NMR experiments. It functions as a "computer spectrometer" by using NMR concepts such as spin systems, nuclear spin interactions, phase cycling and by using specific NMR acquisition and processing parameters. The simulation also uses a single spin-label pair model and literature-based ^{13}CO chemical shift anisotropy (CSA) principal values.[22, 26]

Quantitative comparison between $(\Delta S/S_0)^{exp}$ and $(\Delta S/S_0)^{sim}$ at different values of d and τ provide information on the best-fit internuclear distances. However, there were also contributions to $(\Delta S/S_0)^{exp}$ from natural abundance nuclei. As described in the appendix and other publications,[12, 22] models have been developed to calculate these natural abundance contributions. For each

value of $(\Delta S/S_0)^{exp}$, a "corrected" $(\Delta S/S_0)^{cor}$ was calculated that only reflected the labeled pair.

As an example, calculations of $(\Delta S/S_0)^{cor}$ for IFP-A7$_C$G8$_C$ were based on the following parameters/approximations:

(1). There is 99% labeling of the Ala-7 and Gy-8 ^{13}CO sites.

(2). S_1 = 0 for Ala-7 ^{13}CO/natural abundance ^{13}C or Gly-8 ^{13}CO/natural abundance ^{13}C separated by one or two bonds. The S_1 is not affected by other natural abundance ^{13}Cs.

(3). For natural abundance backbone ^{13}CO sites, $S_1 = S_0$.

Each $(\Delta S/S_0)^{cor}$ value is calculated using the parameters U_C, A_C, n, m_1 and m_2 where: U_C is the fraction of Ala-7 ^{12}CO or Gly-8 ^{12}CO sites; A_C is the fractional ^{13}C natural abundance; n is the number of unlabeled CO sites; and m_1 and m_2 are the number of natural abundance sites which satisfies (2) for Ala-7 and Gly-8 respectively. As described in the appendix as well as in the literature, for each value of $(\Delta S/S_0)^{exp}$, a "corrected" $(\Delta S/S_0)^{cor}$ was calculated that only reflected the labeled pair:

$$\left(\frac{\Delta S}{S_0}\right)^{cor} = \frac{2 - U_C + n A_C}{(1 - U_C)(2 - m_1 A_C - m_2 A_C)}\left(\frac{\Delta S}{S_0}\right)^{exp} - \frac{m_1 A_C + m_2 A_C}{2 - m_1 A_C + m_2 A_C} \qquad (2.7)$$

The values of U_C, A_C, n, m_1 and m_2 are 0.01, 0.011, 26, 3 and 2, respectively, and numerical evaluation of Eq. 2.7 yields:

$$\left(\frac{\Delta S}{S_0}\right)^{cor} = 1.177\left(\frac{\Delta S}{S_0}\right)^{exp} - 0.028 \qquad (2.8)$$

The calculations of $(\Delta S/S_0)^{cor}$ for the REDOR data are detailed in the appendix. The $(\Delta S/S_0)^{cor}$ has the general form $a\times(\Delta S/S_0)^{exp}-b$, where a and b are positive numbers.

The quantitative comparison between $(\Delta S/S_0)^{cor}$ and $(\Delta S/S_0)^{sim}$ requires the knowledge of experimental uncertainties. Uncertainties of S_0 and S_1 spectra, σ_{S_0} and σ_{S_1}, were calculated as the root-mean-squared deviations of integrated intensities in 12 regions of the S_0 and S_1 spectra without signal. The uncertainties in $(\Delta S/S_0)^{exp}$ were calculated:

$$\sigma^{exp}=\sqrt{\frac{{\sigma_{S_1}}^2}{{S_0}^2}+\frac{S_1^2{\sigma_{S_0}}^2}{{S_0}^4}}=\frac{S_1}{S_0}\sqrt{\frac{{\sigma_{S_1}}^2}{S_1^2}+\frac{{\sigma_{S_0}}^2}{{S_0}^2}} \tag{2.9}$$

The values of σ^{cor} were calculated from the σ^{exp} and had the form of $a\times\sigma^{exp}$.

The $(\Delta S/S_0)^{cor}$ could be directly compared to $(\Delta S/S_0)^{sim}$ using a χ^2 analysis:

$$\chi^2(d)=\sum_{i=1}^{T}\frac{\left\{\left(\frac{\Delta S}{S_0}\right)_i^{cor}-\left(\frac{\Delta S}{S_0}(d)\right)_i^{sim}\right\}^2}{\left(\sigma_i^{cor}\right)^2} \tag{2.10}$$

where the sum is over the experimental τ values. The best-fit distance d corresponded to the minimum $\chi^2(d)$ in Eq. 2.10. The uncertainty in the best-fit value was calculated using the d values at $\chi^2 = (\chi^2)_{min} + 5$ which is a generous statistical criterion.

2.4 STATIC SOLID-STATE NMR

1. General static NMR spectroscopy

Alignment of the bicelles was probed with measurement of the anisotropic quadrupolar splittings of ^{2}H nuclei in the lipid acyl chains or anisotropic ^{31}P chemical shift of the lipid head group. Alignment of the IFP helix axis relative to the bicelle normal was probed with measurements of the anisotropic chemical shifts of labeled ^{15}N nuclei in the IFP backbone or the dipolar coupling of the directly bonded ^{15}N–^{1}H pair. Most of the NMR spectra were obtained with the aforementioned 9.4 T spectrometer and a Varian Biostatic $^{1}H/X$ probe with 5 mm coil which was designed for minimizing RF heating in the sample. Some of the chemical shift measurements were done with a regular static $^{1}H/X$ probe which requires a much longer recycle delay compared to the Biostatic probe in order to reduce the RF heating. The ^{2}H frequency was 61.2 MHz. For some of the experiments, a 21.1 T solution/solid state NMR spectrometer (Bruker Avance, Billerica, MA) equipped with "Efree" static $^{1}H/^{15}N$ (^{31}P) probe was used. The Bruker "Efree" probe is similar to the Varian Biostatic probe but uses a different design to minimize RF heating. The ^{1}H and ^{15}N frequencies were 899.9 and 91.2 MHz respectively. For all the experiments, the ^{13}C, ^{15}N and ^{31}P shifts were respectively externally referenced to the methylene resonance of adamantane at 40.5 ppm, to $(^{15}NH_4)_2SO_4$ at 26.5 ppm or to H_3PO_4 at 0 ppm. The bicelle samples were typically heated with nitrogen gas at 40 °C which is near the middle of the temperature range of stable bicelle structure.

2. ^{2}H and ^{31}P spectroscopy

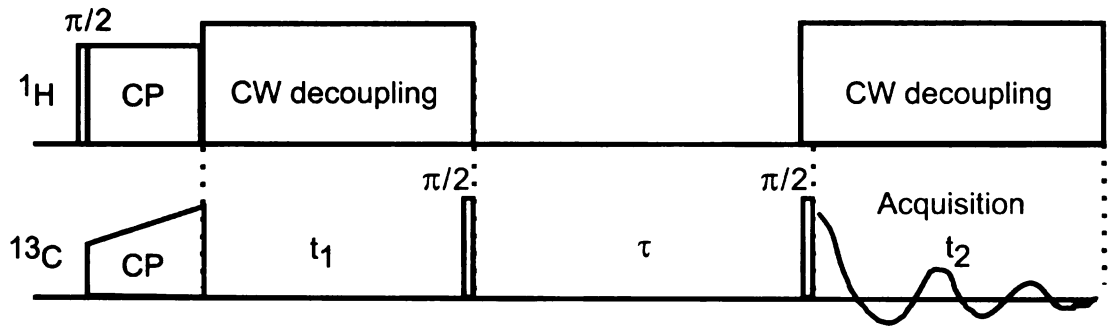

Figure 10. PDSD pulse sequence. Magnetization was transferred from ^{1}H to ^{13}C during the *CP* period. CW decoupling was applied after *CP* on the ^{1}H during t_1 and t_2, but not during τ. t_1 was the evolution time, τ was the magnetization exchange time, and t_2 was the acquisition time.

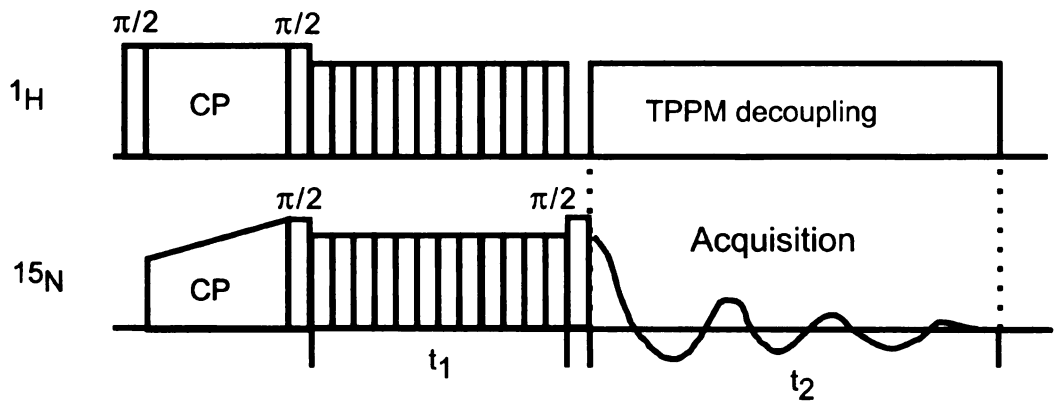

Figure 11. PI-WIM-z pulse sequence. After the magnetization transfer from ^{1}H to ^{15}N during the *CP* period, the $\pi/2$ pulses on each channel flip ^{1}H and ^{15}N magnetization to opposite directions to achieve polarization inversion. The multiple back-to-back $\pi/2$ pulses during the WIM period enable the spin exchange between the ^{1}H and ^{15}N nuclei and suppress the ^{1}H-^{1}H dipolar coupling and chemical shift evolution. TPPM decoupling was applied during the acquisition period.

The ^{2}H spectra were obtained without ^{1}H decoupling and with a $(\pi/2)_0 - \tau_1 - (\pi/2)_{\pm 90} - \tau_2 -$ *acquisition* solid echo sequence. The sequence was used to minimize effects from probe ring-down. The phase of the first $\pi/2$ pulse was *x* and the phase of the second $\pi/2$ pulse alternated between *y* and *–y*. Experimental parameters included 33 kHz ^{2}H Rabi frequency, 50 μs τ_1, 25 τ_2 and 0.5 s recycle delay. The $\pi/2$ pulse was calibrated with a water sample containing 10 % of deuterium oxide.

For ^{31}P experiments, Bloch decay spectra were taken using a recycle delay of 3 s and CYCLOPS phase cycling. The ^{31}P Rabi frequency was 65 kHz and was calibrated with a sample of phosphoric acid.

3. ^{15}N chemical shift measurements

The ^{15}N spectra were obtained with a sequence that contained ^{1}H–^{15}N cross-polarization followed by ^{15}N detection with ^{1}H decoupling. The rf fields were calibrated using a ^{15}N-NAV single crystal. For experiments performed with the regular static probe on the 9.4 T spectrometer, typical experimental parameters included a ~50 kHz ^{1}H $\pi/2$ pulse, 1.0 ms ramped cross-polarization with 18–22 kHz ^{15}N and ~20 kHz ^{1}H Rabi frequencies, ~40 kHz ^{1}H decoupling, and 7 s recycle delay. The long recycle delay reduced rf heating of the samples.

For experiments done with the Biostatic probe on the 9.4 T spectrometer, a ~42 kHz ^{1}H $\pi/2$ pulse, a 1 ms cross polarization with ~ 40 kHz ^{1}H field and 38-44 kHz ^{15}N field and a ~42 kHz ^{1}H decoupling field during acquisition were used. The recycle delay was 1 s.

For experiments done with the 21.1 T solution/solid state NMR spectrometer, the parameters included ~38 kHz ^{1}H $\pi/2$ pulse, 1.0 ms cross polarization with ~33 kHz ^{1}H and ^{15}N Rabi frequencies, and ~28 kHz SPINAL-16 decoupling. During the *CP* period, a ramp 80.100 was added on the ^{1}H channel. The recycle delay was 1 s.

4. ^{15}N chemical shift & ^{15}N–^{1}H dipolar coupling correlation spectroscopy

The heteronuclear dipolar spin interactions such as ^{1}H–^{15}N dipolar coupling can provide valuable information for the structural and dynamic investigations of anisotropic solid samples. The high-resolution dipolar coupling spectrum can be obtained by 2D PISEMA-type experiments which are based on the heteronuclear spin exchange via the local field with efficient homonuclear proton decoupling. In my research, the 2D correlation spectra were acquired by the 2D PI-WIM-z (polarization inversion – windowless isotropic mixing – polarization exchange between z-component of magnetization) technique which was designed to have high tolerance towards chemical shift and frequency offsets and is more suitable for measurements of motionally reduced dipolar couplings.[27] The sequence is shown in Figure 9. After the regular cross polarization period, a $\pi/2$ pulse is applied to ^{1}H and ^{15}N respectively to prepare the two spin polarizations in opposite directions to achieve polarization inversion (PI) which can enhance the experimental sensitivity. The WIM-z sequence (WIM24) is composed of on-resonance back-to-back $\pi/2$ pulses with phase cycling, *-y, x, -y, -y, x, -y, y, x, y, y, x, y, -y, -x, -y, -y, -x, -y, y, -x, y, y, -x, y,* which

are simultaneously applied to both nuclei. The spin exchange between the ^{1}H and ^{15}N magnetizations occurs during this period in much the same way that *CP* transfers the spin locked components and the oscillation frequency was determined by the ^{15}N–^{1}H dipolar coupling. At the same time, the homonuclear dipolar coupling and chemical shift evolution were suppressed by the WIM-z sequence. The resulting scaling factor of the dipolar coupling is 0.67. In this experiment, the t_1 increment is the duration of the 24 $\pi/2$ pulses of the WIM-z sequence which provides a ~7 kHz spectral window to record the dipolar splitting. This width can be doubled by setting t_1 increment to half of the WIM24 cycle, i.e., WIM12.

The ^{1}H and ^{15}N pulses were calibrated with a N15-NAV single crystal sample. The following parameters were typical for PI-WIM-z experiments performed with the 9.4 T spectrometer: ~42 kHz ^{1}H and ^{15}N $\pi/2$ pulses, 1 ms cross polarization with ~ 40 kHz ^{1}H field and 38-44 kHz ^{15}N field, ~42 kHz ^{1}H decoupling field and 1 s recycle delay. For most of the experiments, WIM12 was generally used. For some experiments, WIM24 was also used to indentify aliasing. The parameters for experiments done with the 21.1 T spectrometer are: ~38 kHz ^{1}H and ^{15}N $\pi/2$ pulses, 1.0 ms cross polarization with ~33 kHz ^{1}H and ^{15}N Rabi frequencies (ramp on the ^{1}H frequency channel with ramp80.100), ~28 kHz SPINAL-16 decoupling and 1 s recycle delay. WIM24 was used for the experiments.

5. Static ^{15}N NMR analysis

Nuclear spin interactions are anisotropic which provides the basis for the extraction of the peptide orientation in a lipid bilayer. Specifically, the chemical shift and dipolar coupling frequencies depend on the relative orientation of the corresponding tensors (i.e., chemical shift and dipolar coupling tensors) and the external magnetic field.

The major spin interactions for the ^{15}N nucleus in the rigid lattice are chemical shift anisotropy (H_{CSA}) and ^{15}N-^{1}H dipolar coupling (H_{DIP}), which can be written as:[28]

$$H = H_{CSA} + H_{DIP} \tag{2.11}$$

where

$$H_{CSA} = \gamma_N \hbar \mathbf{B} \cdot (\mathbf{1} - \boldsymbol{\sigma}) \cdot \mathbf{S} \tag{2.12}$$

and

$$H_{DIP} = \frac{\hbar \mu_0}{4\pi} \frac{\gamma_N \gamma_H}{r^3} \left(1 - 3\cos^2 \vartheta\right) S_Z I_z \tag{2.13}$$

B is the magnetic field, γ_N and γ_H are the gyromagnetic ratios of ^{15}N and ^{1}H, and **S** and **I** represent the ^{15}N and ^{1}H spin angular momentum. The chemical shift tensor, $\boldsymbol{\sigma}$, in the principal axis system is given by

$$\boldsymbol{\sigma} = \begin{pmatrix} \sigma_{11} & 0 & 0 \\ 0 & \sigma_{22} & 0 \\ 0 & 0 & \sigma_{33} \end{pmatrix} \tag{2.14}$$

The unit matrix **1** is

$$\mathbf{1} = \begin{pmatrix} 1 & 0 & 0 \\ 0 & 1 & 0 \\ 0 & 0 & 1 \end{pmatrix} \tag{2.15}$$

The ^{15}N-^{1}H internuclear distance is r, and N-H vector makes an angle of ϑ with the magnetic field.

For an ideal α-helical structure with dihedral angles φ = -65° and ψ = -40°, the chemical shift and dipolar coupling frequencies can be calculated using the following equations:[29]

$$\begin{aligned}\sigma(\rho,\tau) = {} & \sigma_{11}(-0.828\cos\rho\sin\tau + 0.558\sin\rho\sin\tau - 0.047\cos\tau)^2 \\ & + \sigma_{22}(0.554\cos\rho\sin\tau + 0.803\sin\rho\sin\tau - 0.220\cos\tau)^2 \\ & + \sigma_{33}(-0.088\cos\rho\sin\tau - 0.206\sin\rho\sin\tau - 0.975\cos\tau)^2\end{aligned} \qquad (2.16)$$

$$\nu(\rho,\tau) = \frac{\nu_{\parallel}}{2}\left(3(-0.326\cos\rho\sin\tau - 0.034\sin\rho\sin\tau - 0.946\cos\tau)^2 - 1\right) \qquad (2.17)$$

where σ_{11}, σ_{22} and σ_{33} are the principal values of the chemical shift tensor and $\nu_{\parallel}$ is the rigid limit ^{15}N-^{1}H dipolar splitting, or dipolar coupling constant $\nu_{\parallel} = (\hbar\mu_0/4\pi)(\gamma_N\gamma_H/r^3)$, which is 22.6 kHz assuming an internuclear separation of 1.024 Å. In the calculations, standard values for the relative orientation of the dipolar and chemical shift tensors σ was assumed (cf. Figure 12a). The axis σ_{33} is in the peptide plane and makes an angle of ~17° from the N-H vector and points between the N-H and N-CO bonds; σ_{11} is perpendicular to σ_{33} and points between the N-H and N-C_α bonds; σ_{22} is perpendicular to the peptide plane and follows the right hand rule. The two Euler angles, ρ and τ (cf. Figure 12b)[29], represent the rotation of a particular residue about the helix axis and the tilt of the helical axis with respect to the magnetic field, respectively. For an ideal helix with a periodicity of 3.6 residues per turn, the increment of ρ is 100° for each consecutive residue.

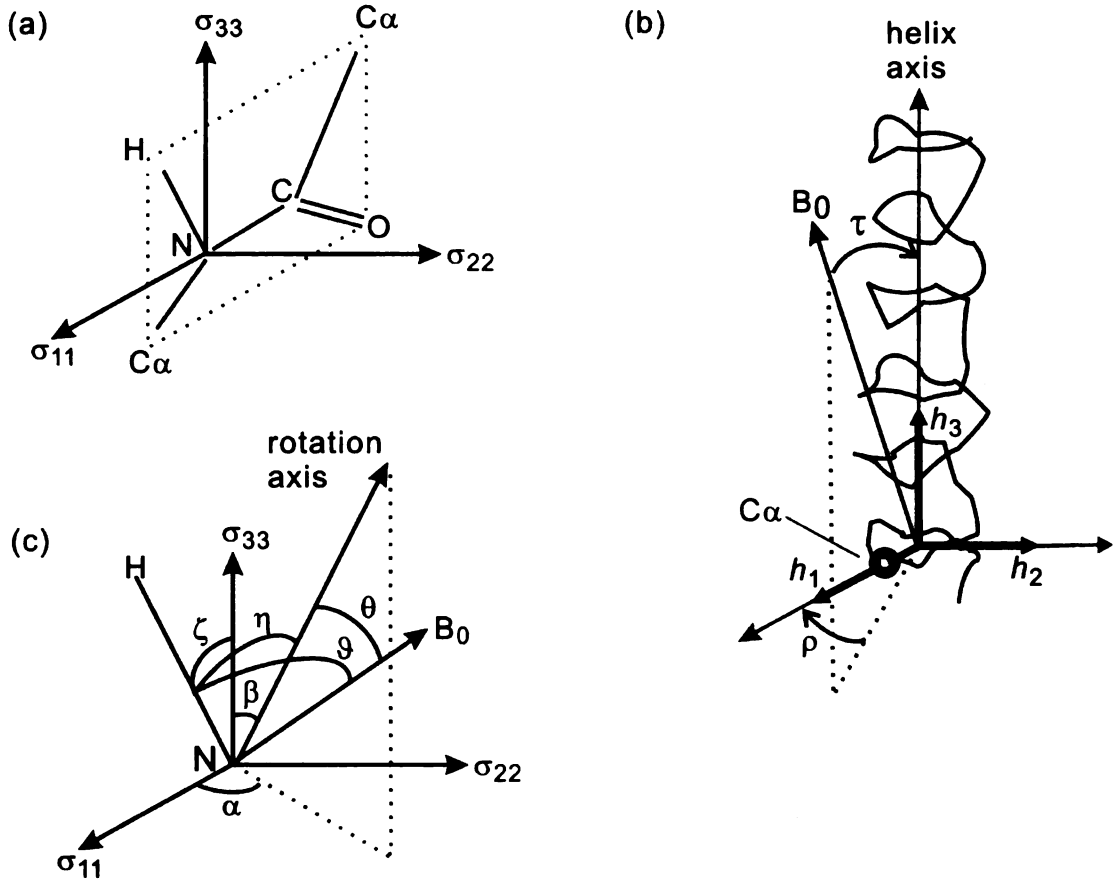

Figure 12. (a) The ^{15}N chemical shift tensor relative to the peptide plane. Axes σ_{11} and σ_{33} are in the peptide plane with σ_{33} pointing between the N-H and N-CO bonds, ~17° away from N-H vector and σ_{11} pointing to N-Cα. Axis σ_{22} is perpendicular to the peptide plane. (b) Definition of helix rotation (ρ) and tilt (τ) angles. The helix axis is defined by h_3 and h_1 is the radial axis that passes through Cα carbon and varies for different residues. The helix tilt angle, τ, is the angle between the helix axis and the magnetic field (B_0). The helix rotation ρ is the angle between h_1 and the projection of $\mathbf{B}_0$ on to the plane perpendicular to h_3. (c) Definition of angles in the system in which the helix has fast rotation around a fixed axis. Angles α and β are the Euler angles of the rotation axis and the chemical shift principal axis system (PAS). The angle between the N-H vector and σ_{33}, the N-H vector and the rotation axis, the N-H vector and $\mathbf{B}_0$, and the rotation axis and $\mathbf{B}_0$ are represented by ζ, η, ϑ and θ, respectively.

In a real biological system, there are generally a lot of motions associated with the proteins or membranes, which cause the motional average of spin interactions when the rates of motions are faster than those of the NMR interaction time scale (~10^{-5} sec based on the typical magnitude of NMR interaction, ~10 kHz). There are two basic motions of membrane-associated protein, fast rotation and libration. In the case of fast rotation around a fixed axis, the rigid lattice chemical shift tensor will be averaged to an axially symmetric tensor σ_{EFF},[28]

$$\sigma_{EFF} = \begin{pmatrix} \sigma_{\perp} & 0 & 0 \\ 0 & \sigma_{\perp} & 0 \\ 0 & 0 & \sigma_{\parallel} \end{pmatrix} = \sigma_i \mathbf{1} + (1/3)\Delta\sigma_{EFF} \begin{pmatrix} -1 & 0 & 0 \\ 0 & -1 & 0 \\ 0 & 0 & 2 \end{pmatrix} \tag{2.18}$$

where $\sigma_{\perp}$ and $\sigma_{\parallel}$ are the components perpendicular and parallel to the rotational axis. The isotropic chemical shift σ_i is

$$\sigma_i = \frac{1}{3}(\sigma_{11} + \sigma_{22} + \sigma_{33}) = \frac{1}{3}(2\sigma_{\perp} + \sigma_{\parallel}) \tag{2.19}$$

And the effective chemical shift anisotropy $\Delta\sigma_{EFF}$ can be written as[28]

$$\Delta\sigma_{EFF} = \sigma_{\parallel} - \sigma_{\perp} = \frac{1}{2}\left(3\cos^2\beta - 1\right)\left(\sigma_{33} - \frac{1}{2}(\sigma_{11} + \sigma_{22})\right) + \frac{3}{4}(\sigma_{11} - \sigma_{22})\sin^2\beta\cos 2\alpha \tag{2.20}$$

where α and β are the Euler angles between the rotational axis (cf. Figure 12c) and the principal axes of the rigid lattice chemical shift tensor.

Therefore, H_{CSA} in the case of fast rotational motion is

$$H_{CSA} = \gamma_N \hbar \mathbf{B} \cdot (\mathbf{1} - \sigma_{EFF}) \cdot \mathbf{S} \tag{2.21}$$

and yields the chemical shift[28]

$$\sigma(\theta) = \frac{2}{3}\Delta\sigma_{EFF}P_2(\cos\theta) + \sigma_{iso} \quad (2.22)$$

where θ is the angle between the rotational axis and the external magnetic field and $P_2(\cos\theta)$ is a Legendre polynomial

$$P_2(\cos\theta) = \frac{1}{2}\left(3\cos^2\theta - 1\right) \quad (2.23)$$

Similarly, the observed dipolar coupling can be calculated as

$$\nu(\theta) = \nu_{\parallel}\frac{1}{2}\left(3\cos^2\eta - 1\right)P_2(\cos\theta) \quad (2.24)$$

where

$$\cos\eta = \cos\beta\cos\zeta - \sin\beta\sin\zeta\cos\alpha \quad (2.25)$$

Angle η is between the N-H vector and the rotational axis; ζ is between the N-H vector and σ_{33}.

All the experimental data for aligned samples were taken with bicelles which are considered to have rapid small angle "wobbling" of the bicelle normal with respect to the magnetic field direction. A parameter describing the magnitude of wobbling, S_{wobb}, was estimated as the ratio of a ^{2}H quadrupolar splitting of $DMPC_{d54}$ in a bicelle sample relative to the splitting in a mechanically aligned bilayer sample that lacks wobbling motion. The value of S_{wobb} is 0.8.[30] This wobbling motion will scale down the effective chemical shift anisotropy and the maximum dipolar coupling. In addition, there is a scaling factor (κ = 0.67) associated with the homonuclear decoupling sequence used in the 2D PI-WIM-z experiment, which also reduces the dipolar coupling. Therefore, the ^{15}N chemical shift and dipolar coupling in a wobbling bicelle become:[28]

$$\sigma(\theta) = \frac{2}{3} \cdot \Delta\sigma_{EFF} \cdot P_2(\cos\theta) \cdot S_{wobb} + \sigma_{iso} \tag{2.26}$$

$$\nu(\theta) = \kappa \cdot \nu_{\parallel} \cdot \frac{1}{2}\left(3\cos^2\eta - 1\right) P_2(\cos\theta) \cdot S_{wobb} \tag{2.27}$$

2.5 REFERENCES

1. Chang, C. D.; Waki, M.; Ahmad, M.; Meienhofer, J.; Lundell, E. O.; Haug, J. D., Preparation and properties of N-a-9- fluorenylmethyloxycarbonylamino acids bearing tert-butyl side chain protection. *Int. J. Pept. Protein Res.* **1980,** 15, (1), 59-66.

2. Lapatsanis, L.; Milias, G.; Froussios, K.; Kolovos, M., Synthesis of N-2,2,2-(trichloroethoxycarbonyl)-L-amino acids and N-(9-fluorenylmethoxycarbonyl)-L-amino acids involving succinimidoxy anion as a leaving group in amino-acid protection. *Synthesis-Stuttgart* **1983,** (8), 671-673.

3. Yang, J.; Prorok, M.; Castellino, F. J.; Weliky, D. P., Oligomeric beta structure of the membrane-bound HIV-1 fusion peptide formed from soluble monomers. *Biophys. J.* **2004,** 87, 1951-1963.

4. Worman, H. J.; Brasitus, T. A.; Dudeja, P. K.; Fozzard, H. A.; Field, M., Relationship Between Lipid Fluidity and Water Permeability of Bovine Tracheal Epithelial-Cell Apical Membranes. *Biochemistry* **1986,** 25, (7), 1549-1555.

5. Han, X.; Bushweller, J. H.; Cafiso, D. S.; Tamm, L. K., Membrane structure and fusion-triggering conformational change of the fusion domain from influenza hemagglutinin. *Nat. Struct. Biol.* **2001,** 8, (8), 715-720.

6. Macosko, J. C.; Kim, C. H.; Shin, Y. K., The membrane topology of the fusion peptide region of influenza hemagglutinin determined by spin-labeling EPR. *J. Mol. Biol.* **1997,** 267, (5), 1139-1148.

7. Li, Y.; Han, X.; Tamm, L. K., Thermodynamics of Fusion Peptide-Membrane Interactions. *Biochemistry* **2003,** 42, 7245-7251.

8. Han, X.; Tamm, L. K., pH-dependent self-association of influenza hemagglutinin fusion peptides in lipid bilayers. *J. Mol. Biol.* **2000,** 304, (5), 953-965.

9. Bodner, M. L.; Gabrys, C. M.; Struppe, J. O.; Weliky, D. P., 13C–13C and 15N–13C correlation spectroscopy of membrane-associated and uniformly labeled human immunodeficiency virus and influenza fusion peptides: Amino acid-type assignments and evidence for multiple conformations. *J. Chem. Phys.* **2008,** 128, 052319.

10. Parkanzky, P. D., *Solid state nuclear magnetic resonance studies of the influenza fusion peptide associated with membrane bilayers.* Ph. D. thesis, Michigan State University: East Lansing, **2006**, 80.

11. Wasniewski, C. M.; Parkanzky, P. D.; Bodner, M. L.; Weliky, D. P., Solid-state nuclear magnetic resonance studies of HIV and influenza fusion peptide orientations in membrane bilayers using stacked glass plate samples. *Chem. Phys. Lipids* **2004,** 132, (1), 89-100.

12. Qiang, W.; Yang, J.; Weliky, D. P., Solid-state nuclear magnetic resonance measurements of HIV fusion peptide to lipid distances reveal the intimate contact of beta strand peptide with membranes and the proximity of the Ala-14-Gly-16 region with lipid headgroups. *Biochemistry* **2007,** 46, (17), 4997-5008.

13. Lenard, J.; Compans, R. W., The membrane structure of lipid-containing viruses. *BBA-Biomembranes* **1974,** 344, (1), 51-94.

14. Hirsh, D. J.; Lazaro, N.; Wright, L. R.; Boggs, J. M.; McIntosh, T. J.; Schaefer, J.; Blazyk, J., A New Monofluorinated Phosphatidylcholine Forms Interdigitated Bilayers. *Biophys. J.* **1998,** 75, (4), 1858-1868.

15. Pereira, F. B.; Valpuesta, J. M.; Basanez, G.; Goni, F. M.; Nieva, J. L., Interbilayer lipid mixing induced by the human immunodeficiency virus type-1 fusion peptide on large unilamellar vesicles: the nature of the nonlamellar intermediates. *Chem. Phys. Lipids* **1999,** 103, (1-2), 11-20.

16. De Angelis, A. A.; Nevzorov, A. A.; Park, S. H.; Howell, S. C.; Mrse, A. A.; Opella, S. J., High-resolution NMR spectroscopy of membrane proteins in aligned bicelles. *J. Am. Chem. Soc.* **2004,** 126, (47), 15340-15341.

17. Morcombe, C. R.; Zilm, K. W., Chemical shift referencing in MAS solid state NMR. *J. Magn. Reson.* **2003,** 162, 479-486.

18. Zhang, H. Y.; Neal, S.; Wishart, D. S., RefDB: A database of uniformly referenced protein chemical shifts. *J. Biomol. NMR* **2003,** 25, (3), 173-195.

19. Igumenova, T. I.; Wand, A. J.; McDermott, A. E., Assignment of the backbone resonances for microcrystalline ubiquitin. *J. Am. Chem. Soc.* **2004,** 126, (16), 5323-5331.

20. Franks, W. T.; Zhou, D. H.; Wylie, B. J.; Money, B. G.; Graesser, D. T.; Frericks, H. L.; Sahota, G.; Rienstra, C. M., Magic-angle spinning solid-state NMR spectroscopy of the beta 1 immunoglobulin binding domain of protein G (GB1): N-15 and C-13 chemical shift assignments and conformational analysis. *J. Am. Chem. Soc* **2005,** 127, (35), 12291-12305.

21. Marulanda, D.; Tasayco, M. L.; Cataldi, M.; Arriaran, V.; Polenova, T., Resonance assignments and secondary structure analysis of E-coli thioredoxin

by magic angle spinning solid-state NMR spectroscopy. *J. Phys. Chem. B* **2005,** 109, (38), 18135-18145.

22. Zheng, Z.; Yang, R.; Bodner, M. L.; Weliky, D. P., Conformational flexibility and strand arrantments of the membrane-associated HIV fusion peptide trimer probed by solid-state NMR spectroscopy. *Biochemistry* **2006,** 45, 12960-12975.

23. Taylor, K. S.; Lou, M. Z.; Chin, T. M.; Yang, N. C.; Garavito, R. M., A novel, multilayer structure of a helical peptide. *Protein Sci.* **1996,** 5, (3), 414-421.

24. Bennett, A. E.; Rienstra, C. M.; Auger, M.; Lakshmi, K. V.; Griffin, R. G., Heteronuclear decoupling in rotating solids. *J. Chem. Phys.* **1995,** 103, (16), 6951-6958.

25. Mueller, K. T., Analytical Solutions for the Time Evolution of Dipolar-dephasing NMR Signals. *J. Magn. Reson. Series A* **1995,** 113, (1), 81-93.

26. Bak, M.; Rasmussen, J. T.; Nielsen, N. C., SIMPSON: A general simulation program for solid-state NMR spectroscopy. *J. Magn. Reson.* **2000,** 147, (2), 296-330.

27. Dvinskikh, S. V.; Yamamoto, K.; Ramamoorthy, A., Separated local field NMR spectroscopy by windowless isotropic mixing. *Chem. Phys. Lett.* **2006,** 419, 168-173.

28. Hemminga, M. A.; Cullis, P. R., 31P NMR Studies of Oriented Phospholipid Multilayers. *J. Mag. Reson.* **1982,** 47, 307-323.

29. Wang, J.; Denny, J.; Tian, C.; Kim, S.; Mo, Y.; Kovacs, F.; Song, Z.; Nishimura, K.; Gan, Z.; Fu, R.; Quine, J. R.; Cross, T. A., Imaging membrane protein helical wheels. *J. Magn. Reson.* **2000,** 144, (1), 162-167.

30. Angelis, A. A. D.; Opella, S. J., Bicelle samples for Solid-State NMR of membrane proteins. *Nature protocol* **2007,** 2, (10), 2332-2338.

Chapter 3 Conformational Studies of Membrane-associated Influenza Fusion Peptide

3.1 BACKGROUND

The secondary structure of IFP associated with membranes or detergents has been the subject of considerable studies. However, variations in sample preparation and lipid composition are common, and there are some discrepancies in the data found in the literature. For membrane-associated IFP, although a major helical conformation was detected by FTIR[1-3], CD[3] and ESR[4], there has been detection of an extended form of IFP when IFP:lipid > 0.1[5] at pH 7.4 or when ~33 mol% of cholesterol is incorporated into the membrane bilayer.[6]

The solution NMR structure of detergent-associated IFP indicated that residues 13-18 adopt α helical form at pH 5.0 and have mostly extended structure at pH 7.4. These structural differences have been thought to be correlated to the different functional activities at different pHs.[7] In the same study, IFP was also shown to have a kink around residue Glu-11 at both pHs, which was proposed to be important for the fusion peptide to be active. From the measurements, this kink is stabilized by the hydrogen bonds between Glu-11 NH and Gly-8 CO and between Asn-12 NH and Phe-9 CO at both pHs. Additional hydrogen bonds between side chain NH of Asn-12 and Gly-8 CO and between Trp-14 NH and Phe-9 CO were also observed in 50% of the conformers of the pH 5 structure and may further stabilize the kink. The proposed "kinked boomerang" structure helps the formation of a hydrophobic pocket in the inner

face of the kink which can potentially disrupt the membrane and trigger the membrane fusion.

This chapter presents a detailed investigation of the secondary structure of membrane-associated IFP using a variety of solid-state NMR methods. The first part considers the effect of membrane cholesterol on local conformation using measurement of the ^{13}CO chemical shifts and Ala-7 ^{13}CO–Gly-8 ^{13}CO distance. These studies were mainly based on the previous observations that the related fusion peptide of the HIV virus adopted β strand conformation in cholesterol-containing membranes.[8-13] Measurement of local conformation and fusion activity of IFP as a function of cholesterol and pH could provide insight into the relationship between fusion activity and a specific conformation.

The next set of solid-state NMR data measured the more subtle pH-dependent changes in the structure of helical IFP in membranes without cholesterol. The goal was to test existing structural models which attempt to explain the much greater IFP-induced fusion at pH 5.0 than at pH 7.4. For example, internuclear ^{13}CO–^{15}N distance measurements were carried out to test whether the pH-dependent structures observed for IFP in detergent micelles were also present in membranes.

The final set of solid-state NMR measurements focused on the middle region of the IFP sequence including residues Ile-10 through Gly-13. It is essential to know the conformation of this region of membrane-associated IFP, which can be compared to the detergent-associated IFP structure determined by solution NMR and provides valuable information on the IFP structure/function

model. The conformations of Ile-10, Glu-11, Asn-12 and Gly-13 were determined by 2D ^{13}C–^{13}C correlation spectroscopy of membrane-associated IFP with scatter uniform labeling. Attempts to determine the conformation of those residues have also been made by using internuclear ^{13}CO–^{13}CO distance measurement of IFP mutants, IFP-E11VN12A or IFP-N12A. HA protein with point mutation of Asn-12 to Ala was determined to have similar fusion activity with wild-type HA at pH 5.0.[14] The HA-E11VE15V mutant (HA mutant with mutations of both Glu-11 and Glu-15 to Val) was shown to induce red blood cell lipid mixing with very similar rates to wild-type HA protein at both pH 5.0 and pH 7.4.[15] However, a similar HA mutant, HA-E11A, does not have the ability to induce red blood cell content mixing even though it can induce the cell lipid mixing.[14] In addition, the vesicle fusion induced by IFP and IFP-E11VE15V were compared. IFP-E11VE15V was shown to induce the lipid vesicle fusion in a greater rate and extent (~4 fold) relative to the wild IFP. The fusion activity of IFP-E11VE15V was barely affected by a pH change to 7.4.[15]

The backbone ^{13}CO and sidechain Cα and Cβ chemical shifts are correlated to the local conformations of proteins. The empirical correlation databases have been established by liquid-state NMR assignments of proteins.[16, 17] These databases are appropriate for solid-state NMR data as evidenced by similar ^{13}C shifts observed for the same protein in either aqueous solution or the microcrystalline state.[18, 19] These chemical shift measurements relied on the IFPs with specific ^{13}C labeling which allows the observation of specific ^{13}C chemical shifts.

The ^{13}CO–^{13}CO distance (r_{CC}) were determined with the fpCTDQBU technique which allows the detection of homonuclear dipolar coupling (d_{CC}) under MAS and MAS was used to obtain sharper and more intense ^{13}C signals.[20-25] For IFP with two ^{13}CO labels at adjacent residues in the sequence, measurement of the ^{13}CO–^{13}CO magnetic dipole-dipole coupling discriminated between separation of the two labeled nuclei by ~2.9 Å and separation by ~3.7 Å. These different distances were respectively consistent with helical and β-strand conformations. The ^{13}C–^{15}N distance measurements rely on the application of the REDOR technique which is an approach to measure heteronuclear dipolar coupling.[26-33] For IFP with a ^{13}CO label and an ^{15}N label at different residues separated by four amino acids in the sequence, the ^{13}CO–^{15}N magnetic dipole-dipole coupling measurement distinguishes between the helical and more extended conformations, which have ~4 Å internuclear separation of the two labeled nuclei or > 9 Å separation respectively.

The ^{13}C–^{13}C correlation spectra were obtained by the PDSD pulse sequence with samples uniformly ^{13}C and ^{15}N labeled at selectively residues.[21] The polarization transfer between backbone ^{13}Cs within a residue enables the ^{13}C assignment. The ^{13}C chemical shifts were analyzed using the TALOS program which was designed to derive backbone dihedral angles of proteins based on the aforementioned empirical databases.[34]

3.2 RESULTS

1. ^{13}CO chemical shifts

For membrane-associated IFP samples with IFP with specific ^{13}CO labeling, solid-state NMR spectra of the ^{13}CO region provided information about the local conformations of the labeled residues. For most of the samples, the lipids were ether-linked and therefore lacked CO functionalities. The unfiltered spectrum did contain natural abundance peptide ^{13}CO signals which represented ~20% of the integrated signal intensity for singly labeled IFP and ~10% of the intensity for doubly labeled IFP. Relative to the contribution from the labeled ^{13}COs, the natural abundance contribution likely had a broader linewidth because it was due to many different amino acid types. Most of the spectra are displayed in Figure 13 and peak ^{13}CO shifts from all of the samples are summarized in Table 2. The typical full-width at half-maximum linewidth was 2-3.5 ppm which indicated a narrow conformational distribution.[35] The exceptions were IFP-$G16_C$ and IFP-$G20_C$ which had 5-6 ppm linewidths. For the IFP-$L2_C$ and IFP-$F3_C$ samples, spectra were also obtained with sample cooling gas temperatures of –50 and 0 °C and the spectra were very similar at the two temperatures, cf. table 2. This result indicated that at least the IFP conformation at Leu-2 and Phe-3 did not change when the sample was frozen. Most of the spectra were acquired at the lower temperature to obtain higher signal-to-noise.

The interpretation of the peak ^{13}CO chemical shifts was based on the well-known correlation between the ^{13}CO chemical shift and the local conformation of a residue.[17-19] In particular, the database distributions of the ^{13}CO shifts of Leu, Phe, Ala, Ile, and Gly residues in helical conformation are 178.53 ± 1.30, 177.13 ± 1.38, 179.40 ± 1.32, 177.72 ± 1.29, and 175.51 ± 1.23 ppm and the

corresponding distributions in β strand conformation are 175.67 ± 1.47, 174.25 ± 1.63, 176.09 ± 1.51, 174.86 ± 1.39, and 172.55 ± 1.58 ppm. For all residues except Gly-1 in samples whose membranes lacked cholesterol, the ^{13}CO shifts were more consistent with helical conformation than with β strand conformation. For these samples, the difference in ^{13}CO shift between the pH 5.0 and pH 7.4 samples was ≤ 0.3 ppm which indicated that helical conformation was pH-independent for these residues. The non-helical shift of Gly-1 is presumably related to its N-terminal location. The liquid-state NMR derived structures of IFP in DPC detergent showed helical conformation for residues Leu-2 to Ile-10 in the pH 5.0 sample, helical conformation for Gly-13 and Gly-16 in the pH 5.0 sample, and non-helical conformation for Gly-13 and Gly-16 in the pH 7.4 sample.[7] There was therefore agreement between the solid- and liquid-state NMR results in the pH 5.0 samples but disagreement for Gly-13 and Gly-16 in the pH 7.4 samples. Helical ^{13}CO shifts were also observed for Gly-13 and Gly-16 in pH 7.4 PC/PG membrane samples which disagreed with the non-helical conformation proposed for these residues in the pH 7.4 liquid-state NMR detergent samples. The pH-dependence of the liquid-state NMR conformation in this region was an important part of the structural model proposed to explain the pH-dependence of IFP-induced vesicle fusion. The pH-independent conformation of membrane-associated IFP indicated by the solid-state NMR ^{13}CO shifts shows that the conformation in this region as well as the structure-function model merits further investigation.

The conformation of IFP associated with membranes that contain cholesterol is of some interest because membranes of respiratory epithelial cells infected by the influenza virus contain ~30 mol% cholesterol.[36, 37] For IFP ^{13}CO labeled at Ala-5, Ala-7 and Gly-8, Phe-9 or Gly-13, the spectra were significantly different in samples with membranes that contained cholesterol relative to samples in which cholesterol was absent, cf. Figure 13 and Table 2. The peak ^{13}CO shifts of these residues in cholesterol-containing samples were more consistent with β strand conformation than with helical conformation and the β strand conformation was observed at both pH 5.0 and pH 7.4. For the samples containing IFP-$A5_C$ and IFP-$F9_C$ in cholesterol-containing membranes at pH 7.4, there was also a downfield shoulder which was consistent with a minor population of IFP with helical conformation at the labeled positions. The cholesterol-dependent and pH-independent structure of IFP can be correlated with the functional results. In particular, pH-dependent and pH-triggered IFP fusion was observed both for vesicles which contained cholesterol and for vesicles in which cholesterol was absent.[38] A reasonable overall interpretation of the structural and functional data is that IFP in both the helical and the β strand conformations can induce vesicle fusion.

Table 2. Peak ^{13}CO chemical shifts for membrane-associated IFP [a]

Residue	Membrane or detergent composition	δ (ppm) pH 5.0	pH 7.4
Gly-1	DTPC/DTPG	171.2	171.3
Gly-1	DTPC/DTPG/CHOL	170.2	170.4
Leu-2	POPC/POPG	177.4	177.4
Leu-2	DTPC/DTPG	177.9	178.1
Phe-3	POPC/POPG	178.0	*n.d.* [b]
Phe-3	DTPC/DTPG	178.1	178.2
Ala-5	DTPC/DTPG	179.5	179.5
Ala-5	DTPC/DTPG/CHOL	175.0	174.4 [c]
Ile-6	DTPC/DTPG	177.8	177.9
Ala-7	DTPC/DTPG	179.3	179.0
Ala-7	DTPC/DTPG/CHOL	175.3	175.5
Gly-8	DTPC/DTPG	175.4	175.5
Gly-8	DTPC/DTPG/CHOL	170.3	170.6
Phe-9	DTPC/DTPG	178.6	178.8
Phe-9	DTPC/DTPG/CHOL	171.9	172.4 [d]
Gly-13	DTPC/DTPG	175.3	175.0
Gly-13	DTPC/DTPG/CHOL	173.5	*n.d.*
Gly-16	DTPC/DTPG	175.2	175.3
Gly-20	DTPC/DTPG	174.7	174.6
Gly-20	DTPC/DTPG/CHOL	175.0	*n.d.*

[a] All the spectra were obtained with IFP:total lipid ~ 0.04 and cholesterol was not considered to be a lipid. Spectra for the POPC/POPG membrane samples were obtained with sample cooling gas at 0 °C. For all the other samples, the gas temperature was -50 °C. The uncertainties in peak shifts are ± 0.2 ppm as determined from measurements on different samples that contained peptide with the same labeled residue.

[b] *n.d.* ≡ not determined.

[c] There is a shoulder (~20 %) around 178.8 ppm.

[d] There is a shoulder (~30 %) around 178.0 ppm.

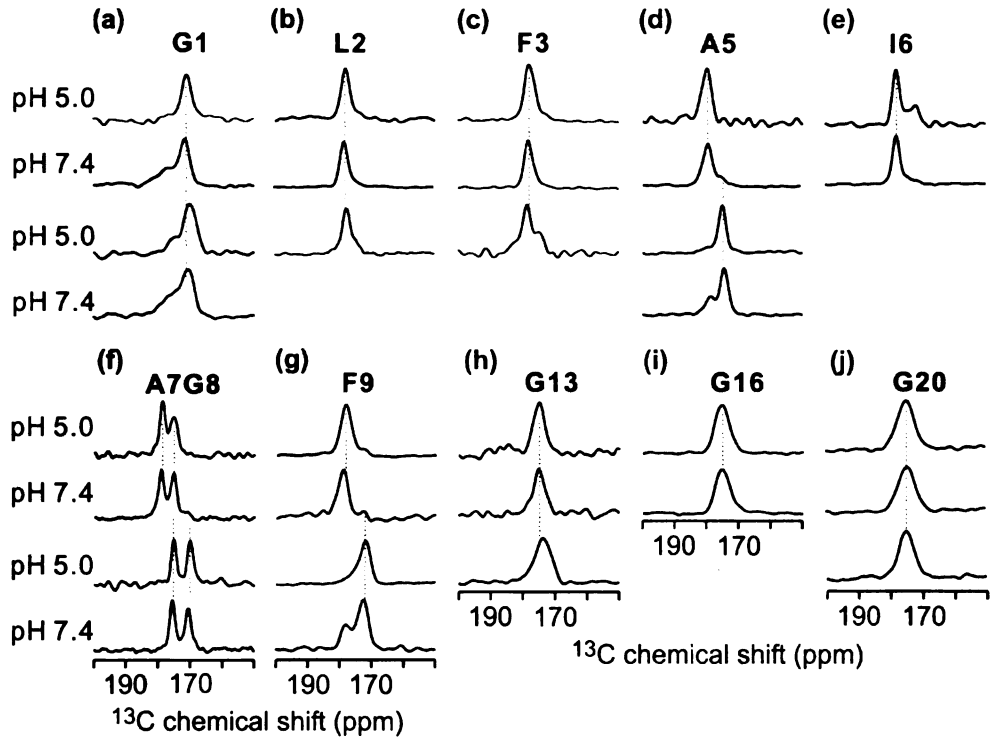

Figure 13. Dependence of ^{13}CO MAS NMR spectra on pH, membrane cholesterol content, and temperature. The ^{13}CO labeled positions are noted above each set of spectra. All spectra were obtained with –50 °C cooling gas temperature except the third spectra in (b) and (c). All samples contained ~0.8 μmol IFP and membranes composed of either ~16 μmol DTPC and ~4 μmol DTPG for the spectra in the first two rows or ~16 μmol DTPC, ~4 μmol DTPG, and ~10 μmol cholesterol for the spectra (except b and c) in the last two rows. The pH was labeled for each row of spectra. There is little pH dependence of the peak shift in the spectra and a strong dependence of spectra on membrane cholesterol content. The observed chemical shifts of Leu-2, Phe-3, Ala-5, Ile-6, Ala-7, Gly-8, Phe-9, Gly-13, Gly-16 and Gly-20 are consistent with predominant helical conformation in membranes without cholesterol. The chemical shifts of Gly-1, Ala-5, Ala-7, Gly-8 and Phe-9 are consistent with predominant β strand conformation in membranes that contained significant cholesterol. For spectra f, the downfield peak is assigned to Ala-7 ^{13}CO and the upfield peak is assigned to Gly-8 ^{13}CO. The third spectra in (b) and (c) were taken with samples contained ~0.8 μmol IFP and membranes composed of ~16 μmol POPC and ~4 μmol POPG with cooling gas temperature 0°C. There were very similar peak shifts in spectra taken for samples at different temperatures which indicates that cooling the sample does not change the peptide structure in membranes without cholesterol. The third and fourth spectra in (f) were obtained using a 4 mm diameter rotor and 12.0 kHz MAS frequency. Other spectra were obtained using a 4 mm diameter rotor and 8.0 kHz MAS frequency. Each spectrum was processed with 200 Hz Gaussian line broadening and was based on 200 – 10000 scans.

2. Ala-7 ^{13}CO–Gly-8 ^{13}CO distance measurements

For samples prepared with IFP-A7$_C$G8$_C$, the Ala-7 ^{13}CO–Gly-8 ^{13}CO dipolar coupling was probed with fpCTDQBU experiments. The goal was to provide additional evidence for the hypothesis that helical conformation was predominant in DTPC/DTPG membranes and that β strand conformation was predominant in DTPC/DTPG/CHOL membranes. For regular α helical structure, the Ala-7 ^{13}CO–Gly-8 ^{13}CO distance will be ~2.9 Å and will result in a ~300 Hz dipolar coupling while for regular β sheet structure, the distance will be ~3.7 Å with corresponding ~150 Hz dipolar coupling.[7, 39]

Figure 14a displays representative fpCTDQBU spectra of the pH 5.0 DTPC/DTPG sample and Figure 14b displays corresponding spectra of the DTPC/DTPG/CHOL sample. The labeled ^{13}COs contribute ~90% of the integrated signal intensity of the S_0 spectra. For each sample, characteristic residue-type chemical shift tables were used to assign the higher shift peak to the Ala-7 ^{13}CO and the lower shift peak to the Gly-8 ^{13}CO. In both samples, the S_1 intensity of each peak was lower than the corresponding S_0 intensity. This difference was expected because of the ^{13}CO–^{13}CO dipolar evolution during the S_1 acquisition and the refocusing of this evolution during the S_0 acquisition. Relative to the DTPC/DTPG/CHOL sample, there was a smaller S_1/S_0 intensity ratio in the DTPC/DTPG sample which is qualitatively consistent with a shorter ^{13}CO–^{13}CO distance in the DTPC/DTPG sample.

Figure 14c shows plots of the "$\Delta S/S_0$" = $(S_0 - S_1)/S_0$ intensity ratio vs dephasing time τ. Lines with error bars are $(\Delta S/S_0)^{cor}$ and were derived from

$(\Delta S/S_0)^{exp}$ with adjustment for the ~10% contribution from natural abundance ^{13}CO signals. The $(\Delta S/S_0)^{cor}/(\Delta S/S_0)^{exp}$ ratio had minor dependence on dephasing time with a typical range $0.9 < (\Delta S/S_0)^{cor}/(\Delta S/S_0)^{exp} < 1.2$. Relative to the DTPC/DTPG/CHOL sample, there was much faster buildup of $(\Delta S/S_0)$ for the DTPC/DTPG sample which qualitatively corresponds to a shorter ^{13}CO – ^{13}CO distance in the DTPC/DTPG sample. The diamonds show the best-fit $(\Delta S/S_0)^{sim}$ and corresponded to Ala-7 ^{13}CO–Gly-8 ^{13}CO distances (r_{CC}) of ~2.8 and ~3.5 Å in the DTPC/DTPG and DTPC/DTPG/CHOL samples, respectively, cf. Table 3. Those ^{13}CO–^{13}CO distances in Å are directly dependent on the backbone dihedral angle φ in degree of the more C-terminal labeled residue:

$$r_{CC}(\varphi) = \sqrt{10.6 - 3.2\cos\varphi} \qquad (3.1)$$

The above equation was derived based on standard bond lengths and bond angles in literature.[40] Therefore the distances can be used to determine angle φ which is correlated to the local secondary structure of a protein. The above calculated distances, 2.8 and 3.5 Å, correspond to Gly-8 backbone φ dihedral

Table 3. Ala-7 ^{13}CO – Gly-8 ^{13}CO dipolar couplings and distances and Ala-8 dihedral angle φ in membrane-associated IFP at pH 5.0

membrane composition	d (Hz) [a]	r (Å)	φ (degree)
DTPC/DTPG	336(15)	2.8(0.1)	-30(30)
DTPC/DTPG/CHOL	176(10)	3.5(0.1)	-121(17)

[a] Uncertainties are given in parentheses and were calculated from the values within the $\chi^2 = \chi_{min}^2 + 5$ region.

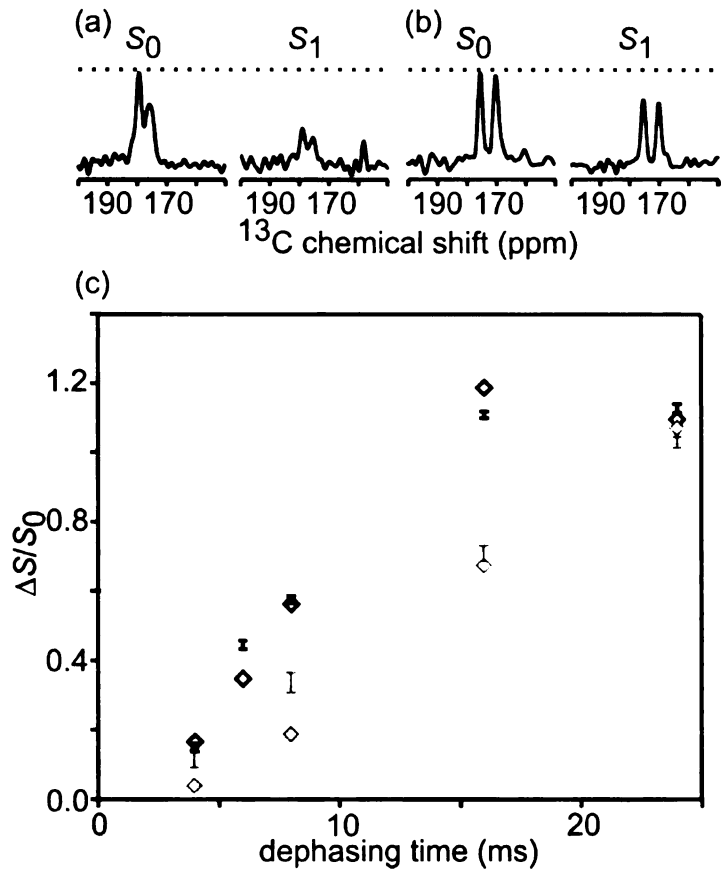

Figure 14. Ala-7 ^{13}CO – Gly-8 ^{13}CO distance measurements that probe the IFP conformational change associated with membrane cholesterol content. The fpCTDQBU spectra at 8 ms dephasing time are displayed for IFP2-A7$_C$G8$_C$ associated with (a) DTPC/DTPG (4:1) or (b) DTPC/DTPG/CHOL (8:2:5) membranes at pH 5.0. Panel (c) displays plots of fpCTDQBU $\Delta S/S_0$ vs dephasing time for the samples containing DTPC/DTPG (darker symbols) or DTPC/DTPG/CHOL (lighter symbols). Experimental data are represented as lines with error bars and best-fit simulated data are represented as diamonds. The displayed experimental data were based on integrations of the ^{13}CO regions of the S_0 and S_1 spectra and have been adjusted for the ~12% contribution of the natural abundance ^{13}CO signal. For the DTPC/DTPG sample, the best-fit Ala-7 ^{13}CO – Gly-8 ^{13}CO distance was 2.8 Å and was consistent with a backbone dihedral angle φ = -30° and helical conformation and for the DTPC/DTPG/CHOL sample, the best-fit distance of 3.5 Å was consistent with φ = -121° and with β sheet conformation. The DTPC/DTPG sample contained ~16 µmol DTPC and ~4 µmol DTPG and the DTPC/DTPG/CHOL sample contained ~16 µmol DTPC, ~4 µmol DTPG, and ~10 µmol cholesterol. Each sample also contained ~0.8 µmol IFP2-A7$_C$G8$_C$ and the sample cooling gas temperature was –50 °C. Each S_0 or S_1 spectrum was processed using 100 Hz Gaussian line broadening and was the sum of: (a) 9000 or (b) 10000 scans. The best-fit χ^2 were: DTPC/DTPG sample, 36; and DTPC/DTPG/CHOL sample, 32.

angles of –30° and –121°, which are consistent with α helical conformation near Ala-7 and Gly-8 in the DTPC/DTPG sample and β sheet conformation in the DTPC/DTPG/CHOL sample.

3. ^{13}CO–^{15}N REDOR Experiments

For IFP associated with DTPC/DTPG membranes, the peak ^{13}CO chemical shifts at selected residues between Leu-2 and Gly-20 were consistent with helical conformation at both pH 5.0 and pH 7.4, cf. Table 2. The pH 5.0 results are generally consistent with the liquid-state NMR structure of IFP in detergent micelles at pH 5.0 but the pH 7.4 results are in some disagreement with the detergent structure at pH 7.4. In particular, the structure in detergent shows predominant extended conformation for residues between Gly-13 and Gly-20 at pH 7.4. The extent of α helical conformation was therefore studied more quantitatively using REDOR measurements of $^{13}CO\cdots^{15}N$ distances in DTPC/DTPG samples containing IFP-$A5_CF9_N$, IFP-$F9_CG13_N$ or IFP-$G13_CM17_N$. For regular α helical structure, the labeled $^{13}CO\cdots^{15}N$ distance in these samples would be ~4.1 Å and would result in a ~45 Hz dipolar coupling while for regular β sheet structure, the distance would be ~11 Å with corresponding ~3 Hz dipolar coupling.

Figure 15 displays REDOR data and best-fit simulations for the three samples at both pHs and Table 4 provides the best-fit $^{13}CO\cdots^{15}N$ distances and dipolar couplings. One important conclusion is that for a given labeled IFP at each dephasing time, $(\Delta S/S_0)^{exp}$ (pH 5.0) ≈ $(\Delta S/S_0)^{exp}$ (pH 7.4). The best-fit

$^{13}CO\cdots^{15}N$ distances in the region covering Ala-5 to Met-17 were therefore approximately independent of pH and the conformation in this region is also likely independent of pH. For the IFP-$A5_CF9_N$ samples, the best-fit Ala-5 $^{13}CO\cdots$Phe-9 ^{15}N distance was 4.0 ± 0.1 Å at both pHs which was consistent with α helical conformation in this region and with the 3.9 – 4.2 Å range of distances of the detergent structures. For the IFP-$F9_CG13_N$ samples, the best-fit Phe-9 $^{13}CO\cdots$Gly-13 ^{15}N distance is 3.6 ± 0.1 Å at pH 5.0 and 3.7 ± 0.1 Å at pH 7.4. These distances are a little shorter than the expected distance in regular α helical conformation. In the detergent-associated IFP structures, this region forms a turn at both pHs with a 3.8 – 5.4 Å range of distances. For the IFP-$G13_CM17_N$ samples, the best-fit Gly-$^{13}CO\cdots$Met-17 ^{15}N distance is 4.5 ± 0.1 Å at pH 5.0 and

Table 4. $^{13}CO\cdots^{15}N$ dipolar couplings and distances in membrane-associated IFP with comparison to distances in detergent-associated IFP [a]

$^{13}CO\cdots^{15}N$ Residues	pH 5.0			pH 7.4		
	membrane		detergent	membrane		detergent
	d (Hz) [b]	r (Å)	r (Å) [c]	d (Hz) [b]	r (Å)	r (Å)
Ala-5···Phe-9	49(3)	4.0(0.1)	4.0 - 4.2	46(2)	4.0(0.1)	3.9 - 4.1
Phe-9···Gly-13	66(6)	3.6(0.1)	3.8 - 5.4	59(3)	3.7(0.1)	3.8 - 5.2
Gly-13···Met-17	35(2)	4.5(0.1)	4.4 - 5.7	31(3)	4.6(0.1)	9.0 - 10.2

[a] Membrane data were obtained with solid-state NMR REDOR experiments on samples containing IFP:DTPC/DTPG, IFP:total lipid ratio of ~0.04, and cooling gas temperature of –50 °C. Detergent data were obtained from the liquid-state NMR pdb structures, 1ibn (pH 5.0) and 1ibo (pH 7.4).[7]

[b] Uncertainties are given in parentheses and were calculated from the values within the $\chi^2 = \chi_{min}^2 + 5$ region.

[c] The displayed ranges are for twenty structures. For these twenty structures, $\langle d \rangle$ was calculated and $(1/\langle d \rangle)^{1/3}$ was calculated for comparison to the membrane derived *r*. For the Phe-9···Gly-13 data, $(1/\langle d \rangle)^{1/3}$ was 4.3 and 4.4 Å at pH 5.0 and 7.4, respectively, and for the Gly-13···Met-17 data, $(1/\langle d \rangle)^{1/3}$ was 5.2 and 9.3 Å at pH 5.0 and 7.4, respectively.

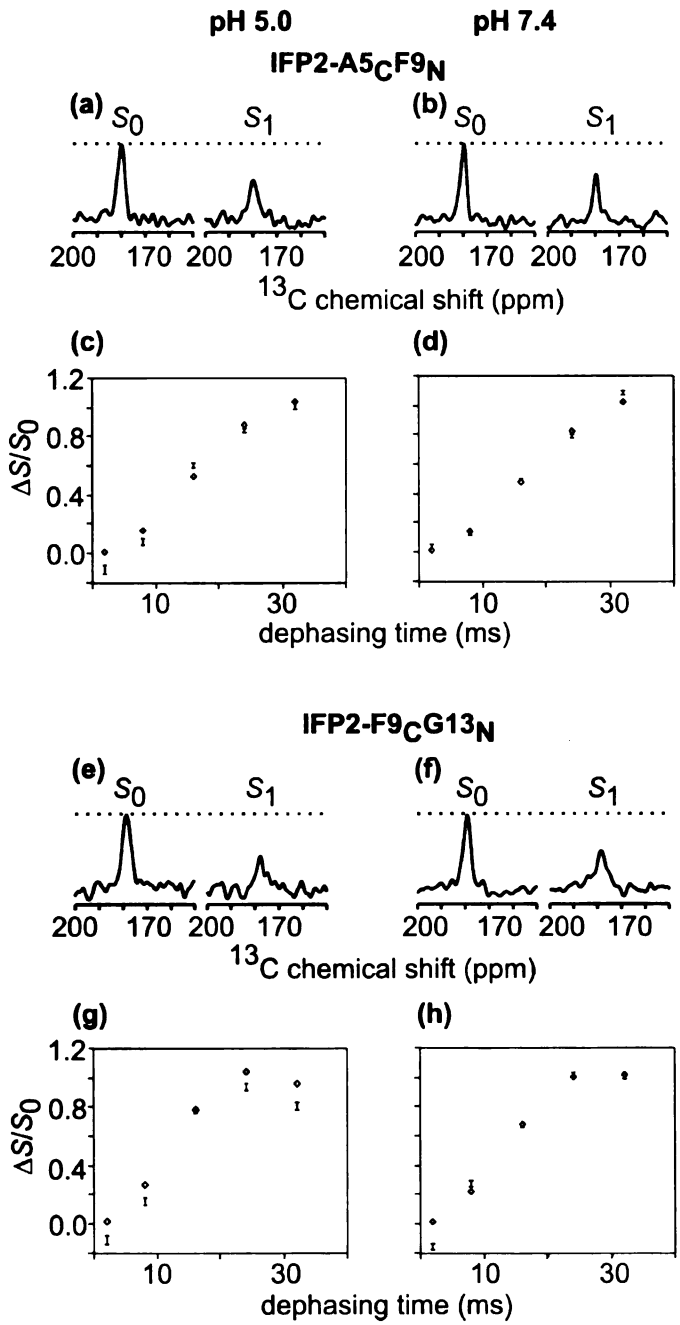

Figure 15. $^{13}CO\cdots^{15}N$ REDOR measurements.

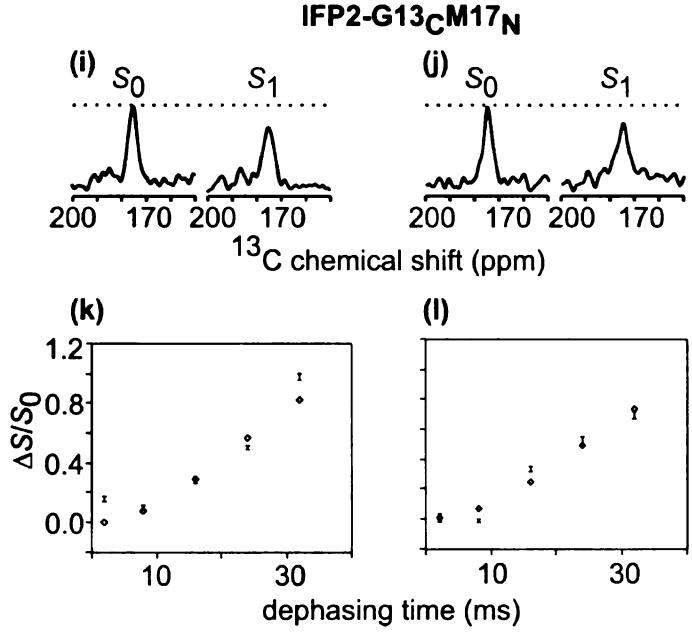

Figure 15. $^{13}CO\cdots^{15}N$ REDOR measurements that probe the pH dependence of helicity of IFP associated with DTPC/DTPG. Data are presented for (a-d) IFP-$A5_CF9_N$, (e-h) IFP-$F9_CG13_N$, and (i-l) IFP-$G13_CM17_N$ and at (a, c, e, g, i, k) pH 5.0 or (b, d, f, h, j, l) pH 7.4. The S_0 and S_1 spectra at 16 ms dephasing time are displayed for (a, b) IFP-$A5_CF9_N$, (e, f) IFP-$F9_CG13_N$, and (i, j) IFP-$G13_CM17_N$, and the corresponding plots of ($\Delta S/S_0$) vs dephasing time are displayed below each set of spectra with the pH 5.0 plot on the left and the pH 7.4 plot on the right. For each sample, the peak ^{13}CO shift was independent of dephasing time. In each plot, experimental data are represented as lines with error bars and the best-fit simulated data are represented as diamonds. The displayed experimental data were based on integrations of the ^{13}CO regions of the S_0 and S_1 spectra and have been adjusted for the ~22% contribution of the natural abundance ^{13}CO signal. Each sample contained ~16 µmol DTPC, ~4 µmol DTPG and ~0.8 µmol IFP and the sample cooling gas temperature was –50 °C. Each S_0 or S_1 spectrum was processed using 200 Hz Gaussian line broadening and was the sum of: (a, b, i, j) ~8000; (e) ~10000; or (f) 16080 scans. The best-fit χ^2 were: (c) 15; (d) 8; (g) 24; (h) 20; (k) 42; and (l) 21.

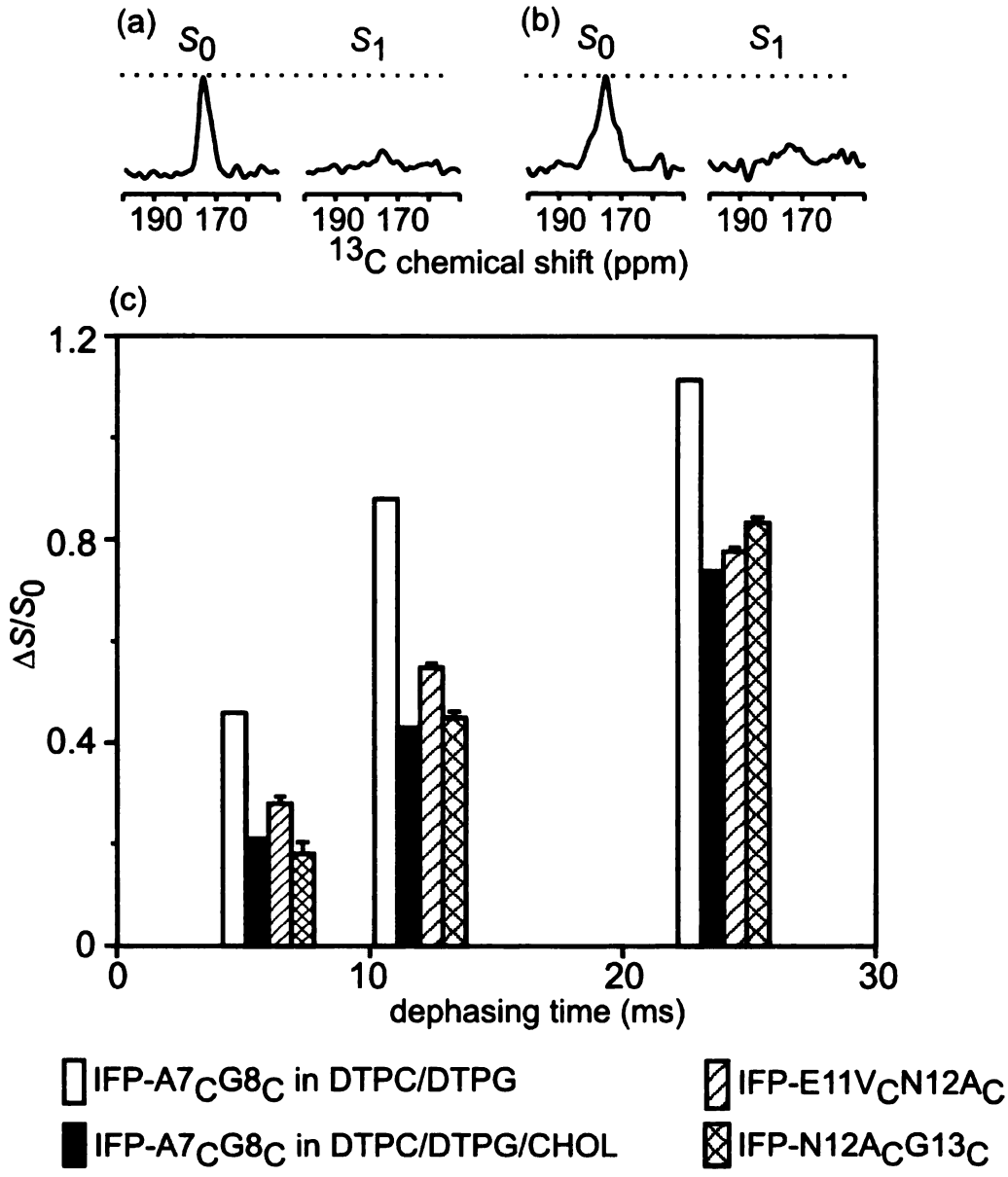

Figure 16. ^{13}CO–^{13}CO distance measurements that probe the conformation of residues 11 through 13 of IFP-E11VN12A and IFP-N12A. The spectra at 24 ms dephasing time are displayed for membrane-associated (a) IFP- E11VN12A and (b) IFP-N12A at pH 5.0. Panel (c) displays the magnitude of dephasing ($\Delta S/S_0$) over dephaisng time, 6, 12 and 24 ms are displayed for IFP-E11V$_C$N12A$_C$, IFP-N12A$_C$G13$_C$ and IFP-A7$_C$G8$_C$ associated with DTPC/DTPG (4:1) membrane or IFP-A7$_C$G8$_C$ associated with and DTPC/DTPG/CHOL (8:2:5) membrane at pH 5.0. The displayed experimental data were based on integrations of the ^{13}CO regions of the S_0 and S_1 spectra. The measured values from IFP-A7$_C$G8$_C$ samples in membranes with or without cholesterol represent data for β strand or α helix structure, respectively. The data from IFP mutants are more consistent with data from DTPC/DTPG/CHOL-associated IFP-A7$_C$G8$_C$ and therefore more consistent β strand structure.

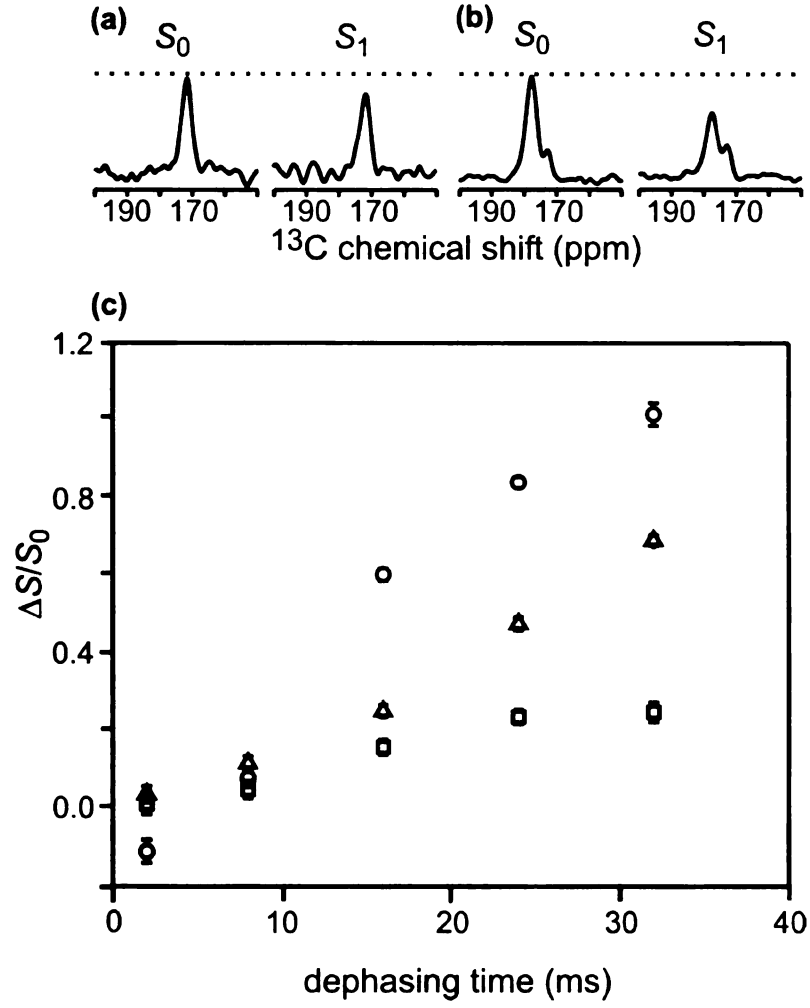

Figure 17. Ala-5 ^{13}CO ··· Phe-9 ^{15}N distance measurements that probe the helicity of IFP mutants associated with DTPC/DTPG at pH 5.0. The S_0 and S_1 spectra at 16 ms dephasing time are displayed for (a) IFP-E11VN12A and (b) IFP-N12A. The peak chemical shifts of IFP-E11VN12A and IFP-N12A correspond to β strand and α helix conformation, respectively. For the IFP-N12A sample, there is also one peak that corresponds to β strand conformation. Panel (c) displays plots of REDOR $\Delta S/S_0$ vs dephasing time for the samples containing IFP-E11VN12A (square), IFP-N12A (triangle) or wild-type IFP (circle). Each of the peptides was ^{13}CO labeled at Ala-5 and ^{15}N labeled at Phe-9. The displayed experimental data were based on integrations of the whole ^{13}CO regions of the S_0 and S_1 spectra and are represented with error bars. The typical uncertainty is ±0.02. Each sample contained ~0.8 μmol peptide, ~16 μmol DTPC and ~4 μmol DTPG and the sample cooling gas temperature was –50 °C. Each S_0 or S_1 spectrum was processed using 200 Hz Gaussian line broadening and was the sum of ~8000 scans.

4.6 ± 0.1 Å at pH 7.4 which are longer than the expected distance in regular α helical conformation. In the detergent-associated IFP structures at pH 5.0, this region forms a 3_{10} helix with a 4.4 – 5.7 Å range of distances. The REDOR distance is generally consistent with this range. However, the detergent-associated IFP structures at pH 7.4 show extended conformation in this region and the REDOR distance is inconsistent with the detergent structure 9.0 – 10.2 Å range of distances. This result is of some significance because the pH-dependent difference in structure in this region in detergent samples is a critical part of the structure-function model for pH dependence of IFP-induced fusion.

4. IFP mutants

An attempt was made to determine the conformation of residues Glu-11 through Gly-13 using backbone ^{13}CO–^{13}CO distance measurements of adjacently labeled residues. As described in part 2, the distance is useful in determining the dihedral angle φ which has different characteristic values for α helix and β strand conformations. In the IFP/detergent model determined by solution NMR, the Glu-11, Asn-12 residues have dihedral angles φ that reflects β strand conformation at both pHs. The IFP forms a turn structure at residues Glu-11 to Asn-12. The distances between Glu-11 and Asn-12 COs are ~3.6 Å at pH 5.0 and ~3.7 Å at pH 7.4 and the distances between Asn-12 and Gly-13 COs are ~3.7 Å at pH 5.0 and ~3.4 Å at pH 7.4.[41, 42] Both the dihedral angle φ and the distance data suggest that the conformation of residues Glu-11 and Asn-12 has the characteristic of an extended structure. But some other previous data have

shown that IFP adopts a continuous helix and these residues are helical.[4] In a helical structure, the distances between Glu-11 and Asn-12 COs and between Asn-12 and Gly-13 COs will be ~2.8 Å. Therefore the distance measurements between the above listed residues are useful in distinguishing the two different structural models and provide valuable insight in correlating the IFP structure and its function. Our first approach is to use two mutants of IFP, IFP-E11VN12A and IFP-N12A to detect the internulcear distances. The reason to choose these mutants instead of wild-type IFP is that the selectively labeled Glu or Asn were not commercially available at the time when those experiments were conducted. In addition, the mutations of Glu-11 to valine and of Asn-12 to alanine do not deteriorate the fusion activity of IFP.[14, 15]

The fpCTDQBU experiments were carried out on samples containing IFP-E11V_CN12A_C or IFP-N12A_CG13$_C$ at pH 5.0 using various dephasing times (τ). The obtained $(\Delta S/S_0)^{exp}$ values at different τ were compared to the corresponding $(\Delta S/S_0)^{exp}$ of IFP-A7$_C$G8$_C$ samples. The data from IFP-A7$_C$G8$_C$ samples in membranes that lacked or contained cholesterol served as standards for α helical or β strand structures, respectively. Figure 16 displays representative results of the IFP-E11V_CN12A_C or IFP-N12A_CG13$_C$ samples compared to IFP-A7$_C$G8$_C$ samples. The spectra of IFP-E11V_CN12A_C and IFP-N12A_CG13$_C$ are shown in Figures 16a and 16b. The peak shifts in the S_0 spectra are 174.5 and 175.0 ppm for IFP-E11V_CN12A_C and IFP-N12A_CG13$_C$ samples respectively and the linewidth of each spectrum is ~5 ppm. The peaks for the two labeled COs in each sample are not well resolved. For the Val and Ala residues, the database

distribution of the ^{13}CO shifts are 177.65 ± 1.38 and 179.40 ± 1.32 for those residues in the helical conformation and the corresponding distribution in β strand conformation are 174.8 ± 1.39 and 176.09 ± 1.51 ppm. The peak shifts of the two samples are more consistent with β strand conformations for the labeled regions of the mutants.

The magnitude of dephasing by ^{13}CO–^{13}CO dipolar coupling, $(\Delta S/S_0)^{exp}$, over different dephasing time for the two mutant samples is displayed in Figure 16c and compared to the corresponding dephasing in IFP-$A7_CG8_C$ samples. Relative to the data from IFP-$A7_CG8_C$ in non-cholesterol containing samples, the $(\Delta S/S_0)^{exp}$ values of both mutant samples are more comparable to the ones from IFP-$A7_CG8_C$ in cholesterol containing samples and consistent with β strand structure. These results further suggest that both IFP mutants have extended structure at the labeled region. The extended conformation is consistent with the wild-type IFP structure in the middle region determined by solution NMR. However the overall structures of the IFP mutants were unknown. The extended structure of the middle region of IFP mutants may suggest the existence of a turn similar to the one in the solution NMR structure of the wild-type IFP or be due to the overall β strand conformation of the mutants. Therefore it is important to know that whether the mutations cause an overall structural change of IFP. The next set of experiments was designed to determine the conformations of the N-termini of the IFP mutants and can provide information on the effect of mutations on the overall structure of IFP.

As described in parts 1 and 3, REDOR experiments provide chemical shift information and ^{13}CO–^{15}N distances, both of which are useful in determining the peptide secondary structure, especially helical forms. Both mutants were ^{13}CO labeled at Ala-5 and ^{15}N labeled at Phe-9 and were examined with ^{13}CO–^{15}N REDOR. Figure 17a and 17b show the example spectra of IFP-E11VN12A and IFP-N12A samples, respectively. For the IFP-E11VN12A sample, the chemical shift of Ala-5 ^{13}CO is 171.6 ppm which is more consistent with the shift representing the β strand structure and the $(\Delta S/S_0)^{exp}$ is ~18 % at τ = 24 ms which is smaller than the corresponding value of a typical helix (~60 %), e.g., the wild-type IFP with the same labels, IFP-$A5_CF9_N$. For the IFP-N12A sample, there are two peaks with one centered at 177.8 ppm and $(\Delta S/S_0)^{exp}$ ~ 60 % and the other one centered at 172.5 ppm and $(\Delta S/S_0)^{exp}$ ~ 30 %, corresponding to helical and more extended structures respectively. Figure 17c compares the dephasing of those two mutants to that of the wild-type IFP which serves as a model for the standard helical conformation. The dephasing from the IFP mutants is significantly smaller than the dephasing from the wild-type IFP. Therefore, the secondary structures of IFP mutants are strongly affected by the mutations and not comparable to the structure of the membrane-associated wild-type IFP. The observed extended conformation of the middle region of IFP mutants, at residue 11 and 12, is probably due to the mutations and can not be correlated to the conformation of the middle region of the wild-type IFP.

5. PDSD Experiments

Since the IFP mutants failed to conserve the N-terminal helical structure that is characteristic of the wild-type IFP, wild-type IFP was studied with uniform ^{13}C and ^{15}N labels at Glu-11 and Asn-12. For samples containing IFP-I10E11$_U$ or IFP-N12G13$_U$, 2D ^{13}C–^{13}C correlation spectra were acquired and analyzed to obtain the backbone ^{13}CO, $^{13}C\alpha$, $^{13}C\beta$, $^{13}C\gamma$, and $^{13}C\delta$ chemical shifts of the labeled residues. The obtained chemical shifts of ^{13}CO, $^{13}C\alpha$ and $^{13}C\beta$ were compared to the characteristic shift values that correspond to the different secondary structures of an individual residue in the Ref-DB[17] and TALOS databases[34]. Both databases are based on the observation that chemical shifts are highly correlated with the local protein secondary structure. By comparing to the chemical shift values of a specific type of amino acid in Ref-DB, qualitative knowledge about the protein local secondary structure can be obtained. The current Ref-DB has 1591 protein chemical shift files. More quantitative predictions can be made by the TALOS approach which uses chemical shift and sequence information to predict the protein backbone dihedral angles φ and ψ. In practice, TALOS uses chemical shift data for three consecutive residues to make predictions for the central residue in the triplet. It searches its database for the 10 best matches for a given triplet in the target protein and when the 10 matches indicate consistent values for φ and ψ of the Ramachandran map TALOS uses their averages and standard deviations as predictions. The TALOS database contains 186 proteins and provides more than 24,000 residue triplets. The predicted dihedral angles were then used to build a model of the protein secondary structure.

The 2D ^{13}C–^{13}C correlation spectra were generated with a PDSD pulse sequence using a 10 ms spin diffusion period during which only intra-residue cross peaks were observed.[43] The inter-residue cross peaks are not observed in these short mixing time spectra. Because only two residues were labeled for each sample, the unambiguous assignments can be easily made using characteristic connecting patterns for each individual residue.

Table 5. Measured ^{13}C chemical shifts for IFP-I10E11$_U$ and IFP-N12G13$_U$ samples compared to the corresponding chemical shifts from the Ref-DB database[17]

		Measured chemical shifts (ppm)[a]				
		CO	Cα	Cβ	Cγ	Cδ
Ile-10[b]		178.0	65.1	38.2	30.0, 17.9[c]	15.2
Glu-11[d]	A	178.7	58.8	28.9	37.2	181.9
	B	174.5	54.0	32.0	37.9	
Asn-12[b]		175.5	51.4	39.8	175.0	
Gly-13[b]		174.5	45.8			
		Chemical shifts from the Ref-DB database (ppm)[e]				
Ile	α helix	177.72(1.29)	64.57(1.74)	37.60(1.15)		
	β strand	174.86(1.39)	60.05(1.57)	39.86(1.98)		
Glu	α helix	178.61(1.21)	59.11(1.16)	29.37(0.99)		
	β strand	175.35(1.40)	55.52(1.67)	32.01(1.98)		
Asn	α helix	176.91(1.55)	55.45(1.42)	38.61(1.31)		
	β strand	174.64(1.65)	52.74(1.47)	40.12(2.07)		
Gly	α helix	175.51(1.23)	46.91(1.10)			
	β strand	172.55(1.58)	45.22(1.17)			

[a] Typical uncertainties are ±0.2 ppm.
[b] For Ile-10, Asn-12 and Gly-13, the chemical shifts are the same for pH 5.0 and pH 7.4 samples.
[c] γ-CH_2 and γ-CH_3 respectively.
[d] Two sets of crosspeaks are present for samples at pH 5.0 and only shift set A is observed for samples at pH 7.4.
[e] Standard deviations of distribution are in parentheses.

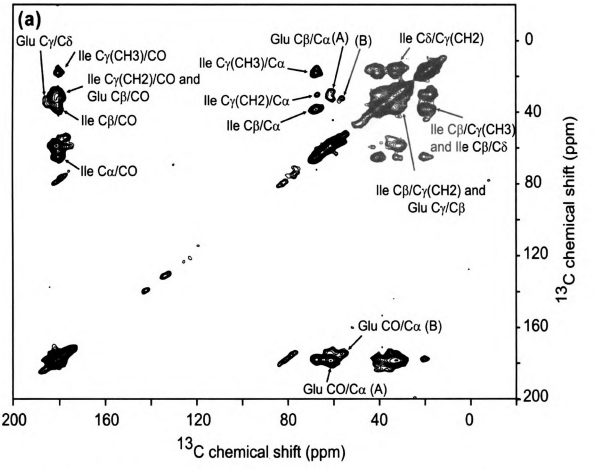

Figure 18. 2D ^{13}C-^{13}C PDSD spectra of membrane-associated IFP-I10E11$_U$

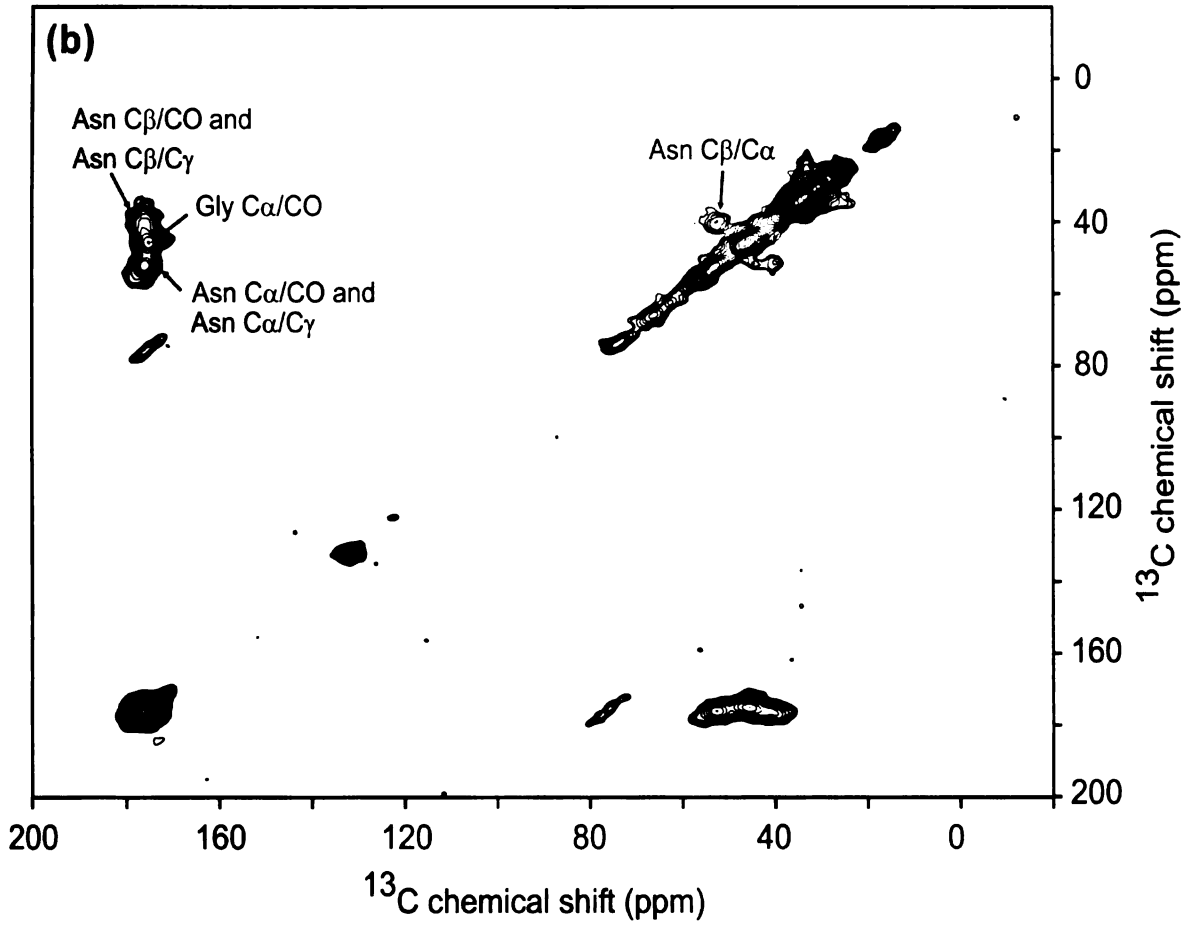

Figure 18. 2D ^{13}C-^{13}C PDSD spectra of membrane-associated (a) IFP-I10E11$_U$ and (b) IFP-N12F13$_U$ at pH 5.0. Each sample contained 16 µmol DTPC, 0.4 µmol DTPG and ~0.8 IFP. The data were collected with 10 ms exchange time and total signal averaging time of ~1.5 days. The MAS frequency was 10 KHz and the temperature of the sample cooling gas was -50 °C. Spectra were processed with 200 Hz Gaussian line broadening in both dimensions. Peak assignments are shown using the convention of assignment in f_1 (vertical axis)/f_2 (horizontal axis).

The spectra of membrane-associated IFP-I10E11$_U$ and IFP-N12G13$_U$ at fusogenic pH are displayed in Figure 18a and 18b, respectively and the ^{13}C shifts are listed in table 5 and are compared to the characteristic chemical shifts of corresponding residues in α helical or β strand conformations. The comparison showed that the labeled region had two conformations rather than a single structure. The shifts of Ile-10 and Gly-13 ^{13}CO are more consistent with local helical structures, while Asn-12 has shifts that have better agreement with a β-strand structure. Two distinct sets of crosspeaks were identified for Glu-11, one of which (A) has shifts that agree with helical conformation while the other shifts set (B) is closer to those expected in β-strand conformation. The ratio of intensities of the two peak sets A:B is ~3:1. The 2D ^{13}C–^{13}C correlation spectrum was previously obtained for membrane-associated IFP at pH 5.0 that was uniformly ^{13}C labeled at the first ten N-terminal residues[43] and the ^{13}C chemical shifts are listed in table 6. The ^{13}C chemical shifts of Ile-10 from table 5 and table 6 were compared and the variations between the two measurements were ≤0.5 ppm.

Table 6. ^{13}C
N-terminal r

Ala		
	(1)	
	(2)	
Gly	(3)	
	(4)	
Ile		
Leu-2		
Phe		

[a] Assignm
were not a
[b] The Phe
were from

T
were ev
were ge
using th
previou
made b
crosspe
and Gl
shifts c
residue
were r
uniform
meas
^{13}CO

Table 6. ^{13}C chemical shifts in ppm for the membrane-associated IFP at pH 5.0 with the first 10 N-terminal residues uniformly labeled[43] [a]

		CO	Cα	Cβ	Cγ	Cδ	C2-C6
Ala		179.4	55.5	18.6			
Gly	(1)	175.9	47.4				
	(2)	170.6	43.6				
	(3)	170.0	46.4				
	(4)	176.1	41.0				
Ile		177.8	65.6	38.1	29.6, 18.0	14.7	
Leu-2		177.5	58.7	42.4	26.7	15.6	
Phe		178.0, 178.6 [b]	60.5	39.7			131.8

[a] Assignments could only be done based on amino acid type. Peaks for each specific residue were not assigned.
[b] The Phe ^{13}CO chemical shifts, which were not available in the previous 2D measurements[43], were from table 2. The two shifts were for Phe-3 and Phe-9 respectively.

The previous shifts [43] (cf. table 6) and the shifts derived from Figure 18 were evaluated using TALOS[34] and the dihedral angles of Leu-2 through Gly-13 were generated and listed in table 7. All the dihedral angles were generated using the measured CO, Cα and Cβ chemical shifts. The assignments of the previously obtained chemical shifts for residues Gly-1 through Phe-9 were only made based on amino acid type. For glycines in the sample, four sets of crosspeaks were observed (cf. table 6). The choices of chemical shifts for Gly-1 and Gly-8 out of these four sets were based on the measured carbonyl chemical shifts of Gly-1 (Table 2). Both shift sets (2) and (3) were used for Gly-1. For residue Gly-4 and Gly-8, only the shift set (1) was tested because those shifts were more consistent with database shifts for helix, which agreed better with the uniform helical conformation for the N-terminal region. This is evidenced by the measured chemical shifts of other residues in the region and the measured Ala-5 ^{13}CO ··· Phe-9 ^{15}N distance which was consistent with α helical structure. The

different values input in the TALOS program had minor effect on the predicted dihedral angles (Predicted values from one set were within the range of error of the values from the other set.). The chemical shifts of Ala and Phe in table 6 were used for both Ala-5 and Ala-7 and for both Phe-3 and Phe-9, respectively. The chemical shifts of Ile in table 6 were used for Ile-6. For residues Ile-10 through Gly-13, the measured chemical shifts in table 5 were used.

The listed values of φ and ψ angles in table 7 are the averages with standard deviations of the 10 best database matches predicted by the TALOS program. For residues except Leu-2, Glu-11, Asn-12 and Gly-13, all the 10 best matches have dihedral angles that fall into a small defined region of the Ramachandran map which has consistent secondary structures (cf. table 7). Residues Leu-2 through Phe-9 have dihedral angles independent of Glu-11 chemical shifts. Residues Ile-10, Glu-11 and Asn-12 have different φ and ψ angles corresponding to the A and B Glu-11 chemical shift sets.

The dihedral angles from IFP structures determined by solution NMR are also listed in table 7. The values for IFP structures at pH 5.0 and pH 7.4 are all included. These φ and ψ angles are based on the average values with standard deviations obtained from 20 IFP structures which are lowest in energy. The dihedral angles of residues Leu-2 through Ile-10 for both membrane-associated and detergent-associated IFPs at both pHs are generally consistent with each other and consistent with a helix structure. Dihedral angles of Gly-13 in membrane-associated IFP are within the error range of dihedral angles of detergent-associated IFP, whose values are not typical for a residue with α

helical conformation (e.g. Gly-4). Gly-13 was determined to be the start of the IFP C-terminal helix in membranes at both pHs and in micelles at pH 5.0. The determined dihedral angles are therefore reasonable considering the flexibility of Gly-13 as the start of a helix. For residues Glu-11 and Asn-12, distinct dihedral angles were obtained corresponding to different shift sets of Glu-11. The dihedral angles corresponding to Glu-11 shift set A in the membrane samples are consistent with the values obtained from IFP in micelles at pH 5.0 by solution NMR. The dihedral angles φ of Glu-11 and Asn-12 in membrane bilayer samples corresponding to Glu-11 shift set B have agreement with the φ angles obtained for detergent-associated IFP sample at pH 5.0, but the dihedral angles ψ are very different between samples containing membrane and detergent. The shifts set A generated $\varphi = -69^{\circ}$ and $\psi = -27^{\circ}$ for Glu-11 which agreed with α helical conformation and $\varphi = -96^{\circ}$ and $\psi = 8^{\circ}$ for Asn-12 which did not agree with helical or β-strand conformation very well. The shifts set B generated $\varphi = \sim -120^{\circ}$ and $\psi = \sim 150^{\circ}$ for both residues, consistent with a β-strand conformation. These two sets of dihedral angles were both used to build IFP structures by the MOLMOL program. In the structures, only the average values of φ and ψ angles from table 7 were used. For residue Gly-1 and residues Trp-14 through Gly-20, dihedral angles from detergent-associated IFP at pH 5.0 were used because these angles are not available from the membrane-associated IFP. For the IFP C-terminal region, the solid-state NMR measurements of Gly-13 and Gly-16 chemical shifts and of Gly-13 $^{13}CO \cdots$ Met-17 ^{15}N distance (described in the chemical shift and the REDOR experiment parts of this chapter) showed that this

region has a helical structure similar to the detergent-associated IFP structure at pH 5.0 determined by solution NMR. At pH 7.4, this region of detergent-associated IFP has extended conformation. The two different sets of dihedral angles resulted in two different structures (cf. Figure 19). In both structures, the membrane-associated IFP adopted a helix-turn-helix conformation. The N-terminal helix ends at Glu-11 or Ile-10 in the structures corresponding to shifts A and B, respectively. In structure A, all the hydrophobic residues at the N-terminal helix are at the bottom face of the structure; in some contrast, all the hydrophobic residues of structure B face to the top side of the structure. Compared with the middle kink of detergent-associated IFP determined by solution NMR,[7] the break in helicity of membrane-associated IFP is more complicated due to the fact that Glu-11 and Asn-12 have two conformations. The conformation corresponding to shift set B is only present for samples at lower pH and absent for samples at poorly fusogenic pH 7.4, as shown in Figure 20. The population of B conformation is ~25% and ~20% for samples at pH 5.0 and pH 4.0, respectively; For the IFP sample at pH 7.4, the population of B conformation is less than 10% because the peak corresponding to the B conformation is not observed in the spectrum and the signal-to-noise of the spectrum is ~10.

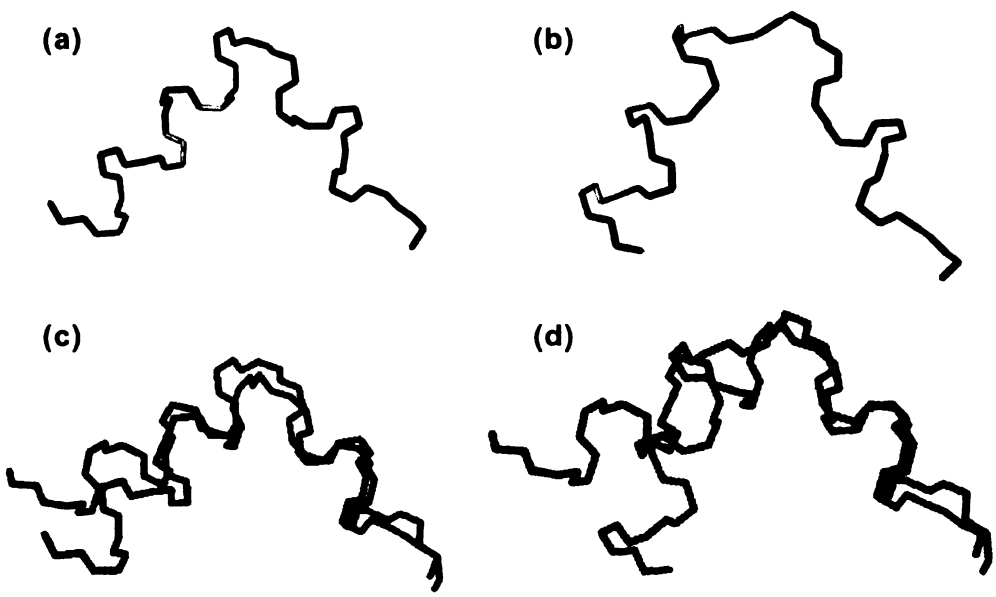

Figure 19. IFP backbone structure based on (a) Glu-11 shift set A or (b) Glu-11 shift set B. All the hydrophobic residues (Leu-2, Phe-3, Ile-6, Phe-9 and Ile-10) at N-terminal helix are shown in gold in (a-b). Residue Glu-11 is in green and residue Asn-12 is in red. The N-terminal helix is from residues 2-11 in (a) or 2-10 in (b). The C-terminal conformation was based on the detergent-associated IFP structure at pH 5.0. In (c) and (d), structure A (red) and B (green) are respectively overlaid on top of the solution NMR structure (blue) which is lowest in energy at pH 5.0.

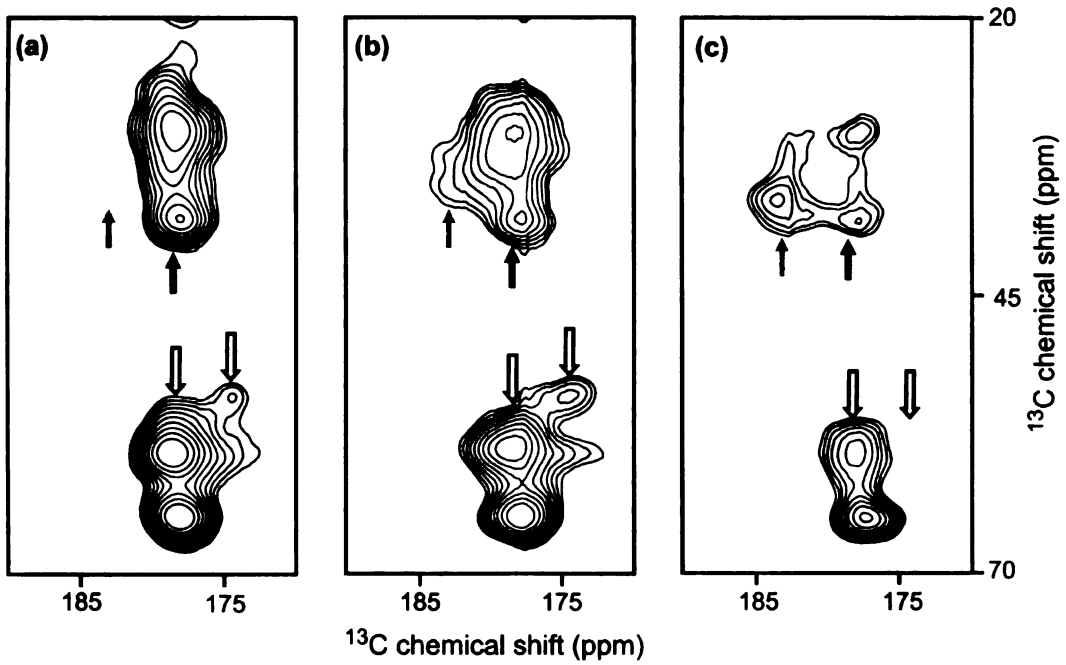

Figure 20. 2D ^{13}C–^{13}C PDSD spectra of membrane-associated IFP-UI10E11$_U$ at (a) pH 4.0; (b) pH 5.0; and (c) pH 7.4. The acquisition and processing parameters are the same as the spectra in Figure 18. Grey arrows point to the crosspeaks of Glu Cγ/Cδ(COO^-) (f_1/f_2). This crosspeak is absent in spectrum (a). Black arrows point to the crosspeaks of Glu Cγ/Cδ(COOH) (f_1/f_2) which are overlapped with other CO peaks. Hollow arrows point to crosspeaks of Glu Cα/CO (f_1/f_2) A (left) and B (right). The crosspeak B is absent in spectrum (c).

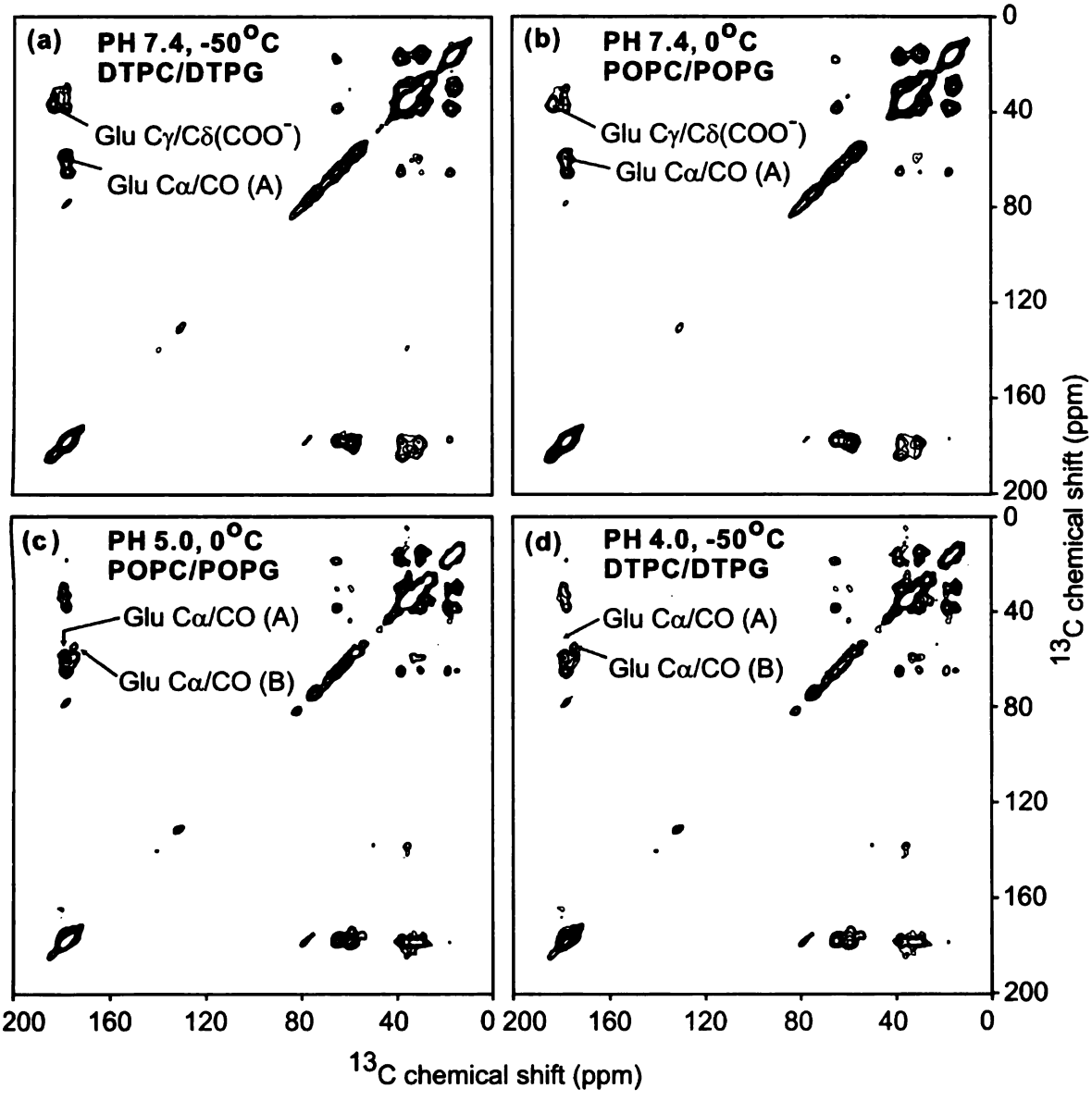

Figure 21. PDSD spectra for membrane-associated IFP-I10E11$_U$ at (a, b) pH 7.4; (c) pH 5.0 and (d) pH 4.0.

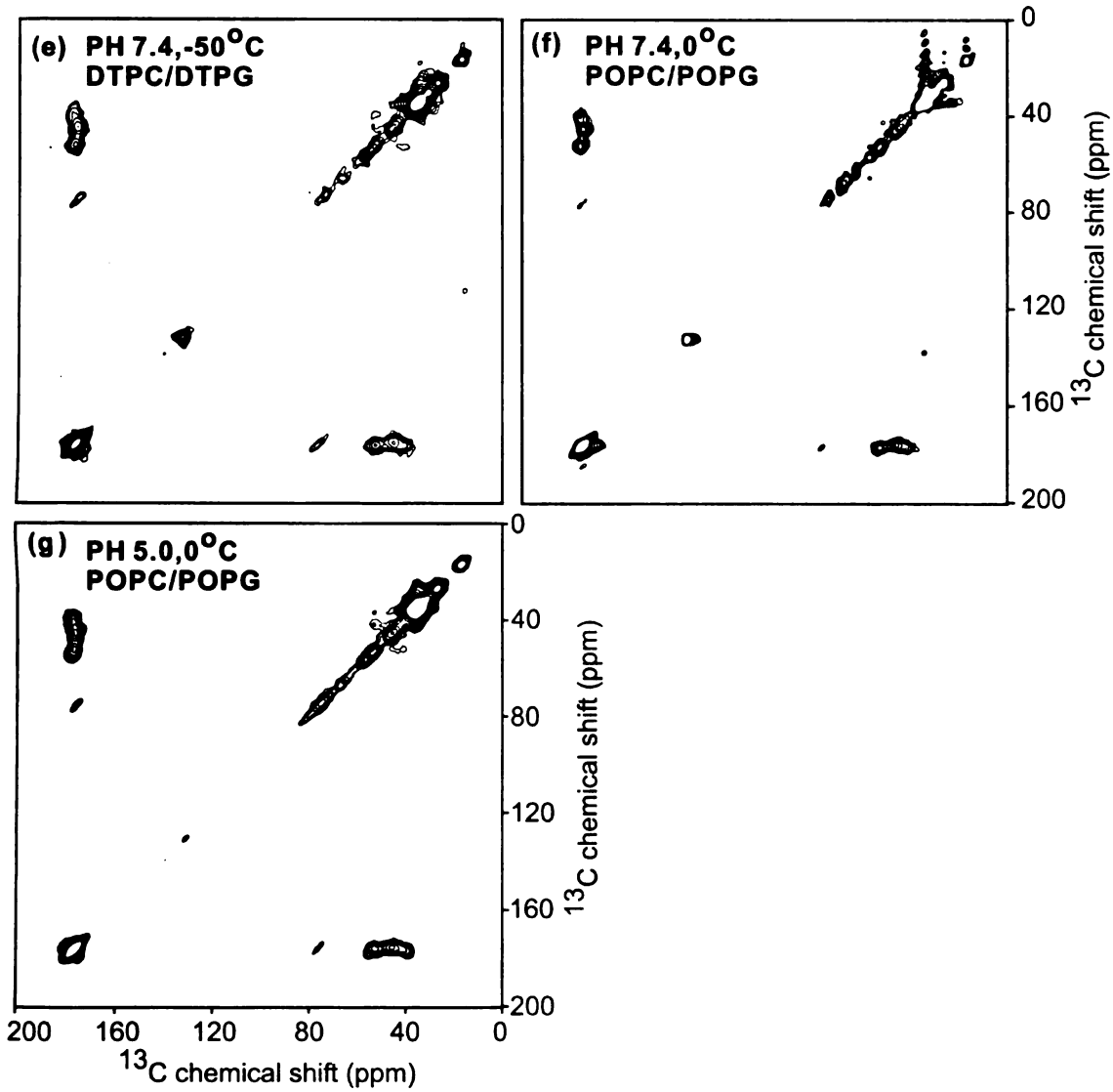

Figure 21. PDSD spectra for membrane-associated IFP-I10E11$_U$ at (a, b) pH 7.4; (c) pH 5.0 and (d) pH 4.0 and for membrane-associated IFP-N12G13$_U$ at (e, f) pH 7.4 and (g) pH 5.0. The membrane composition was (a, d, e) DTPC/DTPG (4:1) and (b, c, f, g) POPC/POPG (4:1). The samples were cooled with nitrogen gas at (a, d, e) –50 °C and (b, c, f, g) 0 °C. The spectra have no temperature dependence from – 50 °C to 0 °C. The spectra were processed with 200 Hz Gaussian line broadening. The total number of scans was (a-c, e-g) ~100000, and (d) ~200000. Some of the peak assignments were shown using the convention of assignment in f_1 (vertical axis)/f_2 (horizontal axis).

Table 7. φ and ψ angles in degrees of residue Gly-1 to Gly-20 from membrane-associated IFP at pH 5.0 and detergent-associated IFP [7]. Standard deviations are in the parentheses.

	Membrane-associated IFP				Detergent-associated IFP			
	φ		ψ		pH 5.0 [41]		pH 7.4 [42]	
					φ	ψ	φ	ψ
Gly-1	N/A [a]		N/A		N/A	-160 (1)	N/A	154 (4)
Leu-2	-59 (2) [b]		-33 (8) [b]		-47 (1)	-44 (1)	-56 (1)	-49 (1)
Phe-3	-63 (8)		-38 (12)		-52 (2)	-35 (1)	-64 (0.1)	-46 (1)
Gly-4	-64 (7)		-42 (7)		-67 (1)	-35 (3)	-53 (1)	-51 (1)
Ala-5	-66 (3)		-37 (7)		-72 (2)	-36 (3)	-62 (1)	-40 (1)
Ile-6	-68 (5)		-45 (5)		-58 (1)	-41 (1)	-64 (0.1)	-63 (1)
Ala-7	-62 (6)		-40 (8)		-66 (1)	-35 (5)	-57 (2)	-31 (3)
Gly-8	-62 (8)		-39(6)		-54 (5)	-52 (6)	-63 (3)	-53 (2)
Phe-9	-67 (5)		-37 (8)		-61 (5)	-44 (4)	-53 (3)	-30 (3)
	Shift set A		Shift set B					
	φ	ψ	φ	ψ				
Ile-10	-63 (5)	-42 (7)	-70 (11)	-34 (13)	-49 (3)	-32 (10)	-66 (4)	-14 (4)
Glu-11	-69 (11) [c]	-27 (13) [c]	-126 (29)	156 (13)	-98 (13)	-2.5 (4)	-121 (7)	5 (4)
Asn-12	-96 (13)	8 (12)	-113 (18) [b]	125 (27) [b]	-137 (24)	34 (39)	-146 (6)	52 (63)
Gly-13	87 (11) [d]	10 (9) [d]	87 (9) [d]	10 (11) [d]	130 (53)	5 (15)	119 (73)	7 (6)
Trp-14					-40 (3)	-42 (4)	-48 (9)	-123 (83)
Glu-15					-53 (4)	-33 (4)	-103 (52)	12 (80)
Gly-16					-70 (6)	-18 (9)	-121 (76)	-19 (23)
Met-17	N/A		N/A		-98 (11)	-11 (4)	-113 (22)	-2 (10)
Ile-18					-71 (6)	-46 (9)	-88 (18)	-1 (46)
Asp-19					-42 (46)	151 (77)	-85 (56)	110 (66)
Gly-20					78 (67)	N/A	-116 (83)	N/A

[a] N/A ≡ not available.
[b, c, d] Number of matches within error ranges is: [b] 9; [c] 8; [d] 7 out of 10.

Figure 21 shows the effect of pH and temperature on the PDSD spectra. The spectra 21 c and g were taken for samples made with POPC/POPG lipids with sample cooling gas at 0 °C and are comparable to the spectra taken for samples containing DTPC/DTPG lipids with sample cooling gas at -50 °C (cf. Figure 18). The membrane prepared from POPC/POPG is in the liquid crystalline phase at 0 °C and the membrane prepared from DTPC/DTPG is in the gel phase at -50 °C. The similar appearance of the spectra taken at different temperatures indicated the local conformation of IFP is not affected when the membrane bilayer undergoes a phase transition. Most of the other spectra were taken at -50 °C to enhance sensitivity.

Compared to the spectra taken for samples at pH 5.0 (cf. Figure 18 and Figure 21 c, g), the spectra for samples at pH 7.4 are very similar (cf. Figure 21 a, b, e, f), except for the lack of shift set B discussed in the previous paragraph (cf. table 5). This similarity suggested that there is no drastic conformational change for IFP samples at fusogenic pH and neutral pH. For samples at pH 7.4, IFP also has the helix-turn-helix secondary structure.

The 2D ^{13}C–^{13}C spectra can also provide information on the protonation states of the Glu-11 side chain carboxylic group. The ^{13}CO chemical shift of the COOH group is generally shifted upfield compared to the COO^- group. In Figure 20, the crosspeaks marked by the grey arrows are due to the correlation between the side chain COO^- and Cγ. The COOH/Cγ crosspeaks are overlapped by other crosspeaks marked by the black arrows. It is difficult to determine the exact COO^-/COOH ratio for samples at each pH because of the overlap. However,

information on the relative COO^-/COOH ratios at different pHs can be estimated. The intensity of the COO^-/Cγ crosspeaks increased as the sample pH was increased and the intensity of the peaks marked by the black arrows decreased suggesting a decrease in the COOH/Cγ crosspeak intensity with the increasing sample pHs. The increasing COO^-/Cγ crosspeak intensity with increasing pH and increasing COOH/Cγ crosspeak intensity with decreasing pH indicated a higher population of Glu-11 COO^- for samples at pH 7.4, a higher population of Glu-11 COOH at pH 4.0 and the intermediate population of both COO^- and COOH for samples at pH 5.0, from which the trend of COO^-/COOH can be estimated as: pH 7.4 > pH 5.0 > pH 4.0. This suggests that Glu-11 is located at the surface of the membrane and has contact with surrounding water and its pH.

3.3 DISCUSSION

The IFP region of the HA2 domain of the influenza hemagglutinin protein has been the focus of considerable studies because of its importance in viral fusion. For membranes which lack cholesterol, previous studies have shown that the IFP mainly adopts an α helical conformation.[1, 4, 6] A population of β strand IFP was also observed for high IFP:lipid mol ratio (~0.1) with 1 M NaCl in the buffer solution at pH 7.4.[5] For IFP associated with membranes without cholesterol at IFP:lipid ≈ 0.04, the present study provides a large number of ^{13}CO chemical shifts and $^{13}CO\cdots^{15}N$ and ^{13}CO–^{13}CO distance measurements that are consistent with predominant α helical conformation between residues Leu-2 and Met-17. However, in membranes containing cholesterol, there is a large fraction of β

strand IFP and the magnitude of this fraction varied from ~0.7 at pH 7.4 to ~1 at pH 5.0. Cholesterol-containing membranes are likely physiologically relevant because the membranes of the respiratory epithelial cells infected by influenza virus contain ~30 mol% cholesterol.[36, 37] The correlation of the β strand conformation with membrane cholesterol content has also been observed for the fusion peptide from HIV (HFP).[9] However, even in membranes lacking cholesterol, there is a significant population of β strand HFP for HFP:lipid ≥ 0.02 which contrasts with the predominant helical IFP conformation observed in samples with IFP:lipid = 0.04.

The correlation of membrane cholesterol content and β strand conformation is not well understood and may be related to the loss of membrane porosity associated with cholesterol.[44] The helical IFPs are likely monomeric whereas the β strand IFPs are likely associated as larger β sheet oligomers through inter-peptide hydrogen bonding. Membrane insertion of the apolar N-terminal region of IFP likely contains a negative free energy term due to hydrophobic IFP/lipid interactions and a positive term due to disruption of membrane packing. The latter term likely becomes larger for membranes containing cholesterol and needs the compensation from the larger more hydrophobic β sheet oligomer.

The IFP induces much greater vesicle fusion at pH 5.0 than at pH 7.4 and additional fusion can be triggered by lowering the pH of the vesicle solution from pH 7.4 to pH 5.0.[38] These functional effects are observed both for vesicles which contain cholesterol and for vesicles which lack cholesterol. In addition, the β

strand conformation is detected for IFP in cholesterol-containing membranes at both pHs. This latter result combined with observation of triggered fusion in both types of vesicles is most consistent with fusogenic activity of both helical and β strand IFPs. Fusogenicity of both conformations might be correlated with enhanced viral fusion and infectivity because it suggests that infection does not depend on the cholesterol content of the host cell membrane. Corollary support for this hypothesis is the previous observation that influenza viral fusion is independent of membrane cholesterol content.[45]

Solid-state NMR detection of predominant helical IFP conformation in membranes lacking cholesterol is consistent with previous data from CD, infrared, and ESR spectroscopies. In addition, the solid-state NMR measurements of ^{13}CO chemical shifts and $^{13}CO\cdots^{15}N$ internuclear distances in samples at pH 5.0 and pH 7.4 provided information about putative conformational changes in IFP which may be related to the large difference in fusion activity at the two pHs. In particular, liquid-state NMR spectra of IFP in detergent micelles suggested that the Gly-13 to Met-17 region adopted helical conformation at pH 5.0 and extended structure at pH 7.4.[7] In some contrast, the membrane data of the present study show that both the Gly-13 and Gly-16 ^{13}CO chemical shifts and the Gly-13 $^{13}CO \cdots$ Met-17 ^{15}N distance are independent of pH and consistent with helical structure.

This chapter also presents the detailed study of the conformation of the IFP middle region in membranes lacking cholesterol. The first approach was to use IFP mutants, IFP-E11VN12A and IFP-N12A, for the sake of inexpensive

isotop

PC/PC

Howe

helica

strand

in the

that

chole

comp

the m

was

amin

had

5.0

arou

resi

(hel

con

pH

tur

de

m

isotopic labeling. The ^{13}CO–^{13}CO distance measurements of those mutants in PC/PG membranes suggested that the middle region of IFP is not helical. However, the mutation of Glu-11 to Val or Asn-12 to Ala altered the overall helical structure of IFP in membranes without cholesterol to partial or complete β strand structure. As discussed previously, β strand IFP structure is fusion active in the cholesterol-containing membrane. The results of the mutants suggested that the β strand structure is also fusion active in the membranes lacking cholesterol because IFP has respective higher or comparable fusion activity compared to wild-type IFP with the mutation of glutamic acids to valines[14, 15] or the mutation of Asn-12 to Ala[14, 15].

The second approach to detect the conformation of the IFP middle region was to use 2D ^{13}C–^{13}C correlation spectroscopy and uniformly ^{13}C, ^{15}N-labeled amino acids. The chemical shifts derived from the spectra indicated that Asn-12 had more extended structural characteristics for membrane samples at both pH 5.0 and pH 7.4. The overall structure of IFP is helix-turn-helix with the turn around residue Glu-11 and/or Asn-12 at both pHs. For samples at pH 5.0, the residue Glu-11 exhibited two distinct conformations with the relative ratio of ~3:1 (helix/turn). For the sample at pH 7.4, only one conformation was detected which corresponds to the major population of the two conformations (helix) observed at pH 5.0. The termination of the IFP N-terminal helix and the formation of a middle turn are consistent with some previous results. Solution NMR experiments on detergent-associated IFP showed that IFP has the helix-turn-helix structure in micelles.[7] Hsu et al. studied an IFP analog which had five glutamic acids in the

sequence, at residue 4, 8, 11, 15, 19 respectively, by solution NMR. This IFP E5 analog exhibits similar fusion activity to the native fusion peptide and also has a helix-turn-helix structure in micelles at pH 5.0.[46] An IFP mutant G13L was shown to interact with membrane bilayers by fluorescence studies but have no fusion activity. The loss of fusion activity was proposed to be correlated to the loss of the ability to terminate the IFP N-terminal helix by Gly-13 due to the mutation.[47] Unlike these studies, either with IFP analogues or using micelles which does not resemble native cell membranes, our studies utilize the native IFPs in the membrane bilayer system and have more biological relevance. A fixed angle boomerang structure of IFP was previously suggested to be necessary for IFP to be fusion active and the kink was observed to be at residues Glu-11 and Asn-12.[14] Our observation of the IFP helix-turn-helix structure is consistent with this result and the additional observation of the two conformations of Glu-11 and Asn-12 in the turn region at pH 5.0 may be correlated to the higher fusogenicity of IFP at pH 5.0. The observation of the two local conformations at an atomic resolution level is important because it provides the direct evidence for the existence of complexity even in a small biological system. It is also important for comparison with simulations which detect the full conformational distributions. In some contrast, the conformation B was not observed by solution NMR which may be due to the lack of IFP B conformation or the rapid motional averaging over the distribution for IFP in detergent micelles.

The information on the protonation state of the Glu-11 side chain carboxylic group was also obtained from the 2D spectra. The data suggested that

the protonation state of the side chain carboxylic group of Glu-11 is affected by the pH of the solution and Glu-11 is likely in contact with water. For the IFP samples at pH 5.0, both COO^- and COOH are present. For the samples at pH 4.0 and pH 7.4, the respective dominant states of Glu-11 are COOH and COO^-. The relative population of COO^-/COOH for samples at different pHs, pH 7.4 > pH 5.0 > pH 4.0, can be compared to the relative population of conformation A/conformation B, pH 7.4 (>90 %) > pH 4.0 (~80 %) ~ pH 5.0 (~75 %), and suggests that the existence of dual protonation states of Glu-11 for samples at pH 5.0 or pH 4.0 is possibly not correlated to the two conformations of this residue. Molecular dynamic studies will benefit from the information on the protonation states of Glu-11 as the detailed knowledge of the charged states of glutamic acids is critical for the simulations. Different protonation states of the acidic residues, e.g. Glu-11, resulted in very different secondary structures and membrane locations of IFP in the previous molecular dynamic studies.[48, 49]

3.4 REFERENCES

1. Luneberg, J.; Martin, I.; Nussler, F.; Ruysschaert, J. M.; Herrmann, A., Structure and Topology of the Influenza-Virus Fusion Peptide in Lipid Bilayers. *J. Biol. Chem.* **1995,** 270, (46), 27606-27614.

2. Ishiguro, R.; Kimura, N.; Takahashi, S., Orientation of fusion-active synthetic peptides in phospholipid bilayers: Determination by Fourier transform infrared spectroscopy. *Biochemistry* **1993,** 32, (37), 9792-9797.

3. Gray, C.; Tatulian, S. A.; Wharton, S. A.; Tamm, L. K., Effect of the N-terminal glycine on the secondary structure, orientation, and interaction of the influenza hemagglutinin fusion peptide with lipid bilayers. *Biophys. J.* **1996,** 70, (5), 2275–2286.

4. Macosko, J. C.; Kim, C. H.; Shin, Y. K., The membrane topology of the fusion peptide region of influenza hemagglutinin determined by spin-labeling EPR. *J. Mol. Biol.* **1997,** 267, (5), 1139-1148.

5. Han, X.; Tamm, L. K., pH-dependent self-association of influenza hemagglutinin fusion peptides in lipid bilayers. *J. Mol. Biol.* **2000,** 304, (5), 953-965.

6. Wasniewski, C. M.; Parkanzky, P. D.; Bodner, M. L.; Weliky, D. P., Solid-state nuclear magnetic resonance studies of HIV and influenza fusion peptide orientations in membrane bilayers using stacked glass plate samples. *Chem. Phys. Lipids* **2004,** 132, (1), 89-100.

7. Han, X.; Bushweller, J. H.; Cafiso, D. S.; Tamm, L. K., Membrane structure and fusion-triggering conformational change of the fusion domain from influenza hemagglutinin. *Nat. Struct. Biol.* **2001,** 8, (8), 715-720.

8. Bodner, M. L., *Solid state nuclear magnetic resonance of the HIV-1 and influenza fusion peptides associated with membranes*. Ph. D. thesis, Michigan State University: East Lansing, 2006; p 122.

9. Qiang, W.; Yang, J.; Weliky, D.P., Solid-state nuclear magnetic resonance measurements of HIV fusion peptide to lipid distances reveal the intimate contact of beta strand peptide with membranes and the proximity of the Ala-14-Gly-16 region with lipid headgroups. *Biochemistry* **2007,** 46, (17), 4997-5008.

10. Yang, J.; Gabrys, C. M.; Weliky, D. P., Solid-state nuclear magnetic resonance evidence for an extended beta strand conformation of the membrane-bound HIV-1 fusion peptide. *Biochemistry* **2001,** 40, (27), 8126-8137.

11. Yang, J.; Prorok, M.; Castellino, F. J.; Weliky, D. P., Oligomeric beta structure of the membrane-bound HIV-1 fusion peptide formed from soluble monomers. *Biophys. J.* **2004,** 87, 1951-1963.

12. Yang, J.; Weliky, D. P., Solid state nuclear magnetic resonance evidence for parallel and antiparallel strand arrangements in the membrane-associated HIV-1 fusion peptide. *Biochemistry* **2003,** 42, 11879-11890.

13. Zheng, Z.; Yang, R.; Bodner, M. L.; Weliky, D.P., Conformational flexibility and strand arrantments of the membrane-associated HIV fusion peptide trimer probed by solid-state NMR spectroscopy. *Biochemistry* **2006,** 45, 12960-12975.

14. Lai, A. L.; Park, H.; White, J. M.; Tamm, L. K., Fusion Peptide of Influenza Hemagglutinin Requires a Fixed Angle Boomerang Structure for Activity. *J. Biol. Chem.* **2006,** 281, (9), 5760-5770.

15. Korte, T.; Epand, R. F.; Epand, R. M.; Blumenthal, R., Role of the Glu Residues of the Influenza Hemagglutinin Fusion Peptide in the pH Dependence of Fusion Activity. *Virology* **2001,** 289, (2), 353-361.

16. Morcombe, C. R.; Zilm, K. W., Chemical shift referencing in MAS solid state NMR. *J. Magn. Reson.* **2003,** 162, 479-486.

17. Zhang, H. Y.; Neal, S.; Wishart, D. S., RefDB: A database of uniformly referenced protein chemical shifts. *J. Biomol. NMR* **2003,** 25, (3), 173-195.

18. Kricheldorf, H. R.; Muller, D., Secondary structure of peptides. 3. ^{13}C NMR cross polarization/magic angle spinning spectroscopic characterization of solid polypeptides. *Macromolecules* **1983,** 16, (4), 615-623.

19. Saito, H., Conformation-dependent ^{13}C chemical shifts - a new means of conformational characterization as obtained by high-resolution solid-state ^{13}C NMR. *Magn. Reson. Chem.* **1986,** 24, (10), 835-852.

20. Balbach, J. J.; Petkova, A. T.; Oyler, N. A.; Antzutkin, O. N.; Gordon, D. J.; Meredith, S. C.; Tycko, R., Supramolecular structure in full-length Alzheimer's b-amyloid fibrils: Evidence for a parallel b-sheet organization from solid-state nuclear magnetic resonance. *Biophys. J.* **2002,** 83, (2), 1205-1216.

21. Bennett, A. E.; Ok, J. H.; Griffin, R. G.; Vega, S., Chemical-shift correlation spectroscopy in rotating solids - radio frequency-driven dipolar recoupling and longitudinal exchange. *J. Chem. Phys.* **1992,** 96, (11), 8624-8627.

22. Gullion, T.; Vega, S., A simple magic angle spinning NMR experiment for the dephasing of rotational echoes of dipolar coupled homonuclear spin pairs. *Chem. Phys. Lett.* **1992,** 194, (4-6), 423-428.

23. Bennett, A. E.; Rienstra, C. M.; Griffiths, J. M.; Zhen, W. G.; Lansbury, P. T.; Griffin, R. G., Homonuclear radio frequency-driven recoupling in rotating solids. *J. Chem. Phys.* **1998,** 108, (22), 9463-9479.

24. Bennett, A. E.; Weliky, D. P.; Tycko, R., Quantitative conformational measurements in solid state NMR by constant-time homonuclear dipolar recoupling. *J. Am. Chem. Soc.* **1998,** 120, (19), 4897-4898.

25. Ishii, Y., ^{13}C-^{13}C dipolar recoupling under very fast magic angle spinning in solid-state nuclear magnetic resonance: Applications to distance measurements, spectral assignments, and high-throughput secondary-structure determination. *J. Chem. Phys.* **2001,** 114, (19), 8473-8483.

26. Gullion, T.; Schaefer, J., Rotational-echo double-resonance NMR. *J. Magn. Reson.* **1989,** 81, (1), 196-200.

27. Anderson, R. C.; Gullion, T.; Joers, J. M.; Shapiro, M.; Villhauer, E. B.; Weber, H. P., Conformation of [1-^{13}C,^{15}N]acetyl-L-carnitine - rotational- echo, double-resonance nuclear-magnetic-resonance spectroscopy. *J. Am. Chem. Soc.* **1995,** 117, (42), 10546-10550.

28. Kimura, S.; Naito, A.; Saito, H.; Ogawa, K.; Shoji, A., Characterization of a-helix structures in polypeptides, revealed by $^{13}C{=}O\cdots H\text{-}^{15}N$ hydrogen bond lengths determined by ^{13}C REDOR NMR. *J. Mol. Struct.* **2001,** 562, (1-3), 197-203.

29. Murphy, O. J., 3rd; Kovacs, F. A.; Sicard, E. L.; Thompson, L. K., Site-directed solid-state NMR measurement of a ligand-induced conformational change in the serine bacterial chemoreceptor. *Biochemistry* **2001,** 40, (5), 1358-1366.

30. Smith, S. O.; Eilers, M.; Song, D.; Crocker, E.; Ying, W. W.; Groesbeek, M.; Metz, G.; Ziliox, M.; Aimoto, S., Implications of threonine hydrogen bonding in the glycophorin A transmembrane helix dimer. *Biophys. J.* **2002,** 82, (5), 2476-2486.

31. Nishimura, K.; Kim, S. G.; Zhang, L.; Cross, T. A., The closed state of a H^+ channel helical bundle combining precise orientational and distance restraints from solid state NMR. *Biochemistry* **2002,** 41, (44), 13170-13177.

32. Toke, O.; Maloy, W. L.; Kim, S. J.; Blazyk, J.; Schaefer, J., Secondary structure and lipid contact of a peptide antibiotic in phospholipid Bilayers by REDOR. *Biophys. J.* **2004,** 87, (1), 662-674.

33. Long, J. R.; Shaw, W. J.; Stayton, P. S.; Drobny, G. P., Structure and dynamics of hydrated statherin on hydroxyapatite as determined by solid-state NMR. *Biochemistry* **2001,** 40, (51), 15451-15455.

34. Cornilescu, G.; Delaglio, F.; Bax, A., Protein backbone angle restraints from searching a database for chemical shift and sequence homology. *J. Biomol. NMR* **1999,** 13, (3), 289-302.

35. Yang, J.; Parkanzky, P. D.; Khunte, B. A.; Canlas, C. G.; Yang, R.; Gabrys, C. M.; Weliky, D. P., Solid state NMR measurements of conformation and conformational distributions in the membrane-bound HIV-1 fusion peptide. *J. Mol. Graph. Model.* **2001,** 19, (1), 129-135.

36. Worman, H. J.; Brasitus, T. A.; Dudeja, P. K.; Fozzard, H. A.; Field, M., Relationship Between Lipid Fluidity and Water Permeability of Bovine Tracheal Epithelial-Cell Apical Membranes. *Biochemistry* **1986,** 25, (7), 1549-1555.

37. Scheiffele, P.; Rietveld, A.; Wilk, T.; Simons, K., Influenza Viruses Select Ordered Lipid Domains during Budding from the Plasma Membrane. *J. Biol. Chem.* **1999,** 274, (4), 2038-2044.

38. Parkanzky, P. D., *Solid state nuclear magnetic resonance studies of the influenza fusion peptide associated with membrane bilayers*. Ph. D. thesis, Michigan State University: East Lansing, 2006; p 80.

39. Longhi, S.; Czjzek, M.; Lamzin, V.; Nicolas, A.; Cambillau, C., Atomic resolution (1.0 A) crystal structure of Fusarium solani cutinase: stereochemical analysis. *J. Mol. Biol.* **1997,** 268, (4), 779-799.

40. Voet, D.; Voet, J. G., *Biochemistry*. John Wiley & Sons, Inc.: New York, **1995**.

41. Han, X.; Bushweller, J. H.; Cafiso, D. S.; Tamm, L. K., NMR structure of hemagglutinin fusion peptidein DPC micelles at pH 5. *PDB #: 1ibn* **2001**.

42. Han, X.; Bushweller, J. H.; Cafiso, D. S.; Tamm, L. K., NMR structure of hemagglutinin fusion peptidein DPC micelles at pH 7.4.. *PDB #: 1ibo* **2001**.

43. Bodner, M. L.; Gabrys, C. M.; Struppe, J. O.; Weliky, D. P., 13C–13C and 15N–13C correlation spectroscopy of membrane-associated and uniformly labeled human immunodeficiency virus and influenza fusion peptides: Amino acid-type assignments and evidence for multiple conformations. *J. Chem. Phys.* **2008,** 128, 052319.

44. Nicol, F.; Nir, S.; Szoka, F. C., Effect of cholesterol and charge on pore formation in bilayer vesicles by a pH-sensitive peptide. *Biophys. J.* **1996,** 71, (6), 3288-3301.

45. White, J.; Kartenbeck, J.; Helenius, A., Membrane fusion activity of influenza virus. *EMBO J.* **1982,** 1, (2), 217–222.

46. Hsu, C. H.; Wu, S. H.; Chang, D. K.; Chen, C. P., Structural characterizations of fusion peptide analogs of influenza virus hemagglutinin - Implication of the necessity of a helix-hinge-helix motif in fusion activity. *J. Biol. Chem.* **2002,** 277, (25), 22725-22733.

47. Matsumoto, T., Membrane destabilizing activity of influenza virus hemagglutinin-based synthetic peptide: implications of critical glycine residue in fusion peptide. *Biophys. Chem.* **1999,** 79, (2), 153-162.

48. Sammalkorpi, M.; Lazaridis, T., Configuration of influenza hemagglutinin fusion peptide monomers and oligomers in membranes. *BBA-Biomembranes* **2007,** 1768, (1), 30-38.

49. Feig, M., *personal discussion with Dr. Michael Feig.*

Chapter 4 Studies of Influenza Fusion Peptide Membrane Location

4.1 BACKGROUND

It has been proposed that the structural bases for the fusion activity of fusion peptides include the interaction of peptides with membranes and the membrane location of fusion peptides is an important structural component to understand this interaction. Some previous ESR studies have suggested that the different membrane locations of IFP are correlated to its different fusogenic activities at different pHs.[1] The membrane location of IFP has been probed by fluorescence and ESR spectroscopies. While some studies detected a pH-dependence of the membrane location of IFP and its analogues, other studies supported an insertion depth which is independent of pH.[1-5]

A fluorescence study indicated that the IFP is near the hydrocarbon-phosphate interface of the membrane and no gross positional change of the peptide between different pH values was detected.[2] Three different groups studied the IFP membrane location with ESR and different results were obtained: (1) Lüneberg et al. used the 20-amino acid length synthetic peptide corresponding to HA2 and suggested that the N-terminal helix of the fusion peptide is located near the hydrophobic acylchain-phosphate headgroup interface and the location is independent of pH;[3] (2) Macosko et al. expressed a major portion of HA2 domain (FHA2, residue 1-127) which was then spin-labeled and studied by ESR and found that the fusion peptide region is inserted into the membrane with a tilt angle of ~75° from the membrane normal with Ile-6 most deeply inserted. The insertion is also pH-independent.[4] (3) Han et al. studied the

synthetic IFP which was linked to a short hydrophilic peptide (GGCGKKKK) and the results suggested that the fusion peptide is inserted into the membrane in a pH-dependent way and the residue with the deepest insertion is Phe-3 or Ile-6 at pH 5.0 or pH 7.4, respectively.[1] This pH-dependent insertion was also observed for some IFP analogues by another group using tryptophan fluorescence emission experiments. In this study, Trp-14 in IFP analogues was used and the observation of a blue shift in the steady-state fluorescence emission spectra for samples at pH 5.0 relative to samples at pH 7.4 indicated a deeper membrane insertion of IFP analogues at pH 5.0.[5] In addition to these different experimental results, molecular dynamics studies predicted distinct insertion as well. Two simulations suggested that IFP is at the membrane-water interface, exposing the polar sidechains to water and the non-polar sidechains to the hydrophobic core.[6, 7] Another two theoretical studies predicted an IFP location at the amphipathic interface between the lipid headgroups and hydrocarbon chains.[8, 9] One simulation proposed that micelle-associated IFP lies at the micelle surface, while for the membrane-associated IFP, the N-terminal region deeply inserts into the membrane bilayer.[10]

I also studied the membrane location of IFP using solid-state NMR. The solid-state NMR measurements can detect the membrane location at an atomic-resolution level without introducing any extra group which may potentially disturb the IFP membrane location. The method is based on the ^{13}C–^{31}P or ^{13}C–^{19}F dipolar coupling measurements corresponding to the distances between IFP backbone ^{13}CO and lipid phosphate groups or between IFP backbone ^{13}CO and

^{19}F in the acylchains in the membrane interior, respectively. The IFP was labeled with ^{13}CO at various positions and incorporated into the membranes that lack cholesterol at pH 5.0 or pH 7.4. As discussed in Chapter 3, IFP adopts helical structure in those membranes based on chemical shift measurements. The ^{13}C-^{31}P and ^{13}C-^{19}F REDOR experiments showed that the N and C-terminal regions of IFP are in close contact with phosphate head groups and residues Phe-3, Ile-6 and Phe-9 have contacts with F(C16) (F labeled at the DPPC C16 position). An inverted boomerang structure of membrane-associated IFP was proposed based on data of the IFP conformational studies in chapter 3 and these ^{13}C-^{31}P and ^{13}C-^{19}F REDOR data. Compared to the IFP samples at pH 5.0, the samples at pH 7.4 have less IFP population inserted into the membrane bilayer and some IFP molecules were proposed to lie in the water layer above the membrane bilayer.

4.2 RESULTS

1. Static ^{31}P spectra

Prior to the development of structural models for IFP/membrane interaction it is essential to know the lipid phase for membranes with bound IFP. In this section, ^{31}P spectroscopy was applied to study the structure of membranes for membrane-associated IFP samples at different pHs. Figure 22a-b shows the representative ^{31}P spectra of IFP membrane samples containing DTPC/DTPG (4:1) at pH 5.0 or pH 7.4. These spectra have similar lineshapes to the spectrum of a DTPC/DTPG membrane sample without bound IFP (cf. Figure

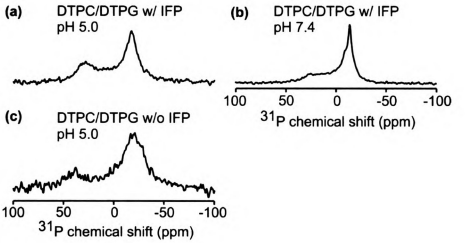

Figure 22. ^{31}P spectra of membrane samples (DTPC/DTPG, 4:1) that (a, b) contained IFP or (c) had no bound IFP at 35 °C. The peptide to lipid mol ratio is 0.04. Each spectrum was processed with 200 Hz Gaussian line broadening and was the sum of 300 to 1000 scans.

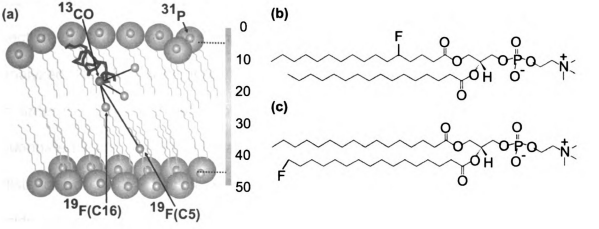

Figure 23. (a) Model of a membrane bilayer with a peptide inserted into a single leaflet and with the positions of ^{31}P, $^{19}F(C5)$, $^{19}F(C16)$ and peptide backbone ^{13}CO labeled. The blue balls represent the phosphate headgroups and the gray lines represent the hydrocarbon chains of lipids. The approximate dimension in Å of the membrane bilayer is shown by the scale bar on the right. The thickness of the membrane bilayer is ~50 Å and the phosphate headgroup is ~8 Å in diameter. The ^{13}CO–$^{19}F(C5)$ and ^{13}CO–$^{19}F(C16)$ distances are shown by the black lines. All the $^{19}Fs(C16)$ are at the bilayer center and have similar distances to the labeled ^{13}CO. The peptide labeled ^{13}CO has a shorter distance to the $^{19}F(C5)$ located at the same leaflet relative to the $^{19}F(C5)$ located at the different leaflet. The ^{13}CO–$^{19}F(C5)$ REDOR data contain information from the ^{13}CO–$^{19}F(C5)$ pair and is dominated by the pair with the shorter distance. The effective concentration of $^{19}F(C5)$ is half of its real concentration for the REDOR measurement. Panels (b) and (c) show the structures of 5-^{19}F-DPPC and 16-^{19}F-DPPC molecules respectively.

22c) and are consistent with a predominant lamellar phase.[11] Therefore, the lipid phase of membranes are not affected by addition of IFP and are independent of pH. The analyses of the following REDOR data were based on the lamellar phase of membranes.

2. Membrane location of pH 5.0 samples

The goal of the IFP insertion studies is to provide a structural model of the location of IFP in membranes at a high resolution level. The studies were carried out with IFP samples at both pH 5.0 and pH 7.4 and the IFP locations in membranes at different pHs can be correlated to their functional activities. In this section, the data of the IFP samples at fusion active pH 5.0 will be displayed and analyzed. Residues throughout the IFP sequence were selectively ^{13}CO labeled in order to study the insertion of the different regions of IFP. In the studies, two fluorinated lipids, 16-^{19}F-DPPC and 5-^{19}F-DPPC, were used in order to detect the distances of the IFP backbone to the center of the membrane bilayer and to the midpoint between the phosphate headgroups and the bilayer center, respectively (cf. Figure 23). The REDOR experiments, denoted as ^{13}CO–^{31}P, ^{13}CO–^{19}F(C16) and ^{13}CO–^{19}F(C5) detected the distances between selectively labeled IFP backbone ^{13}CO and ^{31}P, 16-^{19}F and 5-^{19}F respectively.

Figure 24 shows the REDOR spectra at long dephasing time (32 ms for the ^{13}C–^{31}P REDOR experiments and 24 ms for the ^{13}CO–^{19}F REDOR experiments) for IFP samples at pH 5.0. The peak ^{13}CO chemical shifts from S_0 spectra are listed in table 8. All the shifts are consistent with the shifts listed in

table 2 of chapter 3 and the shifts from residues Leu-2 through Gly-20 are consistent with α helix structure. For membrane samples containing fluorinated DPPC (C5 or C16), most of the spectra have two peaks with the downfield one correlated with the α helical conformation and the upfield one correlated with the β strand conformation. The relative population of the two conformations can be estimated based on the relative intensities of the two peaks. The helical IFP is the predominant population for all the samples.

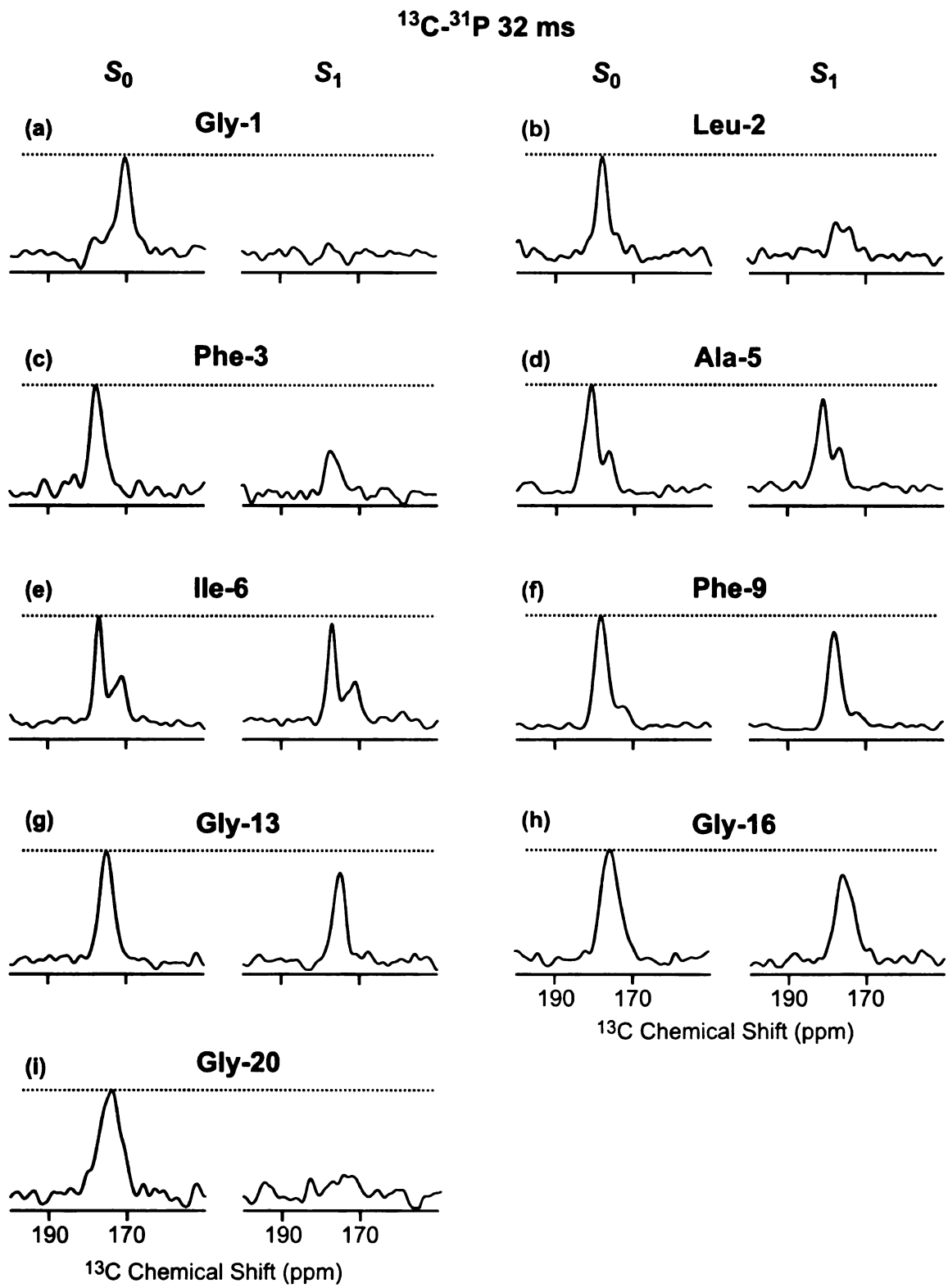

Figure 24 ^{13}C-^{31}P REDOR spectra with 32 ms dephasing time.

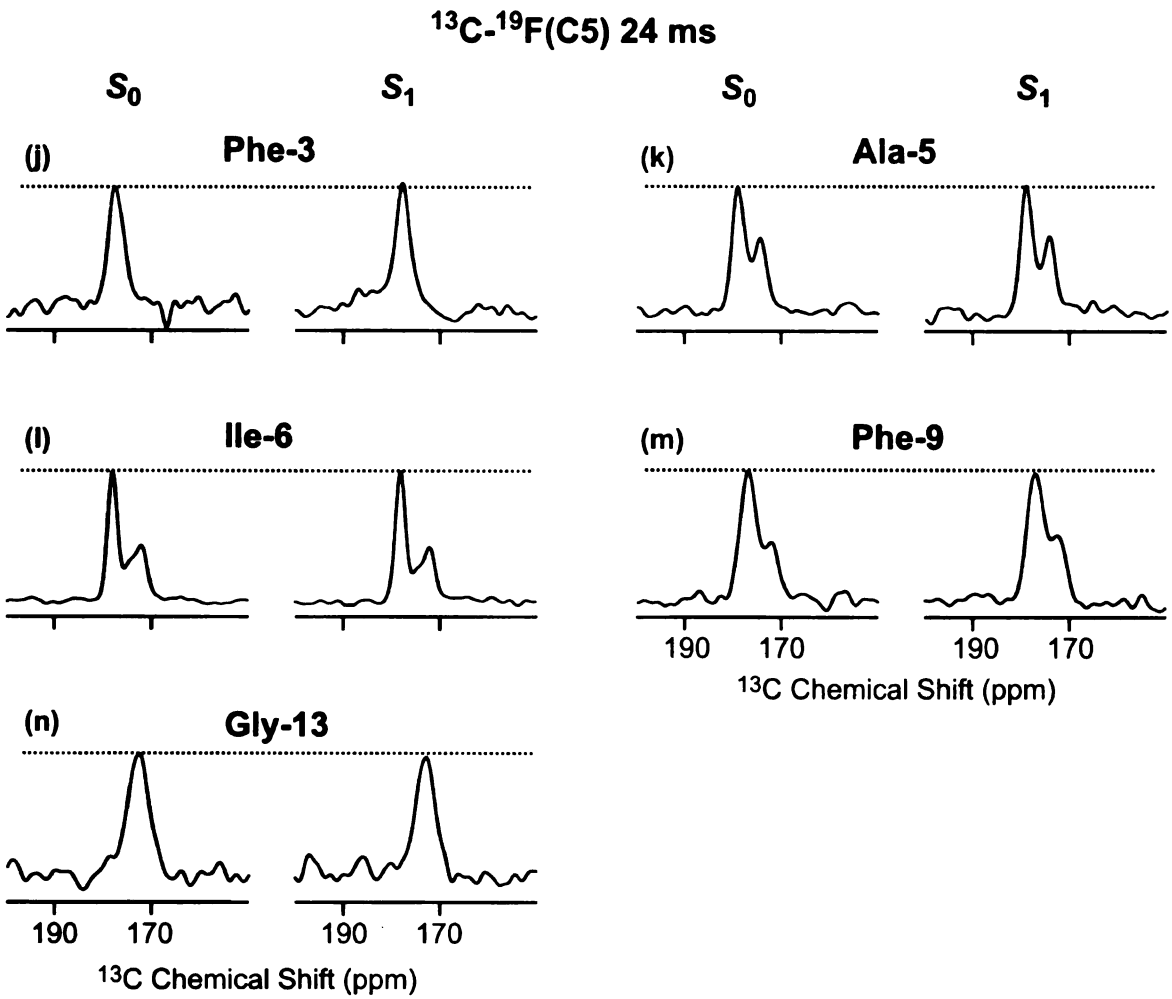

Figure 24 ^{13}C-^{19}F(C5) REDOR spectra with 24 ms dephasing time.

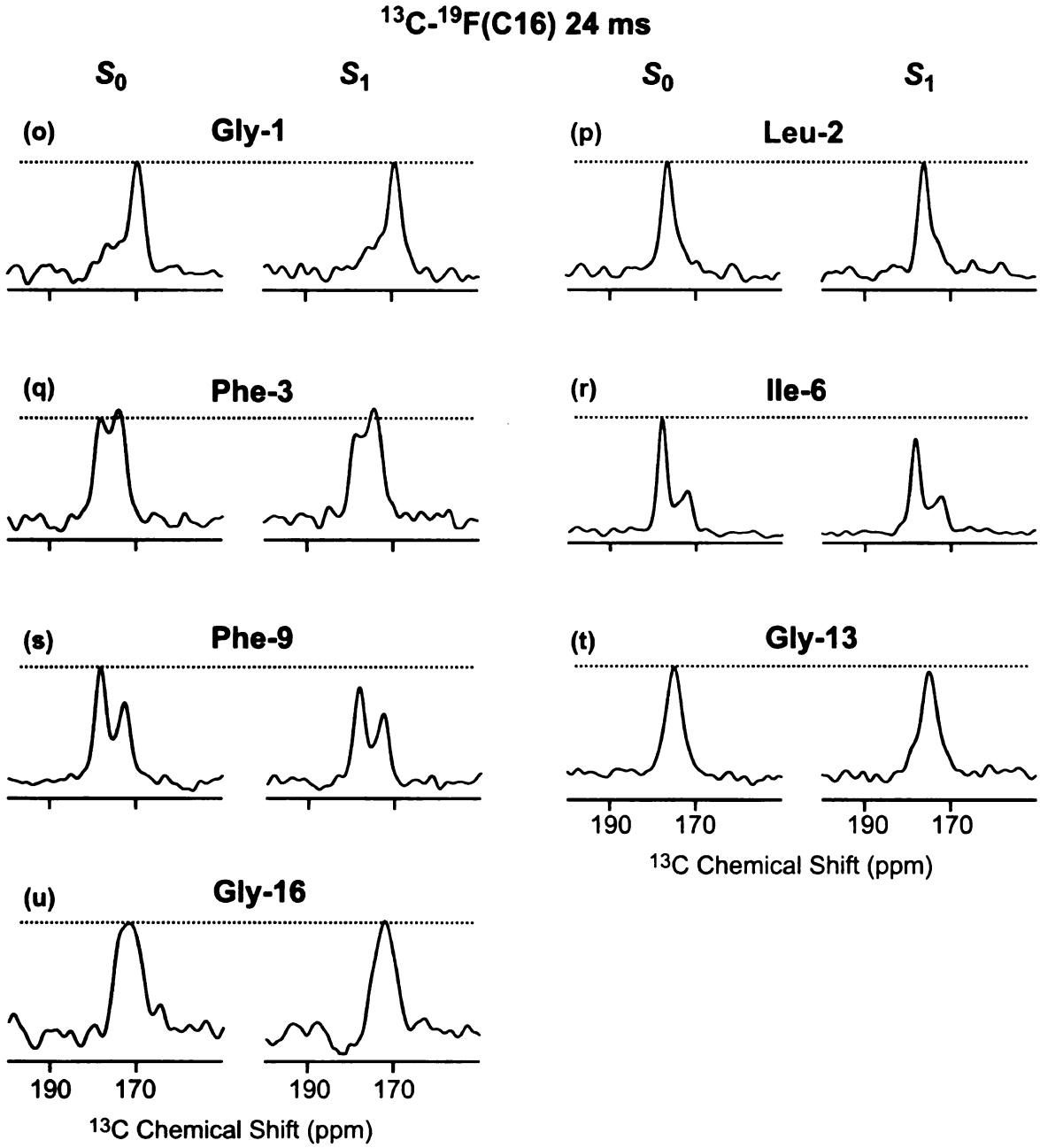

Figure 24. REDOR ^{13}C S_0 and S_1 NMR spectra at long dephasing time for membrane-associated IFP samples at pH 5.0. The experiment type and the dephasing time are labeled on the top of each group of spectra and the ^{13}CO labeled residues are also labeled above each set of S_0 and S_1 spectra. Each sample contained 16 µmol DTPC, 4 µmol DTPG and 0.8 µmol IFP. The samples used to take spectra (d), (e) and (j-n) contained 9 mol% 5-F-DPPC lipid and the samples used to take spectra (o-u) contained 9 mol% 16-F-DPPC lipid. Each spectrum was processed with 200 Hz Gaussian line broadening and was the sum of 20000 – 30000 scans.

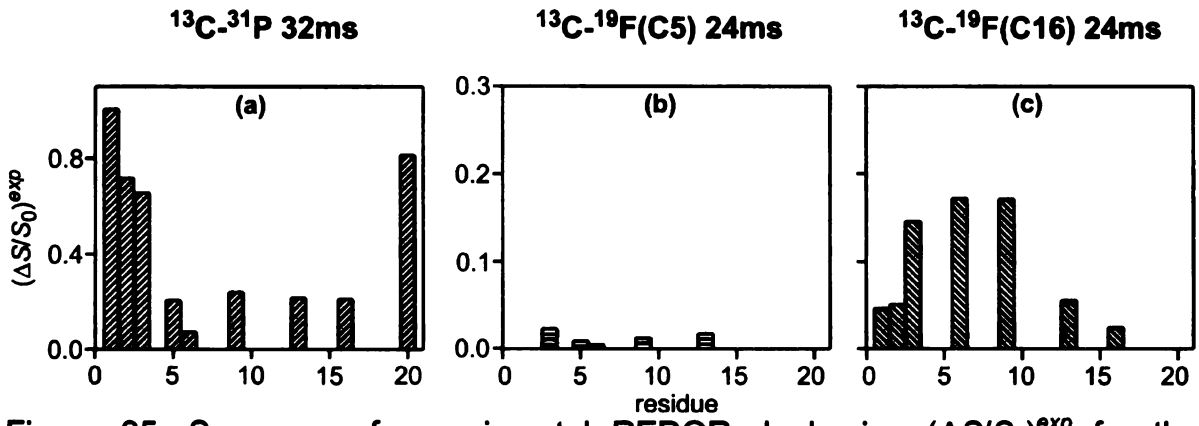

Figure 25. Summary of experimental REDOR dephasing $(\Delta S/S_0)^{exp}$ for the spectra displayed in Figure 24. The $(\Delta S/S_0)^{exp}$ values are shown as bars for different residues and a typical uncertainty is ±0.01-0.02.

Table 8. Peak ^{13}CO chemical shifts in ppm for IFP samples at pH 5.0 [a]

Gly-1	Leu-2	Phe-3	Ala-5	Ile-6	Phe-9	Gly-13	Gly-16	Gly-20
171.2	178.0	178.6	179.4	177.9	178.6	175.5	175.2	174.7

[a] Typical uncertainties in peak shifts are ± 0.5 ppm as determined from the measurements on samples that contained peptide with the same labeled residue but different membranes.

Figure 25 summarizes the dephasing, $(\Delta S/S_0)^{exp}$, corresponding to Figure 24. Compared to the S_0 ^{13}CO–^{31}P spectra of each labeled IFP, the intensities of the S_1 spectra are greatly reduced (> 60%) for the residues at N- and C-terminal regions, i.e., Gly-1, Leu-2, Phe-3 and Gly-20. For most residues at the middle region of IFP, Ala-5, Phe-9, Gly-13 and Gly-16, the intensities of the S_1 spectra are only reduced by ~20 %. In contrast, the intensities of the S_1 ^{13}CO–^{19}F(C16) spectra are the same as the S_0 spectra for residues Gly-1, Leu-2 and Gly-20 and are reduced by ~20 % relative to the S_0 spectra for residues Phe-3, Ile-6 and Phe-9. This suggests that the N- and C- terminal regions of IFP are in close contact to the membrane phosphate headgroups and the middle region of IFP has some contact to the membrane bilayer center suggesting an insertion of the

IFP middle region into the membrane bilayer. Similar conclusions can be drawn from the experimental dephasing curves shown in Figure 26. All the values were obtained based on integrations of 1 ppm of the downfield peaks corresponding to the helical IFPs. More ^{13}CO–^{31}P dephasing was observed for residues at the N- and C- terminal regions than for the residues in the middle region and the ^{13}CO–^{19}F(C16) dephasing was only observed for residues in the middle of the sequence. For all the labeled residues, little ^{13}CO–^{19}F(C5) (< 10 % at 24 ms dephasing time) was detected and the greatest observed ^{13}CO–^{19}F(C16) dephasing is small (< 20 % at 24 ms dephasing time), which is probably due to the small amount of labeled ^{19}F-DPPC used (~9 mol % of total lipids). The ^{19}F atoms at the C16 positions of both layers in a membrane bilayer are located at the center of the membrane and have similar dipolar interaction to the same ^{13}CO of an IFP. The ^{19}F atoms at the C5 positions of different layers in a membrane bilayer have different distances and dipolar interactions to the same ^{13}CO in an IFP and the bigger dipolar interaction makes the predominant contribution to the ^{13}CO–^{19}F REDOR experiment (cf. Figure 23). Therefore, only half of the 5-^{19}F-DPPC is effective for the ^{13}CO–^{19}F(C5) REDOR measurements and the actual effective concentration of 5-^{19}F-DPPC is only ~4.5 mol % compared to the 16-^{19}F-DPPC concentration (~9 mol %). It is reasonable that the observed ^{13}CO–^{19}F(C5) dephasing is smaller than the observed ^{13}CO–^{19}F(C16) dephasing at a specific dephasing time.

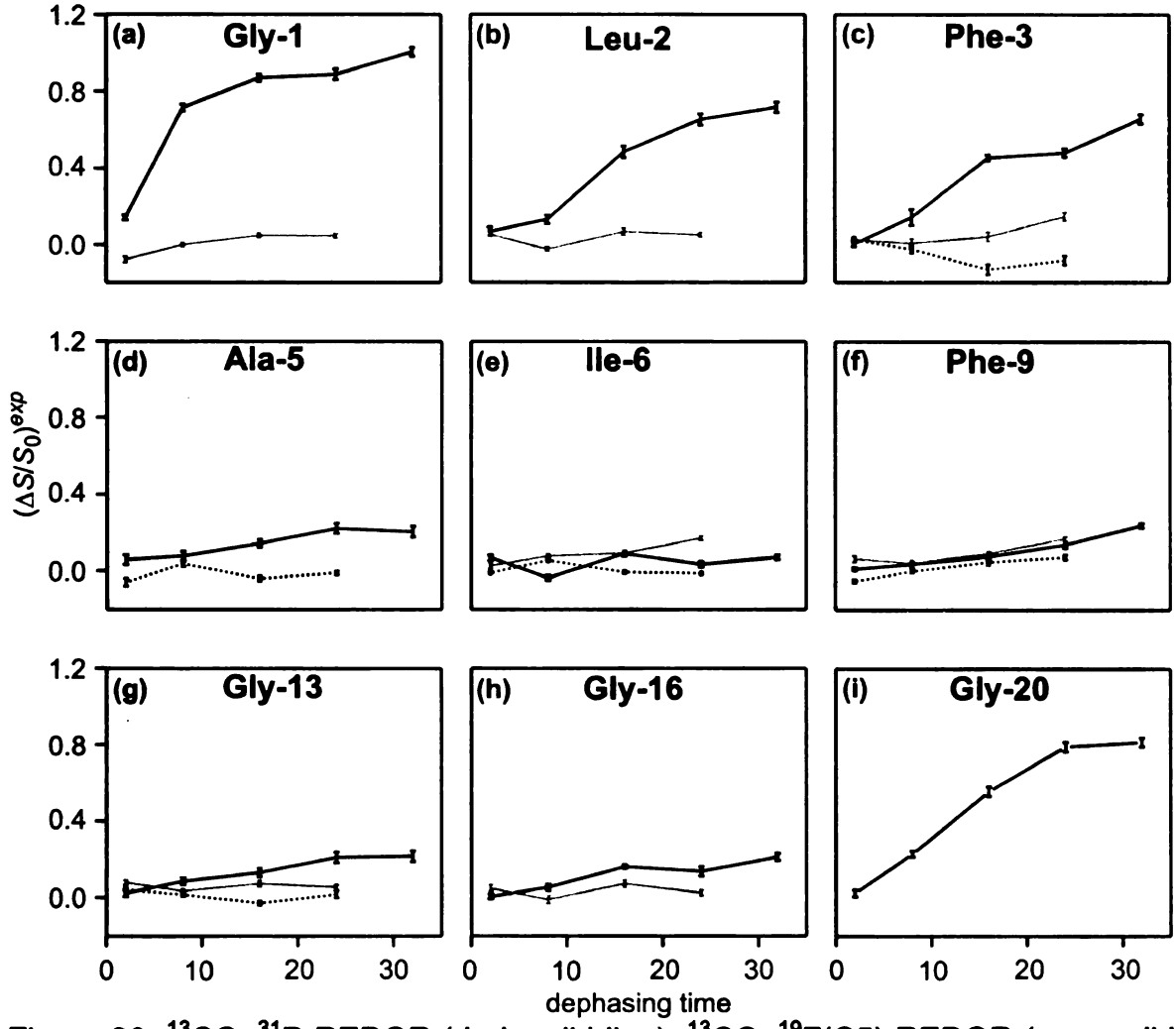

Figure 26. ^{13}CO–^{31}P REDOR (dark solid line), ^{13}CO–^{19}F(C5) REDOR (gray solid line) and ^{13}CO–^{19}F(C16) REDOR (dotted line) experimental dephasing curves for IFP samples at pH 5.0. The uncertainties are represented by the error bars and are typically ±0.01-0.02. The ^{13}CO labeled residues are labeled on top of each spectrum. The samples used were the same as the ones used to take the corresponding spectra in Figure 24.

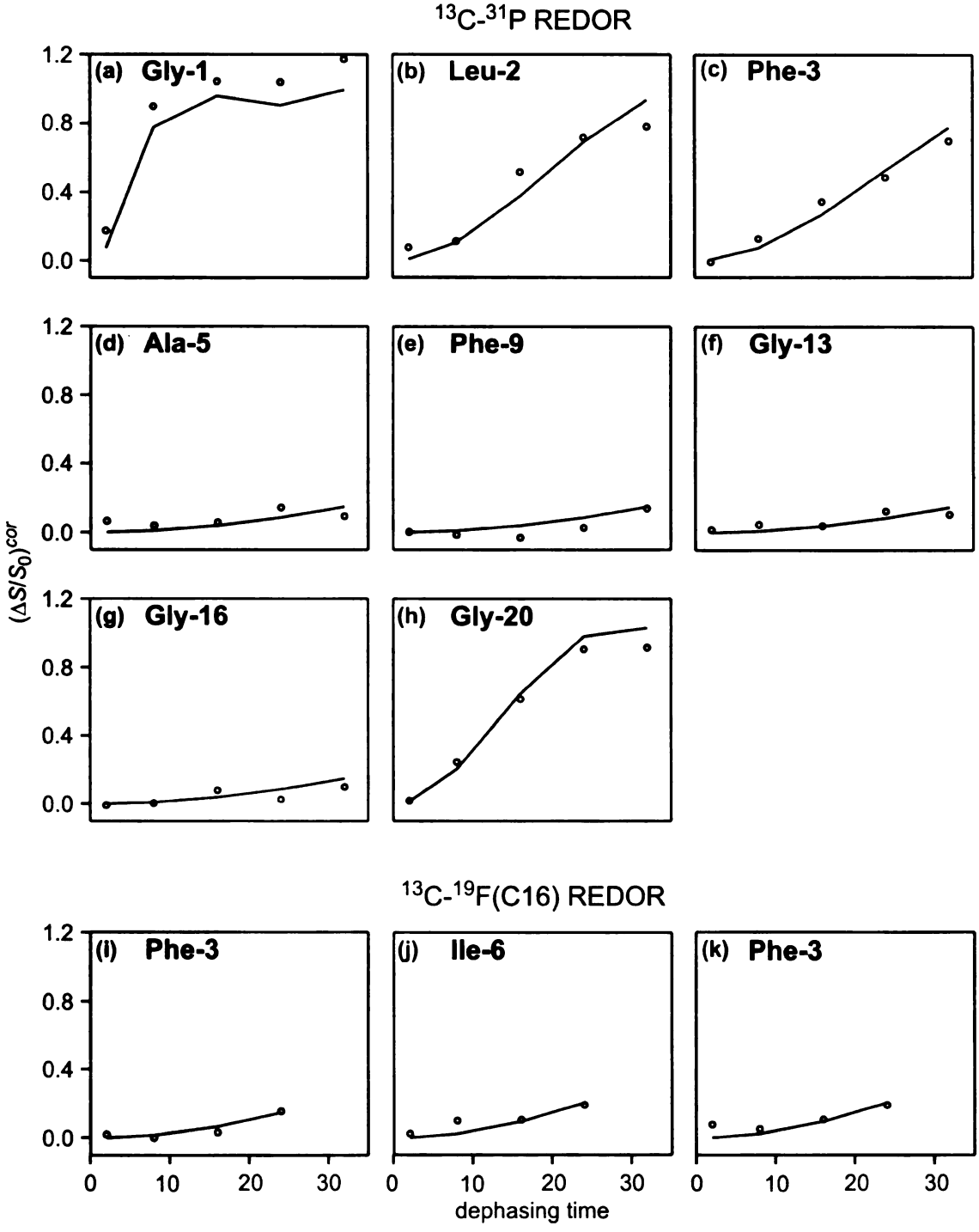

Figure 27. Plots of $(\Delta S/S_0)^{cor}$ (circles) and $(\Delta S/S_0)^{sim}$ (solid lines) vs. dephasing time for ^{13}CO–^{31}P and ^{13}CO–^{19}F(C16) REDOR of IFP samples at pH 5.0. The ^{13}CO labeled residues are labeled at the top of each spectrum.

A more quantitative analysis of the results can be obtained by fitting $(\Delta S/S_0)^{cor}$ to a theoretical dephasing $(\Delta S/S_0)^{sim}$ according to Eq. 2.6 and 2.10, where $(\Delta S/S_0)^{cor}$ was calculated from $(\Delta S/S_0)^{exp}$ by removing the contributions from natural abundance nuclei as described in chapter 2 and in the appendix. A best-fit ^{13}CO–^{31}P or ^{13}CO–^{19}F dipolar coupling frequency can be obtained and correlated to the internuclear distances, r_{CP} or r_{CF}, through Eq. 2.2 and 2.3. Figure 27 displays the fitting for all the build up curves with $(\Delta S/S_0)^{cor} > 0.1$ at long dephasing time (τ = 32 ms for ^{13}CO–^{31}P REDOR and τ = 24 ms for ^{13}CO–^{19}F REDOR). The distances from the fitting are listed in table 9. In the REDOR data fitting, a single membrane location of IFP was assumed and a ^{13}C-X two-spin system was used, where X represents ^{31}P or ^{19}F(C16). From the data fitting, the Gly-1 and Gly-20 ^{13}COs were determined to be respectively 4.5 and 6.0 Å away from the phosphorus and the Leu-2 and Phe-3 ^{13}COs are ~7 Å away from the phosphorus. These data and reasonable values of van der Waals radii (~2 Å for ^{13}CO and ~4 Å for the phosphorus headgroups) are consistent with the close contact of residues Gly-1, Gly-20, Leu-2 and Phe-3 with the phosphorus headgroups. Residues Phe-3, Ile-6 and Phe-9 are calculated to be ~12 Å away from ^{19}F(C16). Molecular dynamics simulations have determined that the distance between ^{31}P and the ^{19}F(C16) of a DPPC molecule in the gel phase is ~24 Å.[12] The ~12 Å fitted ^{13}CO–^{19}F(C16) distance indicated that these middle residues are inserted into the membrane bilayer. These distances combined with the fitted ^{13}CO–^{31}P distances of most of the middle residues from the experimental data (~10 Å) suggest that the middle region of IFP is half-way

inserted into a single leaflet of the membrane. The Ile-6 ^{13}CO–^{31}P dipolar coupling was not detected which is reasonable because of the relative location of Ile-6 to the phosphorus headgroups. The van der Waals radius of a helix backbone is ~4 Å and a residue located at the bottom side of the helix (e.g. Ile-6) will be ~8 Å further away from the phosphorus above the helix compared to the residue located at the top side (e.g. Leu-2) (cf. Figure 32) and is very likely to be too far away to be detected (^{13}CO–^{31}P REDOR detectable limit ~11 Å).

Table 9. Best-fit ^{13}CO–^{31}P and ^{13}CO–^{19}F(C16) distances for IFP samples at pH 5.0 [a]

	Gly-1	Leu-2	Phe-3	Ala-5	Ile-6	Phe-9	Gly-13	Gly-16	Gly-20
^{13}CO–^{31}P distance (Å)	4.5(0.1)	6.7(0.2)	7.2(0.2)	10.1(1.4)	> 11 [b]	10.1(0.5)	10.1(1.4)	10.1(1.0)	6.0(0.2)
χ^2	157 [c]	31	23	14	N/A [d]	48	6	16	22
^{13}CO–^{19}F(C16) distance (Å)	> 14 [b]	> 14	12.1(0.9)	N/A	11.5(0.4)	11.5(0.2)	> 14	> 14	N/A
χ^2	N/A	N/A	4	N/A	6	25	N/A	N/A	N/A

[a] Uncertainties are given in parentheses and were calculated from the values within the $\chi^2 = \chi^2_{min} + 5$ region.
[b] Calculated from the REDOR universal dephasing curve with $\Delta S/S_0 = 0.1$ at long dephasing time (τ = 32 ms for ^{13}CO–^{31}P or τ = 24 ms for ^{13}CO–^{19}F) based on the consideration that only the ^{13}COs with $(\Delta S/S_0)^{exp} > 0.1$ at long dephasing time are fittable.
[c] Regardless of the big χ^2, the fitting is still reasonable and consistent with the result of Gly-1 being close to ^{31}P. The χ^2 may be reduced by using multi-spin (e.g., X-^{13}CO-X) for the fitting.
[d] N/A ≡ not available.

3. Membrane location of pH 7.4 samples

In this section, the data of the IFP samples at non-fusogenic pH 7.4 will be displayed and analyzed. The same residues as in the studies of IFP pH 5.0 samples were selectively ^{13}CO labeled and the same experiments were carried

out in order to have a direct comparison between the results for samples at different pHs.

Figure 28 shows the REDOR spectra at long dephasing time (τ = 32 ms for the ^{13}C–^{31}P REDOR and τ = 24 ms for the ^{13}CO–^{19}F REDOR experiments) for IFP samples at pH 7.4. The peak ^{13}CO chemical shifts from S_0 spectra are listed in table 10 and are consistent with the shifts obtained for IFP pH 5.0 samples as listed in table 8. Unlike the spectra for pH 5.0 samples, most of the spectra only contain single peaks that correspond to the α helical conformation and lack the upfield peaks which correlate with the β strand conformation observed for membrane samples containing fluorinated DPPC (C5 or C16) at pH 5.0.

Table 10. Peak ^{13}CO chemical shifts in ppm for IFP samples at pH 7.4 [a]

Gly-1	Leu-2	Phe-3	Ala-5	Ile-6	Phe-9	Gly-13	Gly-16	Gly-20
171.3	178.0	178.6	179.5	177.9	178.4	175.1	175.4	174.6

[a] Typical uncertainties in peak shifts are ± 0.5 ppm as determined from the measurements on samples that contained peptide with the same labeled residue but different membranes.

The experimental dephasing, $(\Delta S/S_0)^{exp}$, corresponding to Figure 28 are summarized in Figure 29 and the experimental dephasing curves are displayed in Figure 30. Compared to the results of IFP pH 5.0 samples, a similar trend was observed that the residues at N- and C- terminal regions (Gly-1 and Gly-20) have larger ^{13}CO–^{31}P dephasing relative to the residues in the middle region and residue Ile-6 has ^{13}CO–^{19}F(C16) dephasing. These observations suggest a generally similar insertion of IFP in membranes at pH 7.4, i.e., the N- and C-terminal residues are in close contact to the phosphate headgroups and the middle region of IFP is inserted into the membrane bilayer. However, there is some difference between the results of IFP samples at different pHs. For

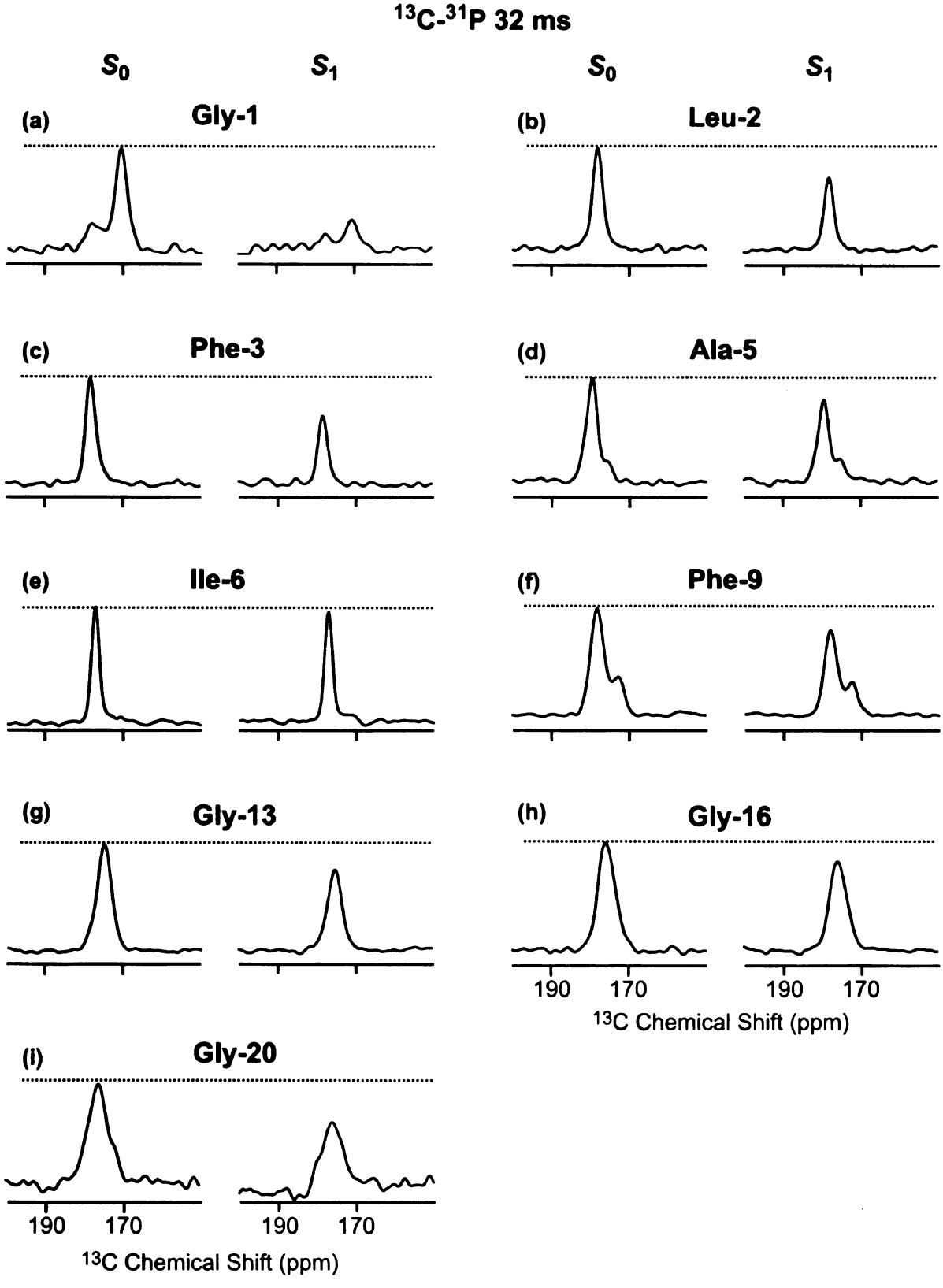

Figure 28 ^{13}C-^{31}P REDOR spectra with 32 ms dephasing time.

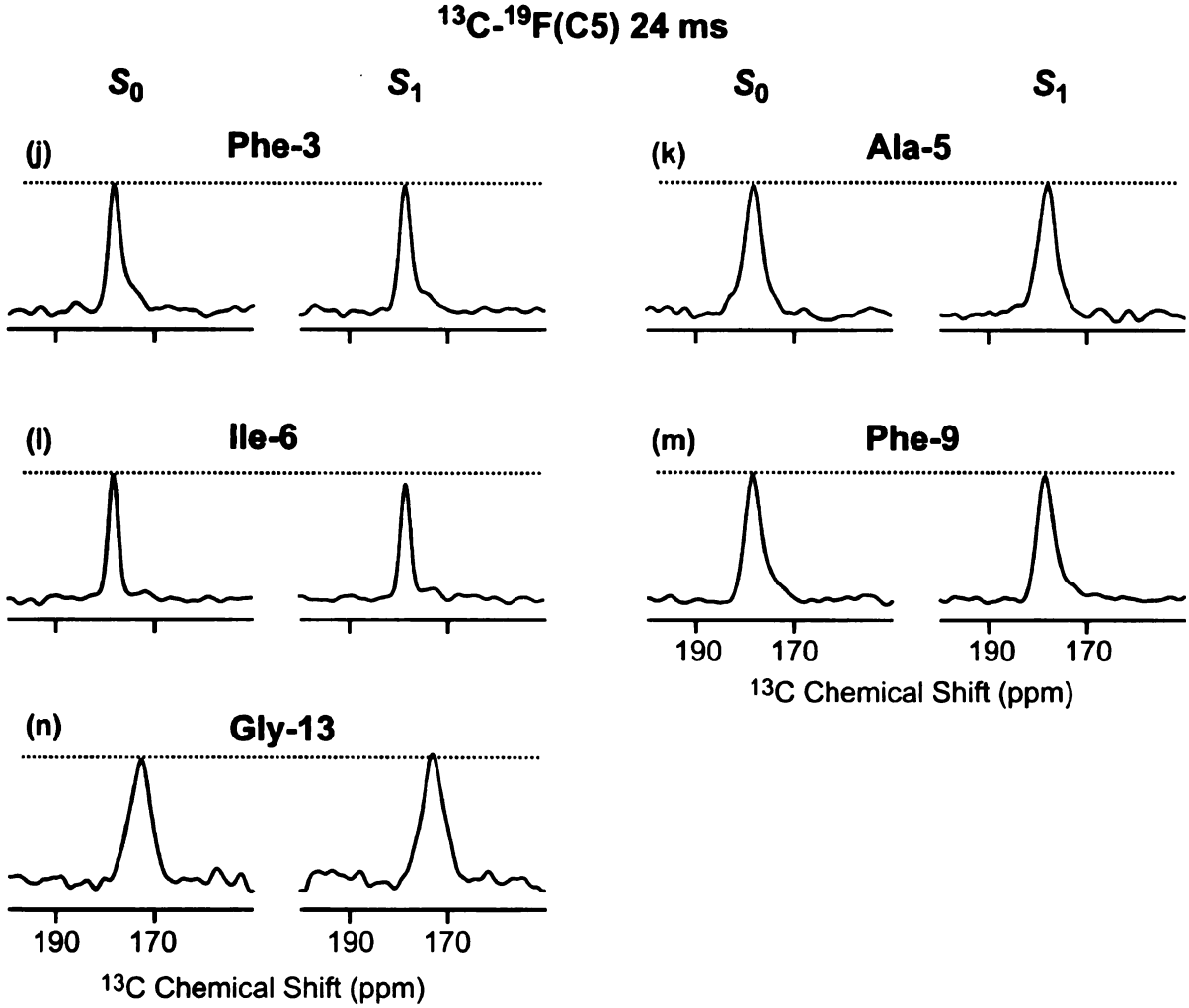

Figure 28 ^{13}C-^{19}F(C5) REDOR spectra with 24 ms dephasing time.

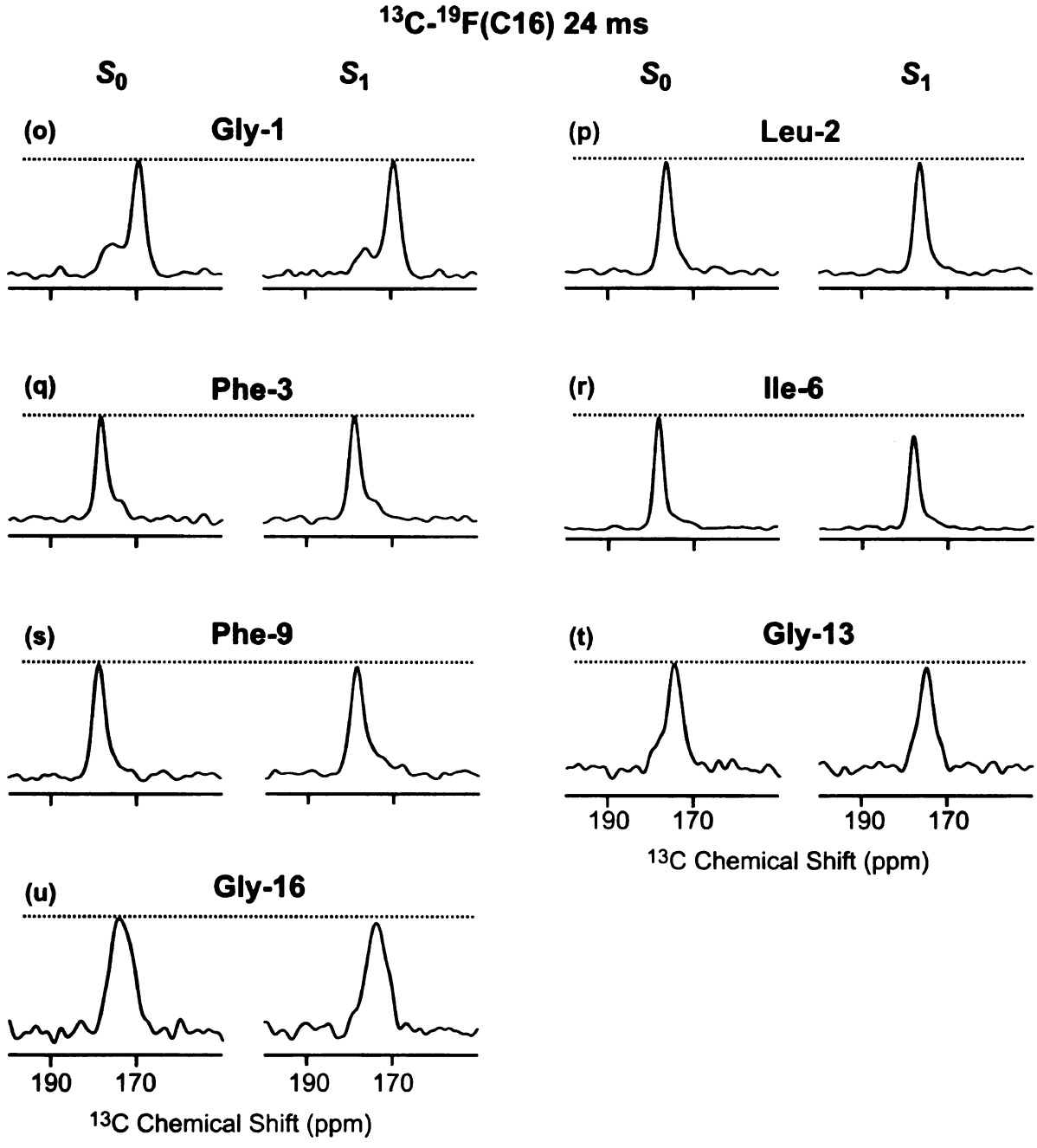

Figure 28. REDOR ^{13}C S_0 and S_1 NMR spectra at long dephasing time for membrane-associated IFP samples at pH 7.4. The experiment type and the dephasing time are labeled on the top of each group of spectra and the ^{13}CO labeled residues are also labeled above each set of S_0 and S_1 spectra. Each sample contained 16 µmol DTPC, 4 µmol DTPG and 0.8 µmol IFP. The samples used to take spectra (d), (e) and (j-n) contained 9 mol% 5-F-DPPC lipid and the samples used to take spectra (o-u) contained 9 mol% 16-F-DPPC lipid. Each spectrum was processed with 200 Hz Gaussian line broadening and was the sum of 20000 – 30000 scans.

samples at pH 7.4, the residues Leu-2 and Phe-3 have less ^{13}CO–^{31}P dephasing at each dephasing time and the residues Phe-3 and Phe-9 have little ^{13}CO–^{19}F(C16) dephasing (< 10 %) at τ = 24 ms compared to corresponding dephasing of the pH 5.0 samples. The latter observation may suggest either a shallower insertion of IFP or less population of inserted IFP for the pH 7.4 samples relative to the pH 5.0 samples. The justification of these statements is that the measured dephasing ($(\Delta S/S_0)^{exp}$) for a system with multiple ^{13}CO–X distances is the combination of the $\Delta S/S_0$ due to each ^{13}CO–X distance. If two different locations of IFP are present in a membrane-associated IFP system, with one location inserted into the membrane bilayer and the other one located at the water layer above the surface of the membrane bilayers (cf. Figure 32), the measured ^{13}CO–^{19}F(C16) $(\Delta S/S_0)^{exp}$ will be smaller relative to the ^{13}CO–^{19}F(C16) $(\Delta S/S_0)^{exp}$ for 100% inserted IFP.

Similar to the IFP pH 5.0 samples, the values of $(\Delta S/S_0)^{exp}$ for IFP pH 7.4 samples were also corrected and the values of $(\Delta S/S_0)^{cor}$ were fitted to the theoretical values, $(\Delta S/S_0)^{sim}$. The corrected data and the best-fit simulated build-up curves are shown in Figure 31 and the best-fit distances are listed in table 11. In the REDOR data fitting, a single membrane location of IFP was assumed and a ^{13}C-X two-spin system was used as for the IFP pH 5.0 samples. The Gly-1 ^{13}CO was determined to be 4.6 Å away from the phosphorus and the middle residues, Ala-5, Phe-9 and Gly-13 ^{13}COs have distances of ~10 Å from the ^{31}P, similar to the pH 5.0 samples. These distances and the flat ^{13}CO–^{31}P dephasing curve observed for Ile-6 of pH 7.4 samples are consistent with the results from

IFP pH 5.0 samples. For residues Leu-2, Phe-3 and Gly-20, the ^{13}CO–^{31}P distances for pH 7.4 samples are longer than the corresponding distances of the pH 5.0 samples. For 100% inserted IFP, the longer distances suggest a deeper insertion of IFP in the pH 7.4 samples and a generally shorter ^{13}CO–^{19}F(C16) distance or bigger ^{13}CO–^{19}F(C16) dephasing will be expected. However, for the pH 7.4 samples, only Ile-6 was detected to be in contact with ^{19}F(C16). A more reasonable explanation for the longer ^{13}CO–^{31}P distances of the pH 7.4 samples is therefore the existence of two different locations of IFPs in the membranes with one in the membrane bilayer and the other one in the water layer above the membrane surface. IFPs with the latter location may be loosely attached to the membrane surface and not close to the phosphorus, which will result in longer average ^{13}CO–^{31}P distances compared to the 100% inserted IFP. The models of these two IFP locations will be discussed and pictorialized in the discussion section.

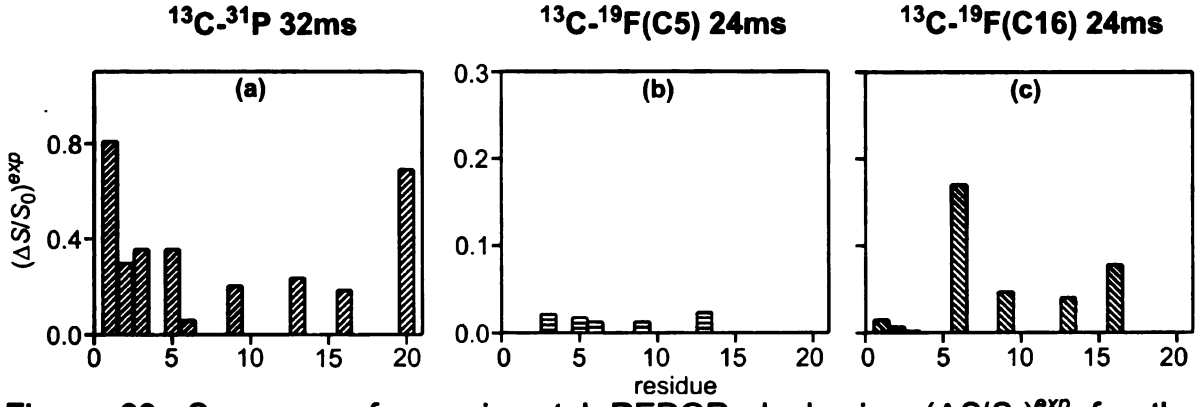

Figure 29. Summary of experimental REDOR dephasing $(\Delta S/S_0)^{exp}$ for the spectra displayed in Figure 28. The $(\Delta S/S_0)^{exp}$ values are shown as bars for different residues and a typical uncertainty is ±0.01-0.02.

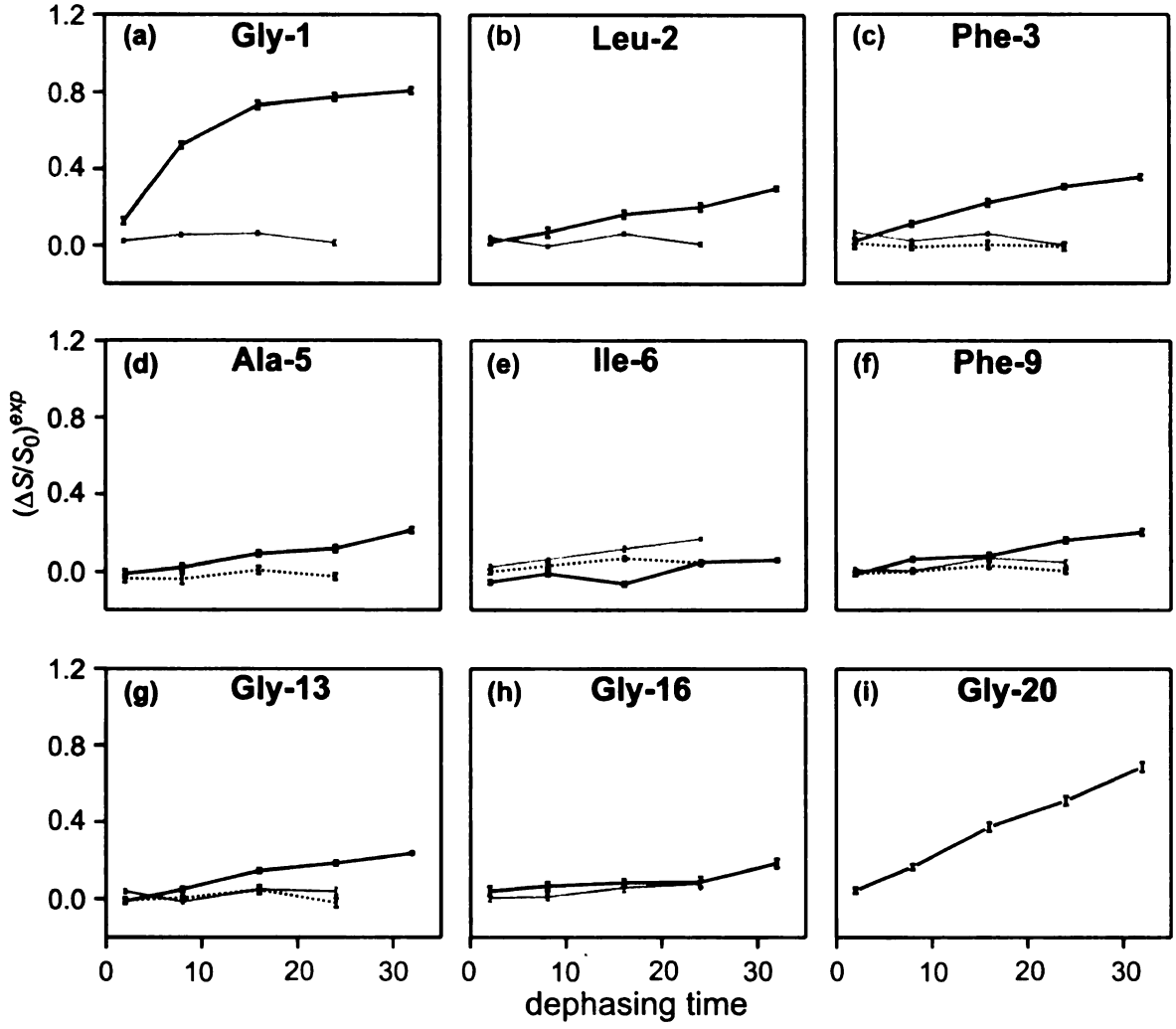

Figure 30. ^{13}CO–^{31}P REDOR (dark solid line), ^{13}CO–^{19}F(C5) REDOR (gray solid line) and ^{13}CO–^{19}F(C16) REDOR (dotted line) experimental dephasing curves for IFP samples at pH 7.4. The uncertainties are represented by the error bars and are typically ±0.01-0.02. The ^{13}CO labeled residues are labeled on top of each spectrum. The samples used were the same as the ones used to take the corresponding spectra in Figure 28.

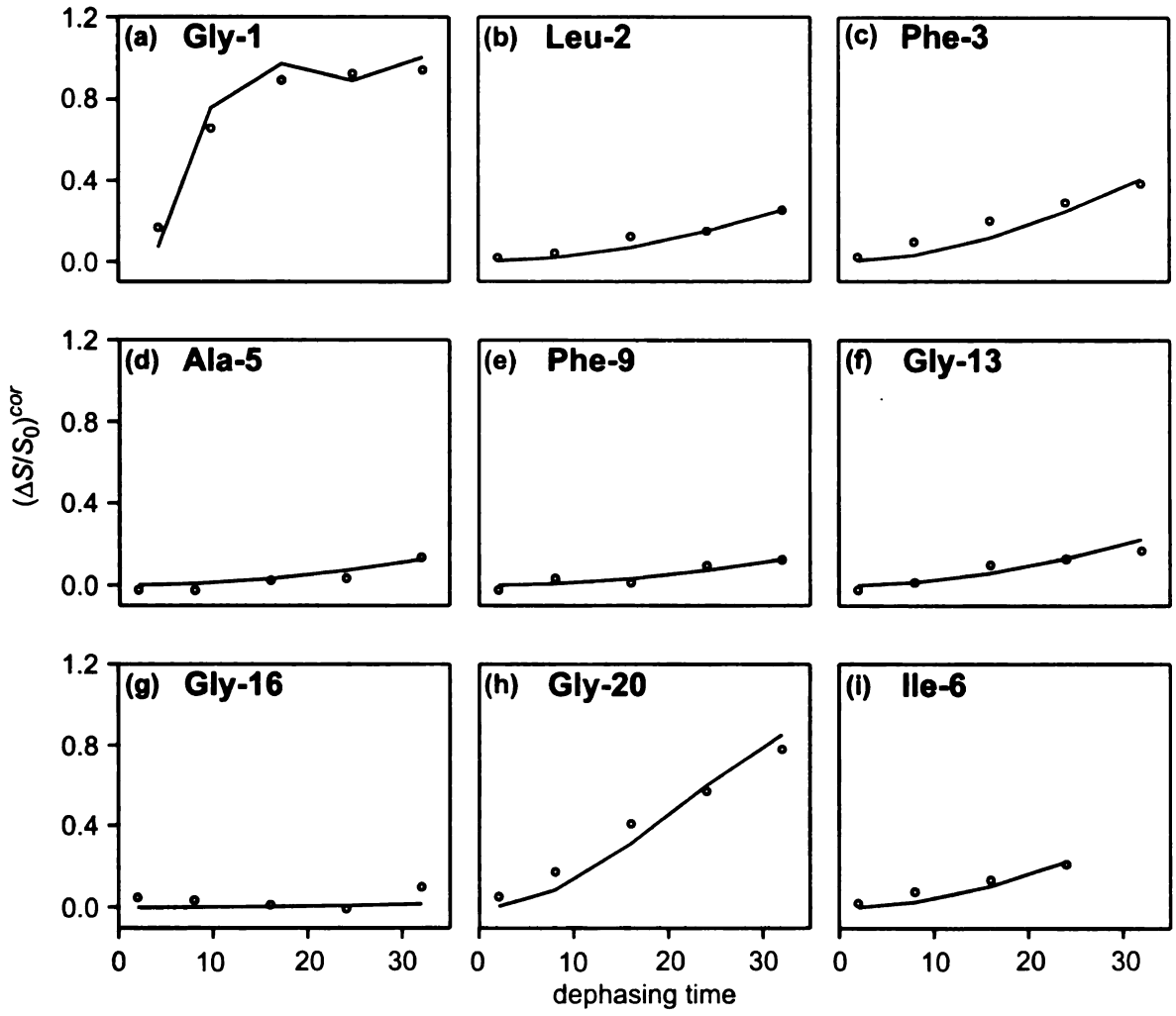

Figure 31. Plots of $(\Delta S/S_0)^{cor}$ (circles) and $(\Delta S/S_0)^{sim}$ (solid lines) vs. dephasing time for (a-h) ^{13}CO–^{31}P and (i) ^{13}CO–^{19}F(C16) REDOR of IFP samples at pH 7.4. The ^{13}CO labeled residues are labeled at the top of each spectrum.

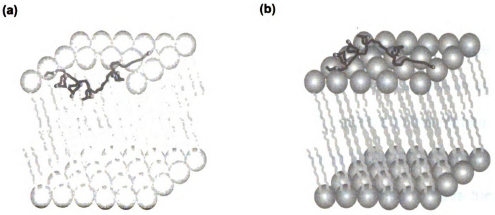

Figure 32. Insertion models for IFP in DTPC/DTPG membranes. The lipid head groups are shown in blue and the alkyl chains are shown in gray. The gray balls represent the labeled IFP backbone ^{13}CO. (a) IFP inserted into the membrane bilayer with the ^{13}CO labeled residues indicated by the corresponding residue number. (b) IFP located at the membrane surface and water layer interface. The ~10 Å water layer is above the membrane surface and is not shown in the model.

Table 11. ^{13}CO–^{31}P and ^{13}CO–^{19}F(C16) distances for IFP samples at pH 7.4 [a]

	Gly-1	Leu-2	Phe-3	Ala-5	Ile-6	Phe-9	Gly-13	Gly-16	Gly-20
^{13}CO–^{31}P distance (Å)	4.6(0.1)	9.1(0.2)	8.4(0.2)	10.4(0.7)	> 11 [b]	10.4(0.3)	9.3(0.5)	> 11	7.0(0.2)
χ^2	59	6	54	6	N/A [c]	12	4	18	44
^{13}CO–^{19}F(C16) distance (Å)	> 14 [b]	> 14	> 14	N/A	11.3(0.2)	> 14	> 14	> 14	N/A
χ^2	N/A	N/A	N/A	N/A	36	N/A	N/A	N/A	N/A

[a] Uncertainties are given in parentheses and were calculated from the values within the $\chi^2 = \chi^2_{min} + 5$ region.

[b] Calculated from the REDOR universal dephasing curve with $\Delta S/S_0 = 0.1$ at long dephasing time (τ = 32 ms for ^{13}CO–^{31}P or τ = 24 ms for ^{13}CO–^{19}F) based on the consideration that only the ^{13}COs with $(\Delta S/S_0)^{exp} > 0.1$ at long dephasing time are fittable.

[c] N/A ≡ not available.

4.3 DISCUSSION

The ^{13}CO–^{31}P and ^{13}CO–^{19}F(C16) distance measurements suggest that both the N- and C- terminal regions of IFP are close to the membrane phosphorus headgroups (^{13}CO–^{31}P distance ≤7 Å) relative to the middle region of IFP (^{13}CO–^{31}P distance > 10 Å) in a membrane with DTPC/DTPG composition. The structure of IFP in this kind of membrane was determined to have the helix-turn-helix motif in the chapter 3. These data can be combined to developt the insertion models of DTPC/DTPG membrane-associated IFP. The IFP can either adopt an inverted boomerang structure inserted into the membrane bilayer as shown in Figure 32a or a boomerang structure located at the membrane surface/water interface as shown in Figure 32b. In these insertion models, the N-terminal region of IFP has α helix structure and a turn is formed around residue Asn-12 followed by a short helix over residues 13-18 followed by some extended structure. These structural characteristics were determined before and discussed in chapter 3 and were retained at both pH 5.0 and pH 7.4. For the IFP samples at pH 5.0, ^{13}CO–^{19}F(C16) dephasing was detected for residues Phe-3, Ile-6 and Phe-9 and data fitting indicated ~ 12 Å ^{13}CO–^{19}F(C16) distances for these residues. IFP is more likely inserted into the membrane bilayer with the inverted boomerang structure at pH 5.0. In this inserted model, Phe-3, Ile-6 and Phe-9 are located at the bottom of the helix and close to the membrane bilayer center and Ile-6 may have the deepest insertion compared to the other labeled residues because no ^{13}CO–^{31}P contact was detected for Ile-6. For the IFP pH 7.4 samples, ^{13}CO–^{19}F(C16) dephasing was detected for only one residue, Ile-6, and

the data fitting also suggested ~12 Å ^{13}CO–^{19}F(C16) distance for Ile-6. It is very likely that there is at least some population of IFP that has the inverted boomerang structure. However, little ^{13}CO–^{19}F(C16) dephasing was observed for residues Phe-3 and Phe-9 for the pH 7.4 samples. The magnitude of ^{13}CO–^{31}P dephasing at 32 ms is also less for some residues (Leu-2, Phe-3, Gly-16 and Gly-20) of the pH 7.4 samples and the data fitting indicated longer ^{13}CO–^{31}P distances compared to the corresponding pH 5.0 samples. A reasonable model for these data is that IFP may have two different locations in the membrane at pH 7.4. As shown in Figure 32a and 32b, IFP may adopt both insertion models in the membrane at pH 7.4. In the latter model, only Gly-1 and Gly-20 are close to the phosphate headgroups and even Gly-20 is a little bit further away from the membrane surface compared to the Gly-20 in pH 5.0 samples. This suggests that IFP is more loosely associated to the membranes at pH 7.4 relative to pH 5.0 samples. Previous studies showed that a ~10 Å water layer is associated with the membrane surface.[12] The other residues including Leu-2 and Phe-3 may be located at this water layer above the membrane surface for IFP samples at pH 7.4. This explains the observed smaller ^{13}CO–^{31}P dephasing and longer ^{13}CO–^{31}P distances for these residues. The less inserted IFP at pH 7.4 may correlate to its lower fusogenic activity at pH 7.4 and is probably associated with the multiple acidic residues in the IFP sequence (Glu-11, Glu-15 and Asp-19), which will be more negatively charged at pH 7.4 and repelled from the negatively charged membrane.

Membrane lipids are very mobile and flexible. For the inserted IFP model, IFP may disrupt the membrane bilayer and push the lipid molecules aside and lipids are not aligned as in a non-disrupted bilayer. In such a system, the measured ^{13}CO–^{31}P and ^{13}CO–^{19}F(C16) distances will not reflect the real distances of labeled ^{13}CO to the membrane surface or the membrane center but rather the distances between the labeled ^{13}CO and nearby ^{31}P or ^{19}F(C16) nuclei. Even for residues that are close to the membrane surface, the detected ^{13}CO–^{31}P REDOR dephasing may be smaller than expected since the lipids are pushed away from the whole IFP. This may explain that the residues Gly-13 and Gly-16 have small magnitude of ^{13}CO–^{31}P dephasing and little ^{13}CO–^{19}F(C16) dephasing. The plasticity of the membrane bilayer may also explain the observation in the Chapter 3 of Glu-11 being in contact with water. There are two additional charged residues at the C-terminus of IFP, Glu-15 and Asp-19, which also have preference to stay in the water layer. Therefore, the membrane may be disrupted by IFP in a way that the whole C-terminal arm is exposed to water while the N-terminal helix remains in the membrane interior. In this case, the lipids around the C-terminus will be highly disordered and water molecules will leak into the membrane and have contact with the IFP C-terminus.

The V-shaped IFP insertion model combined with the IFP backbone structure A and B determined in Chapter 3 (cf. Figure 19) can be correlated to the IFP fusion activity at pH 5.0 and pH 7.4. With the B structure in the membrane bilayer, the hydrophobic residues at the IFP N-terminal helix face the membrane interior and have more favorable interaction with membrane bilayers

compared to the membrane-associated A structure in which the N-terminal helical hydrophobic residues face to the membrane bilayer surface. Since the B structure was only observed at low pHs (pH 4.0 and pH 5.0) and not observed at pH 7.4, the better interaction between the B structure and the membrane bilayer relative to the A structure explains the higher fusion activity of IFP at pH 5.0 compared to pH 7.4.

Our insertion model of IFP generally supports some of the previous experimental results studies by ESR[1, 4] and some theoretical work[10] that the influenza fusion peptide is inserted into the hydrophobic region of membrane bilayers. In the ESR studies of "FHA2" done by Macosko, et al., residues from Ala-5 to Gly-8 and from Asn-12 to Trp-14 were studied and the residue with the deepest insertion in their data fitting was Ile-6. In our study, the residue Ile-6 also seems to insert deeper than other ^{13}CO labeled residues. However our results do not agree with the straight helix structure proposed in this study and also do not agree with the inserted boomerang structure suggested by Han, et al. using ESR studies. An inverted boomerang structure of IFP inserted into the membrane bilayer is more consistent with our data. For samples with different pHs, our results do not support a significant positional change of IFP in the membrane. In my opinion, the membrane-associated IFP system is more complicated than a single structure or a single IFP membrane location. We propose here that IFP may have two different locations in the membrane bilayer with one having the inverted boomerang structure inserted into the membrane and one in the water layer above the membrane surface. We can not determine whether the IFP pH

5.0 samples have some IFP population with the latter location. However, it seems like the IFP samples at pH 7.4 have a larger population of IFP with the latter membrane location.

The HIV fusion peptide (HFP) was also studied using the solid-state NMR methods in our group. It will be interesting to compare the insertion model of IFP with that of HFP because both of them have similar biological function and both HIV and influenza viruses belong to type-I enveloped viruses which share a similar fusion mechanism[13]. The structure of HFP in DTPC/DTPG membranes is only partially helical with a significant population of β strand conformation. This complicated the structural analysis of HFP and the helical part of HFP was not as well determined as IFP. The ^{13}CO chemical shifts studies showed that HFP has helical structure from residue Ile-4 through residue Ala-14. The ^{13}CO–^{31}P and ^{13}CO–^{19}F(C16) REDOR measurements showed that the helical part of HFP is also inserted into a single membrane leaflet. The overall HFP has very similar structure and location[14] as IFP with the N- and C- terminal regions in close contact to the phosphate headgroups and the middle region inserted into the membrane hydrophobic region with contact with ^{19}F(C16).

4.4 REFERENCES

1. Han, X.; Bushweller, J. H.; Cafiso, D. S.; Tamm, L. K., Membrane structure and fusion-triggering conformational change of the fusion domain from influenza hemagglutinin. *Nat. Struct. Biol.* **2001,** 8, (8), 715-720.

2. Clague, M. J.; Knutson, J. R.; Blumenthal, R.; Herrmann, A., Interaction of influenza hemagglutinin amino-terminal peptide with phospholipid vesicles: a fluorescence study. *Biochemistry* **1991,** 30, (22), 5491–5497.

3. Luneberg, J.; Martin, I.; Nussler, F.; Ruysschaert, J. M.; Herrmann, A., Structure and Topology of the Influenza-Virus Fusion Peptide in Lipid Bilayers. *J. Biol. Chem.* **1995,** 270, (46), 27606-27614.

4. Macosko, J. C.; Kim, C. H.; Shin, Y. K., The membrane topology of the fusion peptide region of influenza hemagglutinin determined by spin-labeling EPR. *J. Mol. Biol.* **1997,** 267, (5), 1139-1148.

5. Hsu, C. H.; Wu, S. H.; Chang, D. K.; Chen, C. P., Structural characterizations of fusion peptide analogs of influenza virus hemagglutinin - Implication of the necessity of a helix-hinge-helix motif in fusion activity. *J. Biol. Chem.* **2002,** 277, (25), 22725-22733.

6. Efremov, R. G.; Nolde, D. E.; Volynsky, P. E.; Chernyavsky, A. A.; Dubovskii, P. V.; Arseniev, A. S., Factors important for fusogenic activity of peptides: molecular modeling study of analogs of fusion peptide of influenza virus hemagglutinin. *FEBS Lett.* **1999,** 462, 205-210.

7. Bechor, D.; Ben-Tal, N., Implicit solvent model studies of the interactions of the influenza hemagglutinin fusion peptide with lipid bilayers. *Biophys. J.* **2001,** 80, (2), 643-655.

8. Huang, Q.; Chen, C. L.; Herrmann, A., Bilayer Conformation of Fusion Peptide of Influenza Virus Hemagglutinin:A Molecular Dynamics Simulation Study. *Biophys. J.* **2004,** 87, (1), 14-22.

9. Sammalkorpi, M.; Lazaridis, T., Configuration of influenza hemagglutinin fusion peptide monomers and oligomers in membranes. *BBA-Biomembranes* **2007,** 1768, (1), 30-38.

10. Lague, P.; Roux, B.; Pastor, R. W., Molecular dynamics simulations of the influenza hemagglutinin fusion peptide in micelles and bilayers: Conformational analysis of peptide and lipids. *J. Mol. Biol.* **2005,** 354, (5), 1129-1141.

11. Tilcock, C. P. S.; Cullis, P. R.; Gruner, S., On the validity of 31 P-NMR determinations of phospholipid polymorphic phase behavior. *Chem. Phys. Lipids* **1986,** 40, 47-56.

12. Venable, R. M.; Brooks, B. R.; Pastor, R. W., Molecular dynamics simulations of gel (LI) phase lipid bilayers in constant pressure and constant surface area ensembles. *J. Chem. Phys.* **2000,** 112, (10), 4822-4832.

13. Jardetzky, T. S.; Lamb, R. A., Virology: A class act. *Nature* **2004,** 427, 307-308.

14. Qiang, W., Solid-state nuclear magnetic resonance studies of the structures and membrane insertion of HIV fusion peptide. *Ph.D. thesis*, **2009**.

Chapter 5 Solid-State NMR Studies of the IFP N-terminal Helix in Oriented Lipid Bilayers

5.1 BACKGROUND

The relative orientations of membrane proteins and peptides with respect to the membrane surface or membrane normal are generally interesting topics for research and can be correlated to their biological functions. As an example, there has been a lot of effort to correlate the IFP helix insertion angle to its fusogenicity and it has been proposed that an oblique insertion of the IFP helix in the membrane plays an essential role in the fusion event.[1] Some groups also suggested that the IFP helix has different orientation in membranes at different pHs which is associated with its pH-dependent fusogenicity.[2, 3] However, results from different groups have not reached a consensus. There are two major techniques that have been used to study the tilted angle of IFP helix in the membranes, ATR-FTIR and ESR spectroscopies. Two groups utilized the former technique and proppsed that IFP and its fusion-active analogues had orientations independent of pH but with different insertion angles relative to the bilayer normal, ~45° from one group[1] and ~65° from the other group[4]. In another study using the same technique and a peptide designed to resemble IFP, the peptide is helix with an almost parallel-to-surface orientation at fusogenic pH 5.0 and either a random or 55° insertion angle relative to the membrane normal at non-fusogenic pH 7.4.[2] Two different groups also carried out ESR studies to develop a structural model for the observation that IFP is much more fusogenic at acidic pH than at neutral pH. One group used a major portion of HA2 domain (FHA2, residue 1-127) and

found the fusion peptide portion was α helix tilted 62° from the membrane normal at pH 5 and 65° at pH 7.[5] The other group used just the fusion peptide region linked to a short hydrophilic peptide (GCGKKKK) and observed a 52° tilted angle of the N-terminal IFP helix with respect to the membrane normal at pH 5.0 and a 67° tilted angle at pH 7.4.[3] There have also been efforts from molecular dynamics studies to shed light on the membrane insertion of IFP. There are two studies which supported that the IFP helix is parallel to or slightly tilted from the membrane surface.[6, 7] Other studies showed that the IFP helix is obliquely inserted into the membranes and has a tilt angle either ~65° or ~30° with respect to the membrane normal.[8-10] In addition, the G1V mutant of IFP is fusion-inactive and an IR study from one group supported a membrane surface orientation for the peptide while a study from another group supported a transmembrane orientation.[11, 12]

In this chapter, we investigate the IFP orientational distributions in membrane samples at different pHs using solid-state NMR. As in the conformational studies, measurements at different pHs enable the correlation of IFP insertion angles to its functionality. Experiments were also conducted on membrane samples containing HFP or IFP mutants, IFP-G1V and IFP-G1S, in order to compare the insertion angle of IFP with other fusion peptides. The N-terminus of IFP is highly conserved and particular critical for HA function. The functional activity of Ser HA (point mutation of HA Gly-1 to Ser) was tested with red blood cells and the mutant was found to possess only hemifusion activity, i.e., only the outer leaflets of membranes are fused together with no contents mixing.

In the same study, Val HA (point mutation of HA Gly-1 to Val) was discovered to have no fusion activity.[13] IFP with the mutation of Gly-1 to Val was also probed for is ability to induce liposome fusion and this mutant was found to lack the ability to induce membrane vesicle lipid mixing.[12] It will be interesting to compare the orientations relative to the membrane normal of these mutants to the wild-type IFP because different orientations of these peptides were proposed to be associated with their different fusion activities. Studies from FTIR showed that wild-type IFP has an oblique orientation while the GIV mutant has a transmembrane insertion.[12] ESR studies on IFP GIV mutant indicated an insertion angle of ~66° with respect to the membrane normal.[11] In addition to these IFP mutants, the insertion angle of HFP relative to the membrane normal was also compared to that of IFP. HFP shares common features with IFP of being the N-terminus of the enveloped protein and glycine-rich. Comparison between different native fusion peptides is potentially useful in generating a common structure/function model.

In our study, aligned membranes were obtained by placing bicelles in the magnetic field. Bicelles are generally composed of lipid and detergent molecules in a certain ratio (roughly 2/1 – 5/1), which form rather uniform sized units.[14, 15] The long chain phospholipids such as DTPC form planar bilayers and addition of detergent or short chain lipids such as DHPC can break up the bilayers into small disks and form the disc-shaped phospholipid bilayers (cf. Figure 6).[16] These disc-shaped bicelles can be automatically aligned in the magnetic field. Depending on the lipid/detergent ratio, bicelles are normally 250 – 400 Å in diameter and ~50 Å

in thickness.[17, 18] Compared to lipid vesicles which are solely composed of lipids or to micelles which are solely composed of detergents, bicelles are small enough to be dissolved in the aqueous solution but big enough to not have fast isotropic motions which are not favored by solid-state NMR measurement. Bicelles have many advantages over the classical glass-sandwiched lipid bilayers in which uniaxial orientation of membrane bilayers is achieved by sandwiching phospholipid bilayers between stacked glass plates. Bicelles are easier to prepare, adequately hydrated and easier to adjust pH. In addition, glass plates waste a lot of space in the coil by filling the coil with glass rather by sample, which leads to significantly lower sensitivity.

For peptides embedded in uniaxially oriented bicelles, NMR constraints can be obtained to determine the orientations of the peptides relative to the magnetic field and bicelles. The NMR constrains include anisotropic chemical shifts, dipolar couplings and quadrupolar couplings. These values vary as a function of the orientation of the molecule with respect to the external magnetic field and follow the relation, $\omega(\phi) \propto \frac{1}{2}(3\cos^2\phi - 1)$, where $\omega(\phi)$ is the resonance frequency or internuclear coupling, ϕ is the angle between the concerned tensor (e.g. chemical shift tensor or dipolar coupling tensor) and the external magnetic field. For a liquid sample, isotropic molecular motions average the anisotropic interactions and therefore isotropic sharp peaks can be obtained; while for unaligned solid samples, the NMR spectra are distributions of the resonances due to all alignments and are called powder patterns. These powder patterns reflect all the possible molecular orientations existed in a sample (cf. Figure 33).

However, for a single molecular orientation, a single peak will be observed and the measured value (e.g. chemical shift or dipolar coupling) that corresponds to this peak will change as the alignment is changed. Thus anisotropic NMR constraints can provide valuable information on the orientation of the molecule with respect to the magnetic field. The linewidth of the peak reflects the orientational distribution of a sample.

In this chapter, data on chemical shift, dipolar coupling and quadrupolar coupling measurements of bicelle samples are presented. The quadrupolar coupling of ^{2}H and ^{31}P chemical shift were used to determine the alignment of the bicelles. The ^{15}N chemical shift and ^{15}N–^{1}H dipolar coupling were used to determine the orientation of fusion peptides relative to the bicelle normal.

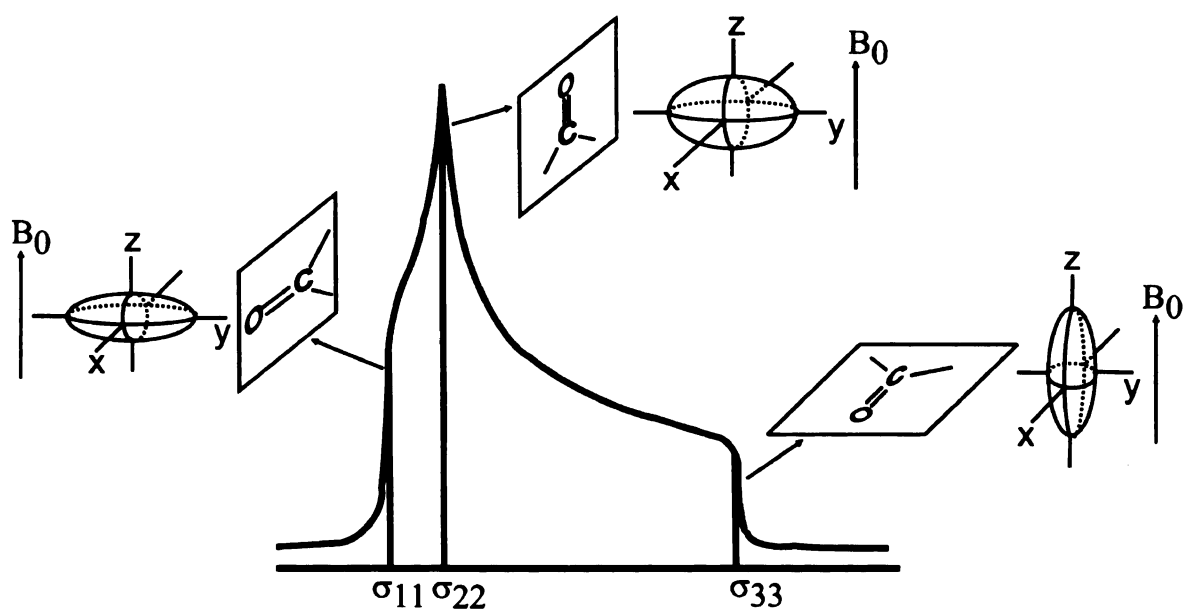

Figure 33. A sample powder spectrum of ^{13}CO with the principal values labeled and the corresponding CO bond orientation. Chemical shift anisotropy arises from the non-spherical distribution of electron density around a nucleus. The degree of shielding or the effect of electron density on chemical shifts depends on the orientation of the electronic cloud. The electron cloud is shown by the ellipsoids and the relative orientation of the ellipsoid is shown for each principal value.

Figure 34. (a) structure of $DMPC_{d54}$. (b–g and k) are ^{2}H spectra obtained with the quadrupolar- echo pulse sequence at 40 °C and processed with (b–g) 25 Hz or (k) 100 Hz Gaussian line broadening. (h–j) are ^{31}P spectra obtained with the 1pda pulse sequence at (h, i) 40 °C or (j) 35 °C and processed with (h, i) 0 Hz or (k) 100 Hz Gaussian line broadening. The peaks in the ^{2}H spectra represent the signals of 2 mol% of $DMPC_{d54}$. The peaks in the ^{31}P spectra represent the ^{31}P signals of the lipid phosphorus headgroups. Compared to the (k) ^{2}H or (j) ^{31}P powder spectra, the spectra in (b–i) have sharp peaks and show the good alignment of pure bicelles (b, c) or bicelles with incorporated IFP (d-i). Spectra (b, d, f, h) are for the unflipped bicelle samples which have their normals perpendicular to the magnetic field. Spectra(c, e, g, i) are for the flipped bicelle samples which have their normals parallel to the magnetic field. The sample composition used to obtain each spectrum was: (b, c) DTPC/$DMPC_{d54}$/DHPC (53:1:17 μmol); (d–i) 0.7 μmol IFP and DTPC/$DMPC_{d54}$/DHPC (53:1:17 μmol); (j) 0.8 μmol IFP and DTPC/DTPG (16:4 μmol); (k) 1.1 μmol IFP and DTPC/$DMPC_{d54}$ (53:1 μmol). The total number of scans was: (b–e, k) ~8000; (f, g, j) ~2000; (h) 3; (i) ~100.

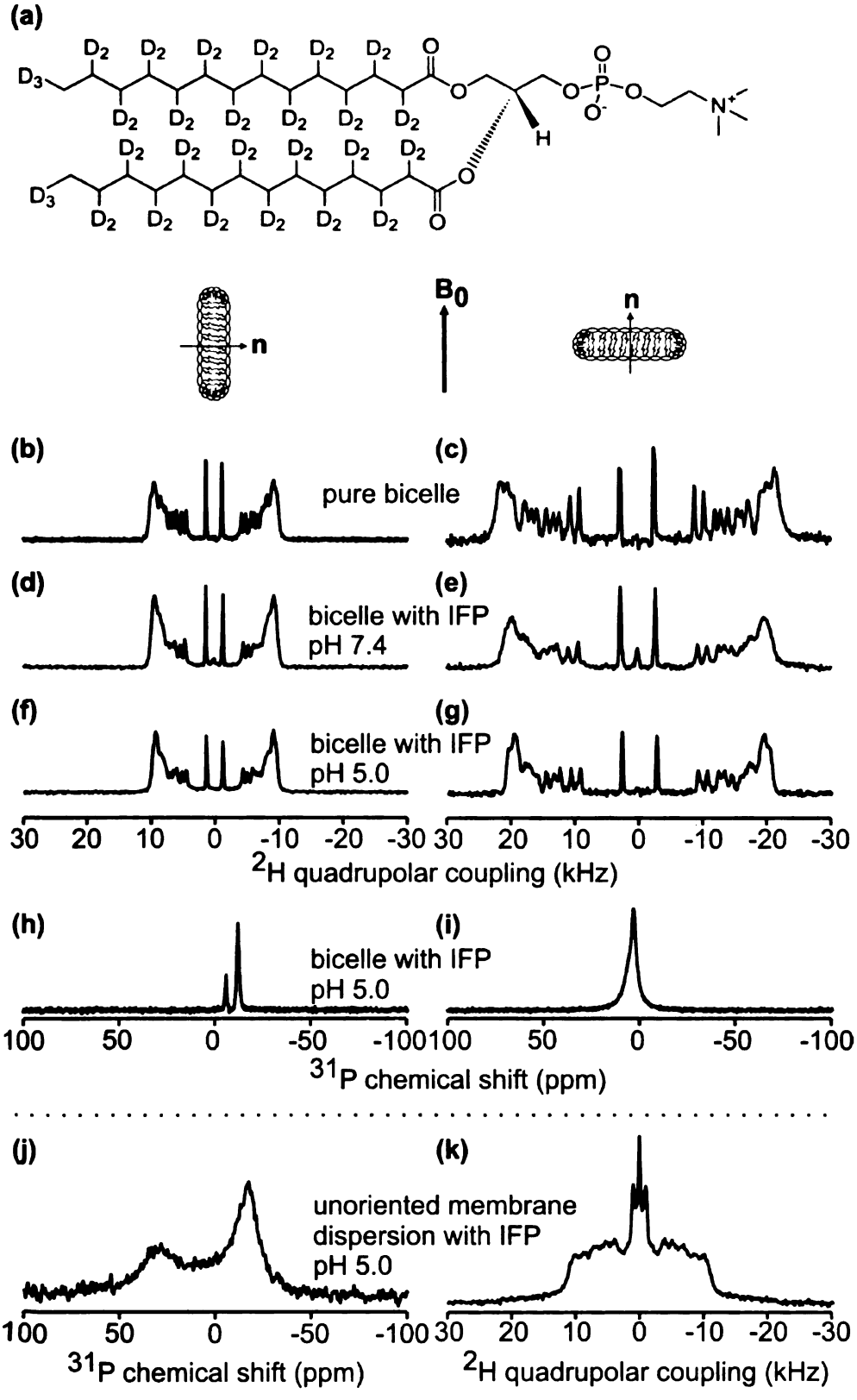
(a)
n
B0
n
(b)
pure bicelle
(c)
(d)
bicelle with IFP
pH 7.4
(e)
(f)
bicelle with IFP
pH 5.0
(g)
30 20 10 0 -10 -20 -30
2H quadrupolar coupling (kHz)
(h)
bicelle with IFP
pH 5.0
(i)
100 50 0 -50 -100
31P chemical shift (ppm)
(j)
unoriented membrane
dispersion with IFP
pH 5.0
(k)
100 50 0 -50 -100
31P chemical shift (ppm)
30 20 10 0 -10 -20 -30
2H quadrupolar coupling (kHz)

5.2 RESULTS

1. Bicelle alignment

It is important that bicelles are intact in the presence of fusion peptides in order to use bicelles as the model system to investigate the peptide orientation in membranes. Potential perturbations to bicelles include the alteration of bicelle diamagnetic susceptibility, distortion of the disc shape of bicelles and disc aggregation or fusion, all of which are likely associated with the loss of alignment of bicelles in the magnetic field and can be manifested by NMR because loss of alignment leads to broadening in the NMR spectrum. The alignments of bicelles were demonstrated with ^{2}H NMR spectra of bicelles containing 2 mol% perdeuterated DMPC and with or without 2 mol% IFP (cf. Figure 34). The difference between the samples in Figure 34b and 34c was the respective absence or presence of 3 mM Yb^{3+} ions. As shown in Figure 34b, each site in the perdeuterated chain (cf. Figure 34a) gives rise to a doublet which is symmetric with respect to 0 kHz. The broad doublet with the largest splitting results from the relatively immobile methylene deuterons near the ester linkage. The doublets with smaller splittings result from the deuterons near the terminal portion of the acyl chain which have bigger mobility. The very mobile terminal methyl groups give rise to the most intense doublets with the smallest quadrupolar coupling. Each of the splittings double when the orientation of the bicelle is flipped by adding paramagnetic lanthanide as shown in Figure 34c. The good resolution of peaks for each ^{2}H labeled site is consistent with good alignment of the bicelles. For an unoriented membrane dispersion, a powder pattern will be obtained in

which no individual peak for an individual ^2H labeled site can be seen (cf. Figure 34k). The doubling in the quadrupolar splitting of flipped bicelles is consistent with the change of bicelle orientation where bicelle normal changes from being perpendicular to parallel to the magnetic field and is the result of a change in order parameter from $S_{zz} = -1/2$ to $S_{zz} = 1$. The order parameter is defined as $S_{ZZ} = \frac{1}{2}(3\cos^2\lambda - 1)$, where λ is the angle between bicelle normal and the external magnetic field.[19] The spectra in Figure 34b and 34c were taken for bicelle samples without fusion peptide and resemble the literature ^2H spectra of bicelles which have corresponding alignment in the magnetic field.[19] The spectra for bicelle samples containing fusion peptide at non-fusogenic pH (cf. Figure 34d and 34e) were very similar to the ones for samples lacking fusion peptide and indicated the good alignment of fusion peptide-incorporated bicelles. This alignment was independent of pH as shown in Figure 34f and 34g. Therefore the bicelle morphology was not altered by having fusion peptide included even at fusogenic pH.

The alignment of bicelles can also be detected by using ^{31}P spectroscopy. There is abundant ^{31}P present in the lipid phosphate headgroups. Figure 34h and 34i show the ^{31}P spectra of aligned bicelle samples containing IFP. The good alignment of the bicelles was evidenced by the upfield or downfield dependence of the peak shifts on respective perpendicular or parallel orientations of the bicelles relative to the magnetic field direction. The spectrum of the unflipped bicelle sample (cf. Figure 34h) resembles the ^{31}P spectrum in the literature of a sample with similar bicelle composition and the downfield peak in the spectrum

was shown to correspond to the ^{31}Ps of DHPC headgroups in the bicelles[17]. Compared to the linewidths of this spectrum, the linewidth for the flipped bicelle sample is broad (cf. Figure 34i) because the added Yb^{3+} is likely associated with the phosphorus headgroups and the paramagnetic ions broaden the peak as traditional broadening reagents. The alignment was stable for the entire measurement time in the NMR spectrometer demonstrated by the ^{2}H or ^{31}P spectra after other NMR acquisitions. In addition, the samples could be stored in a –20 °C freezer, melted, and then re-aligned in the NMR spectrometer.

2. 1D experiments

There has been disagreement in the literature about whether or not there is significant pH dependence to the orientation of the N-terminal IFP helix (Leu-2 to Ile-10) relative to the membrane bilayer normal.[3, 5] This disagreement is of some relevance because a significant change in orientation plays an important role in one of the structure-function models for the pH-dependence of IFP-induced fusion. This section describes the study of IFP orientation using anisotropic ^{15}N chemical shifts.

There appeared to be good alignment of the first ten residues of IFP relative to the bicelle normal as evidenced by much narrower linewidths in bicelle samples containing IFP-U_N, cf. Figure 35e, relative to membrane dispersion samples containing IFP-U_N, cf. Figure 35 a-b. Additional evidence for alignment is the large difference in peak ^{15}N chemical shift of IFP-U_N in unflipped and flipped bicelles, i.e. ~110 and ~150 ppm, respectively. Because the resonance of

each individual ^{15}N site was not well resolved in these spectra, samples containing singly labeled IFP were also studied. Spectra for these IFP samples are shown in Figure 35 f-m. Each ^{15}N spectrum of unflipped bicelles containing singly labeled IFP is composed of a single narrow peak with ~5 ppm full-width at half-maximum linewidth (except for IFP-$A5_N$). Observation of narrow ^{15}N peaks in unflipped bicelles is consistent with the expected fast rotation of the bicelle about its normal axis. The peak ^{15}N chemical shifts in flipped bicelles containing IFPs with single Ala, Phe or Ile ^{15}N labels are very different than the shifts in the respective unflipped bicelles, cf. Table 12. This difference is consistent with the observations in the IFP-U_N samples. For IFPs with a single Gly ^{15}N label, the peak ^{15}N shift has $\leq$14 ppm change for unflipped and flipped bicelle samples, less than the change for other labeled residues which have ~ 30-40 ppm changes in peak ^{15}N shifts. The small ^{15}N chemical shift anisotropy (difference in peak ^{15}N chemical shifts between flipped and unflipped bicelle samples) of Glys relative to other residues was also observed by another group[20] and could result from near isotropic motions of Glys and/or very distinct chemical shift anisotropy (CSA) principal values compared to other residues[21, 22] which will be described later in this chapter. For each flipped bicelle sample, the linewidth (~10 ppm) is larger than in the respective unflipped sample. This difference can be partly explained by the contribution to the linewidth from the mosaic spread of alignment which reflects the errors in alignment and can be interpreted as the variation or probability distribution of the bicelle normal directions in the magnetic field[23]. The mosaic spread in alignment is two times larger for flipped bicelles

which is consistent with the order parameter change from $S_{zz} = -1/2$ to $S_{zz} = 1$, cf. Figure 34b and 34c. Another possible contribution to the linewidth of a flipped bicelle sample is an increased transverse relaxation rate due to the paramagnetic Yb^{3+} ions.

The peak ^{15}N chemical shifts of all the singly labeled IFP samples are listed in Table 12. For most samples containing either unflipped or flipped bicelles, the differences between ^{15}N shifts at pH 5.0 and pH 7.4 are ≤ 3 or ≤ 6 ppm, respectively. These small differences are consistent with only minor pH dependence of IFP N-terminal helix orientation relative to the bicelle normal. This conclusion is further supported by very similar IFP-U_N spectra at the two pHs, cf. Figure 35 e, g and Figure 35 f, h.

A more detailed analysis of IFP orientation based on chemical shifts can provide quantitative information on the IFP N-terminal helix axis orientation with respect to the bicelle normal. The measured chemical shift anisotropies of a molecule can be greatly affected by the molecular motions and quantitative analysis of the IFP N-terminal helix orientation from the ^{15}N chemical shift data must take into account all the motions of IFP. Possible motions considered in the present work include rotations around fixed axes, e.g. helix axis or membrane bilayer normal. Such motions, especially for the rotation around membrane bilayer normal, can be partly assessed by comparing spectra of IFP-U_N in hydrated membrane dispersions to the spectrum of lyophilized IFP-U_N which serves as a standard powder pattern of IFP. The theoretical scaled chemical shift anisotropy ($\Delta\sigma$) of a powder spectrum due to the rotational motions can be

calculated using Eq. 2.20 and then compared to the experimental $\Delta\sigma$ to get an idea on the reasonable Euler angle values (cf. α and β in Figure 12). The spectra in dispersions at pH 5.0 or 7.4 are very similar to the spectrum of lyophilized material (cf. Figure 35 a-c). The ^{15}N chemical shift anisotropy principal values used in data analysis were determined from magic angle spinning spectra of lyophilized IFP-U_N, cf. Figure 35d, and were: σ_{11}, 65±2 ppm; σ_{22}, 78±2 ppm; and σ_{33}, 225±2 ppm resulting in chemical shift anisotropy ($\Delta\sigma$) of 154 ppm using

$$\Delta\sigma = \sigma_{33} - \frac{\sigma_{22} + \sigma_{11}}{2} \tag{5.1}$$

The theoretical scaled $\Delta\sigma$ was calculated for each set of α and β values which vary from 1° to 360° with an interval of 1° and compared to the measured $\Delta\sigma$. The variation in α values has little effect on $\Delta\sigma$, however, variation in β causes some change in the value of $\Delta\sigma$, e.g. a change of β from 0° to 10° results in the change of $\Delta\sigma$ from 154 ppm to 146 ppm. The similarity of the powder spectra between membrane-associated IFP and lyophilized IFP indicated β, the angle between the principal axis σ_{33} and rotational axis is small. Therefore the principal axis σ_{33} is approximately parallel to the rotational axis. This suggests that IFP does not have fast rotation about the membrane bilayer normal because the measured anisotropic ^{15}N chemical shifts do not correspond to a parallel insertion of the IFP helix relative to the bicelle normal. For such an orientation, the ^{15}N chemical shifts from flipped bicelle samples should be close to the downfield edge of the powder pattern, determined from Eq. 2.22 and Eq. 5.1,

$\sigma(0) = \frac{2}{3}\Delta\sigma \cdot \frac{1}{2}(3\cos^2 0 - 1) + \sigma_{iso} = \sigma_{33}$, and this was not observed in our experiments.

For a helix that is tilted from the bicelle normal, the distribution of the measured anisotropic chemical shifts of different ^{15}N labeled residues in flipped bicelle samples is broad, ~30-80 ppm for a helix tilted >10° from the bicelle normal.[24] This distribution can be substantially reduced for molecules with fast motions on the time scale of NMR interactions (i.e., rate of motion >> NMR interaction strength, ~10^{-5} s^{-1} based on ~10 kHz CSA and dipolar coupling interaction). As shown in Table 12, the measured chemical shifts of all the IFP non-glycine residues fall into a very narrow (≤8 ppm) range, centered on ~150 ppm for the flipped samples. This narrow distribution suggests an IFP structural model with significant mobility. The residues Gly-4 and Gly-8 are not considered because they have different CSA principal values compared to other residues and will have very different anisotropic chemical shifts even with the similar orientation and mobility as other residues.

A reasonable model of motion for the bicelle-associated IFPs is the fast rotation of IFP about its own N-terminal helix axis. For IFP molecules with such motions in membrane dispersion samples, the chemical shift tensors will be axially symmetric leading to the powder spectra with steep edges. However, the powder spectra shown in Figure 35a and b are from the ^{15}N labeled first ten residues at the IFP N-terminus and processed with 500 Hz Gaussian line broadening. It is difficult to observe the characteristic symmetric powder patterns in spectra with overlapping signals from 10 residues and broad line broadening.

Using the model of IFP with fast rotation around its helix axis, the angle between the helix axis and the magnetic field, θ, can be calculated based on the measured ^{15}N anisotropic chemical shifts and Eq. 2.22. In this analysis, the standard ^{15}N CSA tensor orientations were assumed as shown in Figure 12a and the CSA principal values were the aforementioned ones derived from the MAS spectrum of lyophilized IFP. These values are generally consistent with the ^{15}N CSA principal values in the literature.[24] For glycines, literature values of chemical shift tensors were used, σ_{11}, 41 ppm, σ_{22}, 64 ppm and σ_{33}, 211 ppm.[21, 22] In this analysis, the bicelle motion relative to the magnetic field direction was also taken into account, including the wobbling motion discussed in chapter 2 and a rapid tumbling motion of bicelle and embedded IFP about the bicelle normal. Based on the Eq. 2.26, the ^{15}N chemical shift of a bicelle sample which rotates rapidly with respect to the average normal direction is:[25]

$$\sigma(\theta) = \frac{2}{3} \cdot \Delta\sigma_{EFF} \cdot P_2(\cos\theta) \cdot S_{wobb} \cdot \frac{1}{2}(3\cos^2\lambda - 1) + \sigma_{iso} \qquad (5.2)$$

where λ is the angle between the bicelle normal and the magnetic field, which is 90° for the unflipped bicelles and 0° for the flipped bicelle samples. In the calculation, 0.8 was used for S_{wobb}; $\Delta\sigma_{EFF}$ was 159 ppm for Gly and 154 ppm for other residues and σ_{iso} was 105 ppm for Gly and 122 ppm for other residues. The angle θ' between the helix axis and the bicelle normal (θ' = 90°–θ for the unflipped bicelle samples and θ' = θ for the flipped bicelle samples) from the measured ^{15}N chemical shift of each labeled residue in unflipped and flipped bicelle samples is listed in Table 12.

Based on the analysis, the IFP N-terminal helix is determined to be tilted ~45° from the bicelle normal. For IFP samples at pH 5.0 with ^{15}N labeled Phe-3, Ala-5, Ile-6, Ala-7 or Ile-10, $|\theta'_{unflipped} - \theta'_{flipped}| \leq 7°$ which supports the accuracy of the analysis. Among these samples, Ala-5 and Ala-7 have the best agreement in the calculated θ' between the unflipped and flipped bicelle samples with $|\theta'_{unflipped} - \theta'_{flipped}| = 1°$ and 3° respectively; Ile-6 and Ile-10 have some agreement in θ' with $|\theta'_{unflipped} - \theta'_{flipped}| = 6°$ and 5° respectively; Phe-3 has the worst agreement with $|\theta'_{unflipped} - \theta'_{flipped}| = 6°$. For samples at pH 7.4, the calculated θ' values are also more consistent between the unflipped and flipped bicelle samples for Ala-7 than for Phe-3, with $|\theta'_{unflipped} - \theta'_{flipped}| = 2°$ or 10° respectively. This is probably because different residues generally have slightly different CSA principal values and the difference between different types of amino acids is even bigger[26]. While a small variation in $\Delta\sigma$ only results in a minor change in θ' (e.g., θ' only changes ±0.2° when $\Delta\sigma$ changes ±2 ppm), a similar variation in σ_{iso} causes a much greater change in θ' (e.g., θ' changes ∓2° when σ_{iso} changes ±2 ppm). In the analysis, only a single set of CSA principal values were used, which were obtained from an IFP-U_N sample. The obtained values may agree better with the CSA principal values of Ala and have more deviation from those of Phe-3, which leads to a bigger $|\theta'_{unflipped} - \theta'_{flipped}|$ for Phe-3. For samples containing IFP with ^{15}N labeled Gly-4 or Gly-8, $|\theta'_{unflipped} - \theta'_{flipped}|$ is 15-21°. This is probably due to the inaccuracy of principal values used and/or existence of additional motions of glycines which were not considered in the calculation. However, this analysis shows a general consistency of Glys' θ's with

other residues. In addition, $|\theta'_{pH\ 7.4} - \theta'_{pH\ 5.0}| \leq 3^{\circ}$ for all samples which suggests that there is little change in N-terminal helix orientation as a function of pH.

Table 12. ^{15}N chemical shifts (σ) and the corresponding orientational analysis for the aligned IFP samples [a]

Residue	pH 5.0				pH 7.4			
	Unflipped bicelle		Flipped bicelle		Unflipped bicelle		Flipped bicelle	
	σ (ppm) [b]	θ' [c, d]	σ (ppm)	θ' [c, d]	σ (ppm)	θ'	σ (ppm)	θ'
Phe-3	107	49	148	42	105	51	153	41
Gly-4	111	29	116	50	108	32	122	47
Ala-5	114	43	148	42	116	41	*n.d.*	*n.d.*
Ile-6	110	47	152	41	109	48	*n.d.*	*n.d.*
Ala-7	116	41	144	44	114	44	150	42
Gly-8	109	31	110	52	*n.d.*	*n.d.*	*n.d.*	*n.d.*
Phe-9	111	46	*n.d.* [e]	*n.d.*	*n.d.*	*n.d.*	*n.d.*	*n.d.*
Ile-10	110	47	150	42	*n.d.*	*n.d.*	*n.d.*	*n.d.*

[a] Data were obtained with bicelle-associated IFP, IFP:DTPC ~0.02, and 40 °C nitrogen gas temperature.
[b] The uncertainty in each chemical shift is estimated to be ±1 ppm as determined from the repetition of measurements.
[c] θ' is in degrees and is the angle between the helix axis and the bicelle normal. $\theta' = 90^{\circ} - \theta$ for the unflipped bicelle samples; $\theta' = \theta$ for the flipped bicelle samples, where θ is the angle between the helix axis and the magnetic field.
[d] The uncertainty in θ' is estimated to be ±3° based on the uncertainty in the chemical shift.
[e] not determined

Figure 35. ^{15}N NMR spectra of IFP which probe the orientation of the N-terminal helix axis relative to the membrane bilayer normal. Panels a-c are ^{15}N static spectra of IFP-U_N that provide information about ^{15}N chemical shift tensor principal values and IFP motion in (a, b) hydrated membrane dispersions or (c) lyophilized dry peptide without membranes. The similar appearances of spectra a, b, and c suggests that there is not large amplitude motion of the N-terminal helix in membranes with respect to the membrane bilayer normal at either (a) pH 5.0 or (b) pH 7.4. Panel d is a ^{15}N MAS spectrum of lyophilized IFP2-U_N that was used to determine ^{15}N CSA principal values. Panels e-m display ^{15}N static spectra of IFPs in the aligned bicelle samples. The incorporated IFP and the sample pH are labeled above each set of spectra. For each labeled IFP, sharp ^{15}N signals were observed and there was a significant change in peak chemical shift as a function of bicelle orientation (IFP-$G4_N$ and IFP-$G8_N$ have less change in the ^{15}N chemical shifts and the possible reasons are explained in the text). Both of these observations were consistent with a well-defined alignment of the N-terminal helix axis of IFP relative to the bicelle normal. For each labeled IFP, there was little change in ^{15}N chemical shift as a function of pH which indicated little change in average helix axis orientation with pH. The samples used to obtain spectra a and b contained ~1 μmol IFP and ~50 μmol DTPC. The samples used to obtain spectra e-m contained DTPC/$DMPC_{d54}$/DHPC (53:1:17 μmol) and 0.7 μmol IFP. All the spectra were obtained with ^{1}H-^{15}N ramped cross-polarization followed by ^{15}N detection with ^{1}H decoupling. For spectrum d, the MAS frequency was 1.5 kHz. The temperature of the gas which flowed around each sample was 40 °C. Spectra were processed using Gaussian line broadening of magnitude (a, b) 500 Hz, (c, d) 100 Hz, (e-m) 50–200 Hz. The number of acquisitions summed for each spectrum was 20000 – 60000.

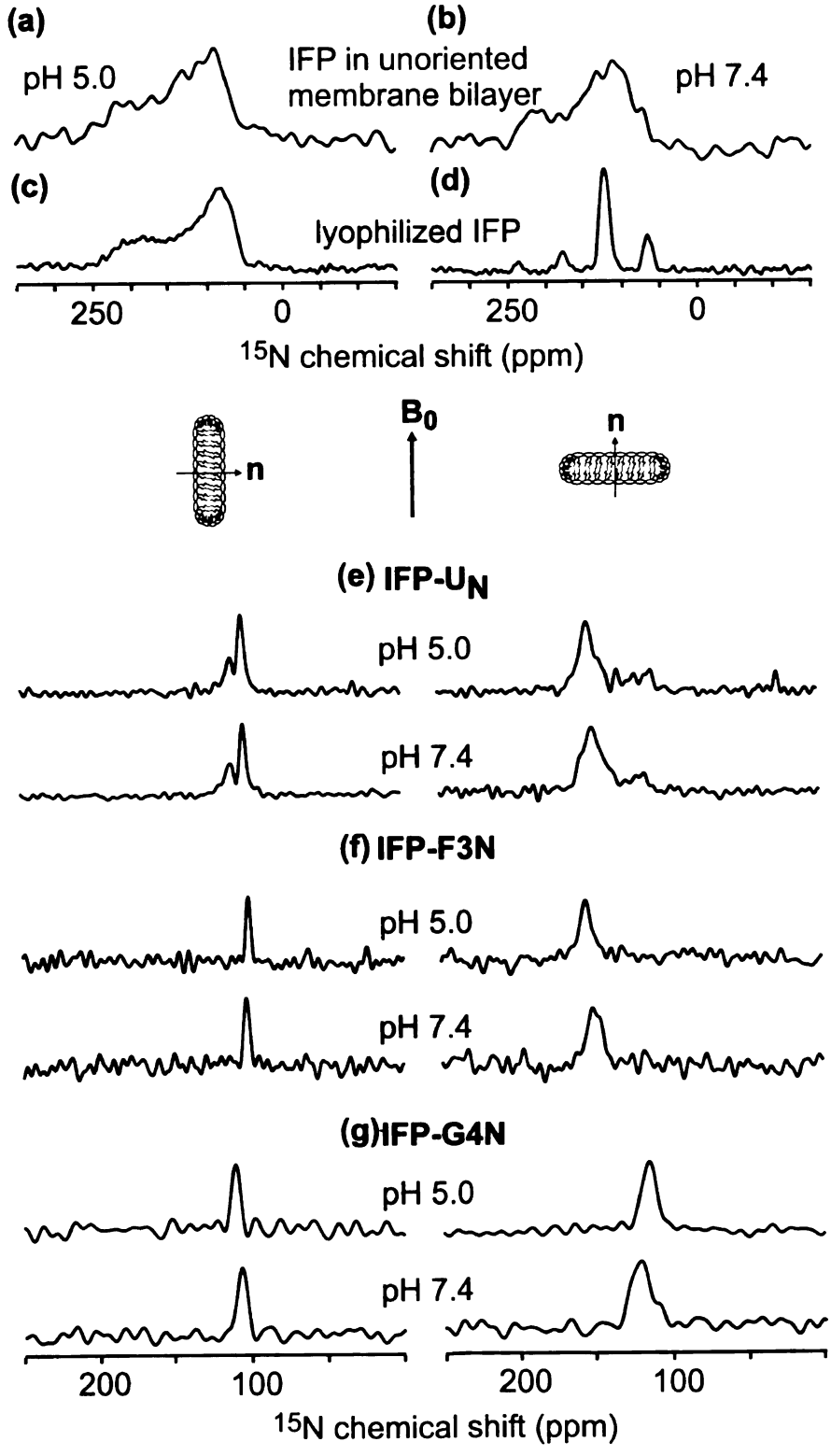
(a)
(b)
pH 5.0
IFP in unoriented membrane bilayer
pH 7.4
(c)
(d)
lyophilized IFP
250
0
250
0
15N chemical shift (ppm)
B0
n
n
(e) IFP-UN
pH 5.0
pH 7.4
(f) IFP-F3N
pH 5.0
pH 7.4
(g) IFP-G4N
pH 5.0
pH 7.4
200
100
200
100
15N chemical shift (ppm)

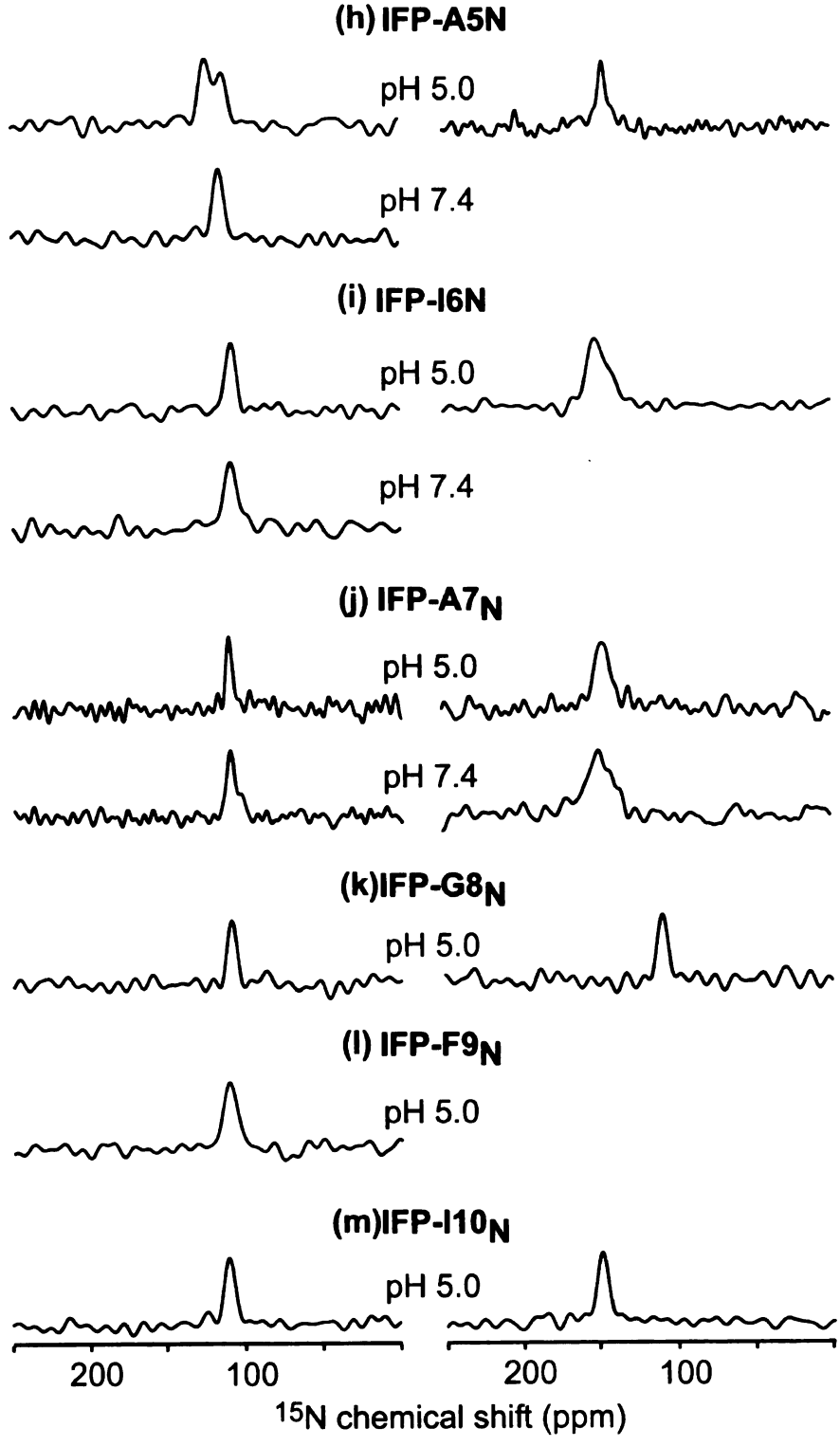

Figure 35. ^{15}N NMR spectra of IFP

3. 2D experiments

The orientation of the IFP N-terminal helix was also assessed by 2D ^{15}N chemical shift and N-H dipolar coupling correlation spectroscopy, which is a better way for orientational determination because the unique axis of the dipolar frame is rigorously along the N-H vector. For the bicelle-associated IFP system, the 2D spectroscopy can also provide additional support for the fast rotational motion of IFP about its helix axis because dipolar coupling will be scaled by the fast rotational motions and the dipolar splitting is determined by the angle between the rotational axis and the magnetic field.

The 2D spectra were acquired for IFP samples with different ^{15}N labels in both unflipped and flipped bicelles at different pHs and are shown in Figure 36. For each IFP sample with a single or double ^{15}N labeled residue(s), a single peak with a relatively narrow linewidth (100 Hz for IFP-$F3_NA7_N$ and 400-500 Hz for other samples) was observed for each ^{15}N labeled site (cf. Figure 36c-j). This is consistent with the good alignment of the IFP N-terminal helix in membrane bicelles and consistent with the chemical shift measurements. The big dipolar coupling change (almost doubles for most of the residues) of the IFP with the same ^{15}N label in the unflipped and flipped bicelle samples provides additional evidence for the IFP good alignment. For the spectra of IFP-U_N, peaks of each individual residue are not resolved and the observed narrow distribution of peaks and the two-fold increase in dipolar coupling from the unflipped bicelle samples to the flipped bicelle samples agree with results from the selectively labeled IFPs. Comparison between the measured dipolar couplings for the sample at different

pHs shows only small changes and supports my hypothesis that the orientation of the IFP N-terminal helix has minor pH dependence (cf. Table 13). Similar to the 1D data, the experimental distribution of crosspeaks can be compared to the theoretical distribution of a tilted helix and can provide some information on the IFP motions. For a tilted helix with a tilt angle of > 10^{o} relative to the bicelle normal, a > 3 kHz distribution of dipolar couplings and > 30 ppm distribution of chemical shifts are expected as calculated from Eq. 2.16 and 2.17. Particularly, for the ^{15}N–Hs of a helix tilted 40 – 50^{o} from the bicelle normal, the theoretical dipolar couplings and chemical shifts fall in a very broad range (0 – 8 kHz and 100 – 200 ppm respectively) and the magnitude of the dipolar splitting or the chemical shift depends on the residue's relative location in the helix.[24] Both the broad spread of chemical shifts and dipolar coupling can be greatly reduced by molecular motions. As shown in Figure 36 and table 13, the distribution of crosspeaks for different ^{15}N labeled IFP is narrow, clustered at ~110 ppm, ~1 kHz for IFPs in the unflipped bicelles, and at ~150 ppm, ~2 kHz for IFPs in the flipped bicelles. This is best manifested by the 2D spectra from the IFP-U_N samples which have only one peak for the unflipped bicelle samples and one peak with a small shoulder for the flipped bicelle samples (cf. Figure 36a and b). This narrow distribution of crosspeaks from bicelle-associated IFP samples provides additional support for an IFP structural model with large mobility, possibly a fast rotation of IFP helix about its own helix axis which fits well with the experimental data.

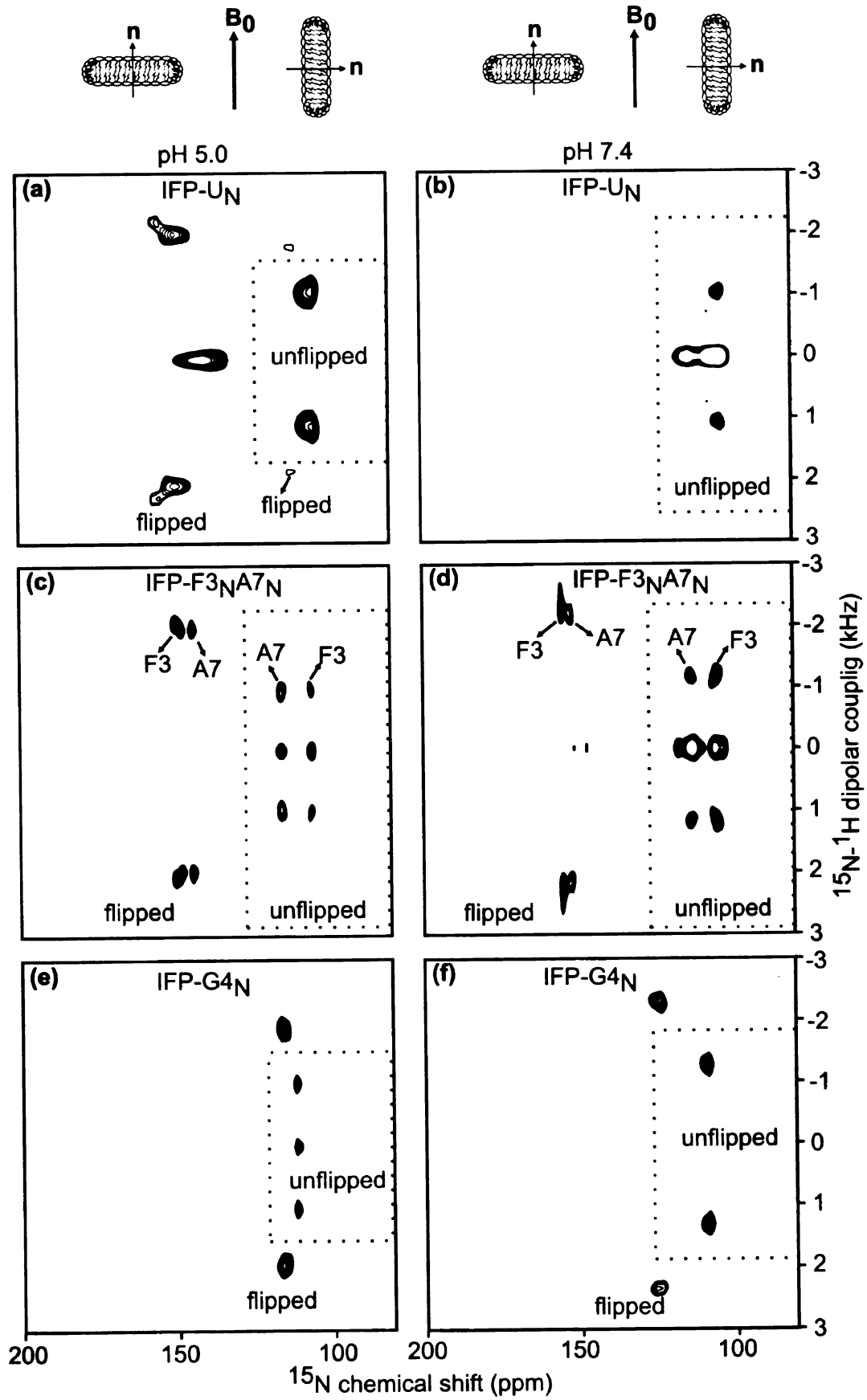

Figure 36. 2D ^{15}N chemical shift and N-H dipolar coupling correlation spectra

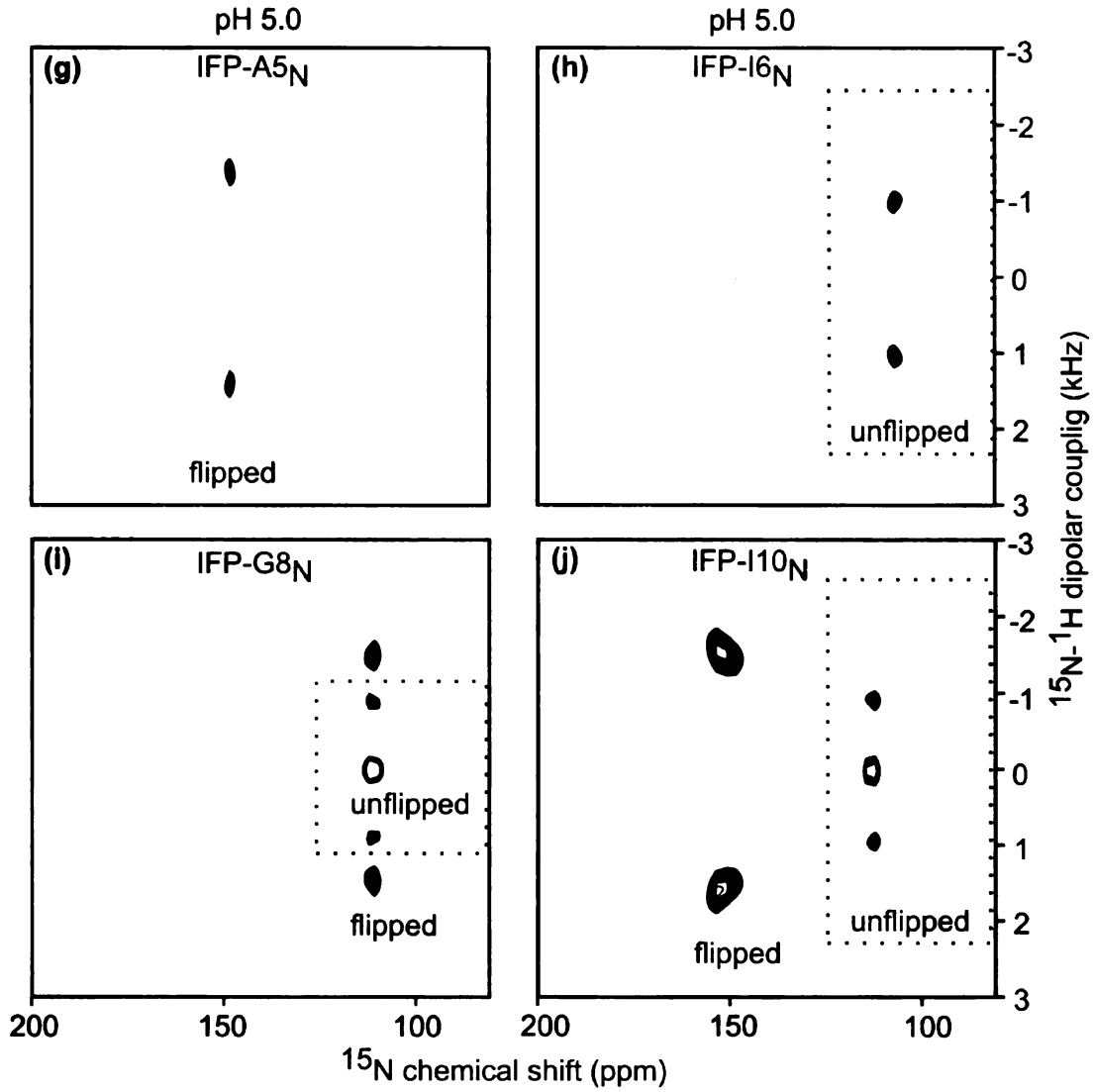

Figure 36. 2D ^{15}N chemical shift and N-H dipolar coupling correlation spectra of bicelle-associated IFP that probe the orientation of the N-terminal helix axis relative to the membrane bilayer normal. The samples used to obtain the spectra contained (a, b) IFP-U_N, (c, d) IFP-$F3_NA7_N$, (e, f) IFP-$G4_N$, (g) IFP-$A5_N$, (h) IFP-$I6_N$, (i) IFP-$G8_N$ and (j) IFP-$I10_N$ at (a, c, e, g-j) pH 5.0 or (b, d, f) pH 7.4. All the samples have the composition of DTPC/$DMPC_{d54}$/DHPC (53:1:17 μmol) and 0.7 μmol IFP. Each panel is separated into two parts by the dotted square with the inside part representing the unflipped bicelle sample and the outside part representing the flipped bicelle samples. For the spectra of IFP-$F3_NA7_N$, peaks were assigned based on the measured chemical shifts of IFP-$F3_N$ and IFP-$A7_N$ in Figure 33. All the spectra were obtained with PI-WIM-z pulse sequence. Spectra c and d were obtained with "Efree" free probe on the 21.4 T spectrometer. Other spectra were obtained with the Varian Biostatic ^1H/X probe on the 9.4 T NMR spectrometer. The temperature of the gas which flowed around each sample was 40 °C. The number of acquisitions for each spectrum was ~100000.

The quantitative analysis of dipolar splitting can be determined using Equ. 2.27 with adjustment to the bicelle rotation around its normal:

$$\nu(\theta) = \kappa \cdot \nu_{\parallel} \cdot \frac{1}{2}\left(3\cos^2\eta - 1\right) P_2(\cos\theta) \cdot S_{wobb} \cdot \left|\frac{1}{2}\left(3\cos^2\lambda - 1\right)\right| \qquad (5.3)$$

where $\kappa = 0.67$, $\nu_{//} = 22.6$ kHz, $S_{wobb} = 0.8$, and λ is 90° for the unflipped bicelles and 0° for the flipped bicelle samples. In the analysis, $\eta = 12°$ was used based on the 8° – 15.8° tilt angle (η) of N–H bond relative to the helix axis for α helices in the literature[27]. The ±4° variations in η correspond to only ±1° variation in the calculated θ. The values of θ' obtained from dipolar couplings are listed in table 13 and are ~45° and comparable to the corresponding angles obtained based on the anisotropic chemical shifts. For all the ^{15}N labeled residues, $|\theta'_{unflipped} - \theta'_{flipped}| \leq 8°$. Unlike the chemical shift analyses which were based on chemical shift principal values with different amino types (especially glycine) having distinct values, dipolar coupling analyses were based on the dipolar coupling constant which is only related to the nuclei types involved and keeps constant for all the residues. Compared to the θ' values obtained for Gly-4 and Gly-8 from chemical shifts, the angle θ' for these two residues from dipolar coupling analyses is more consistent between the unflipped and flipped samples and also more consistent with other residues. For an IFP sample at different pHs, the difference between θ', $|\theta'_{pH\ 7.4} - \theta'_{pH\ 5.0}| \leq 3°$ and supports the observations from the chemical shift measurements that there is little change in the N-terminal helix orientation as a function of pH. The similarity between the spectra of IFP-U_N at different pHs provides further evidence for this pH-independent orientation of the IFP N-terminal helix relative to the bicelle normal.

Table 13. N-H dipolar couplings (ν) and corresponding orientational analysis for the aligned IFP samples [a]

Residue	pH 5.0				pH 7.4			
	Unflipped bicelle		Flipped bicelle		Unflipped bicelle		Flipped bicelle	
	ν (kHz) [b]	θ' [c, d]	ν (kHz)	θ' [c, d]	ν (kHz)	θ'	ν (kHz)	θ'
Phe-3	1.1	43	2.0	48	1.1	43	2.3	47
Gly-4	0.8	41	1.9	48	1.3	44	2.3	47
Ala-5	*n.d.* [e]	*n.d.*	1.6	50	*n.d.*	*n.d.*	*n.d.*	*n.d.*
Ile-6	0.7	40	*n.d.*	*n.d.*	*n.d.*	*n.d.*	*n.d.*	*n.d.*
Ala-7	1.0	42	2.0	48	1.2	43	2.2	47
Gly-8	0.9	42	1.6	50	*n.d.*	*n.d.*	*n.d.*	*n.d.*
Phe-9	*n.d.*	*n.d.*	*n.d.*	*n.d.*	*n.d.*	*n.d.*	*n.d.*	*n.d.*
Ile-10	0.9	42	1.7	49	*n.d.*	*n.d.*	*n.d.*	*n.d.*

[a] Data were obtained with the same samples and same experimental conditions as in table 12.
[b] The uncertainty in each dipolar coupling is estimated to be ±250 Hz.
[c] θ' is in degrees and is the angle between the helix axis and the bicelle normal. $\theta' = 90°-\theta$ for the unflipped bicelle samples; $\theta' = \theta$ for the flipped bicelle samples where θ is the angle between the helix axis and the magnetic field.
[d] The uncertainty in θ' is estimated to be ±3° based on the uncertainty in the dipolar coupling.
[e] not determined

4. Comparison between 9.4 T and 21.4 T data

Some of the 1D ^{15}N chemical shift and 2D ^{15}N chemical shift and N-H dipolar coupling correlation spectra were taken on a 21.4 T spectrometer, which is located in the biomolecular NMR facility in Michigan State University. The 1D spectra of IFP-U_N sample at pH 5.0 and 2D spectra of IFP-$F3_NA7_N$ sample at pH 7.4 from 9.4 T and 21.4 T spectrometers are displayed in Figure 37. Based on the signal-to-noise ratios of the 1D spectra, the sensitivity of the 21.4 T spectrometer is ~4.5 times higher than the sensitivity of the 9.4 T spectrometer. The peaks are better resolved in the spectrum taken with the 21.4 T

spectrometer. The linewidth of the spectrum taken with the 21.4 T spectrometer is ~3.7 ppm. The linewidth of the spectrum taken with the 9.4 T spectrometer is ~6.5 ppm. The resolution is also significantly improved for the 2D spectra of the IFP-F3$_N$A7$_N$ sample when using higher field.

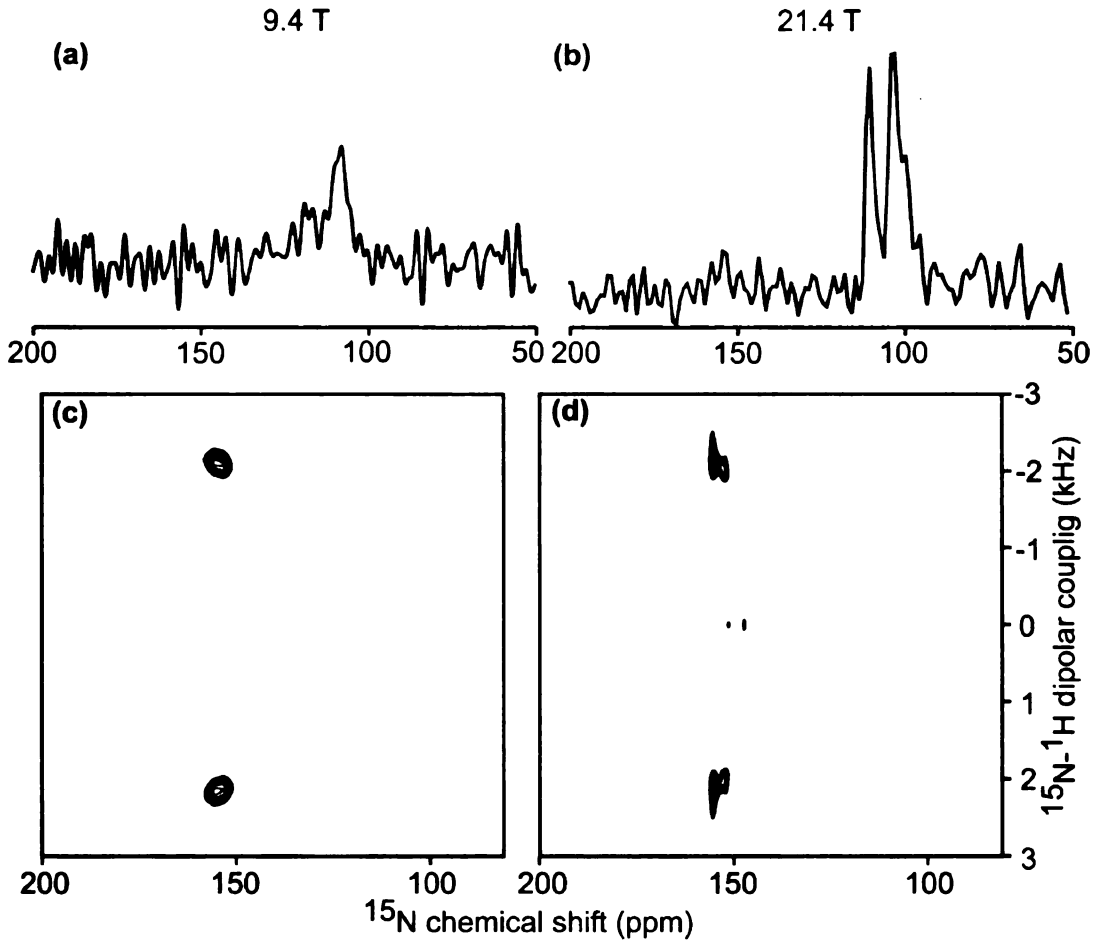

Figure 37. 1D and 2D spectra taken with either a 9.4 T (left) or a 21.4 T (right) spectrometer. The 1D spectra were taken with the unflipped bicelle samples containing IFP-U$_N$ at pH 5.0. The sensitivity of the two spectrometers is estimated to be ~1:4.5 (9.4 T spectrometer:21.4 T spectrometer) based on the signal-to-noise ratios and the numbers of scans of the two spectra. The peak width is reduced from ~6.5 ppm to ~3.7 ppm. The 2D spectra were taken with the flipped bicelle samples containing IFP-F3$_N$A7$_N$ at pH 7.4. The linewidth is narrowed for the spectra taken with 9.4 T spectrometer compared to the spectra taken with 21.4 T spectrometer. All the spectra were processed without line broadening. The number of acquisitions for each spectrum was (a) 5048; (b) 1042; (c) 6144 (*f*2) × 20 (*f*1); (d) 1280 (*f*2) × 92 (*f*1).

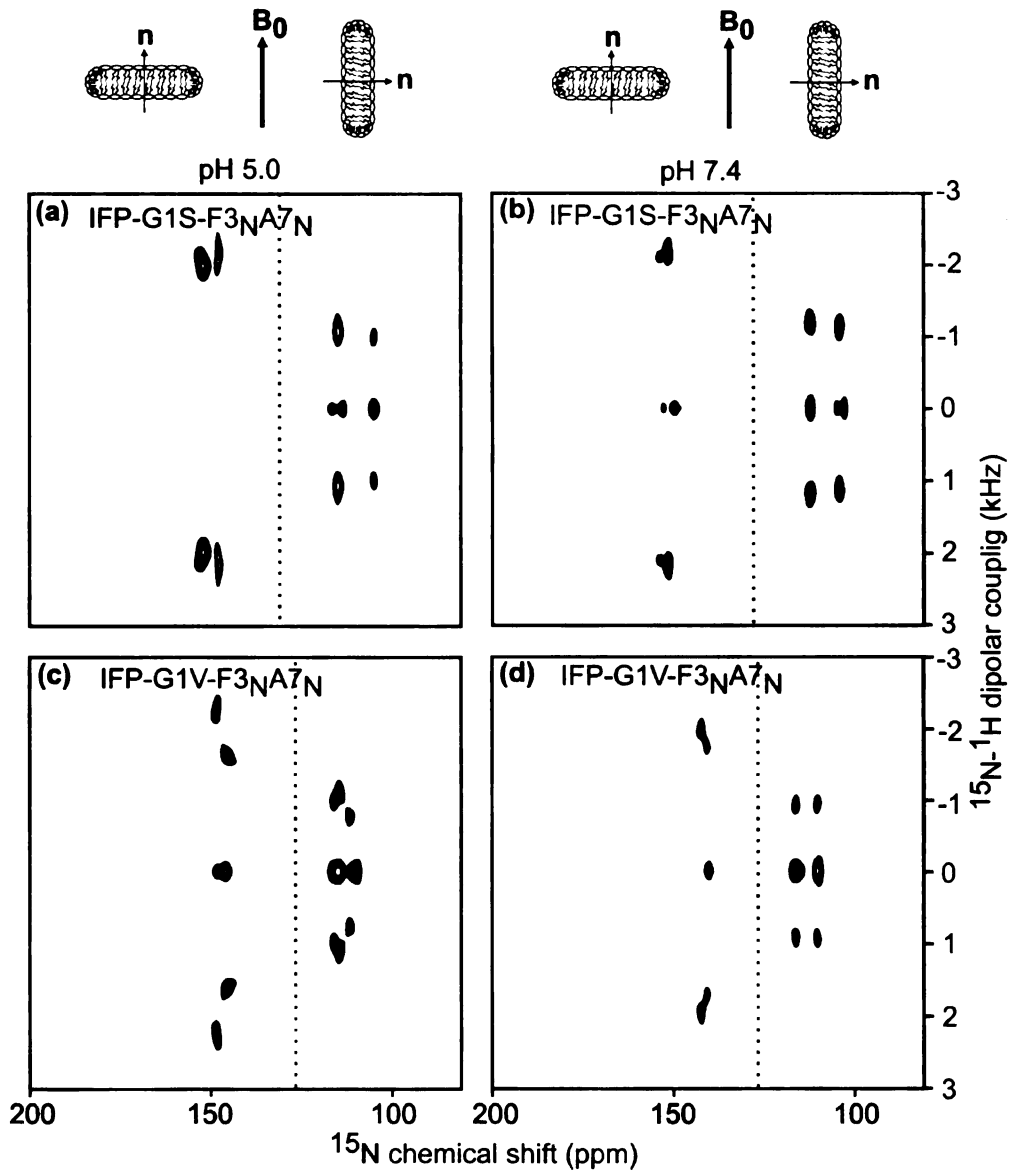

Figure 38. 2D ^{15}N chemical shift and N-H dipolar coupling correlation spectra of bicelle-associated (a, b) IFP-G1S-$F3_NA7_N$ and (c, d) IFP-G1V- $F3_NA7_N$ IFP at pH 5.0 (a, c) and pH 7.4 (b, d), Each panel represents the composite spectra of unflipped (< 130 ppm) and flipped (> 130 ppm) bicelle samples containing same labeled IFP at the same pH. The spectra for IFP-G1S and IFP-G1V resemble each other and resemble the spectra of wild IFP-$F3_NA7_N$ which suggest the N-terminal helix of these two mutants and wild IFP have similar motions and tilted angle. All the spectra were taken with PI-WIM-z sequence. The samples have the same composition as the samples in Figure 23. The number of acquisitions for each spectrum is ~100000.

5. Comparison of the N-terminal helix orientation between IFP and its mutants

It was shown that Gly-1 in the IFP sequence is very important and the only allowed mutation is alanine. HA with a point mutation of HA Gly-1 to Ser can only induce red blood cells lipid mixing without their contents mixing and HA with a point mutation of HA Gly-1 to Val can induce neither lipid mixing nor content mixing.[13] It was proposed that a shallower insertion of the N-terminal helix in the IFP-G1V mutant compared to the wild-type IFP is correlated to this fusion activity loss. While both the wild-type IFP and the IFP-G1S mutant have a tilt angle of ~50° between the N-terminal helix axis and the membrane bilayer normal, this angle for the IFP-G1V mutant is proposed to be ~65°.[11] This big change in the tilt angle should result in an obvious change in the ^{15}N chemical shifts and the N-H dipolar couplings for the same ^{15}N labels in the wild-type IFP and IFP mutants, which can be detected using solid-state NMR.

Figure 38 shows the 2D ^{15}N chemical shift and N-H dipolar coupling correlation spectra for the Phe-3 and Ala-7 ^{15}N labeled IFP-G1S or IFP-G1V mutant samples at pH 5.0 or pH 7.4. The structures of the two IFP mutants in detergent micelles were determined by solution NMR before and were found to have the similar helical structures with the micelle-associated wild-type IFP in their N-terminal regions.[11] Based on the solution NMR results, two assumptions were made in the analysis of 2D data in Figure 38: (1) The N-terminal regions (residue Phe-3 through Ile-10) of both mutants have helical structures similar to the wild-type IFP N-terminal helix in bicelles and are independent of pH; (2) The

relative positions of the Phe-3 and Ala-7 crosspeaks for both mutants are similar to that of the wild-type IFP and the assignments of the two crosspeaks for both mutants were made based on the assignments of the wild-type IFP samples. The chemical shifts and dipolar couplings derived from Figure 38 are listed in table 14. For the samples at each pH with each bicelle alignment, both IFP-G1S and IFP-G1V show very similar spectra compared to the wild-type IFP (cf. Figure 36c, d and 38). The magnitudes of the chemical shifts or the N-H dipolar couplings are independent of the mutations of Gly-1 or the pH changes of the samples (cf. table 12, 13 and 14). The two labeled residues, Phe-3 and Ala-7, have very close chemical shifts and N-H dipolar couplings for the wild IFP and IFP mutants, ~110 ppm and ~ 1 kHz for the unflipped samples and ~150 ppm and ~2 kHz for the flipped samples. The similar appearances of the corresponding spectra for all the samples suggest the aforementioned assumptions are reasonable and also supports similar motional and orientational motifs for the N-terminal helices of wild-type IFP and its mutants. Therefore the ^{15}N chemical shifts and the N-H dipolar couplings were analyzed in the same way as the data from wild-type IFP using Eq. 5.3 and the obtained θ' are included in table 14. As in the wild IFP, both the N-terminal helices of IFP-G1S and IFP-G1V mutants were modeled as experiencing a fast rotation about the helix axis and the helix has a best-fit tilt angle of ~45^{o} relative to the bicelle normal.

Table 14. ^{15}N chemical shifts (σ), N-H dipolar couplings (ν) and corresponding orientational analysis for the aligned IFP mutant samples [a]

Residue		pH 5.0				pH 7.4			
		σ (ppm)[b]	θ' [c, d]	ν (kHz) [e]	θ'	σ (ppm)	θ' [c, d]	ν (kHz)	θ'
IFP-G1S Phe-3	unflipped bicelle	105	52	1.1	43	104	52	1.2	44
	flipped bicelle	151	41	2.0	48	153	40	2.2	47
IFP-G1S Ala-7	unflipped bicelle	114	43	1.2	43	111	45	1.3	44
	Flipped bicelle	147	43	2.2	47	151	41	2.2	47
IFP-G1V Phe-3	unflipped bicelle	111	46	0.8	41	110	47	1.0	42
	Flipped bicelle	148	42	2.3	47	142	45	2.0	48
IFP-G1V Ala-7	unflipped bicelle	114	43	1.2	43	116	41	1.0	42
	Flipped bicelle	145	44	1.7	49	140	46	1.8	49

[a] Data were obtained with bicelle-associated IFP-G1S or IFP-G1V, IFP mutant:DTPC ~0.02, and 40 °C sample nitrogen gas temperature.
[b] The uncertainty in each chemical shift is estimated to be ±1 ppm as determined from the repetition of measurements.
[c] θ' is in degree and is the angle between the helix axis and the bicelle normal. $\theta' = 90° - \theta$ for the unflipped bicelle samples; $\theta' = \theta$ for the flipped bicelle samples.
[d] The uncertainty in θ' is estimated to be ±3° based on the uncertainty in the chemical shift or dipolar coupling.
[e] The uncertainty in each dipolar coupling is estimated to be ±250 Hz.

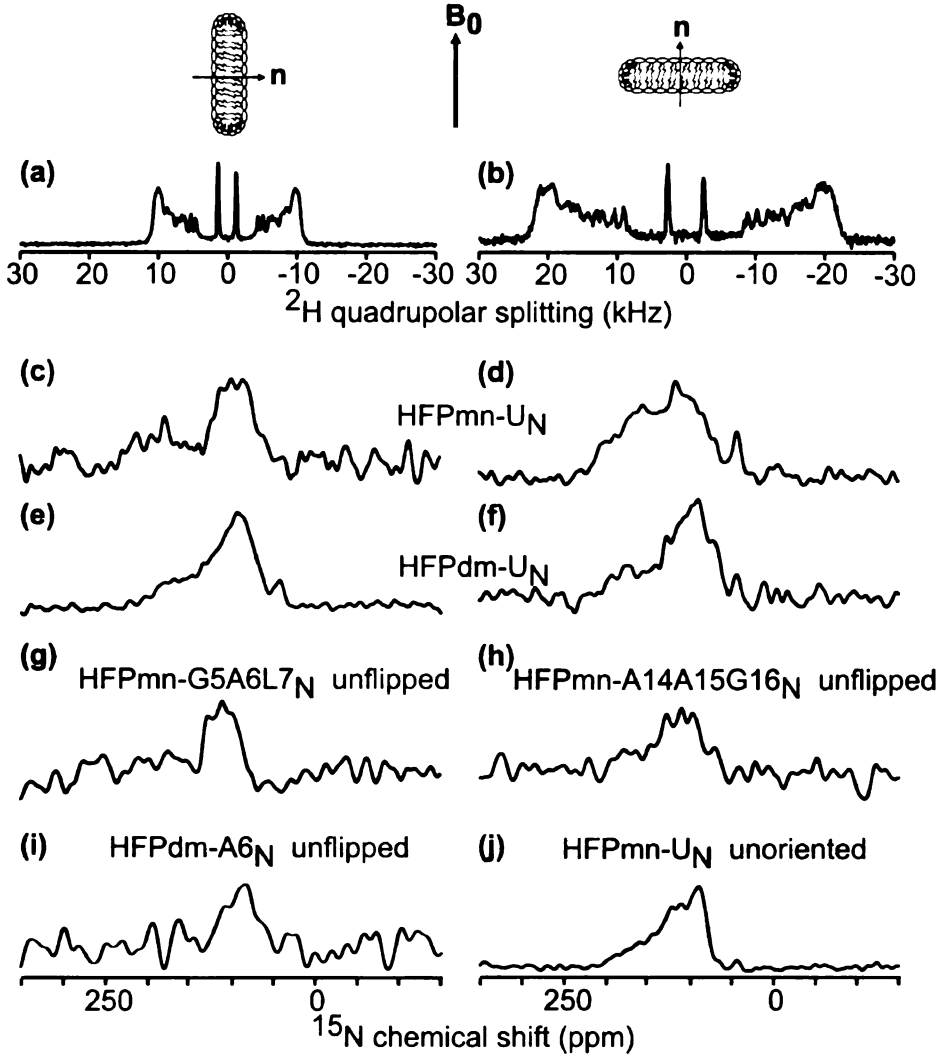

Figure 39. ^{2}H quadrupolar splitting spectra of HFP in (a) unflipped and (b) flipped bicelles show the good alignment of bicelles with incorporated HFP. ^{15}N chemical shift spectra of bicelle-associated HFP (c-i) have similar line shapes to the powder spectrum of HFP (j) and suggest HFP not aligned relative to the bicelle normal. The HFP used for each sample is labeled above each spectrum. All the spectra in the left panels and spectrum (h) were taken with unflipped bicelle samples. The spectra in the first three rows of the right panels were taken with flipped bicelle samples. The spectrum (j) was taken with an unoriented membrane bilayer sample. All spectra were taken with samples that contain 0.7 μmol HFPmn or 0.4 μmol HFPdm and DTPC/DMPC$_{d54}$/DHPC (53:1:17 μmol). The temperature of the gas which flowed around each sample was 40 °C. Spectra were processed using Gaussian line broadening of magnitude (a, b) 25 Hz, (c-f, j) 300 Hz, (g, h) 400 Hz, and (i) 500 Hz. The number of acquisitions summed for each spectrum was: (a) 8000; (b) 3426; (c, f, i) ~26000; (d, g, h, j) ~10000.

6. Comparison of the N-terminal helix orientation between IFP and HFP

Both the HIV and influenza viruses belong to type I viruses and their fusion proteins share similar topology and folding motifs.[28] HFP and IFP are different in sequence, but both of them are rich in glycine. Structural studies show that both peptides have a major helical structure in membranes lacking cholesterol at low FP/lipid ratio and have predominant β strand structures in membranes containing 33 mol% cholesterol.[29] It will be interesting to study and compare the motional and orientational properties of both peptides which can be correlated to the fusion activities. The HIV fusion peptide induces fusion at physiological pH 7.4 upon binding to the target membranes, so experiments were only carried out with the HFP samples at pH 7.4.

Similar to IFP, HFP does not affect the morphology of bicelles and the bicelles have good alignments with incorporated HFP (cf. Figure 39a, b). Figure 39c and d show the ^{15}N spectra of bicelle-associated HFPmn with ^{15}N labeling of the first 14 residues of the N-terminus. Compared to the spectra of IFP-U_N, the spectra of HFPmn-U_N are much broader and the linewidths are similar to the spectrum of HFPmn-U_N in unoriented membrane dispersions (cf. Figure 39j), which suggests that HFPmn is not aligned in the bicelle. The alignment of HFPdm in bicelles was also studied with ^{15}N chemical shifts to examine whether the greater fusion activity of the HFPdm relative to the HFPmn[30] is correlated to an improved alignment of the HFPdm. Figure 39e and f show the spectra of the bicelle-associated HFPdm-U_N with the same ^{15}N labeling as HFPmn-U_N. Those spectra are comparable to the spectra of HFPmn-U_N in either bicelles or

membrane dispersions and are consistent with the unaligned HFPs in the membrane bicelles.

HFPs were shown to have both α helical and β strand conformations in the membranes lacking cholesterol.[29] The existence of these two different conformations of HFPs in bicelles may also cause a broader spread in the measured anisotropic ^{15}N chemical shifts. In addition, partial alignments or multiple alignments of HFPs in bicelles are other possible reasons for a broader distribution of the measured ^{15}N chemical shifts. However, the powder-shaped spectra of bicelle-associated HFPs are probably mainly due to the unaligned HFPs based on the following arguments: (1) Multiple sharp lines instead of a broad peak should be observed for two well-aligned conformations of HFP; (2) For a sample with partly aligned HFPs, at least some sharp peaks should be observed or the appearance of the spectra of the unflipped bicelle and the flipped bicelle samples should be different from each other and from the powder spectrum; (3) The multiple alignments of HFPs should also result in multiple sharp peaks instead of a powder-shaped spectrum. In order to get further evidence for the above arguments, samples of HFPs with selective ^{15}N labels were examined, including HFPmn-G5A6L7$_N$, HFPmn-A14A15G16$_N$ and HFPdm-A6$_N$. The spectra are shown in Figure 39g-i. All the spectra have low signal-to-noise ratio due to the broad distribution of chemical shifts and have powder-lineshapes and are consistent with unaligned HFPs.

5.3 DISCUSSION

The disruption of membrane bilayers by fusion peptides is considered to be important for the membranes to overcome the kinetic barrier to fusion and is correlated to the insertion of fusion peptides into the membranes. The membrane insertion of IFP and HFP has been studied before and a lot of these studies have been focused on the insertion angles of the fusion peptides relative to the membrane bilayer normal. The solid-state NMR data presented in this chapter show that the membrane insertion of FPs can be probed with the bicelle membrane system which is an excellent model system to probe the membrane peptide/protein orientation. It is significant that the bicelles remain intact and aligned with incorporated FPs rather than being strongly perturbed by IFP or HFP. The ^{2}H NMR spectra showed good and controllable alignment of FP-incorporated bicelles and indicated the feasibility of potential measurements of bicelle-associated bigger constructs of fusion proteins (HA2 or gp41 for influenza or HIV virus respectively), which would possibly provide valuable orientational and motional information for the more biologically relevant fusion proteins.

The orientational information of FPs was explored by ^{15}N chemical shifts and ^{15}N-^{1}H dipolar couplings. For the orientation derived from chemical shifts, thorough knowledge of chemical shift tensors including the tensor orientation and principal values is required and both can be determined using the ^{15}N spectra of the unoriented membrane dispersion samples. However the ^{15}N spectra of the membrane-associated FPs with good signal-to-noise ratio were difficult to acquire because of the reduction in *CP* efficiency due to molecular motions and the limited FP concentration. The principal values used for non-glycine residues

of IFP were derived from the spectra of lyophilized IFP-U_N. Two uncertainties exist from this determination: (1) the spectra of the membrane-associated IFP have some subtle difference in lineshapes compared to the spectra of lyophilized IFP and could lead to slightly different principal values; and (2) Each residue may have somewhat different principal values which can not be obtained from the spectra of IFP-U_N. For IFP Glys, their principal values were not experimentally determined in my studies and literature values were used directly. The tilt angle of the IFP N-terminal helix relative to the bicelle normal derived from ^{15}N chemical shifts is subject to these uncertainties and a ~20° difference in θ' for Gly-4 and Gly-8 between the unflipped and flipped bicelles was obtained. Unlike the chemical shift tensors, the N-H dipolar coupling tensor is axially symmetric and independent of residue type. For Glys, the results from dipolar coupling measurements do not have the big deviations as in the results from the chemical shift measurements. For other residues, the results from both chemical shift and dipolar coupling measurements agree well with each other. The measured ^{15}N-^{1}H dipolar couplings are affected by the distribution of bicelle alignment and some variations in the bicelle alignment such as the order parameter and the angle of the bicelle normal relative to the magnetic field (e.g. $\Delta S_{wobb} = \pm 0.1$ and $\Delta\lambda = \pm 10°$ can change the derived ^{15}N-^{1}H dipolar coupling by $\Delta\nu = \pm 0.2$ kHz for the unflipped bicelle samples and $\Delta\nu = \pm 0.4$ kHz for the flipped bicelle samples). The incorporation of FPs into bicelles and the DTPC/DHPC ratio both affect bicelle alignment. Different bicelle-associated IFP samples are very likely to have different S_{wobb} and λ which will lead to variations in the measured ^{15}N-^{1}H dipolar

couplings. Therefore, the spectra of IFP-U_N measure the ^{15}N-^{1}H dipolar coupling of each residue with the same S_{wobb} and λ and the observation of single peaks provides the best evidence for a helix with fast rotational motion. The fast rotational motion of the IFP N-terminal helix can be fitted to the inverted boomerang structural model proposed in the Chapter 4 considering the dynamic nature of membrane lipids in the liquid-crystalline phase. As discussed in Chapter 4, the entire C-terminal region of IFP is likely exposed to water. The surrounding lipid and water molecules may provide enough interaction to stabilize the IFP C-terminus. The IFP N-terminal helix is not restricted by the C-terminal region and can rotate relatively freely.

The present studies probed the dependence of the IFP N-terminal helix orientation on pH and mutations of Gly-1. The data are interpreted as: (1) The IFP N-terminal helix has a fast rotation about its axis; (2) The IFP N-terminal helix has a tilt angle of ~45° relative to the membrane bicelle normal; (3) The angle between the IFP N-terminal helix axis and bicelle normal is independent of the sample pH; (4) This angle is also independent of the mutations of Gly-1 to Ser or Val. The IFP N-terminal helix orientation and its dependence on pH or Gly-1 mutations can be compared to some previous studies.[3, 11] Our result on the IFP N-terminal helix orientation is consistent with the ~45° insertion of IFP detected by ATR-FTIR[1]. Two different groups studied the IFP orientational dependence on pH using ESR and tried to correlate the IFP insertion to its functional activity. The angle between the IFP N-terminal helix axis and the membrane bilayer normal was determined to be 52° at pH 5.0 and 67° at pH 7.4 by one group using a

similar IFP construct as our group.[3] In another study, the IFP part of FHA2 (residue 1-127 of HA2) was found out to be 62° or 65° away from the bilayer normal for the samples at pH 5 or pH 7.[5] The orientation of the IFP N-terminal helix derived from solid-state NMR (45°) does not agree with these angles mentioned above and does not agree with the ~15° change in the N-terminal helix orientation observed by the first group. If the 15° change was correct, we would anticipate a ~30 ppm change in the ^{15}N shifts and ~2.3 kHz change in the ^{15}N-^{1}H dipolar splitting for the flipped bicelle samples at different pHs. This is not inconsistent with our observation of ≤6 ppm and ≤0.4 kHz variations in the ^{15}N chemical shifts and ^{15}N-^{1}H dipolar couplings respectively. Our results fit better with the 3° change which would yield ~5 ppm change in the ^{15}N chemical shifts and ~0.7 kHz change in the ^{15}N-^{1}H dipolar couplings for the flipped bicelle samples at different pHs. The 15° difference in insertion angle between the two pHs has been proposed to be coupled to a difference in the C-terminal conformation (helical vs extended) described in the chapter 3. Our observation of little change in either insertion angle or C-terminal conformation as a function of pH suggest that other models need to be developed to address the structure-pH-dependent fusion activity relationship of IFP. Similar previous studies based on ESR data showed ~15° change in N-terminal helix axis orientation when Gly-1 was mutated to Val. Our data do not support this model based on a similar argument against the big pH dependence discussed above. We observed a respective change of ≤3 ppm or ≤0.3 kHz in the ^{15}N chemical shifts and ^{15}N-^{1}H dipolar couplings between wild-type IFP and IFP-G1S or IFP-G1V mutants. From

our studies, the orientation of the IFP helix axis is an intrinsic property of the peptide sequence. This orientation does not change when the pH of the samples changes or the single residue Gly-1 is mutated. The change in the fusion activity is not correlated to a change in the orientation of the IFP N-terminal helix.

Our studies can also be compared to the results from molecular dynamics simulations. IFP serves as a good model for simulations and extensive work has been done to predict the insertion of the membrane-bound IFP. In one study, the IFP was shown to locate near the lipid phosphate headgroups with an almost parallel alignment to the membrane surface.[7] In other simulations, IFP was found to have oblique insertion relative to membrane bilayer normal. In one study, simulations were also done to examine the effect of pH on the membrane location and little dependence was found. Our results on the IFP N-terminal helix orientation based on solid-state NMR studies provided valuable experimental data to guide the molecular dynamics studies.

There are relatively fewer previous results on the orientational studies of HFPs. One polarized ATR spectroscopy study found that the α helical form of HFP has an insertion angle of ~40° and the β strand form has an insertion angle of ~30° relative to the membrane bilayer normal.[31] In our studies, the HFP has been shown to have complex secondary structures in membranes lacking cholesterol. The β strand forms of HFP are mostly anti-parallel and have multiple registries. The helical conformation extends from Ile-4 to Leu-12, and residues around Leu-9 have the best defined α helical conformation. The complexity in the HFP secondary structures suggests a complicated insertion of HFP which is

supported by our observation of powder-shaped spectra for the HFP in aligned bicelles. In contrast, the N-terminal region of IFP has a single conformation of an α helix in the bicelle system without cholesterol and the N-terminal helix has a single insertion angle of ~45° relative to the bicelle normal.

5.4 REFERENCES

1. Luneberg, J.; Martin, I.; Nussler, F.; Ruysschaert, J. M.; Herrmann, A., Structure and Topology of the Influenza-Virus Fusion Peptide in Lipid Bilayers. *Journal of Biological Chemistry* **1995,** 270, (46), 27606-27614.

2. Ishiguro, R.; Matsumoto, M.; Takahashi, S., Interaction of Fusogenic Synthetic Peptide with Phospholipid Bilayers: Orientation of the Peptide α-Helix and Binding Isotherm. *Biochemistry* **1996,** 35, (15), 4976–4983.

3. Han, X.; Bushweller, J. H.; Cafiso, D. S.; Tamm, L. K., Membrane structure and fusion-triggering conformational change of the fusion domain from influenza hemagglutinin. *Nat. Struct. Biol.* **2001,** 8, (8), 715-720.

4. Ishiguro, R.; Kiura, N.; Takahashi, S., Orientation of fusion-active synthetic peptides in phospholipid bilayers: Determination by Fourier transform infrared spectroscopy. *Biochemistry* **1993,** 32, (37), 9792-9797.

5. Macosko, J. C.; Kim, C. H.; Shin, Y. K., The membrane topology of the fusion peptide region of influenza hemagglutinin determined by spin-labeling EPR. *J. Mol. Biol.* **1997,** 267, (5), 1139-1148.

6. Bechor, D.; Ben-Tal, N., Implicit solvent model studies of the interactions of the influenza hemagglutinin fusion peptide with lipid bilayers. *BIOPHYSICAL JOURNAL* **2001,** 80, (2), 643-655.

7. Sammalkorpi, M.; Lazaridis, T., Configuration of influenza hemagglutinin fusion peptide monomers and oligomers in membranes. *BIOCHIMICA ET BIOPHYSICA ACTA-BIOMEMBRANES* **2007,** 1768, (1), 30-38.

8. Efremov, R. G.; Nolde, D. E.; Volynsky, P. E.; Chernyavsky, A. A.; Dubovskii, P. V.; Arseniev, A. S., Factors important for fusogenic activity of peptides: molecular modeling study of analogs of fusion peptide of influenza virus hemagglutinin. *FEBS LETTERS* **1999,** 462, 205-210.

9. Spassov, V. Z.; Yan, L.; Szalma, S., Introducing an implicit membrane in generalized Born/solvent accessibility continuum solvent models. *JOURNAL OF PHYSICAL CHEMISTRY B* **2002,** 106, (34), 8726-8738.

10. Vaccaro, L.; Cross, K. J.; Kleinjung, J.; Straus, S. K.; Thomas, D. J.; Wharton, S. A.; Skehel, J. J.; Fraternali, F., Plasticity of Influenza Haemagglutinin Fusion Peptides and Their Interaction with Lipid Bilayers. *Biophysical Journal* **2005,** 88, 25-36.

11. Li, Y.; Han, X.; Lai, A. L.; Bushweller, J. H.; Cafiso, D. S.; Tamm, L. K., Membrane Structures of the Hemifusion-Inducing Fusion Peptide Mutant G1S

and the Fusion-Blocking Mutant G1V of Influenza Virus Hemagglutinin Suggest a Mechanism for Pore Opening in Membrane Fusion. *JOURNAL OF VIROLOGY* **2005,** 79, (18), 12065-12076.

12. Epand, R. M.; Epand, R. F.; Martin, I.; Ruysschaert, J. M., Membrane interactions of mutated forms of the influenza fusion peptide. *Biochemistry* **2001,** 40, (30), 8800-8807.

13. Qiao, H.; Armstrong, R. T.; Melikyan, G. B.; Cohen, F. S.; White, J. M., A specific point mutant at position 1 of the influenza hemagglutinin fusion peptide displays a hemifusion phenotype. *Molecular Biology of the Cell* **1999,** 10, (8), 2759-2769.

14. Sanders, C. R.; Hareb, B. J.; Howardc, K. P.; Prestegardc, J. H., Magnetically-oriented phospholipid micelles as a tool for the study of membrane-associated molecules. *Progress in Nuclear Magnetic Resonance Spectroscopy* **1994,** 26, 421-444.

15. Sanders, C. R.; Landis, G. C., Reconstitution of membrane proteins into lipid-rich bilayered mixed micelles for NMR studies. *Biochemistry* **1995,** 34, (12), 4030-40.

16. Sanders, C. R.; Prosser, R. S., Bicelles: a model membrane system for all seasons? *Structure* **1998,** 6, (10), 1227-1234.

17. Sanders, C. R.; Schwonek, J. P., Characterization of magnetically orientable bilayers in mixtures of dihexanoylphosphatidylcholine and dimyristoylphosphatidylcholine by solid-state NMR. *Biochemistry* **1992,** 31, (37), 8898–8898.

18. Forrest, B. J.; Reeves, L. W., New lyotropic liquid crystals composed of finite nonspherical micelles. *chemical review* **1981,** 81, (1), 1–14.

19. Prosser, R. S.; Hunt, S. A.; DiNatale, J. A.; Vold, R. R., Magnetically Aligned Membrane Model Systems with Positive Order Parameter: Switching the Sign of Szz with Paramagnetic Ions. *J. AM. Chem. Soc.* **1996,** 118, (1), 269–270.

20. Yamaguchi, S.; Hong, T.; Waring, A.; Lehrer, R. I.; Hong, M., Solid-state NMR investigations of peptide-lipid interaction and orientation of a ss-sheet antimicrobial peptide, protegrin. *Biochemistry* **2002,** 41, (31), 9852-9862.

21. Lee, D. K.; Wittebort, R. J.; Ramamoorthy, A., Characterization of N-15 chemical shift and H-1-N-15 dipolar coupling interactions in a peptide bond of uniaxially oriented and polycrystalline samples by one-dimensional dipolar chemical shift solid-state NMR spectroscopy. *J. AM. Chem. Soc.* **1998,** 120, (34), 8868-8874.

22. Oas, T. G.; Hartzell, C. J.; DAHLQUIST, F. W.; DROBNY, G. P., THE AMIDE N-15 CHEMICAL-SHIFT TENSORS OF 4 PEPTIDES DETERMINED FROM C-13 DIPOLE-COUPLED CHEMICAL-SHIFT POWDER PATTERNS. *J. AM. Chem. Soc.* **1987,** 109, (20), 5962-5966.

23. Quine, J. R.; Achuthan, S.; Asbury, T.; Bertram, R.; Chapman, M. S.; Hu, J.; Cross, T. A., Intensity and mosaic spread analysis from PISEMA tensors in solid-state NMR. *Journal of Magnetic Resonance* **2006,** 179, (2), 190-198.

24. Marassi, F. M.; Opella, S. J., A solid-state NMR index of helical membrane protein structure and topology. *Journal of Magnetic Resonance* **2000,** 144, (1), 150-155.

25. Hemminga, M. A.; Cullis, P. R., 31P NMR Studies of Oriented Phospholipid Multilayers. *J. Mag. Reson.* **1982,** 47, 307-323.

26. Lazo, N. D.; Hu, W.; Cross, T. A., Low-Temperature Solid-State N-15 Nmr Characterization of Polypeptide Backbone Librations. *Journal of Magnetic Resonance Series B* **1995,** 107, (1), 43-50.

27. Mascioni, A.; Eggimann., B. L.; Veglia, G., Determination of helical membrane protein topology using residual dipolar couplings and exhaustive search algorithm: application to phospholamban. *Chemistry and Physics of Lipids* **2004,** 132, (1), 133-144.

28. Jardetzky, T. S.; Lamb, R. A., Virology: A class act. *Nature* **2004,** 427, 307-308.

29. Qiang, W.; Weliky, D. P., HIV Fusion Peptide and Its Cross-Linked Oligomers: Efficient Syntheses, Significance of the Trimer in Fusion Activity, Correlation of beta Strand Conformation with Membrane Cholesterol, and Proximity to Lipid Headgroups. *Biochemistry* **2009,** 48, (2), 289-301.

30. Yang, R.; Prorok, M.; Castellino, F. J.; Weliky, D. P., A trimeric HIV-1 fusion peptide construct which does not self-associate in aqueous solution and which has 15-fold higher membrane fusion rate. *J. Am. Chem. Soc.* **2004,** 126, (45), 14722-14723.

31. Castano, S.; Desbat, B., Structure and orientation study of fusion peptide FP23 of gp41 from HIV-1 alone or inserted into various lipid membrane models (mono-, bi- and multibi-layers) by FT-IR spectroscopies and Brewster angle microscopy. *Biochim. Biophys. Acta-Biomembr.* **2005,** 1715, (2), 81-95.

Chapter 6 Summary and Future Directions

My work during the past years has been focused on the membrane-associated influenza fusion peptide (IFP) and extensive aspects of IFP have been studied including the secondary structure, membrane location and orientation of IFP. The overall goal is to correlate these structural characteristics to the functional activity of IFP and to gain some insights into the mechanism of IFP-induced vesicle and target cell membrane fusion. All the structural characterizations were done with IFP membrane samples at both pH 5.0 and pH 7.4 in an effort to find the structural basis/bases for the pH-mediated IFP-induced membrane fusion. In my work, solid-state NMR was mainly used.

The secondary structure of membrane-associated IFP was studied by the ^{13}C chemical shift and internuclear (^{13}CO – ^{13}CO and ^{13}CO – ^{15}N) distance measurements. It was shown that the physiologically relevant membrane cholesterol content is correlated with a large population of β strand IFP at both fusogenic pH 5.0 and non-fusogenic pH 7.4. In membranes that lacked cholesterol (DTPC/DTPG, 4:1 or POPC/POPG, 4:1), predominant α helical IFP conformation was observed with C-terminal helical conformation at both pH 5.0 and 7.4. Specifically, the IFP structure starts with an N-terminal helix ranging from Leu-2 to Glu-11 followed by a turn at Asn-12 followed by a C-terminal helix (structure A). This structure was observed for membrane-associated IFP at both pHs. An additional similar structure with some variations in the turn region was observed for the membrane-associated IFP at pH 5.0 with the N-terminal helix

extending from Leu-2 to Ile-10 and the turn at Glu-11 and Asn-12 redirecting the C-terminal helix (structure B). The ratio of structure A/structure B is ~3:1 for membrane-associated IFP at pH 5.0. The structural variation at residue Glu-11 is responsible for the two different structures, namely two different conformations were observed for Glu-11 based on two detected chemical shift sets which were consistent with α helix and β strand structures respectively.

The changes in the protonation states of the Glu-11 side chain COOH were also examined with the ^{13}C chemical shifts for IFP samples at different pHs. As the pH changed from 7.4 to 4.0, the ratio between the population of the protonated state and the non-protonated state ($COOH/COO^-$) was ordered pH 4.0 > pH 5.0 > pH 7.4, which indicated that Glu-11 is sensitive to the solution pH and in contact with the water layer above the membrane surface.

Because membrane disruption is thought to be important during the membrane fusion and is correlated to the membrane insertion of fusion peptide, the membrane location of helical IFP was studied with $^{13}CO - ^{31}P$ and $^{13}CO - ^{19}F$ distance measurements. The detectable contact between the Ile-6 ^{13}CO and ^{19}F (C16) (~12 Å) indicated that the IFP middle region inserts into the membrane outer leaflets at both pHs. The $^{13}CO - ^{31}P$ REDOR data showed that both the N- and C-terminal regions of IFP (Gly-1 and Gly-20) ^{13}COs are close to ^{31}Ps in the lipid phosphate headgroups (≤7 Å). The results of Gly-1 and Gly-20 being close to the membrane surface and the IFP middle region being inserted into the membranes are consistent with the helix-turn-helix IFP structure and suggest an inverted boomerang structure of membrane-associated IFP. Additional contacts

between ^{13}COs of Phe-3 or Phe-9 and ^{19}F (C16) (~12 Å) for membrane-associated IFP at pH 5.0 suggested a deeper/greater population of membrane insertion of IFP at pH 5.0 relative to pH 7.4.

In addition to the membrane location of the helical IFP, I also studied the IFP N-terminal helix orientation relative the membrane bicelle normal using anisotropic ^{15}N chemical shifts and ^{15}N-^{1}H dipolar couplings. The narrow peaks (linewidth < 10 ppm for chemical shift and < 500 Hz for ^{15}N-^{1}H dipolar coupling) and the big change in peak positions between unflipped and flipped bicelle samples (~ 40 ppm in chemical shifts and ~ 1.0 kHz in dipolar couplings) indicated a good alignment of the IFP N-terminal helix in bicelles. The narrow distribution of peaks (the range of chemical shifts $\leq$ 11 ppm for non-glycine residues and the range of dipolar couplings $\leq$0.6 kHz) suggested appreciable mobility of IFP in membrane bicelles. The ^{15}N chemical shifts and ^{15}N-^{1}H dipolar couplings were analyzed and fitted by a model of fast rotation of the IFP N-terminal helix about its helix axis. The analysis showed a ~45^{o} tilt angle of the IFP N-terminal helix relative to the bicelle normal. The similar appearance of spectra for IFP samples at both pH 5.0 and pH 7.4 and for IFP-G1S or IFP-G1V mutants indicated that the IFP N-terminal helix has a common motional and orientational motif regardless of pH or point mutations to Gly-1.

The proposed fast rotational motion of the IFP N-terminal helix may first appear surprising and difficult to fit with the inverted boomerang structure. However, such a rotational motion is possible considering the highly dynamic nature of lipid molecules in the liquid-crystalline phase and the small size of an

IFP molecule (comparable to a lipid molecule). As mentioned previously, the residue Glu-11 is in contact with water. This fact combine with the inverted boomerang structure suggests that the membrane bilayers are likely being disrupted in a way that the entire IFP C-terminal arm is exposed to water while the C-terminus remains associated with the lipid headgroups. The C-terminal region may be stabilized by the interaction with lipids and water but not by the hydrogen bonds between the IFP N- and C-terminal regions. Therefore the IFP molecule is possibly flexible enough to enable the rotation of the N-terminal helix and retain its secondary structure.

My work features a combination of MAS and static solid-state NMR studies of membrane-associated IFP. Extensive aspects of IFP structural characteristics were explored using these methods and demonstrated the power of this combination. Many remaining questions can be further probed with these methods. For trans-membrane proteins/peptides, the bicelle system has been shown to be successful to determine the protein/peptide structure [1-5] and showed little difference from the results from the mechanically aligned samples (stacked glass plates)[5]. However, there is no precedent of its utilization for a peptide with significant motions which only inserts into a single membrane leaflet. The motions of bicelles complicate the analysis of the data and the existence of short-chain lipids may alter the peptide insertion by interacting with the peptide. It will be interesting to use mechanically aligned samples to study the membrane-bound IFP. The 2D ^{15}N chemical shift and ^{15}N-^{1}H dipolar coupling correlation spectra can provide information not only on the IFP orientation but also on the

IFP secondary structure for the mechanically aligned samples with limited motions. The IFP orientation from different sample types should be compared in order to get further support for the proposed IFP motional and orientational model. The comparison between the results from different methods will also shed the light on the suitability of bicelle systems for the non-trans-membrane peptides. In addition, the lipid compositions of bicelles are limited and the lipid compositions of the membrane bilayers for stacked glass plates can be varied substantially and can be used to study the system with cholesterol.

Another interesting question is whether the β strand IFP also inserts into the membrane and has pH dependence of the insertion. Comparison between helical IFP and helical HFP membrane locations indicated that both peptides have similar insertion with the N- and C-terminal regions in close contact to the lipid phosphorus headgroups and the middle region inserted into the membrane. The β strand HFPs were shown to have a similar insertion motif and the depth of insertion is correlated to their functional activities where a deeper insertion correlates to a higher fusion activity. The interpretation of $^{13}CO - ^{31}P$ and $^{13}CO - ^{19}F$ data for β strand HFP seemed to be more straightforward relative to the α helix HFP because the helix forms wheels and the relative locations of residues on the helix need to be considered and complicate the data interpretation. It will be interesting to study the insertion of β strand IFP in cholesterol-containing membranes at different pHs and correlate the insertion to its function at different pHs. Some preliminary data have been obtained for the β strand IFP in membranes than contained cholesterol and are displayed in the appendix.

REFERENCES

1. Angelis, A. A. D.; Opella, S. J., Bicelle samples for Solid-State NMR of membrane proteins. *Nature protocol* **2007,** 2, (10), 2332-2338.

2. De Angelis, A. A.; Nevzorov, A. A.; Park, S. H.; Howell, S. C.; Mrse, A. A.; Opella, S. J., High-resolution NMR spectroscopy of membrane proteins in aligned bicelles. *J. Am. Chem. Soc.* **2004,** 126, (47), 15340-15341.

3. Howard, K. P.; Opella, S. J., High-Resolution Solid-State NMR Spectra of Integral Membrane Proteins Reconstituted into Magnetically Oriented Phospholipid Bilayers. *J. Magn. Reson., Series B* **1996,** 112, 91-94.

4. Kochendoerfer, G. G.; Jones, D. H.; Lee, S.; Oblatt-Montal, M.; Opella, S. J.; Montal, M., Functional characterization and NMR Spectroscopy on full-length Vpu from HIV-1 prepared by total chemical synthesis. *J. Am. Chem. Soc.* **2004,** 126, (8), 2439-2446.

5. Park, S. H.; Nevzorov, A. A.; Wu, C. H.; Opella, S. J., Three-Dimensional Structure of the Transmembrane Domain of Vpu from HIV-1 in Aligned Phospholipid Bicelles. *Biophys. J.* **2006,** 91, (8), 3032-3042.

Appendix I

Natural Abundance Corrections for $(\Delta S/S_0)^{exp}$

This section considers the determination of $(\Delta S/S_0)^{cor}$ for ^{13}C–^{15}N, ^{13}C–^{31}P and ^{13}C–^{19}F REDOR, the contribution to $(\Delta S/S_0)^{exp}$ due only to labeled nuclei. $(\Delta S/S_0)^{cor}$ is equivalently described by the parameter "*f*", the S_1/S_0 ratio for the labeled ^{13}CO nuclei considering only other labeled nuclei. Comparison of $(\Delta S/S_0)^{cor}$ to $(\Delta S/S_0)^{sim}$ yields the labeled nuclei internuclear dipolar couplings and distances. Contributions to S_0 and S_1 are considered for different experiments.

1.Determination of $(\Delta S/S_0)^{cor}$ for ^{13}CO–^{15}N REDOR

Determination of $(\Delta S/S_0)^{cor}$ relied on estimating the natural abundance (*n.a.*) contribution to $(\Delta S/S_0)^{exp}$ and this estimation was based on the following parameters/approximations.

A1. There is 99% labeling of the ^{13}CO and ^{15}N nuclei. $S_1 = S_0$ for a labeled ^{13}CO in IFP with a $^{13}CO\cdots^{15}N$ pair.

A2. (1) $S_1 = 0$ for a labeled ^{13}CO separated by one or two bonds from a natural abundance ^{15}N. The S_1 is not affected by other natural abundance ^{15}N. (2) $S_1 = 0$ for natural abundance backbone ^{13}COs which are separated by one or two bonds from the labeled ^{15}N. $S_1 = S_0$ for other natural abundance backbone ^{13}CO sites. Criteria (1) and (2) are based on the close distance ($\leq$ 2.5 Å) and consequent

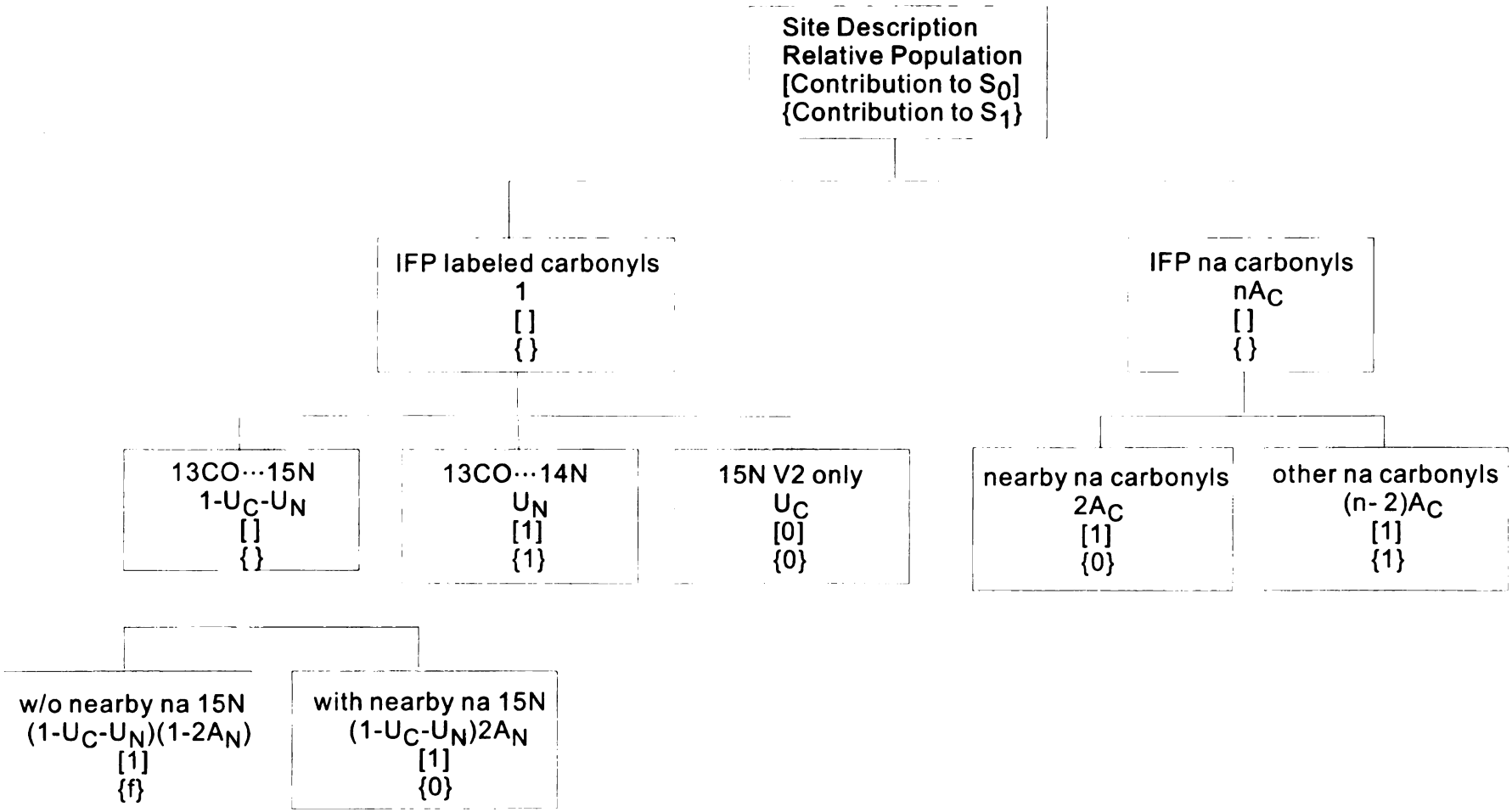

Figure A1. Flow chart of derivation of $(S_1/S_0)^{cor}$ for REDOR of IFP-$A5_CF9_N$, IFP-$F9_CG13_N$ and IFP-$G13_CM17_N$. The four rows in each box are in sequence: the site description, its relative population, and its contributions to S_0 and S_1.

strong (≥ 200 Hz) dipolar coupling of ^{13}CO and ^{15}N nuclei separated by one or two bonds.

The $(\Delta S/S_0)^{cor}$ expression is calculated using the following parameters: U_C and U_N, the fractions of ^{12}CO and ^{14}N of the labeling CO···N sites, respectively; A_C and A_N, the ^{13}C and ^{15}N natural abundances, respectively; and n, the total number of unlabeled peptide backbone CO sites in the IFP. A flow chart for the determination of $(S_1/S_0)^{cor}$ or "f" is given in Figure A1.

A complete derivation of $(\Delta S/S_0)^{cor}$ follows:

$$\left(\frac{\Delta S}{S_0}\right)^{exp} = \frac{S_0^{exp} - S_1^{exp}}{S_0^{exp}} \qquad \text{(A1)}$$

S_0^{exp} is expressed as the sum of contributions from labeled ^{13}CO nuclei (S_0^{lab}) and from natural abundance ^{13}CO nuclei ($S_0^{n.a.}$):

$$S_0^{exp} = S_0^{lab} + S_0^{n.a.} = 1 - U_C + n A_C \qquad \text{(A2)}$$

S_1^{exp} is also expressed as the sum of contributions from labeled ^{13}CO nuclei (S_1^{lab}) and from natural abundance ^{13}CO nuclei ($S_1^{n.a.}$):

$$S_1^{exp} = S_1^{lab} + S_1^{n.a.} \qquad \text{(A3)}$$

with:

$$S_1^{lab} = (1 - U_C - U_N)(1 - 2A_N)f + U_N \qquad \text{(A4)}$$

and:

$$S_1^{n.a.} = (n-2)A_C \qquad \text{(A5)}$$

where $1 - U_N$ is the fractional ^{15}N labeling of IFP, A_N is the fractional ^{15}N natural abundance and the parameter *f*:

$$f = \frac{S_1^{cor}}{S_0^{cor}} = 1 - \frac{S_0^{cor} - S_1^{cor}}{S_0^{cor}} = 1 - \left(\frac{\Delta S}{S_0}\right)^{cor} \tag{A6}$$

Incorporate Eq. A6 into Eq. A4:

$$\begin{aligned} S_1^{lab} &= (1 - U_C - U_N)(1 - 2A_N)\left[1 - \left(\frac{\Delta S}{S_0}\right)^{cor}\right] + U_N \\ &= (1 - U_C - U_N)(1 - 2A_N) - (1 - U_C - U_N)(1 - 2A_N)\left(\frac{\Delta S}{S_0}\right)^{cor} + U_N \end{aligned} \tag{A7}$$

U_C, U_N, and $2A_N$ are much less than 1 so that:

$$(1 - U_C - U_N)(1 - 2A_N) \cong 1 - U_C - U_N - 2A_N \tag{A8}$$

and:

$$S_1^{lab} \cong 1 - U_C - 2A_N - (1 - U_C - U_N - 2A_N)\left(\frac{\Delta S}{S_0}\right)^{cor} \tag{A9}$$

Incorporate Eqs. A5 and A9 in Eq. A3:

$$S_1^{exp} = 1 - U_C - 2A_N - (1 - U_C - U_N - 2A_N)\left(\frac{\Delta S}{S_0}\right)^{cor} + (n - 2)A_C \tag{A10}$$

Combine Eqs. A2, A3, A4, and A10:

$$S_0^{exp} - S_1^{exp} = [1 - U_C + nA_C] - \left[1 - U_C - 2A_N - (1 - U_C - U_N - 2A_N)\left(\frac{\Delta S}{S_0}\right)^{cor} + (n - 2)A_C\right] \tag{A11}$$

and simplify:

$$S_0^{exp} - S_1^{exp} = 2A_C + 2A_N + (1 - U_C - U_N - 2A_N)\left(\frac{\Delta S}{S_0}\right)^{cor} \quad \text{(A12)}$$

Combine Eqs. A2 and A12:

$$\left(\frac{\Delta S}{S_0}\right)^{exp} = \frac{2A_C + 2A_N + (1 - U_C - U_N - 2A_N)\left(\frac{\Delta S}{S_0}\right)^{cor}}{1 - U_C + nA_C} \quad \text{(A13)}$$

and rewrite:

$$\left(\frac{\Delta S}{S_0}\right)^{cor} = \frac{1 - U_C + nA_C}{(1 - U_C - U_N - 2A_N)}\left(\frac{\Delta S}{S_0}\right)^{exp} - \frac{2A_C + 2A_N}{(1 - U_C - U_N - 2A_N)} \quad \text{(A14)}$$

Expressions in Eq. A14 were numerically evaluated using A_C = 0.011, A_N = 0.0037, n = 27, and $U_C = U_N$ = 0.01:

$$\left(\frac{\Delta S}{S_0}\right)^{cor} = 1.323\left(\frac{\Delta S}{S_0}\right)^{exp} - 0.030 \quad \text{(A15)}$$

The uncertainties in $(\Delta S/S_0)^{exp}$ were calculated as:

$$\sigma^{exp} = \frac{\sqrt{S_0^2\sigma_{S_1}^2 + S_1^2\sigma_{S_0}^2}}{S_0^2} \quad \text{(A16)}$$

The σ^{cor} resulted from Eq. A15 was:

$$\sigma^{cor} = 1.323\,\sigma^{exp} \quad \text{(A17)}$$

2. *Determination of* $(\Delta S/S_0)^{cor}$ for ^{13}CO–^{31}P *and* ^{13}CO–^{19}F*(C16) REDOR*

Similar to the ^{13}CO–^{15}N REDOR data correction, the natural abundance correction starts from considering that both S_0 and S_1 come from the labeled

^{13}CO and the natural abundance ^{13}COs (including unlabeled residues of IFP and ^{13}CO from the 9 mol% 16-^{19}F-DPPC):

$$\left(\frac{\Delta S}{S}\right)^{exp} = \frac{S_0^{cor} + S_0^{na}(IFP) + S_0^{na}(DPPC) - S_1^{cor} - S_1^{na}(IFP) - S_1^{na}(DPPC)}{S_0^{cor} + S_0^{na}(IFP) + S_0^{na}(DPPC)} \tag{A18}$$

A few algebraic manipulation leads to

$$\left(\frac{\Delta S}{S_0}\right)^{cor} = (1 + \frac{S_0^{na}(IFP) + S_0^{na}(DPPC)}{S_0^{cor}}) \cdot \left(\frac{\Delta S}{S_0}\right)^{exp} - \frac{S_0^{na}(IFP)}{S_0^{cor}} \cdot \left(\frac{\Delta S}{S_0}\right)^{na}(IFP) - \frac{S_0^{na}(DPPC)}{S_0^{cor}} \cdot \left(\frac{\Delta S}{S_0}\right)^{na}(DPPC) \tag{A19}$$

The terms $(\Delta S/S_0)^{cor}$, $(\Delta S/S_0)^{na}$(IFP) and $(\Delta S/S_0)^{na}$(DPPC) represent the contribution to REDOR dephasing from the labeled ^{13}CO, the natural abundance of the unlabeled residues and the natural abundance ^{13}CO from 16-^{19}F-DPPC, respectively. The S_0 term in Eq. A19 has the numerical values

$$\begin{aligned} S_0^{cor} &= 1 \\ S_0^{na}(IFP) &= 26 \times 0.011 = 0.286 \\ S_0^{na}(DPPC) &= 2.5 \times 2 \times 0.011 = 0.055 \end{aligned} \tag{A20}$$

The values of $(\Delta S/S_0)^{na}$(IFP) were calculated from the experimentally available $(\Delta S/S_0)^{exp}$ for the sample at different pHs and the values $(\Delta S/S_0)^{na}$(DPPC) were calculated using a ^{13}CO–^{31}P or ^{13}CO–^{19}F two-spin system with literature internuclear distance of the DPPC molecule (Venable et al., *J. Chem. Phys.*, 2000, **112**, 4822-4832). Table A1 and A2 provide the numerical values.

Table A1. The $(\Delta S/S_0)^{na}$ (IFP)

		^{13}CO-^{31}P [a]		^{13}CO-(16-^{19}F) [a b]	
Peptide		pH 5.0	pH 7.4	pH 5.0	pH 7.4
	2	0.045	0.018	0.032	0.031
	8	0.160	0.118	0.018	0.020
τ(ms)	16	0.319	0.204	0.070	0.069
	24	0.395	0.266	0.095	0.051
	32	0.460	0.339	*n.d.* [c]	

[a] The ^{13}CO-^{31}P values were based on the $(S_1/S_0)^{exp}$ of samples labeled at Gly-1, Leu-2, Phe-3, Ala-5, Ile-6, Phe-9, Gly-13, Gly-16 and Gly-20. The ^{13}CO-^{19}F(C16) values were based on samples labeled at Gly-1, Leu-2, Phe-3, Ile-6, Phe-9, Gly-13 and Gly-16.
[b] The maximum τ for ^{13}CO-^{19}F experiments was 24 ms.
[c] *n.d.* ≡ not determined

Table A2. The $(\Delta S/S_0)^{na}$ (DPPC) [a]

		^{13}CO-^{31}P	^{13}CO-(16-^{19}F) [b]
	2	0.025	0.000
	8	0.318	0.000
τ (ms)	16	0.695	0.000
	24	0.811	0.000
	32	0.907	*n.d.* [c]

[a] A distance of 15.2 Å was used for ^{13}CO-^{19}F(C16).
[b] The maximum τ for ^{13}CO–^{19}F experiments was 24 ms.
[c] *n.d.* ≡ not determined

Appendix II

Some Additional Data for IFP

This section will present some complementary data for the membrane- or bicelle-associated IFP samples. These data include some ^{31}P spectra of membrane-associated IFP samples, ^{13}CO–^{31}P and ^{13}CO–^{19}F(C5) REDOR measurements for IFP membrane samples that contained cholesterol and two ^{15}N chemical shift and ^{15}N-^{1}H dipolar coupling correlation spectra of the IFP C-terminus.

1. ^{31}P spectra

The dependence of ^{31}P spectra of membranes with bound IFP on pH, temperature and membrane composition was tested and the spectra are displayed in Figure A2. All the spectra have similar appearance with each other and with the spectra shown in Figure 22. The lineshapes of these spectra agree with the lamellar phase of the membrane samples and are independent of temperature, pH and membrane lipid compositions.

2. REDOR measurements

Figure A3 displays the representative ^{13}CO–^{31}P and ^{13}CO–^{19}F(C5) REDOR spectra at long dephasing time (32 ms for ^{13}CO–^{31}P and 24 ms for ^{13}CO–^{19}F(C5) REDOR measurement) for samples that contained IFP/DTPC/DTPG/CHOL (0.8:16:4:10) at pH 5.0. For the ^{13}CO–^{19}F(C5) REDOR measurements, additional 9 mol% of 5-^{19}F-DPPC was also incorporated into the samples. The peak chemical shifts are summarized in table A3 and compared to

the database distribution of the ^{13}CO chemical shifts for corresponding residues with different secondary structures. In particular, Gly, Ala and Phe have the ^{13}CO chemical shifts of 175.51 ± 1.23, 179.40 ± 1.32, 177.13 ± 1.38 ppm for the helical conformation and 172.55 ± 1.58, 176.09 ± 1.51, 174.25 ± 1.63 ppm for the β strand conformation. The measured chemical shifts of Gly-1, Ala-5 Phe-9 and Gly-13 have better consistency with the β strand conformation than with the helical conformation and the peaks for Ala-5 and Phe-9 have relative narrow linewidths (2 ppm) suggesting that at least the region from Ala-5 to Phe-9 has a well defined β strand structure. The peak of Gly-20 is broad (~ 5 ppm linewidth) and agrees better helical conformation.

The ^{13}CO–^{31}P REDOR experiments were carried out for IFP samples at pH 5.0 with ^{13}CO labels at Gly-1, Ala-5 or Gly-20. The intensity of the S_1 spectra of Gly-1 and Gly-20 are greatly reduced (> 60%) compared to the corresponding S_0 spectra, which suggests a close contact between Gly-1 and Gly-20 ^{13}COs with the phosphorus. The S_0 and S_1 spectra of Ala-5 have about equal intensity and indicate that Ala-5 is not close to the lipid phosphate headgroups. As displayed in Figure A4a and b, the experimental dephasing curves of Gly-1 and Gly-20 with fast build-up provide further evidence for the close contact between the ^{13}COs of these two residues and the phosphate headgroups. The flat dephasing curve of Ala-5 (cf. Figure A4c) supports a long distance between the Ala-5 ^{13}CO and the lipid phosphate headgroups.

Table A3. Peak ^{13}CO chemical shifts in ppm for IFP samples that contained cholesterol at pH 5.0 [a]

Gly-1	Ala-5	Phe-9	Gly-13	Gly-20
170.0	175.2	172.0	173.3	175.2

[a] Typical uncertainties in peak shifts are ± 0.4 ppm as determined from the measurements on samples that contained peptide with the same labeled residue but different membranes.

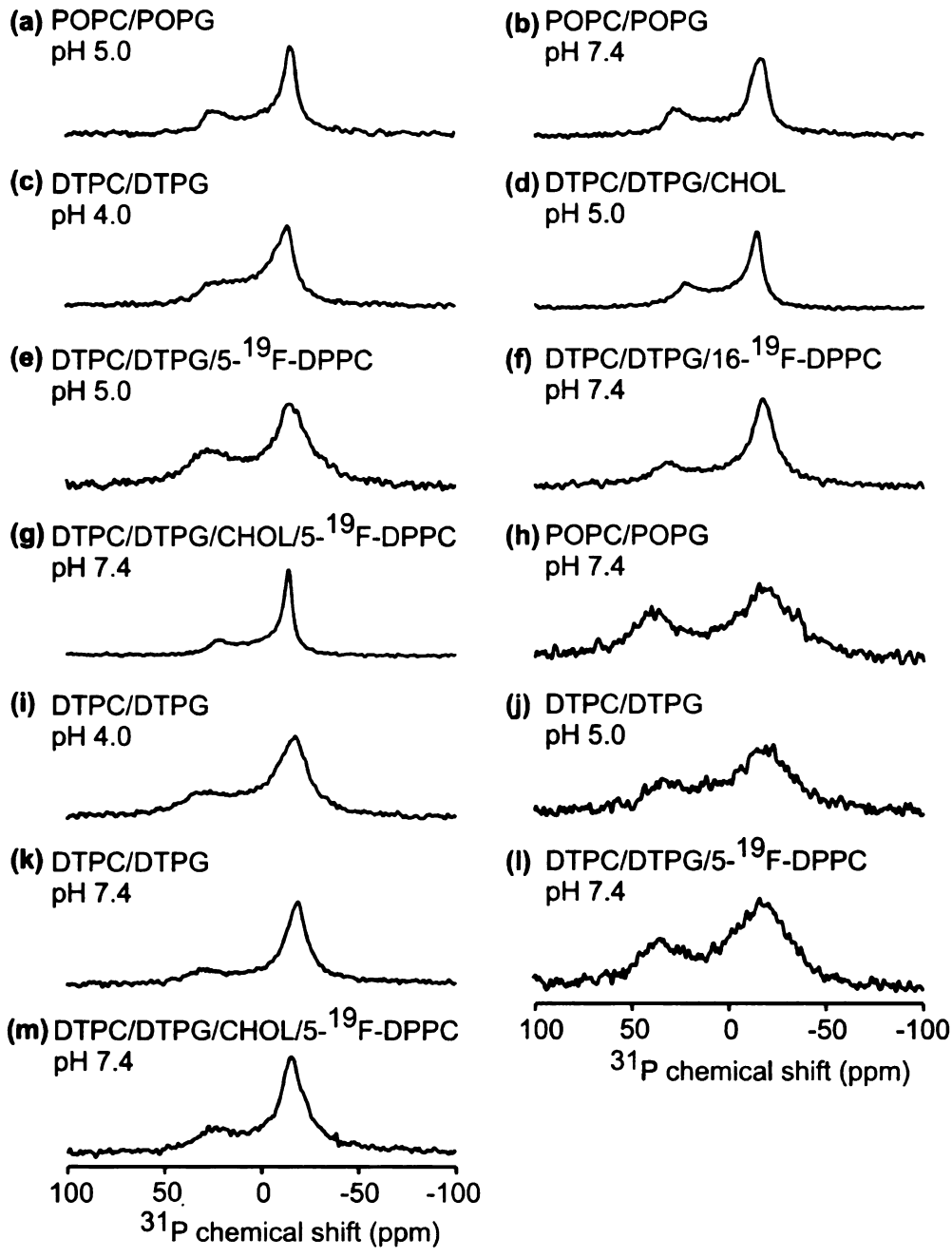

Figure A2. ^{31}P spectra of membranes with bound IFP. The sample composition and pH are labeled on top of each spectrum. The temperature of the gas that flowed around each sample was (a-g) 35 °C or (h-m) 10 °C. The general lipid and peptide ratio was IFP/PC/PG (0.8:16:4 μmol). For some samples, 10 μmol cholesterol or/and 9 mol% 5-^{19}F-DPPC was incorporated. Each spectrum was processed with 200 Hz Gaussian line broadening and was the sum of 400-2000 scans.

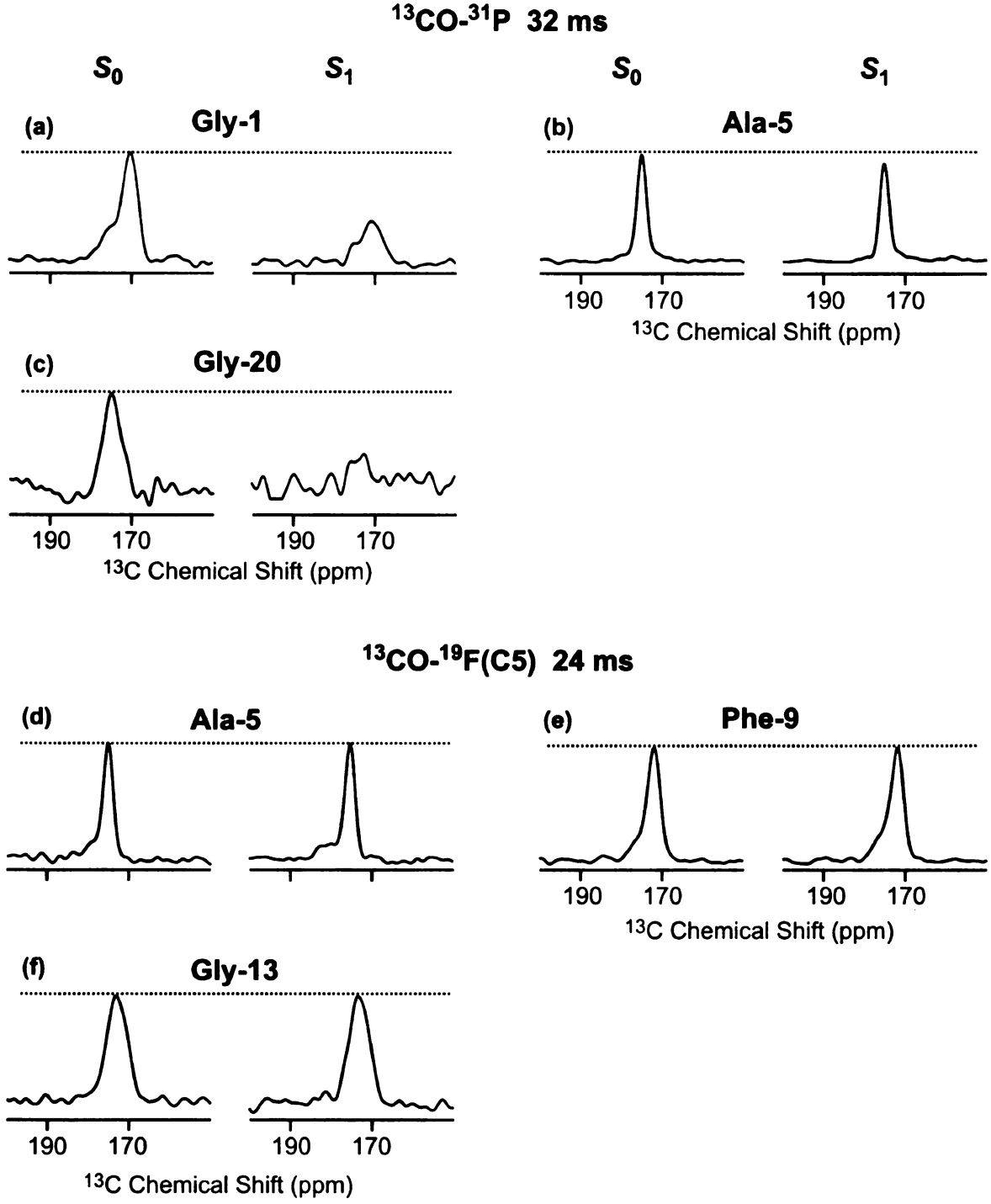

Figure A3. REDOR ^{13}C S_0 and S_1 NMR spectra at long dephasing time for membrane-associated IFP samples at pH 5.0. Each sample had the composition of DTPC/ DTPG/CHOL (16:4:10 μmol) and 0.8 μmol IFP. The samples used to obtain spectra (d-f) contained 9 mol% 5-^{19}F-DPPC lipid. Each spectrum was processed with 200 Hz Gaussian line broadening and was the sum of (a) 22000, (b) 25598, (c) 16650, (d) 1200, (e) 15940 and (f) 7390 scans.

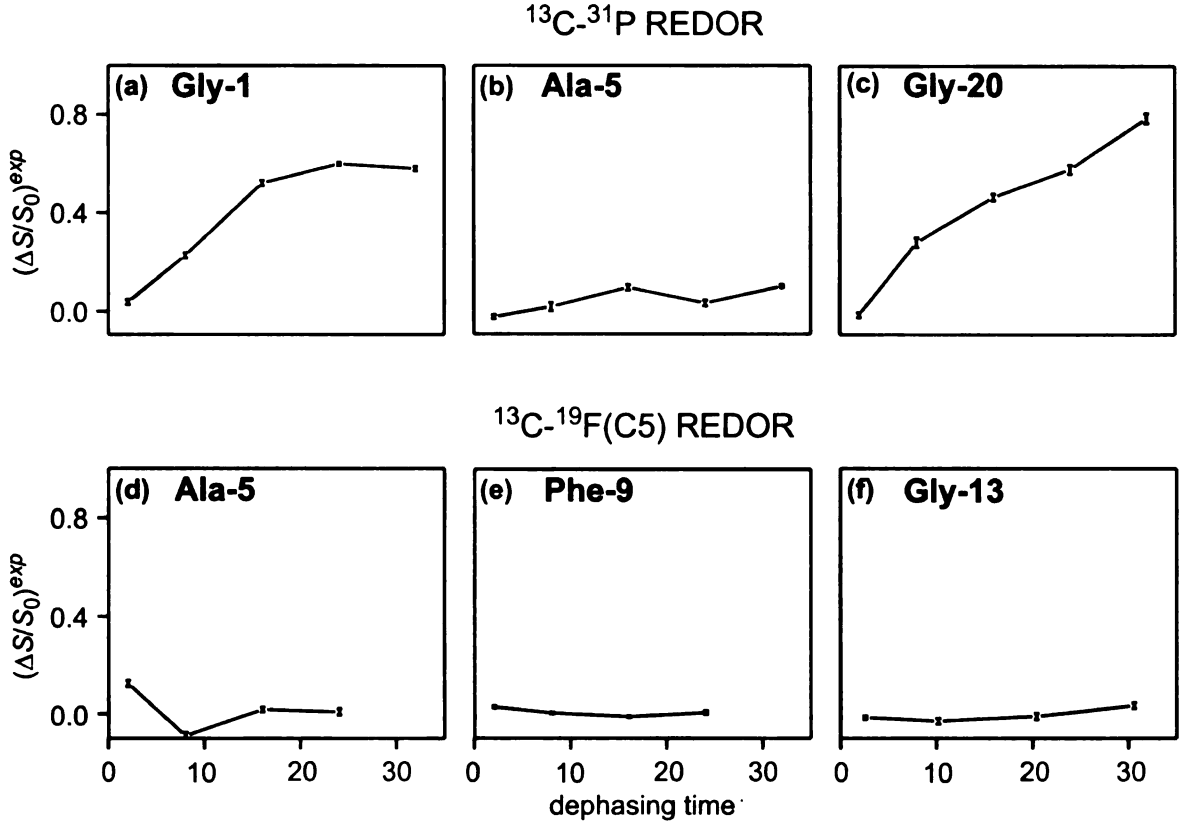

Figure A4. Experimental REDOR dephasing curves corresponding for IFP samples at pH 5.0. The uncertainties are represented by the error bars and typically ±0.01-0.02. The ^{13}CO labeled residues are labeled on top of each spectrum. The samples used were the same as the ones used to take the corresponding spectra in Figure A1.

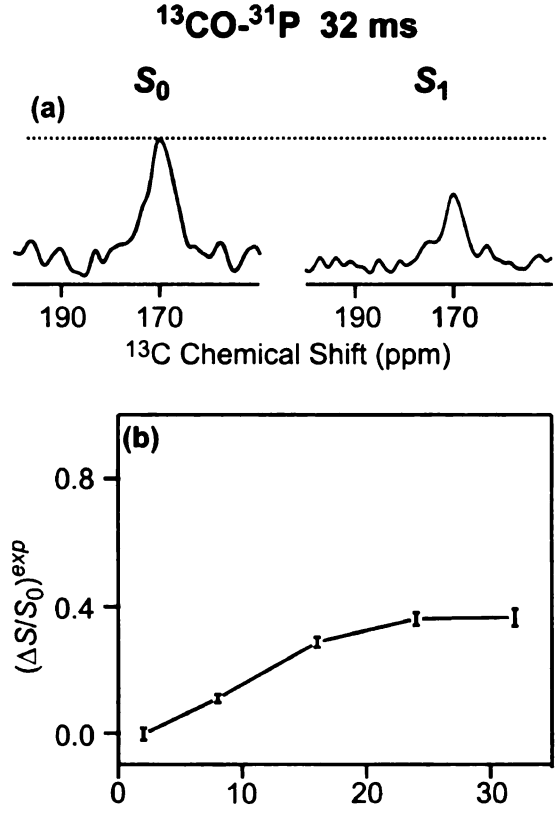

Figure A5. (a) ^{13}CO –^{31}P REDOR S_0 and S_1 NMR spectra at τ = 32 ms and (b) the experimental dephasing curve for membrane-associated IFP-G1$_C$ sample at pH 7.4. The sample used to obtain the data had the composition of DTPC/ DTPG/CHOL (16:4:10 µmol) and 0.8 µmol IFP. The spectra in (a) were processed with 200 Hz Gaussian line broadening and were the sum of ~15000 scans. The uncertainties in (b) are represented by the error bars and typically ±0.01-0.02.

The ^{13}CO–^{19}F(C5) REDOR spectra were taken for IFP samples at pH 5.0 with ^{13}CO labels at Ala-5, Phe-9 or Gly-13. No obvious dephasing was observed for any of the labeled ^{13}COs, evidenced by the similar intensity of the S_0 and S_1 spectra at τ = 24 ms and the flat dephasing curves (cf. Figure A3d-f and A4d-f). This could be due to their long distances relative to ^{19}F(C5) and/or the small population of 5-^{19}F-DPPC incorporated into the lipids s discussed in Chapter 4.

The ^{13}CO–^{31}P REDOR data are generally consistent between the helical IFP and β strand IFP that the N- and C-termini are close to the phosphate headgroups and the middle region is relatively far away from the phosphorus. However, further supports are required to determine whether IFP is inserted into the membrane bilayer.

The ^{13}CO–^{31}P REDOR experiments was also done with an IFP sample that contained IFP/DTPC/DTPG/CHOL (0.8:16:4:10) at pH 7.4. The chemical shift is 170.2 ppm, consistent with β strand conformation. The S_0 and S_1 spectra and the experimental dephasing curve are shown in Figure A5. The S_1 spectrum was reduced by ~36% compared to the S_0 spectrum at τ = 32 ms and the dephasing curve has a slower build-up compared to corresponding curve of the pH 5.0 sample, which suggests a longer distance between Gly-1 ^{13}CO and the lipid phosphate headgroups relative to the pH 5.0 sample.

3. Static NMR

Figure A6 shows the ^{15}N chemical shift and ^{15}N-^{1}H dipolar coupling spectra of the unflipped bicelle-associated IFP-G13$_C$M17$_N$ at pH 5.0 and pH 7.4.

Two crosspeaks were observed for the pH 5.0 sample and may correspond to two slightly different N-H tensor orientations of Met-17. The detected chemical shifts and dipolar couplings (cf. table A5) are comparable to the values obtained for the residues at the IFP N-terminal helix which may be due to the similar orientations and motions between the N- and C- terminus. However, the data from only one residue is not enough to make the conclusion. The measured chemical shifts and dipolar coupling may also reflect a relative static residue without significant motions with a very different orientation from the N-terminus. The measurement of flipped bicelle sample and/or other residues will enable some further analyses.

Table A4. ^{15}N chemical shifts (σ) and N-H dipolar couplings (v) for the aligned IFP-$G13_CM17_N$ samples at pH 5.0 and pH 7.4 [a]

pH 5.0 [b]		pH 7.4	
σ (ppm) [c]	v (kHz) [e]	σ (ppm)	v (kHz)
108	0.5	102	0.7
103	0.8		

[a] Data were obtained with IFP:DTPC ~0.02 and 40 °C sample nitrogen gas temperature.
[b] Two sets of peak were observed for the pH 5.0 sample.
[c] The uncertainty in each chemical shift is estimated to be ±1 ppm based on the uncertainties of other similar experiments (cf. table 12).
[d] The uncertainty in each dipolar coupling is estimated to be ±250 Hz.

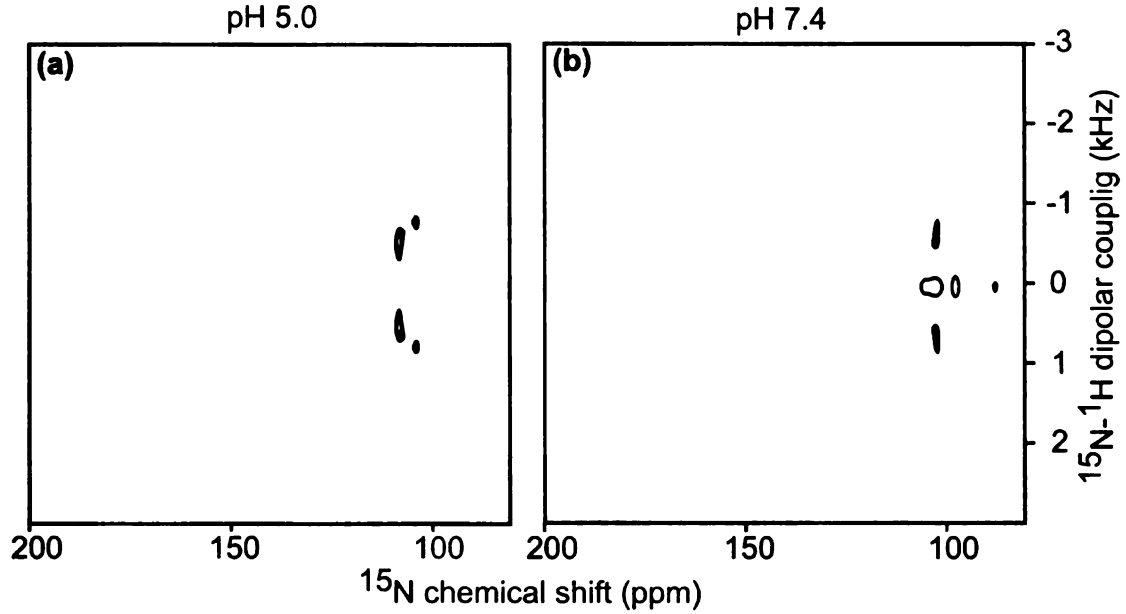

Figure A6. 2D ^{15}N chemical shift and ^{15}N-^{1}H dipolar coupling correlation spectra for the unflipped bicelle-associated IFP-G13$_C$M17$_N$ at (a) pH 5.0 and (b) pH 7.4. The samples used to obtain the spectra had the composition of DTPC/DMPC$_{d54}$/DHPC (1:53:1:17 µmol) and 0.7 µmol IFP. Both spectra with PI-WIM-z sequence and "Efree" probe on the 21.4 T spectrometer. The temperature of the gas which flowed around each sample was 40 °C. The total signal averaging time was ~12 hours.

Appendix III

Alternative way of fitting ^{13}C-^{31}P and ^{13}C-^{19}F data

Some of the ^{13}C-^{31}P and ^{13}C-^{19}F data in Chapter 4 were also fitted with a fraction parameter, *f*, which reflects the maximal fractional ^{13}C-^{31}P or ^{13}C-^{19}F dephasing. The logical basis for the *f* parameter includes: (1) two IFP populations; (2) the ^{13}C-^{19}F $(\Delta S/S_0)^{cor}$ may not reach 1 because of the 0.09 mol fraction of fluorinated lipids.

In this analysis, the χ^2 analysis for $(\Delta S/S_0)^{cor}$ based on Eq. 2.10 becomes:

$$\chi^2(d) = \sum_{i=1}^{T} \frac{\left\{ \left(\frac{\Delta S}{S_0} \right)_i^{cor} - f \left(\frac{\Delta S}{S_0}(d) \right)_i^{sim} \right\}^2}{\left(\sigma_i^{cor} \right)^2} \qquad \text{(A21)}$$

The fraction parameter *f* represents the fraction of ^{13}CO that is close enough to the ^{31}P or ^{19}F nuclei to provide non-zero dephasing. This fraction parameter was considered because $(\Delta S/S_0)^{cor}$ reaches plateau values < 1. The data analysis was shown by contour plots in Figure A7 and A8.

These data can be explained by using the assumption that both the ^{13}C-^{31}P and ^{13}C-^{19}F dephasing are originated from a single IFP membrane location at both pHs. In this assumption, the IFP backbone ^{13}COs can have detectable contact with ^{31}P at the membrane surface or ^{16}F(C16) at the membrane bilayer center. For residues Leu-2 and Phe-3 at pH 5.0, the best-fit *f* of ^{13}C-^{31}P data does not reach 100%, which suggests some undetected population of IFP in the membrane system. For these two residues, the best-fit *f* has very narrow distribution which is peaked at 70%. This indicates ~70% of IFP is associated

with the membrane. The ^{13}C-^{19}F data and the ^{13}C-^{31}P data of Phe-9 are not contradictory to this explanation because of their broad distributions which cover most of the *f* values. The broad distribution is due to the small $(\Delta S/S_0)^{exp}$ which can either be fitted with a high fraction factor *f* and small dipolar coupling or with a low *f* but large dipolar coupling. Similarly, for samples at pH 7.4, the best-fit *f* for the ^{13}C-^{31}P data of Phe-3 has a narrow distribution peaked at 35%, which suggests ~35% of IFP is associated with the membrane at pH 7.4.

These data can also be explained by a two-membrane-location-model. In this model, some population of IFP is deeply inserted into the membrane and some other population of IFP is closer to the membrane surface. The ^{13}C-^{31}P dephasing is only originated from the latter population and the ^{13}C-^{19}F dephasing corresponds to the deeply inserted IFP. For samples at pH 5.0, the narrow distribution of ^{13}C-^{31}P data for Leu-2 and Phe-3 peaked at 70% reflects ~70% of IFP is closer to the membrane surface. The population for the deeply inserted IFP can not be derived from the ^{13}C-^{19}F contour plots due to their broad distribution of *f* values. For samples at pH 7.4, ~35% of IFP is close to the membrane surface because of the 35% peak value of the best-fit *f* for Phe-3 ^{13}C-^{31}P.

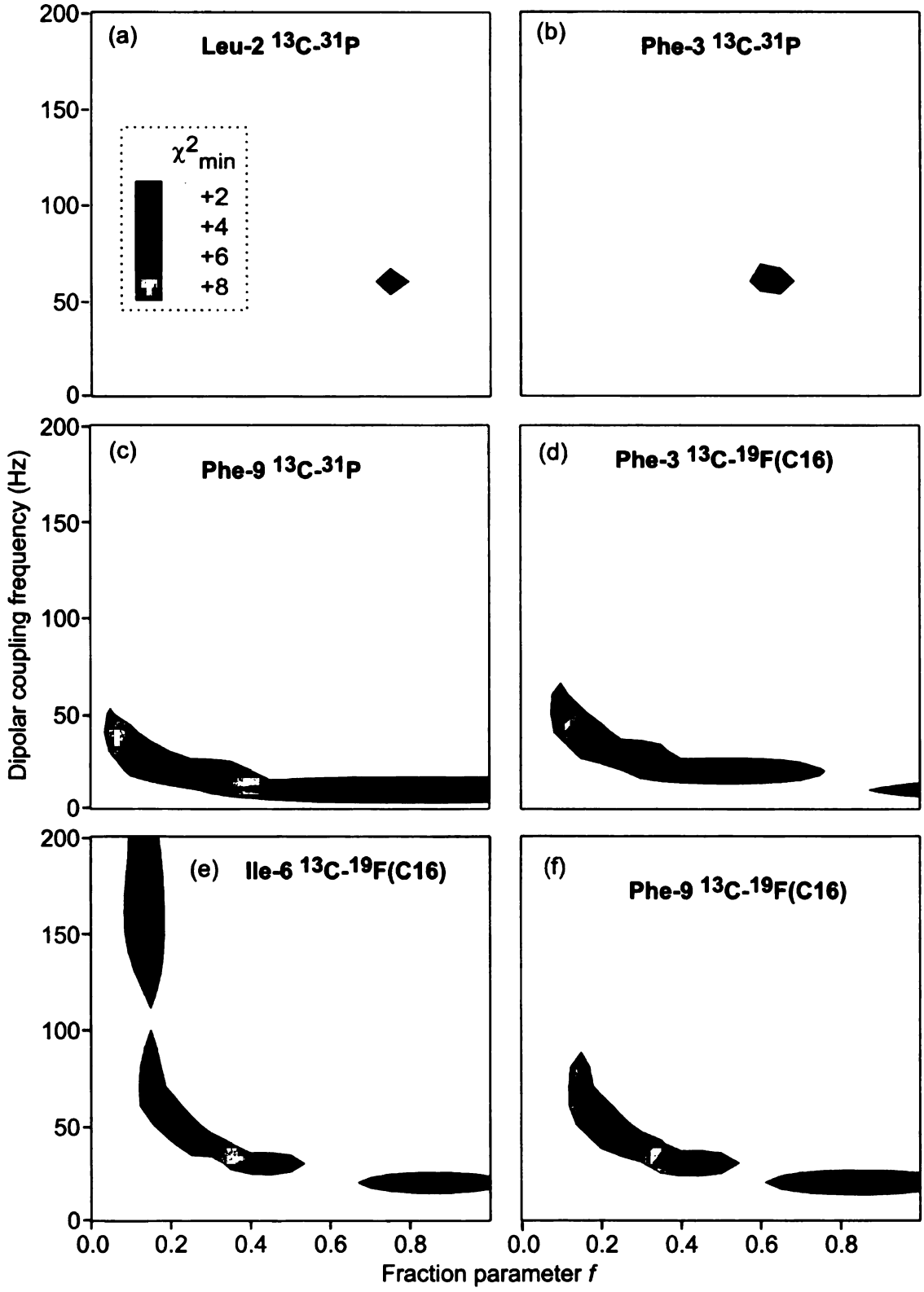

Figure A7. Contour plots for the data fittings of the ^{13}C-^{31}P and ^{13}C-^{19}F data for membrane-associated IFP at pH 5.0. The range of χ^2 used for different region colored regions is represented by scale bar in (a). The value of χ^2_{min} is: (a) 4; (b) 15; (c) 2; (d) 2; (e) 2; (f) 1.

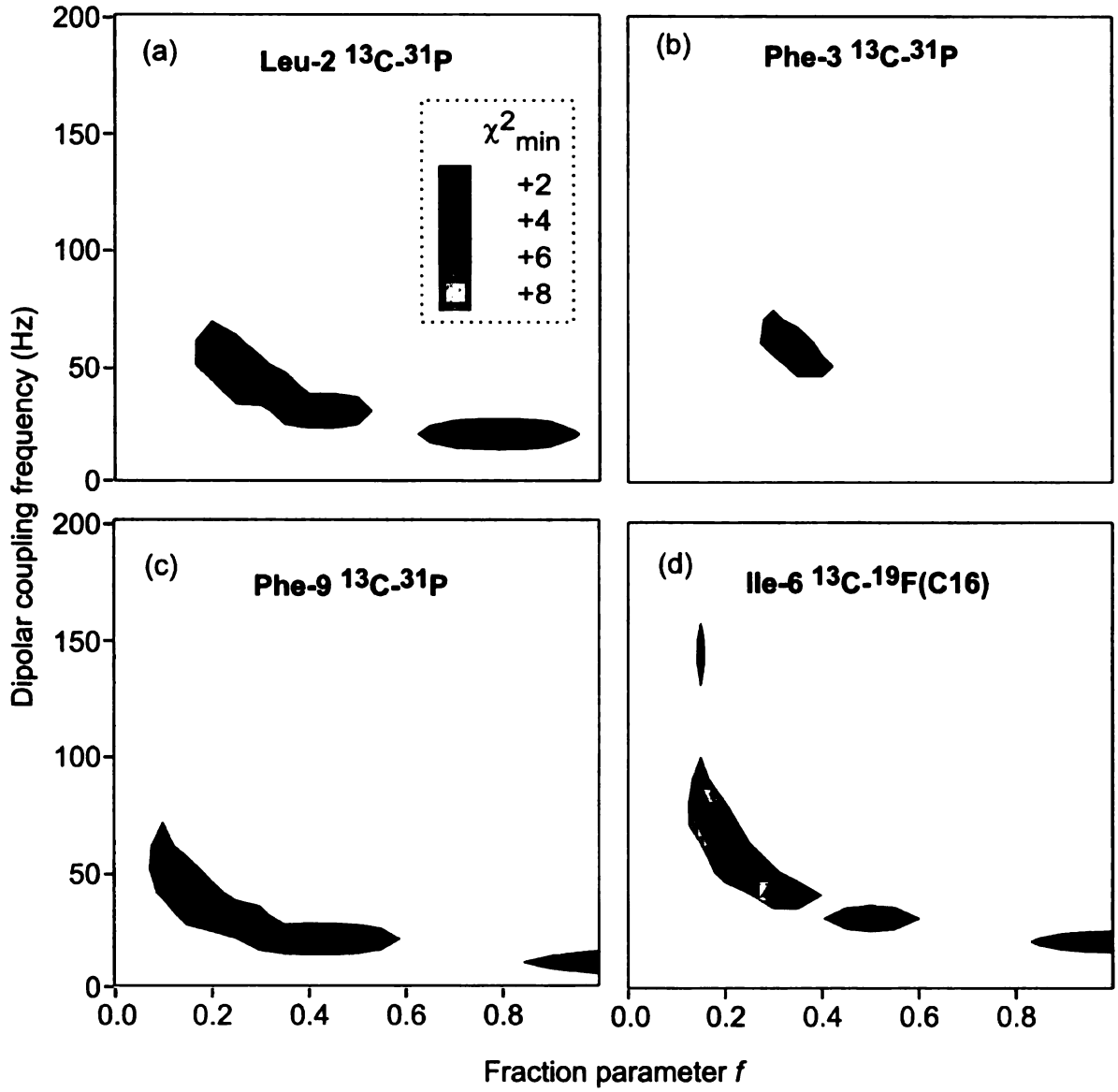

Figure A8. Contour plots for the data fittings of the ^{13}C-^{31}P and ^{13}C-^{19}F data for membrane-associated IFP at pH 7.4. The range of χ^2 used for different region colored regions is represented by scale bar in (a). The value of χ^2_{min} is: (a) 2; (b) 2; (c) 1; (d) 1.

Appendix IV

FMOC protection for amino acids and IFP synthesis

This section includes the typical experimental procedures for FMOC protection of amino acids and manual synthesis of IFPs.

1. FMOC protection of amino acids

The amino acid (4 mmol) was dissolved in 20 mL 9% (w/w) sodium carbonate aqueous solution and the solution was cooled in ice bath for 5 min. N-(9-Fluorenylmethoxycarbonyloxy) succinimide (Fmoc-Osu) (4.2 mmol) in 30 mL dimethylformamide (DMF) was then slowly added to the amino acid solution. The resulting mixture was stirred in the icebath and allowed to warm to room temperature overnight. Water (30 mL) was then added and the aqueous layer was extracted with ether (30 mL × 3). The combined water layer was acidified to a pH of 2 with 6 M HCl solution then extracted with ethyl acetate (20 mL × 4). The combined organic layers were washed with saturated brine (20 mL × 2) and dried with anhydrous sodium sulfate. The organic solvent was removed under stream of nitrogen gas and the solid was put under vacuum to remove residual solvents.

2. Manual solid-phase synthesis of IFPs

In addition to the methods described in Chapter 2 to synthesize IFPs, manual synthesis of IFP was also performed for the preparation of some IFP samples.

(1) Gly-preloaded Wang Resin (0.05 mmol) was washed with DMF (4 mL) and then with CH_2Cl_2 (4 mL). Add another 4 mL of CH_2Cl_2 and soak the resin for 2 h.

(2) After completely draining the resin, add 4 mL 20 % piperidine/DMF (v/v) solution, shake for 5 min and drain.

(3) Add another 4 mL 20 % piperidine/DMF (v/v) solution, shake for 20 min.

(4) Activation of Fmoc-amino acid: Dissolve 0.25 mmol Fmoc-amino acid, 0.23 mmol HBTU and 0.23 mmol HOBt in 4 mL DMF and add 175 μL DIPEA to the resulting solution.

(5) Drain the reaction vessel and wash resin with DMF (4 mL × 6) in order to completely remove piperidine.

(6) Coupling: Add the solution in (4) to the reaction vessel and shake for 2 h for Gly and polar amino acids (Glu, Asn, Asp) and 4 h for non-polar amino acid (Leu, Phe, Ala, Ile, Trp, Met).

(7) Drain the reaction vessel and wash resin with DMF (4 mL × 2)

(8) Add 2 mL solution containing acetic anhydride/piperidine/DMF (2:1:3, v/v/v) to the reaction vessel and shake for 5 min.

(9) Drain reaction vessel and wash with DMF (4 mL × 3).

(10) Repeat steps (2)-(9) for all the other residues.

(11) For the last residue, repeat steps (2)-(3) and then wash the resin with DMF (4 mL × 4) and CH_2Cl_2 (4 mL × 3).

(12) Drain and put the resin under vacuum.

(13) Cleavage: Add 3 mL TFA/thioanisole/EDT/anisole (90:5:3:2, v/v/v/v) solution to the resin and shake for 2.5 h.

(14) Filter the reaction mixture and put the filtrate under the stream of nitrogen gas to remove TFA. Then add 50 mL cold ether (diethyl ether or methy-*t*-butyl ether) to the residual solution.

(15) Centrifuge the ether/IFP mixture and collect the precipitate.

(16) Remove the residual ether from the precipitate by nitrogen gas flow and dissolve the peptide in water. Lyophilize the IFP water solution.

(17) Purify lyophilized IFP with HPLC and indentify IFP with MS spectrometry. Figure A9 shows an example of Mass spectrum of IFP.

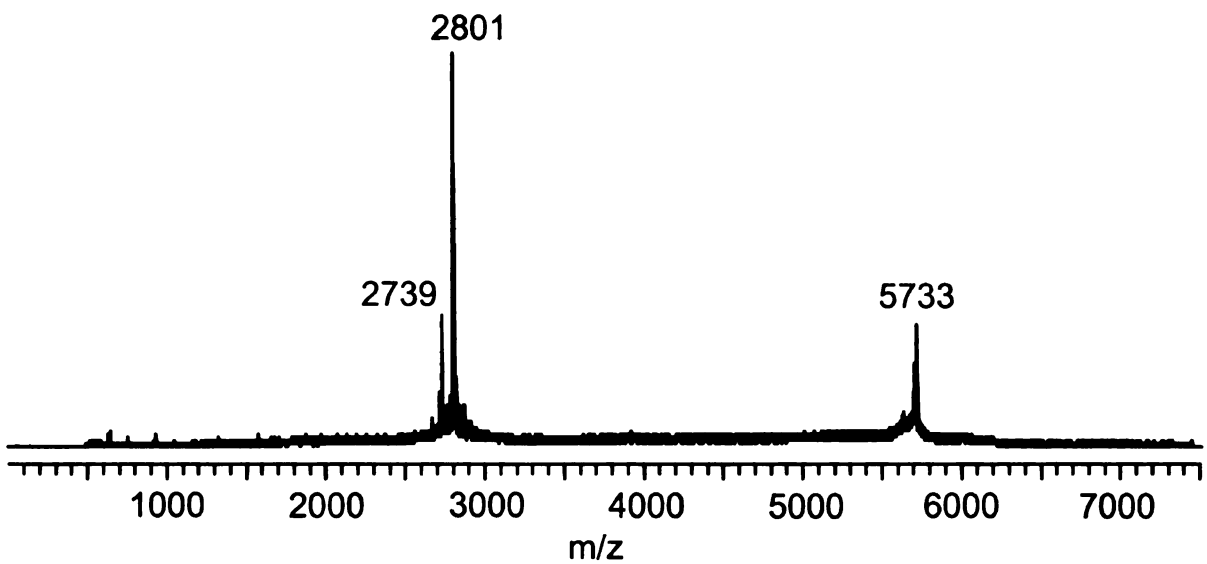

Figure A9. MALDI-TOF MS spectrum for the identification of IFP. The m/z of the major peaks is labeled in the spectrum. The molecular weight of this IFP sample is 2739. The peak with m/z = 2801 corresponds to the IFP molecule associated with one Na^+ and one K^+. The peak with m/z = 5733 corresponds to insulin (5733), which was added to the IFP samples as an internal reference.

Appendix V

Location of NMR data

Figure 13

(a): /home/sunyan4c/data/IFP/redor_CP/PCPG/G1CpH5/2ms S_0
/home/sunyan4c/data/IFP/redor_CP/PCPG/G1CpH7/2ms S_0
/home/sunyan4c/data/IFP/redor_CP/PCPGCHOL/G1C_pH5/2ms S_0
/home/sunyan4c/data/IFP/redor_CP/PCPGCHOL/G1C_pH7/2ms S_0

(b): /home/sunyan4c/data/IFP/redor_CP/PCPG/L2CpH5/2ms S_0
/home/sunyan4c/data/IFP/redor_CP/PCPG/L2CpH7/2ms S_0
/home/sunyan4c/data/IFP/redor_CP/zerodegree/L2CpH5/2ms S_0

(c): /home/sunyan4c/data/IFP/redor_CP/PCPG/F3CpH5/2ms S_0
/home/sunyan4c/data/IFP/redor_CP/PCPG/F3CpH7/2ms
/home/sunyan4c/data/IFP/redor_CP/zerodegree/F3CpH5/2ms S_0

(d): /home/sunyan4b/data/IFP-redor/5AC-9FN/pH5/redor-2ms-070505 S_0
/home/sunyan4b/data/IFP-redor/5AC-9FN/pH7/redor-2ms-043007 S_0
/home/sunyan4c/data/IFP/redor_CP/PCPGCHOL/A5C_pH5/2ms S_0
/home/sunyan4c/data/IFP/redor_CF/5FDPPC/CHOL/A5CpH7/2ms S_0

(e): /home/sunyan4c/data/IFP/redor_CP/PCPG/I6_pH5/2ms-032109 S_0
/home/sunyan4c/data/IFP/redor_CP/PCPG/I6_pH7/2ms-032109 S_0

(f): /home/sunyan4c/data/IFP/ctdqbu/A7G8_IFP_pH5/PCPG/MAS_8kHz/L16-s0
/home/sunyan4c/data/IFP/A7G8-pH7/A7G8_pH7_PCPG
/home/sunyan4c/data/IFP/ctdqbu/A7G8_IFP_pH5/PCPG_chol/MAS_8kHz/L32-s0
/home/sunyan4c/data/IFP/A7G8-pH7/A7G8_chol_pH7

(g): /home/sunyan4b/data/IFP-redor/9FC-13GN/pH5/2ms-sum S_0
/home/sunyan4b/data/IFP-redor/9FC-13GN/pH7/2ms S_0
/home/sunyan4c/data/IFP/redor_CF/redor_CF_C5/PCPGCHOL/F9CpH5/2ms
/home/sunyan4c/data/IFP/redor_CF/redor_CF_C5/PCPGCHOL/F9CpH7/16ms

(h): /home/sunyan4b/data/IFP-redor/13GC-17MN/pH5/redor-2ms-050907 S_0
/home/sunyan4b/data/IFP-redor/13GC-17MN/pH7/redor-2ms-070507 S_0
/home/sunyan4c/data/IFP/redor_CF/redor_CF_C5/PCPGCHOL/G13CpH5/2ms

(i): /home/sunyan4c/data/IFP/redor_CP/PCPG/G16CpH5/2ms S_0
/home/sunyan4c/data/IFP/redor_CP/PCPG/G16CpH7/2ms S_0

(j): /home/sunyan4c/data/IFP/redor_CP/PCPG/G20CpH5/2ms S_0
/home/sunyan4c/data/IFP/redor_CP/PCPG/G20CpH7/2ms S_0
/home/sunyan4c/data/IFP/redor_CP/PCPGCHOL/G20C_pH5

Figure 14

(a): /home/sunyan4c/data/IFP/ctdqbu/A7G8_IFP_pH5/PCPG/MAS_8kHz/L32-s0

(b): /home/sunyan4c/data/IFP/ctdqbu/A7G8_IFP_pH5/PCPG_chol/MAS_8kHz/
L32-s0

Figure 15

(a, c): /home/sunyan4b/data/IFP-redor/5AC-9FN/pH5/

(b, d): /home/sunyan4b/data/IFP-redor/5AC-9FN/pH7/redor-16ms-043007

(e, g): /home/sunyan4b/data/IFP-redor/9FC-13GN/pH5/sum spectra

(f, h): /home/sunyan4b/data/IFP-redor/9FC-13GN/pH7/

(i, k): /home/sunyan4b/data/IFP-redor/13GC-17MN/pH5/

(j, l): /home/sunyan4b/data/IFP-redor/13GC-17MN/pH7/

Figure 16

(a): /home/sunyan4c/data/IFP/ctdqbu/V11A12-pH5/L144

(b): /home/sunyan4c/data/IFP/ctdqbu/A12G13-pH5/032508/L144

Figure 17

(a): /home/sunyan4c/data/IFP/mutants-CNREDOR/V11A12/16ms

(b): /home/sunyan4c/data/IFP/mutants-CNREDOR/A12G13/16ms

Figure 18

(a): /home/sunyan4c/data/IFP/pdsd/U-I10E11_pH5/minus50/sum

(b): /home/sunyan4c/data/IFP/pdsd/U-N12G13-pH5/minus_50C/pdsd_N12G13
_pH5

Figure 20

(a): /home/sunyan4c/data/IFP/pdsd/U_I10E11_pH4/sum_minus50

(b): the same as figure 18(a)

(c): /home/sunyan4c/data/IFP/pdsd/U-I10E11_pH7/pdsd-minus50

Figure 21

(a): the same as figure 20(c)

(b): /home/sunyan4c/data/IFP/pdsd/U-I10E11_pH7/pdsd-I10E11ph7-081308_0C

(c): /home/sunyan4c/data/IFP/pdsd/U-I10E11_pH5/zerodegree/pdsd-081208-I10E11

(d): the same as figure 20(a)

(e): /home/sunyan4c/data/IFP/pdsd/U-N12G13-pH7/minus50C/pdsd_U-N12G13-pH7-minus50

(f): /home/sunyan4c/data/IFP/pdsd/U-N12G13-pH7/pdsd_U-N12G13-pH7-0C

(g): /home/sunyan4c/data/IFP/pdsd/U-N12G13-pH5/POPC_POPG_0C/pdsd_N12G13-0C_pH5

Figure 22

(a): /home/sunyan4c/data/IFP/P31/P31_spectra_membranes/DTPCPG_pH5

(b): /home/sunyan4c/data/IFP/P31/P31_spectra_membranes/DTPCPG_pH7

(c): /home/sunyan4c/data/IFP/P31/P31_spectra_membranes/PCPG_noIFP

Figure 24

(a): /home/sunyan4c/data/IFP/redor_CP/PCPG/G1CpH5/32ms

(b): /home/sunyan4c/data/IFP/redor_CP/PCPG/L2CpH5/32ms

(c): /home/sunyan4c/data/IFP/redor_CP/PCPG/F3CpH5/32ms

(d): /home/sunyan4c/data/IFP/redor_CP/PCPG/A5CpH5/32ms

(e): /home/sunyan4c/data/IFP/redor_CP/PCPG/I6_pH5/32ms

(f): /home/sunyan4c/data/IFP/redor_CP/PCPG/F9CpH5/32ms

(g): /home/sunyan4c/data/IFP/redor_CP/PCPG/G13CpH5/32ms

(h): /home/sunyan4c/data/IFP/redor_CP/PCPG/G16CpH5/32ms

(i): /home/sunyan4c/data/IFP/redor_CP/PCPG/G20CpH5/32ms

(j): /home/sunyan4c/data/IFP/redor_CF/redor_CF_C5/PCPG/F3pH5/24ms

(k): /home/sunyan4c/data/IFP/redor_CF/redor_CF_C5/PCPG/A5C-pH5/24ms

(l): /home/sunyan4c/data/IFP/redor_CF/redor_CF_C5/PCPG/I6_pH5/24ms

(m): /home/sunyan4c/data/IFP/redor_CF/redor_CF_C5/PCPG/F9C-pH5/24ms

(n): /home/sunyan4c/data/IFP/redor_CF/redor_CF_C5/PCPG/G13-pH5/24ms

(o): /home/sunyan4c/data/IFP/redor_CF/redor_CF_C16/PCPG/G1CpH5/24ms

(p): /home/sunyan4c/data/IFP/redor_CF/redor_CF_C16/PCPG/L2CpH5/24ms

(q): /home/sunyan4c/data/IFP/redor_CF/redor_CF_C16/PCPG/F3_pH5/24ms

(r): /home/sunyan4c/data/IFP/redor_CF/redor_CF_C16/PCPG/I6_pH5/24ms

(s): /home/sunyan4c/data/IFP/redor_CF/redor_CF_C16/PCPG/F9_pH5/24ms

(t): /home/sunyan4c/data/IFP/redor_CF/redor_CF_C16/PCPG/G13_pH5/24ms

(u): /home/sunyan4c/data/IFP/redor_CF/redor_CF_C16/PCPG/G16CpH5/24ms

Figure 28

(a): /home/sunyan4c/data/IFP/redor_CP/PCPG/G1CpH7/32ms

(b): /home/sunyan4c/data/IFP/redor_CP/PCPG/L2CpH7/32ms

(c): /home/sunyan4c/data/IFP/redor_CP/PCPG/F3CpH7/32ms

(d): /home/sunyan4c/data/IFP/redor_CP/PCPG/A5CpH7/32ms

(e): /home/sunyan4c/data/IFP/redor_CP/PCPG/I6_pH7/32ms

(f): /home/sunyan4c/data/IFP/redor_CP/PCPG/F9CpH7/32ms

(g): /home/sunyan4c/data/IFP/redor_CP/PCPG/G13CpH7/32ms

(h): /home/sunyan4c/data/IFP/redor_CP/PCPG/G16CpH7/32ms

(i): /home/sunyan4c/data/IFP/redor_CP/PCPG/G20CpH7/32ms

(j): /home/sunyan4c/data/IFP/redor_CF/redor_CF_C5/PCPG/F3_pH7/24ms _031809

(k): /home/sunyan4c/data/IFP/redor_CF/redor_CF_C5/PCPG/A5CpH7/24ms

(l): /home/sunyan4c/data/IFP/redor_CF/redor_CF_C5/PCPG/I6_pH7/24ms

(m): /home/sunyan4c/data/IFP/redor_CF/redor_CF_C5/PCPG/F9_pH7/24ms

(n): /home/sunyan4c/data/IFP/redor_CF/redor_CF_C5/PCPG/G13-pH7/24ms

(o): /home/sunyan4c/data/IFP/redor_CF/redor_CF_C16/PCPG/G1CpH7/24ms

(p): /home/sunyan4c/data/IFP/redor_CF/redor_CF_C16/PCPG/L2CpH7/24ms

(q): /home/sunyan4c/data/IFP/redor_CF/redor_CF_C16/PCPG/F3_pH7/24ms

(r): /home/sunyan4c/data/IFP/redor_CF/redor_CF_C16/PCPG/I6_pH7/24ms

(s): /home/sunyan4c/data/IFP/redor_CF/redor_CF_C16/PCPG/F9_pH7/24ms

(t): /home/sunyan4c/data/IFP/redor_CF/redor_CF_C16/PCPG/G13_pH7/24ms

(u): /home/sunyan4c/data/IFP/redor_CF/redor_CF_C16/PCPG/G16_pH7/24ms

Figure 34

(b): /home/sunyan4c/data/bicelle/Bicelle-C13/purebicelle-1/bicelle-nopeptide-3-102605

(c): /home/sunyan4c/data/bicelle/Bicelle-C13/purebicelle-1/flipped/bicelle-nopeptide-flipped

(d): /home/sunyan4c/data/bicelle/IFP/A7-N15/pH7/unflipped/quecho-1-102706

(e): /home/sunyan4c/data/bicelle/IFP/A7-N15/pH7.4/flipped/quecho-1-110906

(f): /home/sunyan4c/data/bicelle/IFP/uniform-N15/pH5/unflipped/quecho-1-101106

(g): /home/sunyan4c/data/bicelle/IFP/uniform-N15/pH5/flipped/quecho-1-101106

(h): /home/sunyan4c/data/bicelle/IFP/Oct08/A5N_pH5_unflip/p31

(i): /home/sunyan4c/data/bicelle/IFP/Oct08/I10N_pH5_flip/P31

(j): /home/sunyan4c/data/IFP/P31/P31_spectra_membranes/ DTPCPG_pH5

(k): /sunyan4c/data/bicelle/HFP/uniform-N15-bicelle/powder/quecho-1-100306

Figure 35

(a): /home/sunyan4c/data/bicelle/IFP/uniform-N15-2/powder/ph5-4/sum1

(b): /home/sunyan4c/data/bicelle/IFP/uniform-N15-2/powder/pH7-3/sum

(c): /home/sunyan4c/data/bicelle/IFP/uniform-N15-2/drypeptide/ drypep-cp_ramp-110406

(d): /home/sunyan4c/data/bicelle/IFP/uniform-N15-2/drypeptide/MAS/cp_ramp-1-010207

(e): /home/sunyan4c/data/bicelle/IFP/uniform-N15-2/pH5/unflipped/cp_ramp-1-102606
/home/sunyan4c/data/bicelle/IFP/uniform-N15-2/pH5/flipped/cp_ramp-2-110206
/home/sunyan4c/data/bicelle/IFP/uniform-N15-2/pH7/unflipped/cp_ramp-1-102706
/home/sunyan4c/data/bicelle/IFP/uniform-N15-2/pH7/flipped/cp_ramp-2-110306

(f): /home/sunyan4c/data/bicelle/IFP/F3-N15/pH5.0/unflipped/cp_ramp-2-112806
/home/sunyan4c/data/bicelle/IFP/F3-N15/pH5.0/flipped/cp_ramp-1-120306
/home/sunyan4c/data/bicelle/IFP/F3-N15/pH7.4/unflipped/cp_ramp-2-112706
/home/sunyan4c/data/bicelle/IFP/F3-N15/pH7.4/flipped/cp_ramp-2-120106

(g): /home/sunyan4c/data/bicelle/IFP/Oct08/G4N_pH5_unflip/cp-110308
/home/sunyan4c/data/bicelle/IFP/Oct08/G4N_pH5_flip/cp_ramp_112308
/home/sunyan4c/data/bicelle/IFP/Oct08/G4N_pH7_unflip/cp-110308
/home/sunyan4c/data/bicelle/IFP/Oct08/G4N_pH7_flip/cp_ramp-110508

(h): /home/sunyan4c/data/bicelle/IFP/Oct08/A5N_pH5_unflip/sum
/home/sunyan4c/data/bicelle/IFP/Jan09/A5_pH5_flip_2

/home/sunyan4c/data/bicelle/IFP/Oct08/A5N_pH7_unflip/cp-122308

(i): /home/sunyan4c/data/bicelle/IFP/Oct08/I6N_pH5_unflip/cp-110908
/home/sunyan4c/data/bicelle/IFP/Oct08/I6N_pH5_flip/cp_112208
/home/sunyan4c/data/bicelle/IFP/Oct08/I6N_pH7_unflip/cp_ramp

(j): /home/sunyan4c/data/bicelle/IFP/A7-N15/pH5/unflipped/cp_ramp-3-102306
/home/sunyan4c/data/bicelle/IFP/A7-N15/pH5/flipped/cp_ramp-2-102906
/home/sunyan4c/data/bicelle/IFP/A7-N15/pH7/unflipped/cp_ramp-2-102505
/home/sunyan4c/data/bicelle/IFP/A7-N15/pH7/flipped/sum

(k): /home/sunyan4c/data/bicelle/IFP/Oct08/G8N_pH5_unflip/cp-120408
/home/sunyan4c/data/bicelle/IFP/Oct08/G8N_pH5_flip/sum

(l): /home/sunyan4c/data/bicelle/IFP/Oct08/F9N_pH5_unflip/sum

(m): /home/sunyan4c/data/bicelle/IFP/Oct08/I10N_pH5_unflip/cp-120808
/home/sunyan4c/data/bicelle/IFP/Oct08/I10N_pH5_flip/sum

Figure 36

(a): /home/sunyan4c/data/bicelle/IFP/Oct08/uni_pH5_unflip/piwimz_122508
/home/sunyan4c/data/bicelle/IFP/Oct08/uni_pH5_flip/piwimz-110308

(b): /home/sunyan4c/data/bicelle/IFP/Oct08/uni_pH7_unflip/piwimz-103108

(c): /home/sunyan4c/data/bicelle/900M_data/IFP_F3A7_pH5_unflip_2D
/home/sunyan4c/data/bicelle/900M_data/IFP_F3A7_pH5_flip_2D

(d): /home/sunyan4c/data/bicelle/900M_data/IFP_F3A7_pH7_unflip_2D
/home/sunyan4c/data/bicelle/900M_data/IFP_F3A7_pH7_flip_2D

(e): /home/sunyan4c/data/bicelle/IFP/Oct08/G4N_pH5_unflip/piwimz-102508
/home/sunyan4c/data/bicelle/IFP/Oct08/G4N_pH5_flip/piwimz-110808-1

(f): /home/sunyan4c/data/bicelle/IFP/Oct08/G4N_pH7_unflip/piwimz-102908
/home/sunyan4c/data/bicelle/IFP/Oct08/G4N_pH7_flip/piwimz-110508

(g): /home/sunyan4c/data/bicelle/IFP/Jan09/A5_pH5_flip_PIWIMZ

(h): /home/sunyan4c/data/bicelle/IFP/Oct08/I6N_pH5_flip/piwimz-112208

(i): /home/sunyan4c/data/bicelle/IFP/Oct08/G8N_pH5_unflip/piwimz-120408
/home/sunyan4c/data/bicelle/IFP/Oct08/G8N_pH5_flip/piwimz-121908-2

(j): /home/sunyan4c/data/bicelle/IFP/Oct08/I10N_pH5_unflip/piwimz-120808

/home/sunyan4c/data/bicelle/IFP/Oct08/I10N_pH5_flip/piwimz_121708

Figure 37

(a): /home/sunyan4c/data/bicelle/IFP/Oct08/uni_pH5_unflip/cp_ramp_al_512

(b): /home/sunyan4c/data/bicelle/900M_data/IFP_uni_pH5_unflip_1D

(c): /home/sunyan4c/data/bicelle/IFP/Oct08/F3A7_flip_pH7/piwimz_111308

(d): the same as Figure 36(d)

Figure 38

(a): /home/sunyan4c/data/bicelle/900M_data/IFPG1S_F3A7_pH5_unflip_2D
/home/sunyan4c/data/bicelle/900M_data/IFPG1S_F3A7_pH5_flip_2D

(b): /home/sunyan4c/data/bicelle/900M_data/IFPG1S_F3A7_pH7_unflip_2D
/home/sunyan4c/data/bicelle/900M_data/IFPG1S_F3A7_pH7_flip_2D

(c): /home/sunyan4c/data/bicelle/900M_data/IFPG1V_F3A7_pH5_unflip_2D
/home/sunyan4c/data/bicelle/900M_data/IFPG1V_F3A7_pH5_flip_2D

(d): /home/sunyan4c/data/bicelle/900M_data/IFPG1V_F3A7_pH7_unflip_2D
/home/sunyan4c/data/bicelle/900M_data/IFPG1V_F3A7_pH7_flip_2D

Figure 39

(a): /home/sunyan4c/data/bicelle/HFP/uniform-N15-bicelle/unflipped/quecho-1-100306

(b): /home/sunyan4c/data/bicelle/HFP/uniform-N15-bicelle/flipped/quecho-2-100306

(c): /home/sunyan4c/data/bicelle/HFP/uniform-N15-bicelle/pH7/unflipped/cp_ramp-1-101706

(d): /home/sunyan4c/data/bicelle/HFP/uniform-N15-bicelle/flipped/cp_ramp-1-100406

(e): /home/sunyan4c/data/bicelle/HFP/uniform-N15-dimer/unflipped/cp_ramp-1-110806

(f): /home/sunyan4c/data/bicelle/HFP/uniform-N15-dimer/flipped/cp_ramp-2-111306

(g): /home/sunyan4c/data/bicelle/HFP/FP3K-5GAL-N15/bicelle/cp_ramp-2-070806/

(h): /home/sunyan4c/data/bicelle/HFP/FP3K-14AAG-N15/unflipped/cp_ramp-4-082406

(i): /home/sunyan4c/data/bicelle/HFP/FPdm-A6-N15/cp_ramp-3-091506

(j): /home/sunyan4c/data/bicelle/HFP/uniform-N15-bicelle/powder/cp_ramp-1-100706

Figure A2

(a): /home/sunyan4c/data/IFP/P31/P31_spectra_membranes/POPC_PG_pH5

(b): /home/sunyan4c/data/IFP/P31/P31_spectra_membranes/POPCPG_pH7

(c): /home/sunyan4c/data/IFP/P31/P31_spectra_membranes/DTPCPG_pH4

(d): /home/sunyan4c/data/IFP/P31/P31_spectra_membranes/DTPCPG_CHOL_pH5

(e): /home/sunyan4c/data/IFP/P31/P31_spectra_membranes/PCPG_pH5_5FDPPC

(f): /home/sunyan4c/data/IFP/P31/P31_spectra_membranes/DTPC_PG_PH7_16FDPPC

(g): /home/sunyan4c/data/IFP/P31/P31_spectra_membranes/DTPCPGCHOL_5FDPPC_pH7

(h): /home/sunyan4c/data/IFP/P31/P31_spectra_membranes/POPCPG_pH7_10degree

(i): /home/sunyan4c/data/IFP/P31/P31_spectra_membranes/DTPCPG_pH4_10degree

(j): /home/sunyan4c/data/IFP/P31/P31_spectra_membranes/DTPCDTPG_pH5_10C

(k): /home/sunyan4c/data/IFP/P31/P31_spectra_membranes/DTPCPG_pH7_10C

(l): /home/sunyan4c/data/IFP/P31/P31_spectra_membranes/DTPCPG_PH7_5FDPPC_10C

(m): /home/sunyan4c/data/IFP/P31/P31_spectra_membranes/DTPCPGCHOL_5FDPPC_pH7_10degree

Figure A3

(a): /home/sunyan4c/data/IFP/redor_CP/PCPGCHOL/G1C_pH5

(b): /home/sunyan4c/data/IFP/redor_CP/PCPGCHOL/A5C_pH5

(c): /home/sunyan4c/data/IFP/redor_CP/PCPGCHOL/G20C_pH5

(d): /home/sunyan4c/data/IFP/redor_CF/redor_CF_C5/PCPGCHOL/A5CpH5

(e): /home/sunyan4c/data/IFP/redor_CF/redor_CF_C5/PCPGCHOL/F9CpH5

(f): /home/sunyan4c/data/IFP/redor_CF/redor_CF_C5/PCPGCHOL/G13CpH5

Figure A4

/home/sunyan4c/data/IFP/redor_CP/PCPGCHOL/G1C_pH7

Figure A6

(a): /home/sunyan4c/data/bicelle/900M_data/IFP_M17N_pH5_unflip_2D

(b): /home/sunyan4c/data/bicelle/900M_data/IFP_M17N_pH7_unflip_2D